3D SIMULATION OF EXTERNAL BEAM RADIOTHERAPY

Vom Fachbereich Informatik

der Technischen Universität Darmstadt

zur Erlangung des akademischen Grades eines

Doktor der Ingenieurwissenschaften (Dr.-Ing.)

genehmigte Dissertation

von

M.Sc. Grigorios Karangelis

aus Trikala, Griechenland

Referent: Prof. Dr. –Ing. José Luis Encarnação
Korreferent: Prof. Dr. –Ing. Georgios Sakas

Tag der Einreichung: 29 Oktober 2004
Tag der mündlichen Prüfung: 13 December 2004

Darmstaedter Dissertation - D17

Acknowledgments

Hereby, I show gratitude to all the persons who have involved and contributed directly or indirectly to my work and to this thesis.

I would like to express my deepest appreciation to my supervisor, Prof. José Luis Encarnação, for giving me the chance to share probably the most important part of my carrier in an ideal scientific environment, which he and his partners manage to build over years at FhG-IGD in Darmstadt. His guidance and support has been for me the best supplies to go accomplish this task.

Comprehensive thanks go to Prof. Georgios Sakas, for giving me the chance to visit Germany and to initiate here my career. His constant support on the preparation of this thesis, on scientific projects and on life matters have been by far the most valuable supplies for me all these years. The same valuable feelings I express for Prof. Nikolaos Zamboglou, the father of Exomio, for his extremely helpful scientific input during the project Exomio, offering an excellent clinical environment to develop our application. I would also like to thank him for his comments and suggestions on my work. I will never forget his motivation and emotional support on several issues. Further more I would like to thank the directors of Medintec GmbH, Ulrich Borman and Erik Van Hoft, for the financial support of the Exomio project. In addition special thanks goes to Prof. Dr. Dimos Baltas for his valuable support on different matters.

I feel deeply grateful to my formal director in Technical Institution of Athens for his encouragement on taking a big step in my life, Prof. Dr. Dionisis Cavouras. Further more I would thank all my colleagues and students in the department of Cognitive Computing and Medical Imaging, for providing me so much help all these years. Among them, I would express my special thanks to all persons involved in the Exomio project developments, and mostly to my old friend and colleague, Wenli Cai, for his support during my first years in Darmstadt. Analogous thanks I express to Stefan Volmer and Stefan Walter. My special thanks goes also to my IGD colleagues Min Wang, Evelyn Firle, Stefan Wersag and Wei Chen. Special thanks goes to the formal IGD visitor Eliana Vasquez Osiorio, for the excellent scientific cooperation and brainstorming. Part of recognition goes to her Prof. Oscar Ruiz for an excellent cooperation during his visit.

My appreciative thanks goes to all colleagues in Medcom GmbH for their contribution during Exomio project, especially to Marcus Grimm and Roland Ohl. My Greek thanks I would like to offer to the Greek engineering group composed from Jianni Nomikos, Stelios Zimeras and Ilias Saxpazidis for the nice times we had together. Also, I like to express my thanks to all the other formal IGD members and students working or having worked in our InViVo family, including Michael Richtscheid, Stefan Großkopf, Jürgen Jäger, Michael Lahanas, Matthias Balwierz, Marian Wischkony, and Nicolas Weber.

Finally, I would like to thank the most precious people of my life; my family and especially my wife for her unlimited patience and support all these years.

Preface

Computer Graphics (CG) is the technology with which pictures – in the general sense (synthetic graphics as well as grayscale and color images) – are generated or acquired, managed, displayed, processed in an application-oriented manner by means of computers, and with which pictures are also correlated with non-graphical application data (From IGD - Computer Graphik TOPICS Magazine). The evolution of CG the last 30 years enabled important computer science and information technology trends to incorporate in many daily life aspects [Encar03]. As an example, although CG technology and medicine are two sciences very different to each other, excellent results for the patient diagnosis and treatment outcome can be achieved if both are combined, improving this way the quality of life.

In the last 25 years the introduction of the computers in medicine was mend to open new horizons for several medical applications. The evolution started using computers for complex and time-consuming calculations. This could involve the processing of large amount of data or the derivation of complex mathematical results. Beyond that assistance the greatest evolution in medical technologies was brought through medical imaging and applied computer graphics in medicine. The applications are several and can be separated into simple diagnostic procedures up to very complex treatment surgery. Although that medical imaging applications in radiation therapy can be separated into several categories and many of them require intensive calculations, imaging components are essential. The use of properly build technology allows nowadays non-expert computer users in medicine, usually medical oriented users, to administrate software applications and to contribute in the daily clinical outcome with much higher influence.

Most medical imaging application base their functionality on replacing the physical patient model with the digital data of the patient coming from any medical imaging modality. Medical imaging techniques offer unique capabilities on collecting digital data of the human body. Nowadays technical evolutions allow the generation of 3D data within a few moments. This is a fact for several imaging modalities. The 3D data set have a great benefit over conventional 2D images, especially in cases with complex anatomy or pathology. Clinical evaluations of current 3D techniques imaging have demonstrated their usefulness in both diagnostic and therapeutic applications. Computed tomography is the most common modality used in radiation oncology mostly due to the use of the HU and their relation with the electron densities of the tissues. Recent advances in the specific area are the helical CT and nowadays the volumetric helical CT scanner. These systems have the capability to generate CT volumes with high contrast, high resolution and low noise with in a few seconds.

Radiotherapy treatment is a very demanding cancer treatment process. The aim of the treatment is to cure or to limit the disease having as minimum as possible damage of healthy tissues, the process is composed from several steps that they are highly depended to each other in order to bring the wanted result. One could separate them into three deferent categories; the treatment planning and evaluation, the planning verification before and after treatment and finally the treatment itself. It is reasonable to think that a very precise planning of a treatment would be a failure if the patient positioning during treatment were wrong; and of course vice versa, an exact patient positioning during treatment would be useless as long as the planning process has been done incorrectly. To avoid any of the above cases to occur they must be evaluated using the appropriate verification tools and procedures, which also must be accurate and previously clinically established. Since a few years ago a big part of the above procedures use to take place with

several hardware components involved. Currently more and more procedures are going digitally and it has become a common aim for the oncology clinics to go filmless, which is a cost effective and productive solution.

The above, present the state of the art. This work is a contribution in the chain of the radiotherapy process from the medical software application point of view. The results of this work are focusing, to provide direct and indirect assistance to a group of patients suffering from cancer disease. In principle the digital patient data are used instead of the physical patient in order to perform the geometric planning. The results of this work involve the planning and partly the evaluation steps of the radiation therapy process.

Fully 3D definition of volumetric structures is a unique feature introduced from this thesis. Such functionality provides higher degree of freedom to the clinicians for investigating fully the 3D information of the digital volumes. Semi-automatic segmentation of the spine is an essential tool used delay for the extraction of the spine's volume in order to prevent its exposure on high dose levels. Main advantages of the methods are the increased efficiency and the improved time rates during volume segmentation.

An interesting part of this work is the compensation of breathing artifacts as they are recorded and reconstructed on the surfaces of the acquired computed tomography medical volumes. This kind of artifacts is a source for potential errors during treatment planning and treatment evaluation. In this work we present a method for eliminating these inaccuracies and thus improving the treatment outcome.

Volume rendering is the basis for a 3D-Simulation system. Thus interactive volume reconstruction of specific body regions is always an essential tool for such systems. In this work a unique method is presented that improves reconstruction of sensitive anatomical structures and requires the minimum possible user interaction. The results of the method are unique and revolutionary for radiation therapy planning.

Finally we address a very essential issue related with the treatment planning verification. Standard methods involve the use of quantitative and numerical statistics methods of the treatment dose distribution over the target volume and the segmented organs. In this work we present methods for the visualization of the dose distribution in relation to the standard patient anatomy and the segmented anatomical structures. The results provided are unique for the qualitative treatment plan evaluation.

The solutions provided have been hosted under the 3D simulator system called ***Exomio***. ***Exomio*** aims to assist clinicians to improve the geometric planning of the patient treatment and to replace the conventional simulator system in the oncology clinics. Thus beyond the improvement of the clinical outcome and the reduced patient treatment administration bottle-neck, the clinics can reduce the patient treatment expenses using a cost effective software solution.

Frequently Used Abbreviations

1D, 2D, 3D	{one, two, three}-dimensional
3D-Sim	3D Simulation Software System
BEV	Beam's Eye View
BTF	Back-to-Front
CT	Computed Tomography
CTV	Clinical Target Volume
DICOM	Digital Imaging and Communications in Medicine
DVR	Direct Volume Rendering
DVH	Dose volume Histogram
DRR	Digital Reconstructed Radiography
GUI	Graphics User Interface
Exomio	3D simulation system
HU	Hounsfield Unit
InViVo	Interactive Visualizer of Volume Data
LN	Linear Interpolation
LiNAC	Linear Accelerator (External beam treatment unit)
LUT	Look Up Table
MIP	Maximum/Minimum Intensity Projection
MPR	Multiplanar Reconstruction - 2D image interpolated from 3D data
MRI	Magnetic Resonance Imaging
OEV	Observer's Eye View
PET	Positron Emission Tomography
Planning	Cancer Treatment Planning
PTV	Planning Target Volume
RTP	Radiotherapy Treatment Planning
RT	Radiotherapy Treatment
ROI	Region of Interest
Simulator	Radiotherapy Simulator Machine
SAD	Source to Axis Distance
SID	Source to Image detector Distance
SPECT	Single Photon Emission Computed Tomography

SR	Surface Rendering
SSD	Source to Skin Distance
TCP	Tumor Control Probability
TF	Transfer Function
TPS	Treatment Planning System
VOI	Volume Of Interest
VS	Virtual Simulator
VSS	Virtual Simulation System
voxel	Volume Element

Table of Contents

Table of Figures

Chapter 1

Introduction

1.1 Introduction

Cancer belongs to a group of disease characterized by tumor growth and spread, and is the most significant health care problem in European and Western Countries. The clinical processes used to treat cancer can be separated into drug treatments, radiation therapy [Meyer96] (RT) treatment or even a combination of them [Zambo94]. RT uses radiation in order to deliver a very accurate dose of radiation to a well-defined target volume with minimal damage to surrounding healthy tissues. The wanted result is the eradication of the disease and the improvement or prolongation of patient's life. The amount of required dose can be applied on the tumor site using external beam radiotherapy or brachytherapy [Kolot99]. Hence RT is a very demanding process that requires accuracy and affectivity not only for the elimination of the cancer sells but also for the protection of the healthy organs within the human body. In this dissertation it is of interest the radiation therapy process (RTP) using external beam radiotherapy (EBRA).

1.2 The External Beam RT Process

The RTP for malignant disease is complex and can be carried out in several steps. In the following paragraph we will go through these steps and briefly describe each one of them including the clinical specialist and the system involved each time (see Figure 1-1).

1.2.1 Target Volume Determination

The first step on the process is the patient diagnosis. The diagnostic study can be carried out on any diagnostic system including conventional x-rays or a 3D imaging modality like computed tomography (CT), magnetic resonance (MR) or nuclear medicine (Gamma-Camera, PET, SPECT). Follows the very crucial step of definition and localization of the disease (tumour) and its extensions relative to adjacent critical normal organs and tissues (target volume definition). This can be done with several ways, depending on the case study, ranging from simple clinical examinations to complex. In this step the main specialist involved is the physician and the system traditionally used is the treatment planning system (TPS).

For simple cases the X-ray fluoroscopy images produced on the real simulator can be used for the disease localization. For complex treatment cases, the data used are coming mainly from a CT scanner. The CT scanner might belong to the radiotherapy department or to a diagnostic department, but in both cases the CT's table-top must be flat and not curved (which is usually the case for diagnostic CT scanners). Further more, the CT room must be equipped with at least, three laser projectors. This laser arrangement is crucial for the patient alignment and repositioning through the RT process and exists in the simulation and treatment room as well.

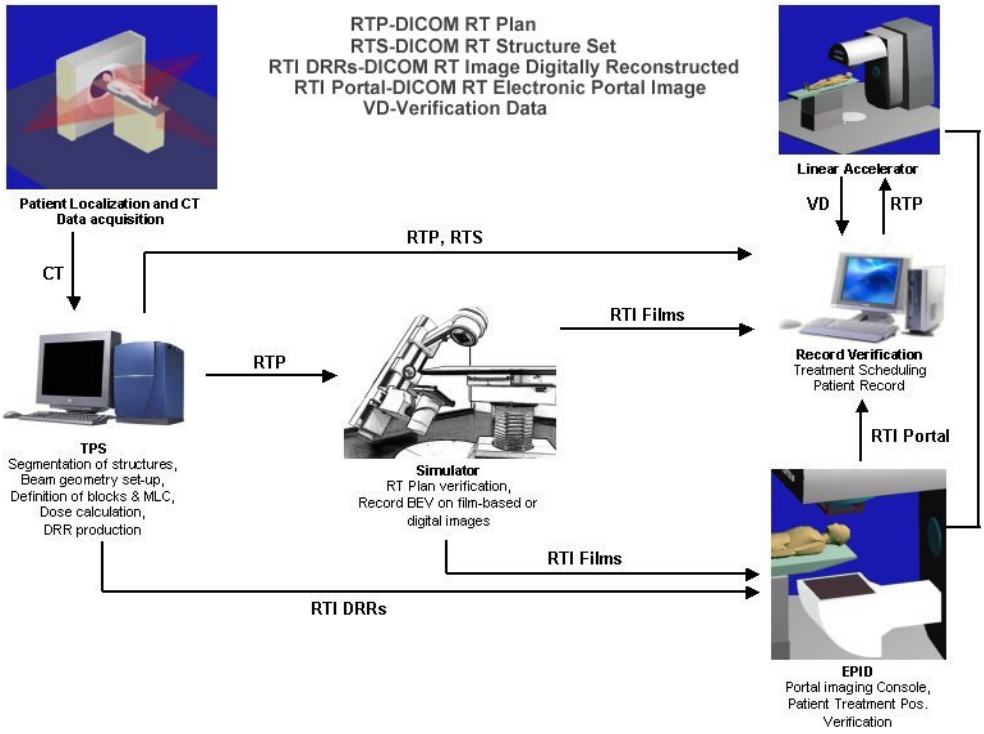

Figure 1-1. RT clinical routine and data workflow for external beam treatment planning and delivery using the conventional simulator.

1.2.2 Treatment Planning

Another step of the process is the radiation field placement, which serves to adequately cover the tumour site minimizing the dose exposure of healthy normal tissues. The specialist involved in this step is the physicist. Having the necessary number of beams placed to the appropriate anatomical location, the dose distribution for this plan will be calculated using the TPS.

1.2.3 Treatment Verification

Treatment verification is the last step before initiating the treatment. At this step treatment plan needs to be confirmed by an imaging procedure to ensure that each beam's location and shape traverses the desired anatomical volume and avoids critical structures as much as possible. The verification process usually takes place on the real simulators or on the treatment machine with the use of the portal-imaging device. In this step two specialists are involved: the physicist and the physician.

1.2.4 Treatment Delivery

The final step of the RT process is the actual treatment delivery, which takes place on the treatment machine (LiNAC) and high-energy photon or electron beams are used. In this step the patient location relative to the laser system is established using the appropriate

table translations and the beam shape and orientation is applied according to the treatment plan.

1.3 Role of Simulation in RT process

The ***Simulation*** of the RT process belongs to the most important steps of whole treatment process. During Simulation the defined treatment set-up, which is prepared on the TPS, will be simulated on the Simulator using the light field projection and the radiographic or fluoroscopic modes provided by the conventional Simulator. This process will help to mimic the radiation therapy beams in terms of divergence. In principle the Simulation process will optimise the original treatment in order to have the optimum target coverage while minimizing the dose to normal tissues. The final configuration will be recorded permanently on radiographic film.

1.3.1 The Conventional Simulator

Traditionally the device that performs the RT simulation is the Simulator (see Figure 1-2). The Simulator is a machine that emulates the geometry and the movements of the treatment unit but diagnostic quality x-rays instead of high-energy treatment rays. The Simulator has multiple functions and tends to be used somewhat differently in every RT department. The most common functionalities of the Simulator are described with more details in chapter 2. Unfortunately there are a number of disadvantages in the use of the Simulator:

a) **Image Quality:** Although the Simulator is a useful tool to define the localization of the disease and the surrounding healthy tissues, there are many cases where soft tissues due to their low x-ray absorption are not visible on the fluoroscopy or radiography. To overcome this problem often contrast medium is used. Further more, while using the fluoroscopy mode, the magnetic coils of the Simulator image intensifier suffer from distortions resulting to a distorted final image. Also, the limited size of the image intensifier detector limits the amount of the visualized patient's volume.

Figure 1-2. Illustration of the conventional Simulator. On the lower right corner the fluoroscopy of the Alderson phantom.

b) **Accuracy:** The Simulator is a hardware device composed of several mechanical parts including the x-rays head, the collimator, the gantry and the treatment couch. The mechanical components often introduce inaccuracies to the Simulation process. Therefore systematic quality control tests are needed. If the component under test does not fulfil the requirements it must be replaced.

c) **Design Constrains:** The design of the Simulator components is such that they mimic the treatment machine. Even though in some treatment cases it is not possible to perform the simulation because of difference between the LiNAC and the Simulator. One such example is the non-coplanar beam set-up with combined table and gantry rotation. This set-up can be applied on the treatment machine in absence of the

portal imaging component, but not on the real Simulator due to the interference of the tabletop with the image intensifier.

d) Clinical Costs: The installation of a Simulator is a high investment for the clinic in terms of hardware equipment, space, time and personnel. The Simulator must be installed on a room as a stand-alone device. This room of course requires the installation of special components that are necessary for the appropriate function of the Simulator. To manipulate the Simulator at least two specialised persons are needed: a technical assistance and the radiation oncologist. Furthermore the verified result of the Simulator must be recorded on radiographic films, which require an expensive process for their development.

1.3.2 The Virtual Simulator

The alternative to the Simulator device is the use of the Virtual Simulator (VS) or CT-Simulator or 3D-Simulator. Although this concept has been originally introduced, scientifically and clinically, as VS and CT-Simulation in this work we prefer to use the term ***3D-Simulation*** or 3D-Sim. The reason for that is that the 3D-Sim systems nowadays include several different functionalities that spread much further than the standard volume definition and geometric field planning, which used to be the standard system functionality for the CT-Simulators. In addition one can work using any 3D imaging modalities beyond the CT scanner, such as MR and PET for example.

The simple concept of CT-Simulation was first proposed by Sharehouse [Shero87] and has been characterised as one of the significant technological advances in radiation oncology in the past 20 years. Since today several reports have been written proven the advantage of the 3D-Sim in the RT clinical routine [Nagat90], [Nishi90], [Rosen91], [Perez94], [Perez95], [Vijay95], [Butke96], [Micha96], [Rose96], [Ragan96], [Conw97], [ValiA97], [ValiB97], [DasCh98], [Gripp99], [Vuong00], [Schie00], [McJur01]. More recent studies highlight not only the advantages of the 3D-Sim applications, but further presented results on how well the 3D-Sim packages integrate in the modern clinical RT environment [EdWon02], [Zambo02], [Houst02], [Karan02], [Bolle03], [Dicks03], [Valen03], [VanSo03], [Stras04], [StraV04]. The 3D-Simulation concept is based on the use of the digital patient data, mainly CT slices, instead of the real patient. The patient has to go first through the CT scanner. The laser localizers will be used again here for the definition of the reference point. The projected on the skin laser beams will be marked and aluminium markers will be attached the same locations prior to the CT acquisition. The volumetric CT data then will be imported on the 3D-Sim application and will be used to perform the Simulation process virtually, lack of the physical patient presence.

Similar to the conventional Simulation process, this includes the tumour localisation, placement and delineation of the necessary number of beams and verification of the beam tumour coverage (see Figure 1-3). In chapter 2, we will see that computer graphics science provides the appropriate tools to compose and generate such an environment. The RT process has to be modified and adapted to the use of the 3D-Sim. The main benefits of the 3D-Sim over the conventional Simulator are:

a) Absence of the physical patient: During the conventional Simulation process the physical patient must be present and get positioned on the Simulator couch. In 3D-Sim the patient's electronic data, mainly CT, are used for the simulation. 3D-Sim avoids the often-experienced ***bottlenecks*** in patient workload flow within a department

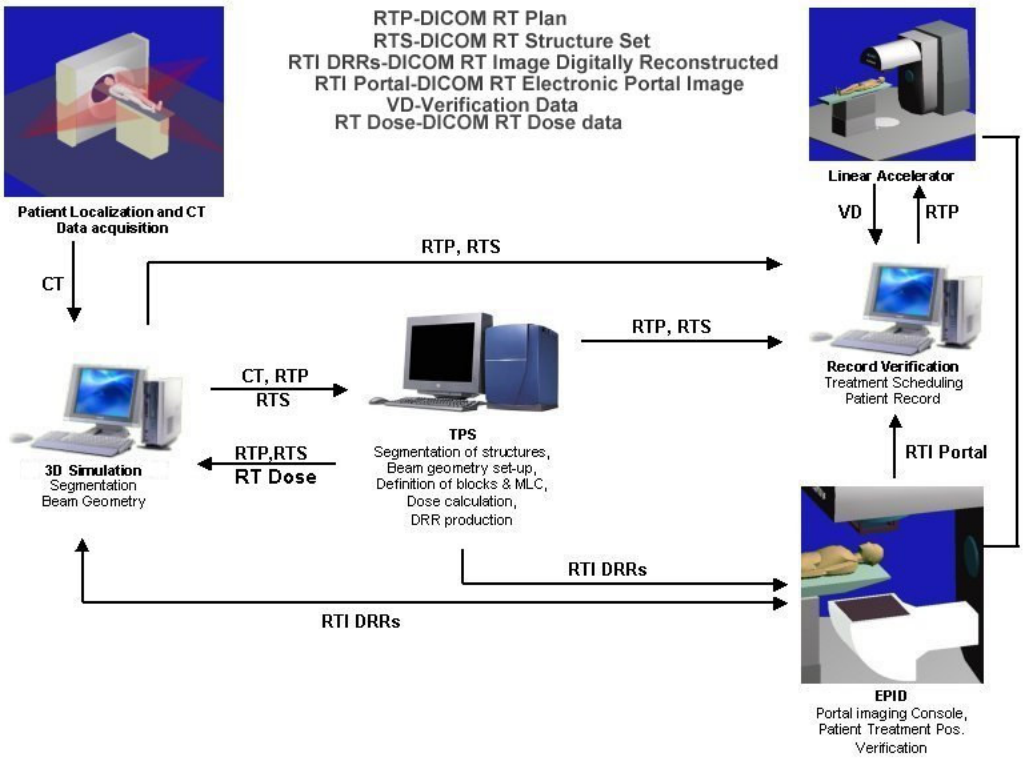

Figure 1-3. RT clinical routine and data workflow for external beam treatment plan and delivery using the ***3D-Simulation***. In this clinical environment all information can be transferred digitally lack of X-ray films.

of radiation oncology and reduces the systematic error caused due to the patient's re-positioning on the Simulator's couch.

b) Reduced Simulation Time and Personnel: Using the Simulator the average time needed to perform the Simulation process is about 20min. The 3D-Sim provides tools and technique that can reduce the time needed for the Simulation process up to 50%. In addition the only professional involved to the simulation process in the radiation oncologist.

c) Less Constrains: 3D-Sim will never face the problem mentioned in paragraph (1.2.1-c). The component limitation of different treatment units can be adapted by the 3D-Simulator and additionally collision detection algorithms can be applied as well in order to verify the geometric treatment validity.

d) Advanced Visualization: As already mentioned the Simulator can verify the simulation process using the light field projection and the 2D radiographic image. The 3D-Simulator can reconstruct the computerized reconstructed radiograph (CRR) in real time and simulate this way the fluoroscopy mode of the Simulator. CRR has a number of benefits against the conventional fluoroscopy, like the large field of view that can be used to reconstruct the patient volume and the selection of the tissues that will contribute to the reconstruction of the final image. In addition 3D-Simulators can visualise as supper imposed structures on the CRR, the target volume and the or-

gans at risk. The multi planar reconstruction views provide an ideal navigation tool to investigate complex anatomy within the patient's volume.

e) Lower Investment: Finally the 3D-Simulator is a lower investment for an oncology clinic in terms of money and space compared to the real Simulator. The only hardware needed is a personal computer (PC). The final treatment set-up can be recorded digitally or as hard copy on conventional printing paper.

1.4 Related Work

Although the idea of 3D-Sim is relatively old, only the last few years these systems became popular. The main reasons for this wave are the advances in CT technology and computer hardware technology. The invention of spiral CT was a great step towards high-speed acquisition of CT data. These days the reconstruction time of a slice for a conventional CT scanner can reach the times from 0.75 to 0.45 sec. Hence the acquisition of high-resolution volume data can be done within a few hundred seconds. Most oncology clinics will potentially obtain their own CT scanner since the CT imaging modality has become the standard modality for the oncology clinics nowadays.

The advances of the low cost computer hardware technology on the other hand, mainly processing power, graphics libraries supported by hardware and memory, allow the processing of larger volumetric data within real time. Last decade, when 3D-Sim systems start to be presented, is has been reported [Shero90] [Shero91] that the DRR images were calculated only after the definition of the final beam configuration, due to the high computational cost. A few years later different authors [Culli93] presented a near to real time calculated DRR. They used reduced interpolation rate for the ray casting applying nearest neighbour sampling. For a volume data with resolution $V = (X, Y, Z) = (256x256x128)$, the preview image needed about 1sec to be reconstructed and the final high quality $I_m = (U, V) = (512x512)$ pixel image was completed after 5-6sec. Galvin in his study [Galvi95], used a volume data set of $(X, Y, Z) = (512x512x50)$, and manage to compute a $(U, V) = (512x512)$ DRR image in 8sec. The hardware platform used for the experiments was a Voxel Q with the processing power of 10 million trilinear interpolations per second. A standard CT data acquisition performed on a spiral CT, contains typically 80-100 slices equally spaced to $3mm$ each, with grid resolution $(512x512)$. Currently to reconstruct this amount of data on a 1GHz processor requires less than 4 secs. High-resolution CT data offer the possibility to render high quality DRR images, approaching the spatial resolution of the real X-ray images produced by the conventional Simulator. Further more high quality data sets allow the visualization of any complicate anatomy in surface or transparent modes. Advances in both technologies, CT scanner and processors, promote the use of the 3D-Sim. We have to clarify that some 3D treatment planning systems offer 3D-Sim functionality with limited capabilities. The reasons that are:

a) The complicate design of the systems that require a well trained user to perform the simulation and planning and

b) The limited visualization capabilities they offer in comparison to 3D-Sim systems.

These systems are designed for physicist, scientists who are educated in use of software and computers. In general TPS systems are complicated due to their purpose, which is the dose calculation. This is the main reason why TPS systems are rarely used from physicians. Dose calculation algorithms on the other hand require high processing power in relation with the amount of data used: the less data used the faster the calcula-

tions will be completed. Thus even nowadays TPS systems can handle limited amount of data. It is common understanding that limited data resolution result to limited anatomical information. In addition for the dose calculation algorithms a surface representation of the organs of interest is required. These organs involve the body contour, the target volume and the organs at risk. Therefore these systems use basically polygon-based techniques to represent anatomical structures in 3D.

Currently there are a very small number of the dedicated Virtual Simulator (VS) systems, such as AcQsim [AcqSim], AdvantageSim [GE], [Schie00], SmartSim [SmartS], FocalSim [FocalS]. A direct comparison of between these systems it is relatively difficult to be performed. The major weaknesses or deficiencies of the current 3D-Simulator systems are:

a) Complicated user interface and therefore reduced effectiveness in user-software interaction.

b) The lack of auxiliary tools for volume definition as well as for the realization of the simulation plan.

c) In some cases limited visualization capabilities is also an issue that reduces the system performance.

User interface is a critical issue for every software system. 3D-Sim systems are complicate software with dedicated functionality. If such a system is designed with complicated user interface, the result will be the requirement of extensively training for the users as well as the complicated and time-consuming interaction. Further more the lack of effective and interactive volume definition and beam editing tools will increase the time required to simulate a treatment plan. Limited visualization capabilities might affect the outcome of the patient treatment since the high-resolution data will be less comprehensively examined from the physicians in order to localize accurately all areas of interest.

1.5 Challenges in 3D-Simulation

Although the idea of the 3D-Sim is relatively old starting from the early eighties there is still areas for improvements. Advances in technologies of radiation oncology and diagnostic imaging modalities demand the adaptation and the refinement of the 3D-Sim systems to the new technologies. In the following we will focus only on some of the challenges in the 3D-Sim and radiotherapy treatment planning, that this thesis contributes.

- **General considerations:** A very important issue is the demand for compatibility, flexibility, interactivity and user friendliness of the 3D-Sim system. The appropriate system design and the platform selection are critical in order to guarantee system compatibility and flexibility. The 3D-Sim systems must be designed for users who are not computer experts. In addition a 3D-Sim system must be capable to import large amounts of data, to process them in real time and easily manipulate them. In addition the synergy of several functional tools is critical to assure the best clinical outcome. For example the accurate visualization of the irradiation field guaranties accuracy during plan verification. Therefore the field must be reconstructed in two and also in three dimensions together with the patient volume data. The most important issue here is the visualization of irradiation field as a light projection on the patients skin. This is the most common way for verification of the field location on the external patient anatomy.

- **Interactive Volume Segmentation:** The interactive definition and visualisation of volume of interest is a demand for every 3D-Sim and treatment planning system. A special condition exists in 3D-Sim since high-resolution digital data are used. This is of great benefit for the physicians especially in cases where they have to investigate complex anatomy. But when it comes to the definition of the target volume and the organs at risk the process becomes laborious since traditionally this process takes place on the 2D axial anatomic plane stepping slice-by-slice. In addition the segmented volumes must be visualised accurately and fast.
- **Motion Artifacts Correction:** The greatest challenge probably in cancer treatment and visualization techniques is the compensation of the motion artifacts and the prediction of the moving organs during data acquisition. Although the reconstruction time for the CT scanners has been tremendously decreased, there are internal organs that their movement might cause rigorous blurring artefacts on the acquired CT images, since their deformation speed is higher than the acquisition speed. In addition the CT scanner acquires the digital images of the patient at a time moment. This means that although the internal organs are moving we see their location in space just at one moment in time. In this work we will concentrate on the reduction of the breathing artifacts that cause deformation of the skin surface.
- **Imaging:** The main difference between 3D-Sim and TPS systems is that the later perform the dose calculation and the plan optimisation according to the dose distribution on the target volume and the organs at risk. For that reason the role of 3D-Sim is getting confused, although VS provides superior quality on visualization aspects. Therefore there is a great challenge on finding techniques that can provide optimum qualitative evaluation of field configuration based on the geometric parameters and also on the dose distribution in relation to the treatment organs.

1.6 Summary and Contributions

This dissertation results from the research work while designing and implementing the 3D-Sim system called ***Exomio***. Main attention is given to techniques, which increase interactivity, accuracy and liability of the 3D-Sim system, in order to provide solutions to most of the problems addressed as challenges in the previous paragraphs.

The next chapter, Chapter 2, gives a brief overview of state-of-the-art in the 3D-Sim systems. In addition the concept of the 3D-Sim in the clinical routine is presented, as it has been established in most of the oncology clinics these days. Further more the appropriate components needed to construct a 3D-Sim system are presented. These tools involve the hardware and software platforms, the user interface and the graphic algorithms needed for the realization of the 3D-Sim. For example different transfer functions that can be used for the reconstruction of the DRR images are analysed as well their advantages and disadvantages against the real X-ray images.

A number of volume definition issues are presented in Chapter 3. As previously mentioned volume definition is the most important step of the treatment planning process. The reason of course is that for the most treatment cases, the shape and location of the target volume is a crucial factor for the irradiation field configuration. Chapter 3 presents the most common techniques used for defining structures in radiation therapy. A novel technique for volume definition is introduced, that uses closed planar contours from orthogo-

nal planes and gives the ability to generate 3D anatomical shapes with minimum user effort when compared to the traditional 2D slice-by-slice procedures. In addition a semi-automatic algorithm based on 3D contour tracing that can detect the spinal cord anatomy is presented and evaluated.

Chapter 4 describes a novel approach on compensating the surface respiratory artifacts produced during the CT acquisition. Briefly the patient's surface is used in several calculations in radiation therapy, mainly for treatment verification of the patient positioning. The value daily measured in clinical practice is called source-to-skin-distance (SSD) and represents the distance between the irradiation source and the patient skin along the iso-center axis, for the current field configuration. The calculated SSD values under standard conditions are affected from the respiratory process of the patient, which is recorded on the acquired CT data. Our algorithm will cause a shape refinement of the cross section contours that are used to define the body surface.

Volumetric visualisation has been always a challenge in radiation therapy and especially in 3D-Sim. Chapter 5 presents visualisation techniques that assist the RT process. We focus mainly on the 3D reconstruction of the thoracic region using CT data, which is especially interesting since it contains structures with very different tissue densities. A new interactive method is presented that isolates the lung volume in the pre-processing step of the volume visualisation pipeline. In addition multi-volume visualisation techniques are presented in order to visualise simultaneously the CT data volume, the target volume and the treatment field geometry, enhancing on the maximum information an observer could retrieve using volume rendering techniques.

In Chapter 6 we will present the visualization workflow that describes an integrated 3D irradiation dose display process within the 3D-Sim environments. The work of Chapter 6 is separated in two main parts: the dose re-sampling and dose visualization part. The first part involves the interpolation of the original dose volume data; a critical step when aiming to produce accurate calculation results as well as high quality 3D illustrations. The second part involves the mixed visualization between the dose and the CT-volume in two and three dimensions. Volume rendering is the vital component used for the implementation of the visualizations tools that will be presented, and aim to augment the qualitative verification of the dose distribution, the volumes of interest and the CT data.

The conclusions of this work can be found in Chapter 7. The research work of this thesis rose as challenges from the design and implementation process of the 3D-Sim called ***Exomio*** [Exomio], [Karan01], [Zambo02]. Some of the challenges in 3D-Sim have been addressed in this work and the results represent state-of-the-art components for a 3D-Simulation system. Nevertheless there is always place for improvements and future research.

Chapter 2

3D Virtual Simulation: System Concept

2.1 Introduction

The RT process is demanding and complex, composed of several steps that have been already described generally in chapter 1. One important step in this process is labelled as ***simulation.*** Repeating the principle of simulation, it is basically the localisation of the target volume, the area that will receive the maximum amount of dose, and the organ at risk, volumes that must receive the minimum dose. Once these structures have been well defined, the next step is the definition of the irradiation fields in relation with the target volume and the organs at risk. In addition during treatment the patients receive their therapy via a number of fractions. Therefore there must be a confirmation that the irradiation orientation and the structure localization have remained unmodified.

Both steps described above can be performed on the conventional simulator. There are studies shown that the use of the sophisticate treatment techniques including the use of the treatment simulator, improve the patient outcomes in contrast to treatments that lack the simulator. In other words it has become the last two decades a common understanding that the simulator is an essential component in the RT. The last decade there is an evolution in the technology of the computed tomography scanners (CT) that tend to become more common in the radiotherapy departments as part of the standard equipment. Part of this evolution is also the use of the 3D-Sim software systems that together with the CT scanners and some additional equipment integrate the clinical procedure called CT-Simulation. Nowadays the 3D-Sim systems fulfil or even go beyond the criteria of a real simulator for most treatment cases, replacing in many radiation oncology departments the later.

The information and functional level of a 3D-Sim software, should be comparable with that of a real simulator and further more it should provide high quality imaging algorithms for 3D data visualization and manipulation. In addition they aim to “virtualise” the real clinical environments of the RT process up to a level. This means that there are several procedures that must be simulated and modelled and these can be separated in two groups:

a) Simulation of the mechanical movements of the real machine. This includes the rotation of the components gantry, collimator and couch, as well as translation of the couch table-top to the directions vertical, lateral and longitudinal. The manipulation of these components is necessary in order to achieve the optimum field configuration for each treatment case.

b) Reconstruction of the same type of images produced from the conventional simulator and LiNAC machines [1] (the differences of the two systems LiNAC and Simulator have been given in chapter 1). This involves the generation of digital reconstructed radiographs, simulating kilovoltage and megavoltage X-ray images. The generation of a real 2D X-ray image, is based on the attenuation of the energy of the X-ray beams while they are travelling through a material, and in our case through the patient body. The attenuated beam energy is detected on the X-rays radiographic film or on the surface of the image detector or intensifier. Since several decades these 2D X-ray images are used for localization and treatment verification in radiation oncology.

c) Reconstruction of the patient's surface, external or internal anatomy, using the digital patient data sets, coming mainly from the CT scanner. This concept is important due to the lack of the physical patient. These images can be used for verification purposes in order to detect the interaction of the treatment beams with the patient's body.

d) Modelling of the irradiation machine or the simulator machine including patient orientation. This information will provide an overview of the simulation process, indicating in approximation the localization area of the patient for the specific treatment as well as the orientation of the patient on the treatment couch.

This chapter is separated in two parts. In the first part the hardware components of the real simulator and their role is briefly described so as to better clarify the functionality of the real machine. In the second part the minimum required tools that can compose a virtual simulator system are described.

2.2 The Treatment Simulator

The treatment simulator serves two purposes in the oncology department: as tumour localization tool and as a verification tool adapting the same treatment configuration and patient localisation, as would happen on the treatment machine. An industrial simulator (Elekta) for external beam radiotherapy is illustrated in Figure 2-1. Nowadays several industrial vendors provide real Simulators, with special mechanical features in order the simulator to be adapted to different LiNAC configurations. For many years the film-based simulation (digital images are acquired through digitisation of radiographic films), was adequate and thus there have been very few improvements in the technology of the treatment simulators. However in recent years the need for digital simulation image has grown significantly following the new innovations in radiotherapy technology such as computerized multileaf collimator, electronic portal imaging device, and networking of patient data. The direct acquisition of digital images during patient simulation, allow an immediate, easy and efficient association of the above-mentioned information in combination to the treatment simulation information [Atari95].

The most advanced development of the simulator involves the conversion/upgrade of the treatment simulator to emulate digital volume acquisition as done using the cone-beam CT. Cone-beam CT performs direct 3D reconstruction from a set of 2D projection data obtained with a cone-shaped beam geometry, in contrast to the conventional CT where 1D projections are obtained with a fan-beam geometry and are used to reconstruct

[1] Since the two systems, LiNAC and Simulator have the same geometry, any movement performed in one machine coincides absolutely on the other. There for we have to simulate only one of them. Their main difference is at the energies they are using and therefore at the X-ray images produced.

2D information [Smith90]. The cone-beam volume reconstruction in radiotherapy has been proposed from several authors. The idea has been applied on the simulator [Cho98], [Verel99], [Agost01] as well on the treatment accelerator. In the first group, which is of our concern, the aim has been the integration of the Sim-CT functionality in the clinical routine attempting to replace the digital data acquisition using the conventional CT scanner. A typical diagram of the hardware configuration of the radiotherapy simulator as proposed in [Cho98] is shown Figure 2-2. Important components in this configuration are considered the digital fluoroscopy unit (digital spot imager or DSI), commonly used in diagnostic imaging and the volume CT reconstruction algorithm combined with the distortion correction algorithm. To improve image quality, the digital simulator images have been acquired using pulsed X-rays at high tube current. Unavoidable geometric distortion influences the image appearance due to the imperfection of the electron optics and thus was necessary to correct for geometric distortion before applying the CT reconstruction algorithm.

Figure 2-1. An industrial simulator type from Elekta.

An additional problem is also produced from the limited size of the detector, which restricts the application to be used in large body sections. Verellin ***et al.*** in their work [Verel99] used a detector array composed of 288 cadmium tungstate single crystal scintillators attached externally to the simulator image intensifier. That configuration was free from distortions and in addition one could select three different kinds of fields of view (25cm, 35cm and 50cm). The results of their work showed that the HU values produces in the volumes generated using the cone-beam simulator are very near to those produced from the CT scanners and thus dose distribution can be also calculated with good precision. The integration of Sim-CT in the clinical environment was successful up to a level. The limitations are coming mostly from the mechanical components such as the high current required for the X-ray tube, the limited field of view on the acquired volumes was a result of the detector size. In addition the data processing and the volume reconstruction phase is really time consuming for high-resolution volumes.

The image detectors and the X-ray technology continuously improves and probably some of the above limitation will be solved within the next few years. In any case the product of a Sim-CT is a reconstructed high-resolution volume that will be used to feed a TPS or a 3D-Sim software. It is common that the 3D-Sims are preferred due to their ability to deal will large amount of data. The clinical workflow where the Sim-CT is used is still a research topic and only in a few centres. Usually in the standard clinical routine an average of four to seven digital images are acquired during treatment simulation. The 3D-Sim can be used as a replacement or add on to the conventional radiotherapy simulator. In either way it is for sure that 3D-Sim can improve the treatment planning workflow. In the next paragraphs we will go through the most important mechanical parts that com-

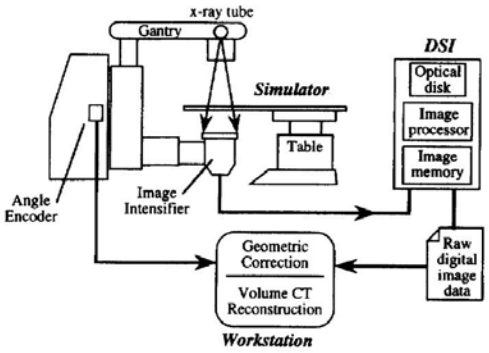

Figure 2-2. Hardware configuration of the digital radiotherapy simulator.

pose the simulator. We will describe their geometry and function in order to better understand which functionalities must/can be simulated from a software system and how.

In the hardware configuration diagram of Figure 2-2 one can notice the main mechanical simulator components, which are: the simulator's gantry (hosts the imaging components) and the simulators couch (composed by the table top and the table support). When patient lies down on the simulator's top table, X-rays are emitted from the irradiation source of the simulator, passing through the patient, and detected by image receptor. The detected X-ray image presents the structures (parts of the patient), which are penetrated by X-ray. Using the LiNAC, these structures will be irradiated by the radiation source, if the LiNAC is set by the same parameters as in the simulator. This is a very important tool for physicians to investigate the relationship between beam and patient tissues (including tumor, and other critical organs). Besides this image, physicians also can use their views to check the motion of the machine and the radiation projection area on the patient body. The former is what the detector sees, which is called Beam's Eye View (BEV), and the later is what physician sees, which is called Observer's Eye View (OEV). Both BEV and OEV are basic visual information in RTP.

2.2.1 Simulator's Gantry

The gantry is a common part for the simulator and the LiNAC, with similar geometry and the same degree of freedom. Nevertheless internal and external components are very different for both systems. In a simulator the gantry hosts the low energy diagnostic X-ray source, the collimator, the light source, the wires for the generation of the treatment field, the block tray and the image intensifier. In contrast the gantry of the LiNAC hosts, the treatment source, the collimator that defines the shape of the irradiation field, the multileaf collimator (MLC) if available, the block tray and the portal imaging device.

In the real simulator the X-ray source is responsible for the generation of the appropriate energy of photon beam. The shape of the irradiation beam can be modified using the collimator, the lead blocks or the MLC. The direction of the irradiation field can be changed be rotating the gantry or the collimator. The gantry can perform rotations around the axis Yf as can be seen in Figure 2-3 and the collimator around the Z-axis.

As already mentioned, the "head" of the simulator's gantry host a normal light source that is used for verification purposes and as an indicator of the irradiation field. The light field is always activated prior to the generation of the X-ray image, indicating the field shape and orientation projected on the patient's skin. The light field verification is the most important visual tool used for the verification of the field orientation and shape relative to the patient position.

2.2.1.1 Imaging Components

In this paragraph we will try to briefly describe the components that contribute to the generation of the X-ray image on a treatment simulator. To perform a comparison of the virtual generated X-ray images, DRR and MIP, with the real X-ray images produced from the simulator we have to focus to those components that affect the image quality. To generate X-ray images on the real simulator the same principle and components are used as in diagnostic imaging. The major components involved are: the high voltage generator, the X-ray tube, the image detector (or image intensifier), the video display monitor, the film cassette and the X-ray film. The real simulator allows the generation of two types of X-ray images: radiographic (static) images that are captured on the X-ray film and the dynamic real time fluoroscopy, that allows the observation of internal organs and structures in relation to time.

However, if we compare the diagnostic imaging and the radiotherapy imaging, there is a major difference between the two techniques. That is the large distance between the focal spot and the image intensifier for the simulator. This distance varies on the simulator between 100cm to 170cm depending on the treatment case, and results to attenuation of the beam intensity at a high level, increasing scatter to the detector. Although techniques have been developed to compensate the scatter effect it still remains a major reason for generating low quality X-ray images.

The image detector can be also a reason for mechanical collisions, which are another constrain of the real simulation especially in cases where the couch and gantry are rotated. Figure 2-4 illustrates such a case. The collision is coming from the image intensifier, which is located on the lower end of the simulator's gantry. Although this treatment case can be applied in the treatment machine, the real simulator cannot handle it.

As previously mentioned the real simulator can generate real time X-ray images (fluoroscopy mode) and static. Although real time images have a great advantage against static there is a limitation in the design of the X-ray generators, since fluoroscopy mode takes much more time than radiographic exposures. In order to avoid melting of the generator a much lower tube current must be used. Further more for wider heat spreading on the target a double focal spot is used, larger in the case of fluoroscopy than the radiographic exposure. The impact of the larger focal spot is that objects will appear to have "blurred" edges due to larger penumbra.

The component that cooperates with the X-ray beam to generate the real time images is the image intensifier. The use of the image intensifier gives the ability while the fluoroscopy mode is on to move other com-

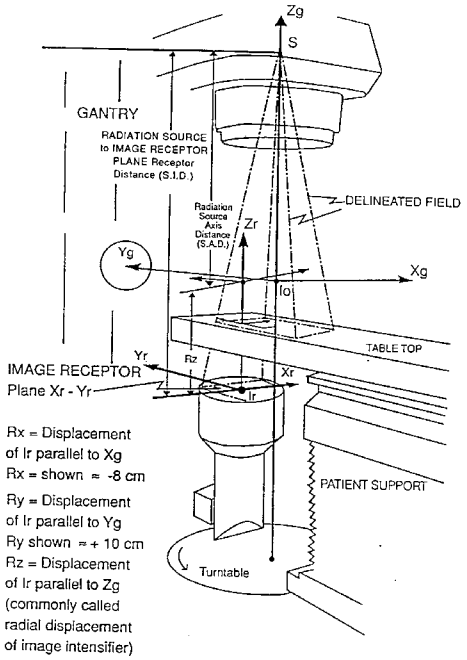

Figure 2-3. Basic simulator components and coordinate system as defined from IEC 1217

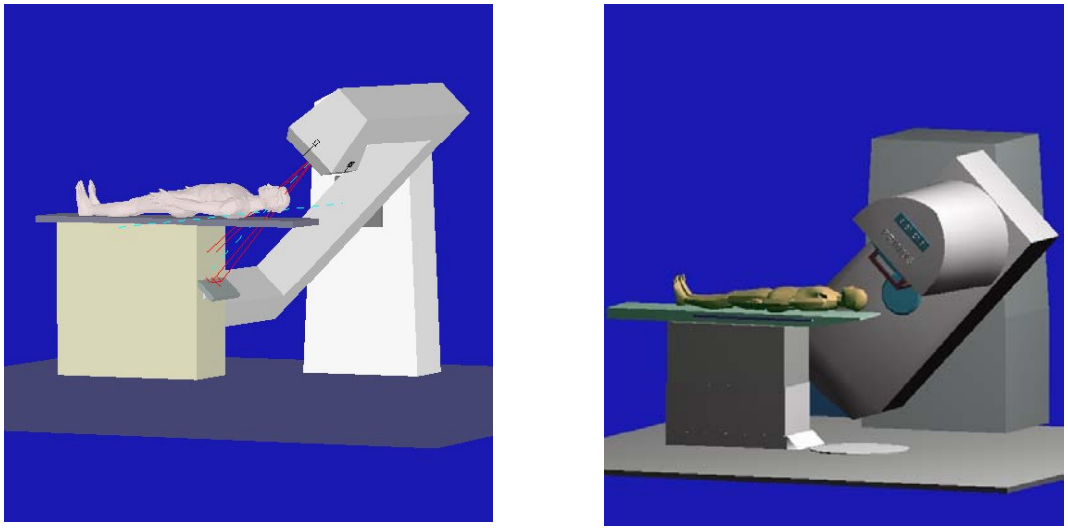

(a) (b)

Figure 2-4. Simulated collision for a simulator model based on IEC 1217 (a) and a Siemens LiNAC model (b). The table is rotated isocentric 90° and the gantry 45°. On the conventional simulator this case cannot by simulated since the image detector would collide with the table support (a). However on the treatment machine this case can be applied (b).

ponents of the simulator, like treatment couch, gantry, collimator and so on, and to investigate optimum localization positions for the current treatment case. Analyzing the structure of an image intensifier is beyond the scope of this work. Here we will try to see the limitation of the image produced from the image intensifiers in contrast to the virtually reconstructed X-ray images. Indeed the greatest constrain of the image intensifier against the use of 3D-Sim, which uses data coming form CT or MR scanners, is the limited field of view that offers. This restriction results from the mechanical components that compose the image intensifier. The diameter of the field of view ranges between the 23 and 40 cm. Further more the X-ray images produced for the image intensifier suffer from geometrical distortions, due to lens optics or electron optics (see Figure 2-5).

Finally the image quality is highly influenced by the veiling glare. Briefly the veiling glare creates a uniform over the entire field of view of the image intensifier. This effect is enhanced in cases where minimally attenuated and highly attenuated structures are exposed simultaneously on the field of view. To compensate this artifact usually they close the jaws of the collimator, when this is allowed from the treatment case, creating an even smaller field of view.

2.2.2 Simulator's Treatment Couch and Couch Table Top

The treatment couch is separated into two parts the couch support and the couch tabletop. The couch (or table) support is responsible for the vertical movement and the eccentric rotation of the table. The tabletop is responsible for the lateral and longitudinal translations and also the non-eccentric table rotation. The simulator's table is different from the LiNAC table in several senses. Material is an issue of less importance. What mostly counts are other metal parts that compose the table top and are used for the mechanical stability and strength. Assuming now that a treatment field is planned using a treatment

planning system, then applied on the simulator for verification is approved. However if during patient set-up on the LiNAC a metallic part of the table-top interferes in the field prior to the patient then the plan cannot be applied.

2.3 3D-Simulator: System Concept

The 3D-Simulator of RT process has a different concept and different functionality compared to the real simulation. The 3D-Sim is fully performed using a system-software and thus digital information are used instead of the physical patient its self. The primary data can be collected from a CT device means of axial slices that compose a volumetric grid with a specific resolution depending on the treatment case. For the processing, manipulation and simulation of real incidents in radiotherapy, 3D visualization technique must be employed. Stand-alone 3D visualization techniques are commonly used in medicine to generate images that will be used in diagnosis or treatment [Sakas01]. Most common application involve the 3D volume visualization stations where the medical data are used

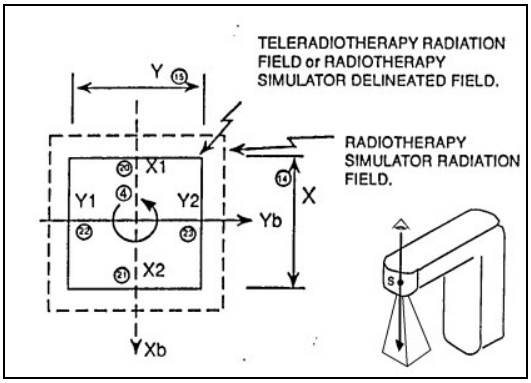

(a)

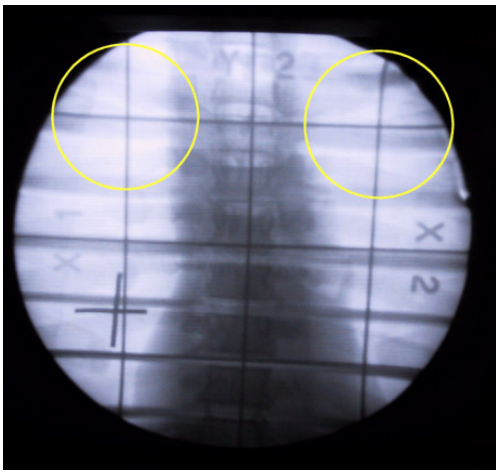

(b)

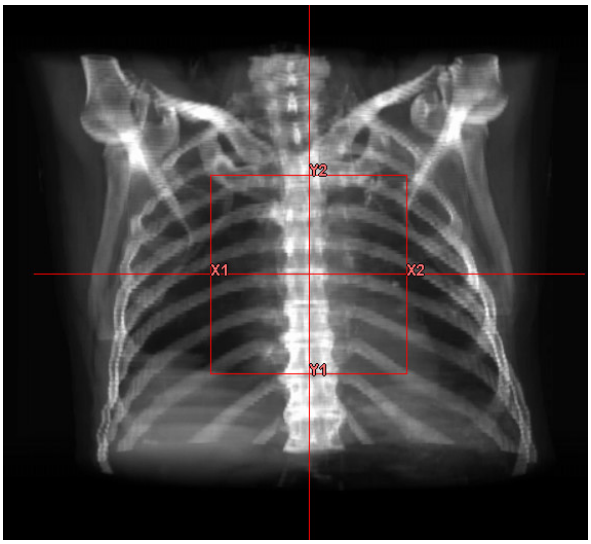

(c)

Figure 2-5. Definition of the real Simulator treatment field. In (a) a sketch of the treatment field as viewed from radiation source down to the radiation field. The image in (b) is captured from the image intensifier of the simulator using a wooden phantom as subject. The yellow circles indicate the deformed edges of the field. In (c) an illustration of a DRR with overlay of the treatment field, lack of distortions.

coming from different imaging modalities, and reconstruct 3D images for diagnosis on lesions. In order to generate a system for dedicated medical purpose a more complicate design and combination of state-of-the-art visualization tools is required. Computer graphics science, offers great tools that can be further developed and composed in order to finally create a system. As in several medical imaging applications, the implementation of a 3D-Sim requires the use of simple 2D procedures like line drawing, polygon scan conversion and pixel tracking up to 3D volume rendering and polygon modelling techniques. An overview of a 3D-Sim is given in Figure 2-6. The system is composed of two main parts; the system database and the functional 3D-Simulator. The database is responsible for performing DICOM data communication and storage. That includes normal DICOM imaging data and DICOM radiotherapy structures such as treatment plan parameters, segmented structures and treatment dose volumes. This information is communicated from and to the 3D-Sim system. The functional part of the 3D-Sim involves the memory storage of the digital information and of course the generation of all necessary new structures involved in the 3D-Sim process. Responsible for the generation of this information is considered the user who can manipulate and modify most of them. During data manipulation or interaction the system is responsible for the 2D and 3D display of the treatment information. Finally the system can export the produced information in digital or hardcopy format. The next paragraphs provide an overview of the visualization components that should be considered as essential for a 3D-Sim system.

2.3.1 Volume Rendering: An essential part in 3D-Sim systems

Volume rendering is the technique according to which a scalar field of data with discrete values, volume data, is selectively sampled in order to generation a useful image in relation to the sampled values. A volume data set is typically a set of discrete samples of one or more physical properties in a limited object space, $\boldsymbol{V(x),\ x \in R^n}$, in which $\{\boldsymbol{x}\}$ is a set of sampling points; $\boldsymbol{n}$ is the dimension of the sampling space, usually $\boldsymbol{n=3}$, i.e. 3D volume data; $\boldsymbol{V}$ represents the sampling values, it can be a single-valued or multi-valued function. According to the distribution of sampling points (i.e. the structure of $\boldsymbol{x}$), volume data sets are classified into structured and unstructured data sets. In medical imaging, volume data is usually a structured data set, typically organised as a stack of slices; $\boldsymbol{V}$ can be single-valued (e.g. the CT Hounsfield value) or multi-valued (e.g. density, T_1, T_2 in MRI). The resulting data structure is an orthogonal 3D array of voxels, each representing a sampling value.

A general pipeline of volume visualisation in medicine can include several steps [Sakas93]. Depending upon the application field, individual-processing steps may be neglected, combined, or reversed. Important to notice is that the final 3D rendering image can be obtained in two ways: either through the intermediate surface representation or through the volume representation (i.e. direct volume rendering). In general, pipelines employing the intermediate surface representation are collectively called surface-based visualisation techniques, as opposed to voxel-based. In addition the reconstruction modes can be separated into parallel, the Observer Eye View (OEV) and the perspective projection, Beam Eye View (BEV). The importance of these visualization tools have been addressed from several studies in different periods [Nagat90], [Purdy93], [Kalet97], [Gerst99], [Grees00], [Schie00], [Killo01], [McJur01], [Houst02], [Zambo02], [Dicks03].

2.3.1.1 Transparent modes

Two are the most common transparent modes used in medical visualisation. The Digitally Reconstructed Radiograph (DRR) and the Maximum Intensity Projection (MIP). In this paragraph both rendering methods will be briefly described, but focusing mostly on the virtual X-ray reconstruction since this is the most important image for the physicians that have been trained for years to use this kind of images for orientation and planning.

Maximum Intensity Projection (MIP): MIP is used in angiography, CT based or MR based. Nevertheless can be also applied to conventional CT, MRA and also to 3D-ultrasonic data sets. Using MIP one can reconstruct images emphasising to structures with high density within the data set. The difference between MIP and other volume shading models is that, in MIP only comparison between voxel values is requested, accumulation and opacity blending are not employed (we call other models as accumulation models). Due to the difference between maximum comparison and accumulation, most MIP algorithms use only ray casting to traverse volume data and select the maximum value among all accessed voxels along a ray. Using ray-casting techniques, one has to traverse

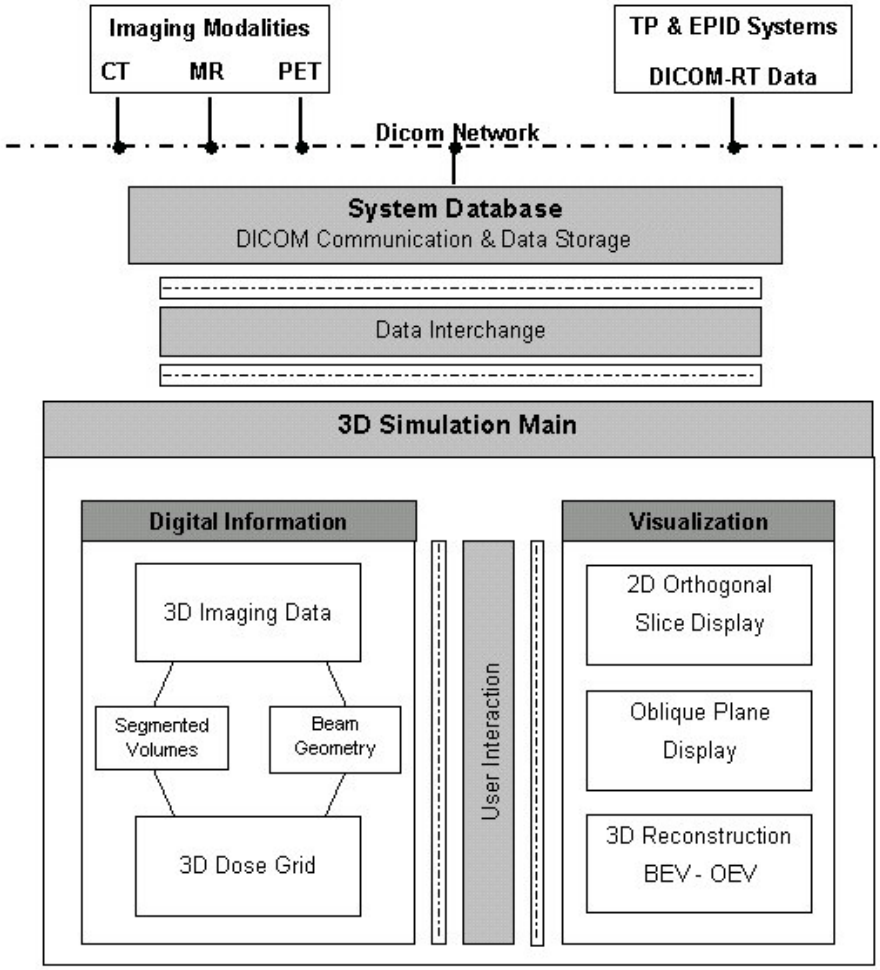

Figure 2-6. Simple block diagram of the 3D-Simulation system for radiation therapy.

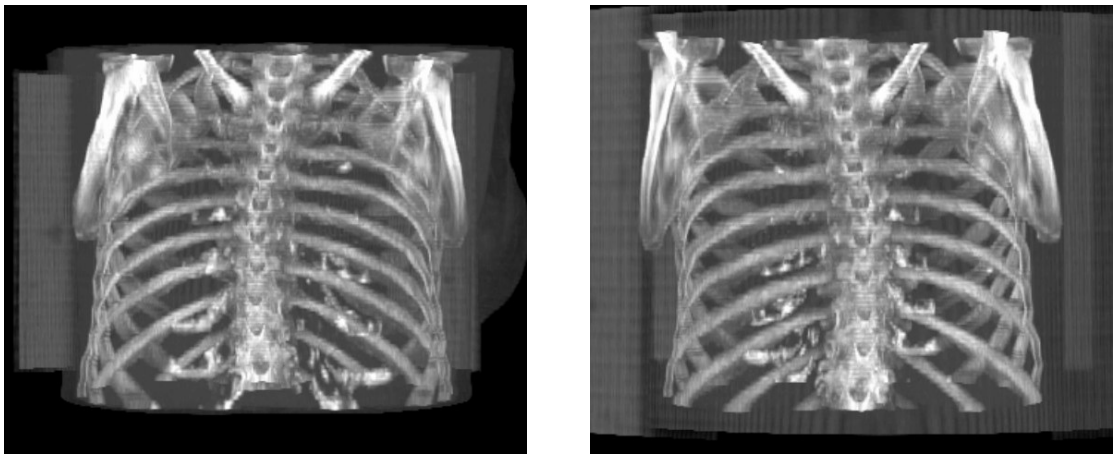

(a) (b)

Figure 2-7. Reconstruction of a CT chest volume using MIP. In (a) MIP reconstruction of the chest is presented using perspective projection with gantry angle 0°. In (b) the same principle and data are used but gantry angle is set to 180°. Bony structures are enhanced but depth information is missing.

all voxels on a ray in order to select the maximum value among them. Using MIP, structures with higher data value lying behind an object with lower data value will appear in front of it. The most common way to assist the interpretation of such images is to animate them or interactively change the viewpoint while viewing the data set. An example of MIP reconstruction is illustrated in Figure 2-7. The CT volume is reconstructed from two different viewing directions: 0° and 180°. In both cases bony structures are enhanced but depth information is not preserved. The scapula bones are displayed as they are in the front of the chest bones. In reality this is the case only when the chest volume is viewed from 180°.

Several researchers contributed to optimise MIP reconstruction. Sakas ***et al*** [Sakas95] evaluated cell maxima only if the maximum value of the examined cell is larger than the ray-maximum calculated so far. For additional speedup they use integer arithmetic for ray traversal and a cache-coherent volume storage scheme. Zuiderveld ***et al*** [Zuide95] used a similar approach in order to avoid trilinear interpolations Cells containing only background noise (usually rather low values) are not interpolated. For further speedup a low-resolution image containing lower-bound estimations of the maximum of pixel clusters is generated before the main rendering step. Heidrich ***et al.*** used conventional polygon rendering hardware to simulate MIP.

Other approaches exploit the advantages of shear-warp rendering 5 to speed up MIP. Cai ***et al***. [Cai98] incorporated an intermediate “worksheet” for composing interpolated intensity contributions of voxels for projection of a single slice of the volume. The worksheet is then combined with the shear image to obtain the maxima. However the shear warp rendering approaches do not allow the reconstruction of perspective projection. Morz ***et al,*** [MorzH00] showed that many of the voxels do not contribute to the MIP image. By identifying them prior to reconstruction significant speed is gained. Further more Morz ***et al.*** [MorzK00] presented a method for generating high-quality MIP images (parallel projection), using trilinear interpolation within cells. Their method was much faster then conven-

tional brute-force MIP reconstructions and comparable optimized techniques. This speed-up is accomplished by using an alternative storage scheme for volume cells (sorted by value) and by removing cells, which do not contribute to any MIP projection (regardless of the viewing direction) in a preprocessing step.

Digitally Reconstructed Radiograph (DRR): On the conventional simulator during fluoroscopy mode only a small part of the patient's anatomy can be visualised. This drawback comes due to the limited size of the detection surface of the image intensifier. On the radiographic film this problem is improved but those images suffer from other limitations. 3D-Sim offers unique features that no conventional X-ray system can provide. This comes basically due to the use of CT data, where the patient anatomy is captured using different field-of-view specifically selected for each study. The reconstruction of whole patient anatomy is of great benefit for the physicians.

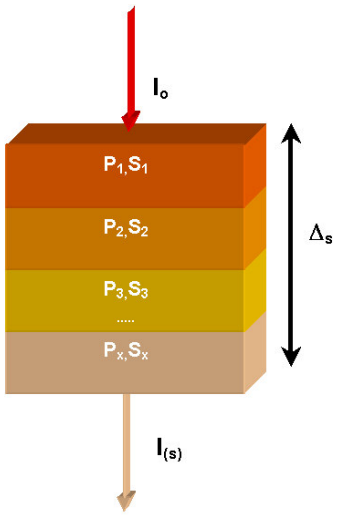

Figure 2-8. Attenuation of original ray energy I_o to $I_{(s)}$ though a sequence of materials.

DRR images are also important for comparison and verification purposes with the portal-imaging device of the treatment machine [Mock99]. The portal imaging device is used as the last step before the irradiation procedure for verification and localization of the patient position. To produce an image on the portal imaging device high energy X-rays are used. The quality of these images is relatively poor since the tissue discrimination at high energies is very low. 3D-Simulators must produce the same type of images in order to be able to compare their simulation result with the treatment position.

DRR images generated from CT digital volumes are often called using the term digitally reconstructed radiographs (DRRs). The term DRR is used when we refer to those X-ray images that are generated with an unrealistic way using direct volume rendering techniques or to those images that are generated from volume data using a better approximation of the physical model. In both cases we try to simulate the attenuation of the X-ray through a medium, in our case through the digital patient's body. This can be achieved by using different transfer functions simulating the classical way of X-ray image reconstruction.

Assuming that a ray with initial energy $\boldsymbol{I_o}$ enters a volume, which has a thickness of Δs. and is composed from different materials (see Figure 2-9). Using discrete values the final energy of the ray is a product of the following equation:

$$I(s) = I_0 \exp(-(p_1 s_1 + p_2 s_2 + p_3 s_3 + ... + p_x s_x)) \qquad \text{Eq 2. 1}$$

Where $I(s)$ is the attenuated energy after leaving the volume, Io the original energy of the ray, $\boldsymbol{p_i}$ the linear attenuation coefficient for the corresponding voxel material, $\boldsymbol{s_i}$ the corresponding distance from the ray entrance point to the ray exiting position of the voxel. In medical data the material type corresponds of course to the different tissue type. For detailed description of the optical model of the X-ray please refer to [Max95].

The contrast intensity of the final DRR image on the screen level can be calculated using the equation:

$$I_p = I_0 * (1 - L) + I_{background} * L \qquad \text{Eq 2. 2}$$

With ***L*** representing $L = \exp(-(p_1 s_1 + p_2 s_2 + p_3 s_3 + ... + p_x s_x))$

To simulate with accuracy the real concept of the X-ray optical model is a complicated task. The main reasons are that the X-ray photon absorption is related to the material properties and the energy of the ray. Basically there are two physical phenomena that occur during ray interaction with the material:

1. **The photoelectric phenomenon.** During this process the energy of the X-ray photon is completely absorbed from the material, irritating an electron on a specific orbit by giving to it more energy, to jump to new orbit with higher energy. After a very small time phase ***dt*** the electron returns back to its old orbit emitting a photon. This principle corresponds to an optical model with absorption.
2. **The Compton phenomenon.** This process occurs when the energy of the X-ray photon is higher than any corresponding energy an electron of the specific material can accept. The result is either emission of a new photon from the material or scattering of the current travelling photon of the X-ray beam to a different direction.

In diagnostic X-ray imaging, the X-ray generators produce a spectrum with multiple photons energies. As a result the low energies are absorbed very quickly when travelling through the material, loading with low energy, but not wanted, dose the subject under examination. High-energy rays are responsible for the Compton effect that produces artifacts in the image quality, usually blurring. So the “good” energies that are responsible for generating high image quality are those that are completely absorbed from the material. During simulation of the X-ray model all authors use ray with single energies. This simplifies significantly the model and also avoids the artifacts spectra X-ray energy produces.

To reconstruct a DRR the digital CT data of the patient are used. There are also researchers that try to reconstruct DRR images from MR data [Rams98]. However our focus is on the contrast quality of the DRR image using CT data. Each voxel acquired using CT has an value that is called the Hounsfield unit upon the name of the father CT. The HU can be estimated using the following formula:

$$HU = \frac{(\rho_\mu - \rho_{water})}{\rho_{water}} * 1000 \qquad \text{Eq 2. 3}$$

Where $\boldsymbol{p}_\mu$, $\boldsymbol{p}_{water}$ are the attenuation coefficient of the material for the specific voxel and the water respectively. When on the above equation one replaces the $\boldsymbol{p}_\mu = \boldsymbol{p}_{water}$, then will receive a $HU_{water} = 0$. In addition the ***air*** as material corresponds to –1000HU, since $\boldsymbol{p}_{air} = 0$. The Hounsfield units have no upper limit but usually for medical scanners a range between –1024 to +3071 is provided. Apparently 4096 different HU values are provided and therefore to illustrate the complete range of the HU on a volume 12bit voxels are required. It is common understanding that in order to simulate the DRR using CT data the Eq 2. 3 must be used to find the $\boldsymbol{p}_\mu$ of the corresponding tissue.

Imaging with CT offers a great advantage against the conventional radiographs [Kalen01]. Although both imaging methods, radiograph and CT, use X-rays, they provide

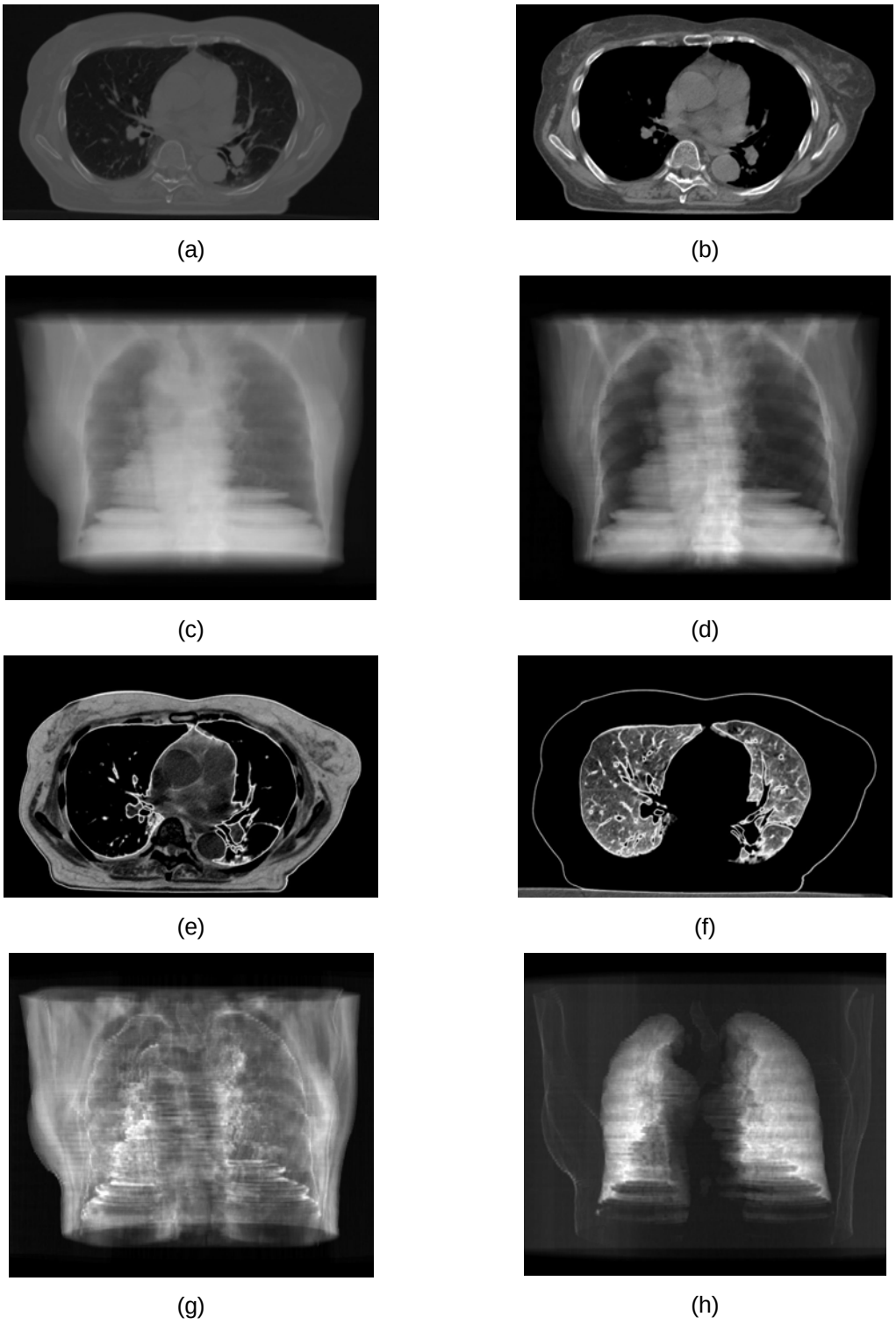

Figure 2-9. DRR reconstruction of CT chest volume. The results are produced using manually manipulated transfer functions. On can observe the corresponding 2D contrast effect on the CT slices in (a), (b), (e), (f).

information about different quantities. Basically in conventional radiograph each picture element displays the integral of the attenuation components along a line, superimposing all visited structures along the ray. On the other hand contrast in CT imaging is determined locally, by the composition of the tissues, while neighbouring structures have no or little influence to the final contrast. Since the CT values have a wide range it is necessary to use also a similar range of grey value for displaying. However, human observers can see up to 60 or 80 different grey levels. To improve the contrast of a CT image, a contrast enhances technique known as image windowing is usually applied on the original range of the HUs in means of look-up-table (LUT) affecting only the final, displayed values [Kalen01]. The most common type of image window is known as the linear ramp window. The basic features of this window are its upper and lower limit and its centre. Values that are below the lower limit will be displayed with black colour and values above the upper limit will be displayed with white colour. One can generate several types of image windows, like non linear, broken and so on.

Assuming now that one uses the accumulation model described in Eq 2.1. The final reconstructed image will be suffer from poor contrast due to the following reasons:

a) The high range of the HU that manipulated to their complete range and

b) The superimposing of all HU along the line, since the same principle is used as in the conventional radiography. This issue cannot be avoided due to the principle of the model we want to simulate.

What can be improved is the tissue range selection from the complete volume, in order to increase the contrast of the final reconstructed image, similar to the 2D image display. In this case the range selection LUT will have the same result as on the 2D image. Figure 2-7, illustrates the effect how the most simple LUT used for displaying 2D CT images can be applied on reconstructing 3D DRRs. When applying such value mapping tables in volume reconstruction we use the term transfer function (TF). Images from (a) to (d) have been generated using the ramp LUT/TF. Images from (e) to (h) have been generated using a tent LUT/TF. Important to notice images (a) and (c) since they have been generated with the original distribution of the HU. In other words no HU range selection has been given. For the sake of completeness the next paragraphs will present the most popular technique to generate transfer functions in direct volume rendering and especially in the application field of radiation therapy.

Several researchers reported ways to generate transfer functions for direct volume rendering but not specifically for DRR. He ***et al*** [HeHoK96] proposed a method where the search of the transfer function was treated as parameter optimisation problem and was addressed with stochastic search techniques. Their approach generated a number of transfer function for the user avoiding the user to perform the same process using the "trail and error" approach. Fang ***et al*** [FangB98] define a model for generating transfer functions as sequence of 3D image processing procedures. The user had to adjust a number of qualitative and descriptive to achieve their visualisation goal. The freeform design of transfer functions has the advantage that the user can manipulate any of their parameter to get a final result. The drawback of these methods is that it is difficult to be evaluated and accepted in the daily clinical routine. An intuitive way for TF specification from weighted component functions is presented in [Castr98]. A small number of parameters is used, which is sufficient to completely describe a TF. The user is the one who con-

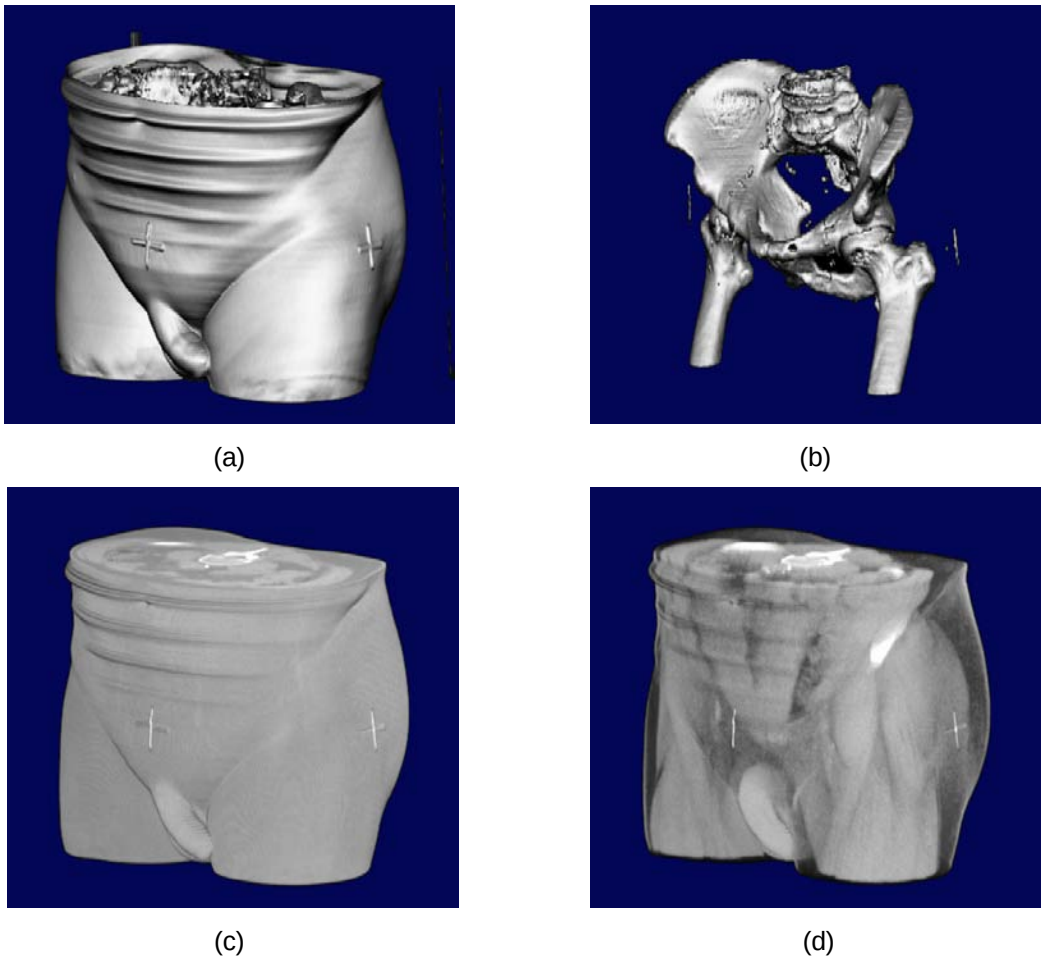

Figure 2-10. Direct volume surface reconstruction. In (a) & (b) reconstruction of volume surface using auxiliary gradient volume estimation [Levoy88]. In (c) & (d) direct surface reconstruction based only on colour and opacity TF.

trols the parameters according to the dataset used defined a specification scheme for semi-automatic TF search techniques.

Galvin ***et al*** [Galvi95] presented the use of DRR in treatment planning and CT simulation. They reconstruct DRR images using freeform transfer functions and generate unique images that could not be produced with conventional radiography. Adapting similar thinking Cai ***et al*** [Cai99] presented a method for creating transfer functions for the reconstruction of DRR. He mainly focused on the continuity of the transfer function, especially when sampling at the boundaries of two materials. The realised method could generate a partially composed transfer function for reconstructing DRRs, considering the continuity between different tissue types. He investigated the two types of continuities the linear (C^0) and cubic (C^1). Advantages of these methods are the smoothness of the final image and the flexibility to modify the attenuation coefficients for each tissue type as well as the appearance of specific tissue in the final image result. These features make this approach most convenient and optimal for clinical routine.

Killoran ***et al*** [Killo01], try to optimise the contrast of the chest DRR using as guide the traditional radiograph. Their aim was to resemble traditional radiograph of the chest en-

hancing similar structures the traditional X-ray image does. This approach gave good results on chest DRR, but restricted the visualisation capabilities on producing to specific type of images, since two 2D images hade to produced and then merged on a different step.

2.3.1.2 Surface reconstruction

Generally there are two methods for reconstructing surfaces: the polygon based and the voxel based techniques. Polygon based techniques can by further subdivided into those methods that generate triangles from planar contours [Boiss88], [Geige93], [Payne94], [Bajaj95], those that generate polygon surfaces iso-values from a discrete scalar field [Loren87], those that reconstruct surfaces from arbitrary 3D points [Hoppe92], [Ament98] and to those methods that use polynomial functions to optimally match the shape of the geometric object they want to represent [Kobbe98], [Morse01], [Carr01], [Turk02]. In medical imaging usually we deal with volume data and thus it is very common to use voxel-based techniques to reconstruct the surface of anatomical structures. The basic idea on these techniques is to determine the edges of the anatomical structures is usually the thresholding through a TF or combined with the opacity volume (gradient or iso-value modes). In both cases the data values are mapped directly to the rendering image.

Probably the most common methods for reconstructing surfaces directly from voxels are the gradient surface and iso-surface model. This rendering model is widely used in almost all medical data sets to render the surface detected by the gradient operator. Levoy ***et al.*** presented this concept [Levoy88], which is effectively used in most medical imaging applications for the last decade. The opacity calculated by the TF is blended in the final pixel with the local surface illumination model. An example of that method is presented in Figure 2-10 (a) & (b). Another aspect of voxel-based surface rendering is the use of TF. By using transfer functions one can assign optical properties to the original data values, like opacity and colour [Sabel88], [Drebi88], [Höhne90]. The final rendering result is directly affected from the selection of the transfer function. This involves the regions that will be visualized as well as the quality especially at the boundaries of the structures (see Figure 2-10 (c) & (d)).

2.3.2 Radiation Beam Arrangement and Visualization

Conventionally the RT verification process is based on external landmarks, manual drawing of the irradiation field on the patient's skin and portal image verification using high energy X-ray. The external landmarks are marked on the patient during real simulation as indicators of the projection of the radiation beam. This projection involves very often, delineated field shapes according to the radiation blocks that are used for protecting the healthy structures. A necessary tool in 3D-Sim and generally in treatment planning is the 3D projection of the shape of the radiation field and its virtual light together with the CT volume data. This tool increases the physician's ability to appreciate the 3D shape geometry and orientation of the radiation field in the space, a tool that is not available on the physical simulator. Additionally the light field projection of the patient's skin is used as the standard verification tool for the field arrangement. In this work our concern is the real time projection of the radiation polygon geometry and its projection on the surfaces of the CT data. To achieve this we use a convex polygon scan conversion algorithm combined with the Z-buffer information provided from the 3D rendered image. In this work we do not aim to present a new polygon-volume hybrid rendering reconstruction scheme. Instead a

solution to the problem of real-time and accurate treatment light field illustration is shown. For more information on the hybrid rendering concept the reader can refer to [Levoy90], [LevoB90] and [Bhale00].

2.3.2.1 Polygon Scan Conversion

To realize the features mentioned above we employ a hybrid volume rendering approach. Our method is based on a 3D triangle polygon scan conversion (PSC) and contributes on the rendering scheme on the image level. Detail information about similar algorithms can be found in [Gordo94], [Encar96]. In this work our focus is to describe the combination of the PSC approach with the Z-buffer in order to produce the wanted results. In order to achieve our aim first the beam polygon is constructed. Since our PSC method can be applied only on convex objects, every polygon object used in the rendering scene must be a tetrahedral (product of triangles). To represent in 3D the radiation field we consider the 2D radiation field size. Basically a pyramid is generated that corresponds to the perspective of the radiation field. This shape is composed from six triangles, four compose each side of the pyramid and two triangles its rectangular base. In relation to the physical parameters the high of the pyramid represents the source to detector distance and the size of the pyramid the actual field size scaled at the perspective factor. Before processing the polygons that compose the field for the scan conversion algorithm, we apply to them homogeneous coordinate transformation means of matrix form in order to match the CT volume geometry and to register the virtual simulator parameters of the planning components (gantry and couch). The next step will be the hither clipping against the 3D image

For the polygon reconstruction follows the generation of the data structures. The necessary data structures for realizing the PSC are:

1. The edge list ***Pi(x, y, z)*** (EDGE). This list hosts the actual vertex information from every 3D polygon.
2. The sorted edge list (SEL). This list is generated after sorting the list of EDGE's in top-to-bottom y order of the first vertex.
3. The active edge list (AEL). The active edge list is the current polygon edge list that will be scanned.

The main body of the algorithm, passes iteratively loops through the SEL and then through the AEL. Aim of the scan conversion is to generate a semi-transparent effect of the radiation field polygon so as to allow the viewer to see the surface of the structures behind the radiation field and also to indicate-highlight the field intersection volume with the patient volume. Both tasks should be accomplished at the same step. To achieve that we calculate the Z-depth of the polygon side during scan conversion and we compare the estimated value with the current Z-depth of the surface volume. Of course this step assumes that for the current 3D reconstructed image a Z-depth have been calculated. This means that the proposed method can be applied only when the surface location of the volumetric structure is known.

Figure 2-11 illustrates this principle in a simplified 2D case. We assume that the 3D scheme is viewed from the top and the viewer, the 2D image plane, is located on the left of the image. Let us consider three different Z-depth values for an arbitrary edge of the polygon with $Zp_{10}<Zp_4<Zp_1$. One can very easily understand that the observer from the image plane will be able to see the polygon object at the levels Zp_1 and Zp_{10}. The pixel value

I_4 will contain information only from the volume surface since the depth value Zp_4 is smaller than the Z-depth Zv_2 of the surface. In a similar manner every polygon is scanned and its depth value is compared with the corresponding surface Z-depth. The colour value for the corresponding triangle position is weighted with the optical depth of the 3D scene in order to more accurately indicate the beam pyramid location in the space relative to the observer and the CT volume. Finally the pixel colour at the position $I(x, y)$, will be composed from the colour of the 3D image pixel $Iv(x, y)$ and the colour polygon pixel $Ip(x, y)$ using a linear blending function.

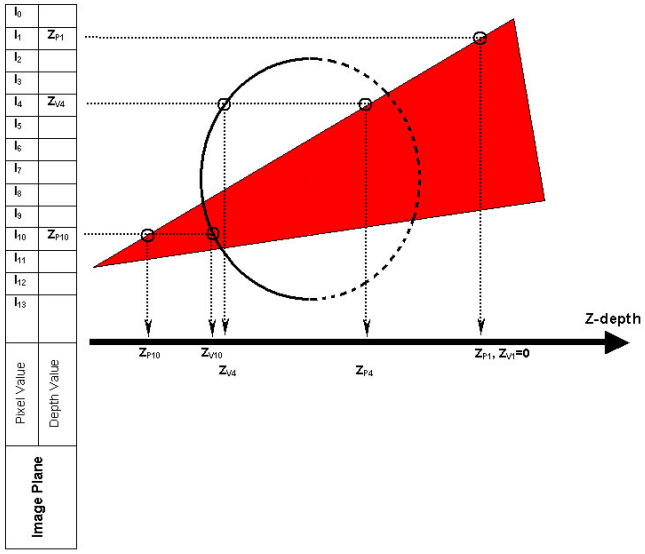

Figure 2-11. Simplified Z-depth estimation during polygon scan conversion. The red triangle indicates the treatment beam polygon and the ellipse the CT data.

The above polygon reconstruction principle can be applied with success on rectangular field shapes, symmetric or asymmetric. In case that more that one fields are involved in the visualization scheme the PSC is applied iteratively for every beam polygon. Figure 5.12(a) presents visualization examples of the above process. To reconstruct more complicate polygon objects involved in the field delineation, a different approach must be followed during polygon generation. It is common one to generate a shielding block in terms of a 2D contour on the DRR. Prior to scan conversion the 2D contour shape must be projected of the 2D DRR image space to the volume space in order to generate the corresponding 3D polygons with perspective geometry. This contour shape can be arbitrary and its convexity varies. Since the PSC algorithm we use can handle only convex polygons, we have to triangulate the 2D contour in order to maintain convexity of the polygon. This step is performed using the two-dimensional Delaunay. Once the 2D block contour is triangulated we must estimate its projection to the virtual detector level. This process will generate equal number of tetrahedral as the original 2D triangles. The scan conversion process in then applied for each tetrahedral object, as performed with the radiation field pyramid.

2.3.2.2 Projection of the Virtual Light Field

A significant aspect for the verification of the radiation field is the virtual light field projection on the patient skin [LuH99]. In physical simulators, a light source is located near the irradiation source. The orientation of the light intensity is diverted through the gantry head using a mirror aperture. The outcome of this process is the exact projection of the radiation field on the patient's skin. The two main axis of the field are indicated as line shadows. In case the radiation field is delineated using shielding blocks, then the light field area is also modified accordingly. This process described above should be performed in a similar manner in the virtual simulation process. In order to realise this principle we take

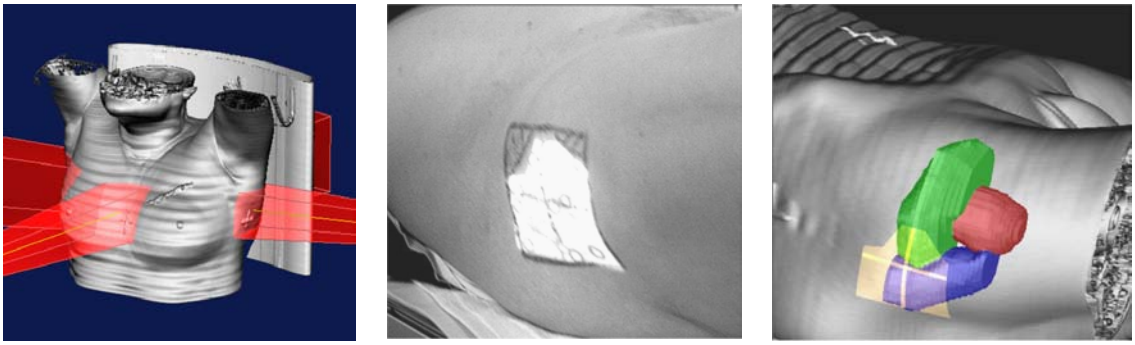

(a) (b) (c)

Figure 2-12. Projection of treatment field with patient anatomy. In (a) reconstruction of polygon treatment fields. In (b) a real treatment case of a prostate case. In (c) the simulated case of the same patient with the volumes of interest segmented and the virtual light field projected on the 3D reconstructed surface.

advantage of the convexity of the tetrahedral objects and the Z-depth information derived during polygon scan conversion.

For simplicity let us consider a 2D example. Assume that the back edge, in relation to the object position, is currently under scanning. We use a 2D image that has the same size as the reconstructed one, in order to indicate that the corresponding pixel has been visited during polygon scanning process. We will call this array light mask. At this step we introduce the values Z-buffer $Z_V(i,j)$ as they are acquired during the volume rendering process. If one compares the current edge Z-depth $Z_P(i,j)$ with the value of the image Z-buffer then could make the following two assumptions:

- if $Z_P(i,j) < Z_V(i,j)$ then the current polygon edge is behind the volume and is hidden from the viewer. In this case no value for the light mask is accumulated.
- if $Z_P(i,j) > Z_V(i,j)$ then the current polygon edge is in the front of the volume and is visible from the viewer. In this case one value for the light mask is accumulated.

It is known that the polygon objects we use during scan conversion are convex. In case all polygons are scanned without any object to obstruct the back polygon, then there will be only two indices for each pixel that was visited during polygon scanning. Two are the maximum number of indices we can achieve on the light mask. Considering the viewing location, at the level where the beam polygon intersects the volume surface the light mask goes from value two to one. This means that all pixels in the light mask that have index one should be considered as the projection of the light field. The virtual light field follows every orientation of the radiation beam, including any modification in one of the parameters gantry, collimator or couch. Mixing of the volume surface information and the light mask information occurs similar to the polygon projection on the image level. The corresponding pixel colour of the 3D image will be modified at those locations when the light mask is indexed with value one.

To generate the visual effect of the delineated radiation field in cases where shielding blocks are used, we use a second 2D array, similar to light mask, named block mask. The block mask is filled using exactly the same principle with the Z-depth values of the polygon edges and the volume surface described above. In case that the block mask is marked with zero index then the block polygon is hidden from the volume. Index one in

the block mask means that one polygon edge is hidden from the volume and the other one is visible hence an intersection of the block polygon with the volume surface exists. If the block mask is flagged with two indices then both planes of the block polygon are closer to the user than the volume surface. To produce the final image we combine the two masks accumulated above, the light mask and the block mask. Pixels regions that overlap and have common values, index one and two, are omitted during image shading. A clinical example of a real prostate light field projection is shown in Figure 5.12(b). The corresponding virtual light field is shown in Figure 5.12(c). Further clinical examples and the clinical importance of this method can be found in [Zambo02] and [Houston02]. Our approach for visualizing treatment beam polygons and light field projection offers a significant speed advantage when displaying the treatment fields on 2D slice and on 3D. This property is very important when the user changes the orientation and the size of the filed, or when applies fine-tuning of the block or MLC shapes. In this case we are able to display in real time the modifications that occur on the 2D and 3D field projection. This way one can focus on a specific anatomical location and can observe the field adjustments in relation to that point.

2.3.3 Room View

The conventional simulation and treatment procedure are taking place in specialized sites where the observation of the real hardware machine and the patient location on the couch of the treatment device should be available (see Figure 2-13). The treatment rooms are always monitored with external cameras in order to assure maximum secure and protection for the patients and of course the working personnel. General causes for accidents in daily routine are unpredictable. However the most potential reasons for accidents are usually collision between mechanical components or even between components and the patient under treatment. Also misalignment in patient setup (e.g. wrong patient orientation) or inaccurate submission of the treatment parameters might result to a long-term but severe injury of patient's vital organs. In clinical routine most of the treatment cases must be planed through a TP or a VS system. Currently in 3D conformal treatment planning, semi-automatic and automatic techniques for beam placement have been introduced, in order to improve treatment outcome. These techniques result to a large number of beams with complex arrangement. It is often the case that complicated techniques cannot be applied on the treatment machine due to prospective mechanical collision or due to interference of metal components in the irradiation field.

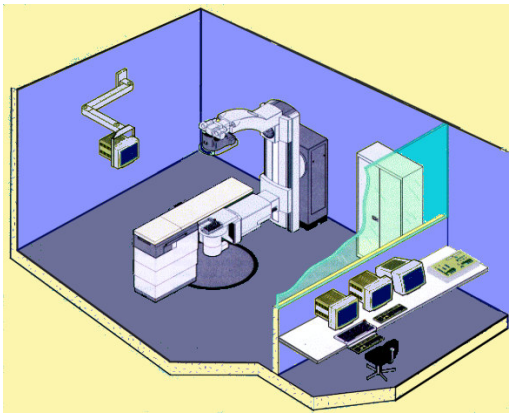

Figure 2-13. Graphical representation of the conventional simulator environment.

The above reasons advocate the demand of a graphical simulation tool of the clinical room environment in the TP and VS systems. The first overview came from Sherouse [Shero91] who reconstructed a very simple 3D model of the treatment machine in order to provide visual feedback of the machine configuration (gantry and couch). The graphical model of the treatment machine was updated accordingly after a treatment pa-

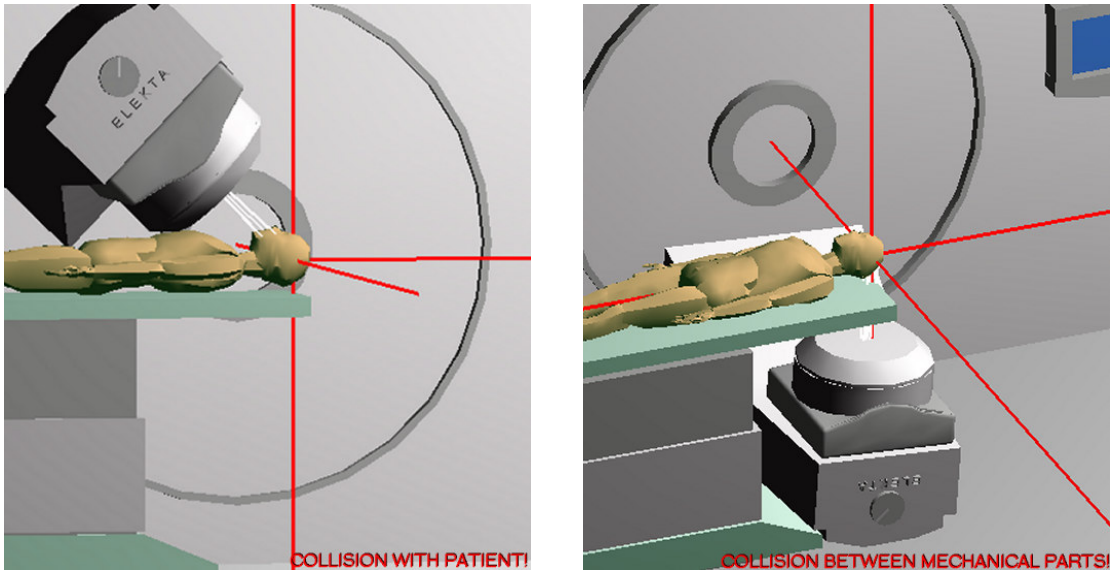

(a) (b)

Figure 2-14. Indication of potential collisions during RT treatment using ARIS. A potential collision between patient and mechanical parts is shown in (a). Similarly (b) shows a collision between mechanical components of the LiNAC.

rameter was modified. The term Room View (RV) was introduced from Purdy ***et al*** [Purdy93]. However that term was used to describe the 3D view the patients body contour and internal organs. The RV was reconstructed using polygons and contour lines and provided interactivity to the user in order to observe beam interaction with the patient body, critical organs and target volume in three dimensions. In this work, we will refer with the term RV or "room's eye view" (REV) to the representation of the treatment machine's room with or without the model of the patient.

Realistic and functional modelling of the treatment machine and its components is reported from several authors. Among the most important was Humm ***et al.*** [Humm95] who introduced an application for collision avoidance using the REV. The treatment machine and the patient's body, were reconstructed using polygon surface rendering compiled by the OpenGL, graphics language. A phantom model, reconstructed from the corresponding CT data, replaced the patient's body anatomy, located on an arbitrary position on the treatment machine's couch. This collision detection approach could provide the planner with an immediate feedback of the feasibility of each field during treatment set-up. If a potential collision was detected then either the couch configuration was remedied or the closest allowed gantry angle was calculated and used replacing the old one that result to collision.

In the content of computer–controlled systems, which is used to apply the current treatment set-up to the treatment machine, Kessle ***et al*** [Kessl95] presented a software application for controlling the treatment machine including its exact polygon representation. Characteristic of this approach was the use of an "icon-based treatment script manager". Each icon represented the configuration steps that the treatment machine should follow in order to reach the final field orientation. The collision detection was applied in every step of the sequence. In case of detected collision on a specific step, the script

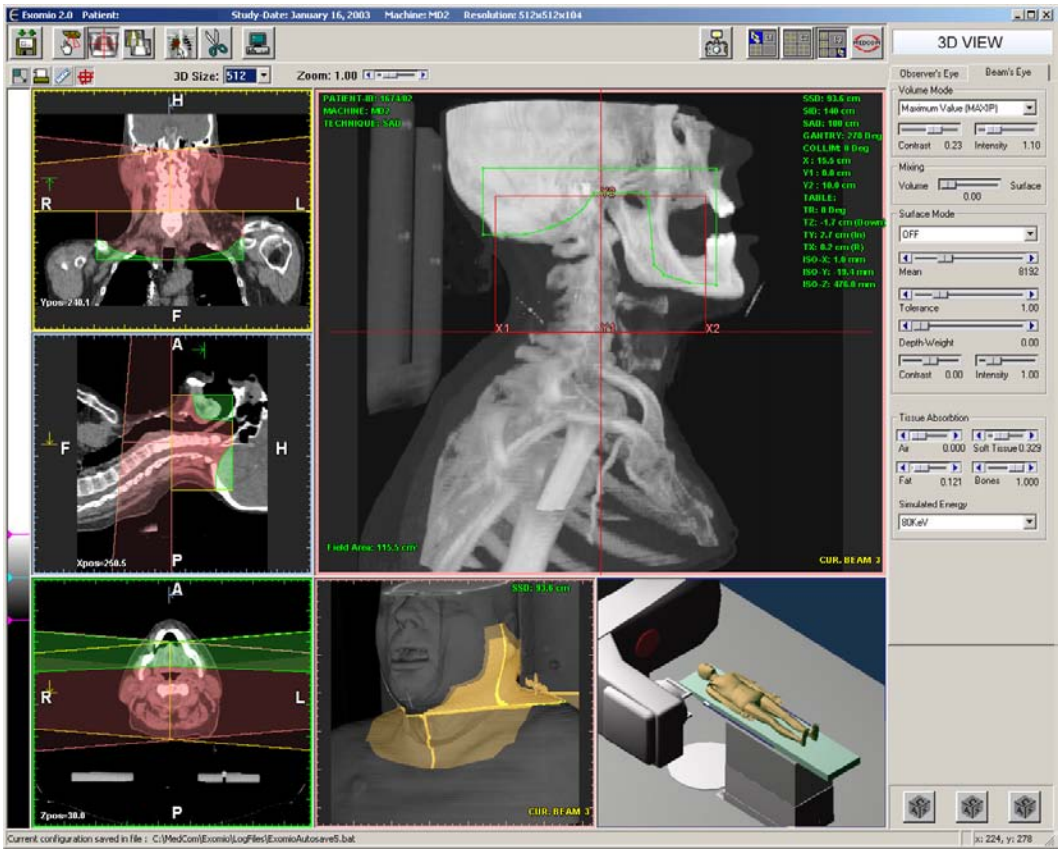

Figure 2-15. A representation of the 3D-Simulator (Exomio). On the left side of the screen is shown the representation of the original and reconstructed CT slices (top-coronal, middle-sagittal, lower left-axial). Beam and block overlay are present over the neck region. On the top right window a MIP reconstruction of the BEV. The OEV with the three light field projections is presented on the lower middle window. Finally a realistic representation of the treatment unit (LiNAC) as provided using the ARIS visualization engine is shown on the lower right image.

manager was used to modify the sequence of the icons, rearranging the order of the icon-steps resulting to the correct sequence. This approach could provide an excellent feed-back to the user about each step of the treatment set-up. Only drawback of this approach was the lack of the model of the patient's body.

Tsiakalos ***et al*** [Tsiak01] also presented an approach for automatic collision detection in the conformal and stereo tactic radiotherapy treatment planning using the REV. The treatment machine was reconstructed with exact geometry using the OpenGL graphical library. An average model of the patient was used as an approximation of the patient's body anatomy. However the user has the option to modify the size of the patient model in all three dimensions. To detect the collision between polygon structures the Coldet library was used. By detection of a collision a warning indication was appeared describing the type of the collision (e.g. collision between couch and gantry). The greatest advantages of this approach are:

1. The simplicity of modelling any treatment machine geometry and their external components if any.

2. Easily incorporated to any 3D-Sim or TP system.

The above reasons support this approach as the most potential solution for integration into an already established software environment of a 3D-Sim system. An example of the system is given Figure 2-14 where a model of the Elekta treatment machine is illustrated simulating two potential collisions.

2.4 Summary

This chapter provides an overview of the most important component of the conventional simulator and the 3D-Sim. We consider this as necessary step in order to appreciate these two different concepts. For the conventional Simulator we formulate the most important mechanical and practical limitations. On the other hand we presented the alternative solution to the conventional Simulator that is the 3D-Sim concept, which is a software system composed of several graphics and visualization tools.

Input to the system are 3D data from medical imaging modalities and especially data coming from CT. Without questioning the “heart” of a 3D-Sim system is the volume-rendering engine. Volume rendering allows the system to reconstruct DRR and surface images of the patient anatomy. Compared to standard X-rays in DRRs one can manipulate the tissue weight and contribution to the final image producing interesting and unique information. In a similar manner volume surface images can be reconstructed with user defined TF.

Essential visualization component is the 2D and 3D the display of the treatment field in relation to the patient anatomy. Further more the display of the virtual light field can be used as verification for comparing digital results produced in the 3D-Sim system and the real world, before patient treatment. Finally incorporation of a collision detection solution in the 3D-Sim environments, using the real LiNAC geometry for modelling, allows the evaluation of the plan applicability before further treatment actions are taken. An illustration of the ***Exomio*** 3D-Simulator software is shown in Figure 2-15**.**

Chapter 3

Segmentation of Anatomical Structures: Manual volume definition and semi-automatic extraction of the spinal cord

3.1 Introduction

Segmentation is the process that separates an image into its important features (primitives) so that each of them can be addressed separately. This converts the planar pixel of the image into a distinguishable number of individual organs or tumour that can be clearly identified and manipulated. The segmentation process might involve complicate structures and in this case usually only an expert can perform the task of the identification manually on a slice-by-slice base. Humans can perform this task using complex analysis of shape, intensity, position, texture, and proximity to surrounding structures. Of course, all these features are differently qualified depending on the experience of the user. To perform a similar procedure automatically using a computer since today has been proved a very difficult task. In other cases where simpler anatomical regions with a very distinguishable shape must be identified an algorithm can perform this task. Currently there are only dedicated algorithms for different regions of the human body. To generate a “complete”, with a general meaning of the term, segmentation application numerous tools and algorithms must be combined [Kuszy95].

We will investigate the volume segmentation aspects within the frame of radiation therapy. From the engineering point of view volume definition seems probably to be a simple and straightforward line drawing process. However, from the clinical point of view, it is a very serious task. The clinicians consider this action as more than line drawing, since this process will define the precise borders between disease and healthy tissues. The first aim of the segmentation process in RTP is to define as accurately as possible the target that will be irradiated. This process is a manual process and usually is performed from an expert oncologist. With the terms of manual process, we mean that the physicians will exam the digital volume, slice-by-slices and using the mouse cursor will illustrate the shape of the tumour. The coordinates of the shape of the tumour are stored from the system for further processing. The target definition process is probably the most time consuming process involving an expert during the RT planning [Ketti97]. It would be almost impossible to perform the same process using a computer. The following describes a number of reasons proving that the automatic target volume definition is still very difficult to be performed from an expert system. The obvious reasons found in the daily clinical routine are:

1. The irregular tumour properties, like shape, texture, volume, relation with surrounding regions.
2. Location within the human body. A tumour theoretically could grow anywhere within the patient’s body. There are cases where the disease statistically appears

on common organs like prostate to males and mamma to females. In these cases, a region-based automated segmentation process could probably be suitable for solving the problem.

3. Tumour spreading and variation. Depending from the region the tumour is grown, disease cells might spread to the surrounding region. The disease cell distribution cannot be predicted and detected on the digital patient's data. Since the internal organs in the human body perform several vital processes are active very often their moving. A very common example is the prostate variations since the bladder change its volume very easy and the rectum contracts [Dawso98], and abdominal and lung tumours that vary according to patient respiration [Aruga00].
4. Artifacts in the acquired digital data. When treating elderly patients it is often the case to have prosthesis, usually metallic (heart irritating) like hip prosthesis. These patients cannot be examined in a MRI modality and therefore CT imaging is the only alternative for their RTP. Nevertheless, it is well known that metallic components generate severe artifacts in CT imaging that reduce image quality and blur tumour borders.

Further, the physicians must follow a number of regulations determined be international comities in RTP [Purdy96]. Nowadays several 3D RTP and 3D-Simulation systems are available and are widely used in most of the oncology clinics throughout the world. These systems have such planning capability, that leads to new treatment techniques, which in many cases are much more complex than the tradition methods like IMRT that irradiate the tumour cells with higher dose rates. Thus, the accurate manual target volume definition is even more necessary nowadays. So far only a very few techniques propose physicians one or more alternatives for volume definition [Ketti97], [Belsh97]. Recently Pekar ***et. al.*** [Pekar04] reported a method based on an adaptation of 3D deformable surface models to the boundaries of the anatomic structures of interest. The adaptation was based on a tradeoff between deformations of the model induced by its attraction to certain image features and the shape integrity of the model. Nevertheless, to make the concept clinically feasible, interactive tools where also introduced that allow quick correction in problematic areas in which the automated model adaptation may fail.

In the following paragraphs, we will discuss a unique contour interpolation method that can accelerate and improve the quality of the manual segmentation process of tumours and other normal structures. The algorithm is based on a fully 3D interpolation scheme given the user all possible flexibility during segmentation. Considering spine as an organ of high importance that has to be protected during patient treatment, in the last paragraphs of this chapter we present a semi-automatic method for extracting the spine volume with high accuracy.

3.2 Manual Definition of Structures

The manual definition of structures is a process that requires the intervention of an expert in order to define the shape of a structure, usually tumour or disease growth. Traditionally in most applications, this process takes places in the original acquired image. Since here the focus is on the CT modality, the indicated image direction is the axial. The CT images are collected on a plane that has its normal vector moving parallel to the longitudinal axis of the CT table and therefore longitudinal of the patient as well. Image quality is and will always be a very important factor for the accurate definition of anatomical structures.

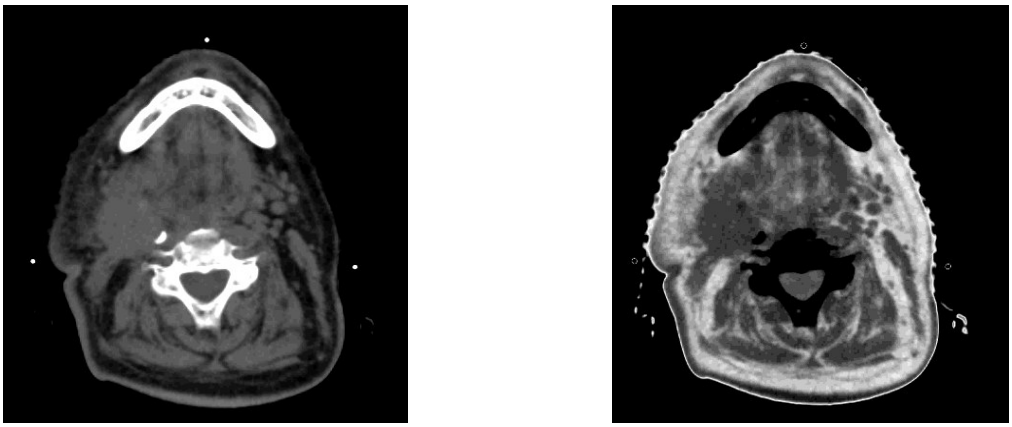

(a) (b)

Figure 3-1. Illustration of CT slices using different windowing functions. In (a) contrast adjustment using standard linear ramp function. In (b) a rather unusual contrast set-up for radiotherapy, using linear triangle function.

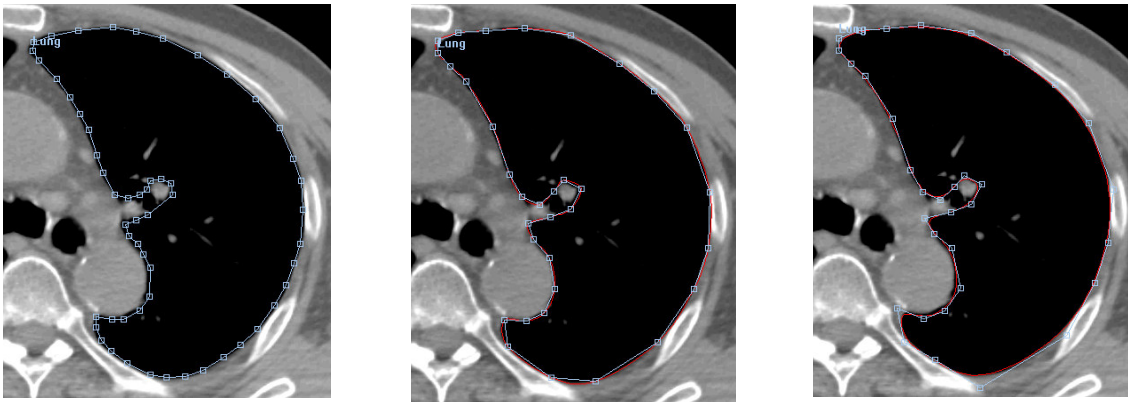

(a) (b) (c)

Figure 3-2. Manual segmentation of the left lung region. In (a) linear interpolation is used to connect the 56 key points defined from the user. In (b) the same contour but with smother shape is interpolated using cubic interpolation and half of the points needed in (a). Similar in (c) where B-Spline interpolation is used.

Even the set-up of different image contrast and intensity (image windowing) might affect the decision making during volume definition. Image grey level enhancement is related with the:

- Improved illustrations of the edges, which be broaden or narrow depending on the windowing function used
- Improved display of the wanted structure and the surrounding tissues

Figure 3-1 shows an example of a tumour case in the lymph nodes of the neck region. The contrast of the image on the left side has been adjusted using the standard ramp window. The right image is shown using a triangular window. One can observe the tumour

shape and the small structures better on the right images since the lower intensity structures at the background have brighter colour. Further more simple issues as the line thickness during volume segmentation can indicate user uncertainty and in general can characterize the accuracy of the segmentation process.

Complementary information to the CT data, but essential in many aspects on tumour volume definition is the use of multimodality imaging like MRI [Khoo97], [Rams98] and PET [Maise02], [O'Doh02], [Geets04]. The use of different modalities beyond CT has been proven extremely valuable to investigate tumour shape, size and spread. Usually MR imaging is used to describe better tumours of the brain and cervical regions. As a result, the tumour contrast enhances so as its borders, and that can drastically improve the definition of the target volume. In addition, MRI has the ability to reconstruct anatomical images on different planes like sagittal, coronal or arbitrary planes, where several tumour cases can be clearly illustrated. On the other hand, the use of PET studies provides functional information related to lung tumours. This can result to the detection of tumour spreads and tumour size extension [Caldw03]. Considering this information will eventually assist the improved tumour control. CT is considered as the primary modality for the RTP. Thus the complementary imaging modalities must be fused with CT in order to have the optimum outcome. Several studies exist for volume registration in the frame of RT, that proposed semi-automatic and automatic ways to register different volumes [VanHe94], [Kwa98], [CaiJ99]. In addition, currently technological developments allow the combination of two modalities in one offering automatic matching of the CT and PET information [Beyer00], improving registration accuracy.

Currently the tool used to perform the volume definition is the mouse cursor. The user defines a number of digital points on the image level, closing the first and the last point of the contour to generate this way a structure. The connectivity between the ***key points*** can be linear or higher order. The higher order connectivity can be achieved using interpolation models like Hermitte cubic, Spline curves, Bezier curves [Laure94], [Spath95], [Cohen01], which are the most common and successfully used techniques for smoothing curves in the CAD systems. Aim of the high order interpolation techniques is to reduce the amount of input points required to describe a smooth shape. This concept can be easily adapted in medicine since most human organs are smooth and round. This thesis does not focus on analysing the properties of the interpolation techniques instead we aim is to indicate the importance of such methods and their advantages. Performing a simple comparison between C^0 order (linear) and higher order interpolation, one can find out that the amount of points used to illustrate the shape of a structure using linear interpolation require at least twice as many samples as by using the higher order interpolation algorithms (see Figure 3-2).

A common methodology used to combine high order interpolation and image edge properties is the use of active contour models. The active contour models or Snakes can be 2D image curves [Kass87], [Blake98] or 3D polygon meshes [Terzo88], which are adjusted from an initial approximation to the image or volume features by a movement caused by simulated forces. Image features provide the so-called external force. An internal tension of the curve resists against highly angled curvatures, which makes the Snakes movement robust against noise. After a starting position is given, the Snake adapts itself to shape by relaxation to the equilibrium of the external force and internal tension. Snakes has been proven efficient and fast for a number of applications in medicine involving different imaging modalities [McIne96], [Gross98], [Behr00], [Sakas01], [Gross02].

3.2.1 Volume Interpolation from Parallel & Non-Parallel Contours

The interpolation techniques described above, are usually applied only on a single slice level (2D). The use of high resolution CT data in 3D-Sim, allows the use of multiplanar reconstructions (MPR) for the sagittal and coronal direction, in relation with the patient anatomy. These two images are orthogonal to each other and perpendicular with the axial plane. The navigation though these images help in the observation of complex anatomy. The sagittal and coronal views often offer a better overview of organs 3D shape. Defining volumes in these directions could be of benefit since several organs are aligned along the longitudinal body axis. Although this can be just a visual trick, since physician have used to work with X-ray images observing structures in relation with the rest of the anatomy, they consider the multiplanar reconstructed images provide additional, information for the shape of the organ. The MPR techniques are used in MRI imaging where the image reconstruction plane can be placed in oblique orientation for the investigation of complex anatomy of brain tumours.

However, there are very few reports illustrating the benefits of the MPR while defining medical volumes. Probably the reason is due to the standards of the imaging modalities, since most of them generate images on a transverse plane to longitudinal direction to the human body. The presented method here is based on the ability to define contours on the two MP directions sagittal and coronal as well. The idea of this tool came from the fact that some anatomical structures cover larger areas when they are visualized on the coronal or sagittal directions. In other words, by defining a contour on a MP image we include several axial images at one step. Now if one can define several contours in the MP images, have created a 3D contoured object. What must be done now is to accurately interpolate the 3D contours and extract a new shape out of them. This approach could accelerate the volume definition process extremely.

The problem we have to solve in our case is the generation of a surface and contours from structured closed parallel and non-parallel contours. The data points represent the contour points as they are generated from the user on the different levels of the axial slices or/and on the MPRs. The most common approaches used to reconstruct surfaces form parallel contours and are well establish in medical imaging applications [Boiss88], [Meyer92], [Payne94], [Bajaj95], [Weist00]. The limitation of these algorithms is that they cannot be applied on non-parallel contours. The problem of the non-parallel contours could be also formulated as generation of surfaces from scatter data, which are very common in industrial applications [Hoppe92], [Ament98]. There is a large variation of solution to that problem. Gibson [GibsM98] extracted smooth surface models treating the existing binary data as a constraining element in an energy minimizing deformable surface system. The resulting data structure can be used either to create Euclidean distance maps for direct volume rendering or employed directly as a polygonal surface model [Gibso98]. Whitaker [Whita00] presented a modified version type of the constrained deformable surface model. His constrained level-set model approach creates smooth models while bypassing the need for separate surface representation. However, while these methods generate smooth surface representations, both the level set model and the surface net remain discretely sampled and retain the problem that they are non-scale invariant.

For our application, we selected the approach presented from Turk [Turk99], [TurkB99]. Their method adapts earlier work on thin plate splines and radial basis inter-

polants to create a new technique in generating implicit surfaces. Their method allows direct specification of a complex surface from sparse, irregular scatter samples. The main restriction of the method is the relatively small number of sample data that can be handled. This drawback makes the above approach unsuitable for a number of applications that a large number of sampling points are needed. The topic of computational complexity by using implicit surface interpolation was addressed by Morse ***et. al.*** [Morse01]. They explore the method in [Tukr99], applying compactly supported radial basis functions to create an efficient algorithm for computing interpolated surfaces. As a result their technique produces significant improvements in memory utilization and computational efficiency. They used a family of radial basis functions with the necessary continuity but also with compact local support. The result is a sparse system whose solution can be accelerated and the result is single and closed form analytic representation of the desired surface. Yoo ***et. al.*** [Yoo01] used the approach of compactly supported radial basis functions to reconstruct the surface of the in-vivo bovine aorta from non-parallel, non-uniformly sampled ultrasound slices.

In this work, we demonstrate the use of implicit function interpolation to reconstruct 3D organ shapes from closed planar parallel and non-parallel contours that have been defined selectively by the user. The total number of contour points will be used as the input data to the implicit surface algorithm with arbitrary order. The number of these sampling points will not exceed the level of few hundred, and therefore the calculation times will be in acceptable ranges despite the complexity of the algorithm. The output result of the reconstruction algorithm is provided in two forms: as a triangulated mesh or as multiple parallel contours extracted in arbitrary plane directions. For the RTP applications we focus mostly on the reconstruction of contours in the axial direction. The algorithm can be separated into different modules from the point editing until the reconstruction of the surface and contours as follows:

1. Collection and processing of the given contour points. This step involves the generation of the contour constrains and filtering of unwanted.
2. Calculation of the implicit functions in 3D. In this step the information produced in step one will be used to solve a linear equation system that will provide the coefficients representing our interpolation function.
3. Evaluating the implicit function over a 2D or 3D grid we extract 2D planar contours or 3D polygon meshes respectively.

Before presenting technical details of the algorithms, we first introduce some definitions related to radial basis functions (RBF) and implicit surfaces.

3.2.1.1 Radial Basis Function Approximation

Our approach relies on scattered data interpolation to solve the shape transformation problem. The problem of scattered interpolation is to create a smooth function that passes through a given set of data points. The two-dimensional version of this problem can be stated as follows: Given a collection of ***k*** constraint points $\{c_1, c_2 \ldots, c_k\}$ that are scattered in the plane, together with scalar height values at each of these points $\{h_1, h_2 \ldots, h_k\}$, construct a smooth surface that matches each of these heights at the given

locations. We can think of this solution surface as a scalar-valued function $f(x)$ so that $f(c_1) = h_i$ for $1 \le i \le k$.

One common approach to solve scattered data problems is to use variational techniques (from the calculus of variations). This approach begins with an energy that measures the quality of an interpolating function and then finds the single function that matches the given data points and that minimizes this energy measure. For two-dimensional problems, thin-plate interpolation is the variational solution when using the following energy function E:

$$E = \int_{\Omega} f_{xx}^2(x) + 2 f_{xy}^2(x) + f_{yy}^2(x) \qquad \text{Eq 3.1}$$

The notation f_{xx} means the second partial derivative in the $f(x)$ direction, and the other two terms are similar partial derivatives, one of the mixed. The above energy function basically a measure of the aggregate squared curvature of $f(x)$ over the region of interest Ω. Any creases or pinches in a surface will result in a larger value of E. A smooth surface that has no such regions of high curvature will have lower value of E. The thin-plate solution to an interpolation problem is the function $f(x)$ that satisfies all of the constraints and that has the smallest possible value of E.

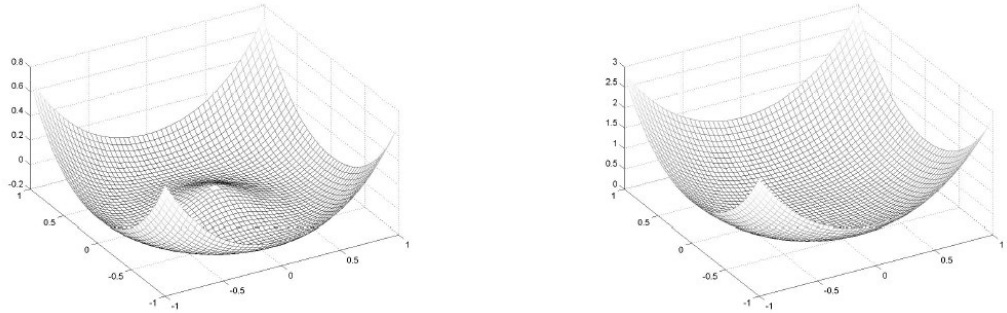

$\phi(x) = |x|^2 \lg(|x|)$ $\phi(x) = |x|^3$

(a) (b)

Figure 3-3. 3D representation of RBFs used in this work. In (a) the biharmonical radial basis function used in 2D interpolation schemes and in (b) the triharmonical radial basis function applied in 3D schemes.

As described in [Turk99], the scattered data interpolation problem can be formulated in any number of dimensions. When the given points c_i are positions in N-dimensions rather than 2D, this is called the N-dimensional scattered data interpolation problem. In this work, we will perform interpolation in three dimensions. When we refer to problems for great than 2D then the term thin-plate is less meaningful. The alternative term used is the variational interpolation and means the generalization of thin-plate techniques to any number of dimensions.

The scattered data interpolation task as formulated above is a variation problem where the desired solution is a function, $f(x)$, that will minimize Eq 3.1 subject to the interpolation constraints $f(c_i) = h_i$.

Eq 3.1 can be solved using weighted sums of a radial basis function (RBF) (see Figure 3-3). Common choices for RBF include the following (but not limited to):

1. Linear: $\varphi(x) = x$
2. Thin-plate spline: $\varphi(x) = |x|^2 \log(|x|)$.
3. Triharmonic: $\varphi(x) = x^3$

Using the appropriate RFB function, in our case we found as most appropriate the triharmonic, we can then express the interpolation function as:

$$f(x) = \sum_{j=1}^{n} d_j \varphi(x - c_j) + P(x) \qquad \text{Eq 3.2}$$

In the above equation, c_j are the locations of the constraints, the d_j are the weights, and $P(x)$ is a degree one polynomial that accounts for the linear and constant portions of f. Because the thin-plate radial basis function naturally minimizes Eq 3.1, determining the weights d_j, and the coefficients of $P(x)$ so that the interpolation constraints are satisfied will yield the desired solution that minimizes Eq 3.2 subject to the constraints. To solve for the set of d_j j that will satisfy the interpolation constraints $h_i = f(c_i)$, we can substitute the right side of Eq 3.2 for $f(c_i)$, which gives:

$$h_i = \sum_{j=1}^{k} d_j \varphi(c_i - c_j) + P(c_i) \qquad \text{Eq 3.3}$$

Since this equation is linear with respect to the unknowns, d_j and the coefficients of $P(x)$, it can be formulated as linear system. For interpolation in 3D, let $c_i = (c_i^x, c_i^y, c_i^z)$ and let $\varphi_{ij} = \varphi(c_i - c_j)$. Then this linear system can be written as follows:

$$\begin{bmatrix} \varphi_{11} & \varphi_{12} & \cdots & \varphi_{1k} & 1 & c_1^x & c_1^y & c_1^z \\ \varphi_{21} & \varphi_{22} & \cdots & \varphi_{2k} & 1 & c_2^x & c_2^y & c_2^z \\ \vdots & \vdots & & \vdots & \vdots & \vdots & \vdots & \vdots \\ \varphi_{k1} & \varphi_{k1} & \cdots & \varphi_{kk} & 1 & c_k^x & c_k^y & c_k^z \\ 1 & 1 & \cdots & 1 & 0 & 0 & 0 & 0 \\ c_1^x & c_2^x & \cdots & c_k^x & 0 & 0 & 0 & 0 \\ c_1^y & c_2^y & \cdots & c_k^y & 0 & 0 & 0 & 0 \\ c_1^z & c_2^z & \cdots & c_k^z & 0 & 0 & 0 & 0 \end{bmatrix} \begin{bmatrix} d_1 \\ d_2 \\ \vdots \\ d_k \\ p_0 \\ p_1 \\ p_2 \\ p_3 \end{bmatrix} = \begin{bmatrix} h_1 \\ h_2 \\ \vdots \\ h_k \\ 0 \\ 0 \\ 0 \\ 0 \end{bmatrix} \qquad \text{Eq 3.4}$$

The above system is symmetric and positive semi-definite. So there will always be a unique solution for the d_j and p_j. The above system can be solved directly with the symmetric LU decomposition as long as the number of constrains are limited to a few thousand. In this work we used symmetric the LU decomposition from [NuRec93] to solve this system.

3.2.1.2 Prepare constrains for 2D input contours

We can create smooth functions for a given 2D or 3D shape using implicit functions. Our interest is the use of 2D planar contours as input and to generate a smooth 3D shape as output. We aim to fit an implicit function to a surface where all points lying on surface will satisfy the equation:

$$f\left(c_i^x, c_i^y, c_i^z\right) = 0 \qquad \text{Eq 3.5}$$

In order to avoid the trivial solution that F is zero everywhere the off-surface points are appended to the input data and are given non-zero values, revising the interpolation problem:

$f\left(c_i^x, c_i^y, c_i^z\right) = 0$, ***i=1…, n*** ***(for on-surface points)***

$f\left(c_i^x, c_i^y, c_i^z\right) = h_i$, ***i=n+1…, N*** ***(for off-surface points)***

The boundary constraints are refer to the on-surface points. The question now comes how to generate the off-surface points. Since in this approach we use closed planar 2D curves we have to specify the number of points that should be interior and exterior to the curve. Paired with each boundary constraint is a normal constraint, which is a location at which the implicit function is required to take any non-zero positive and negative value (off-surface points). The locations of the normal constraints should be towards the interior of the desired curve, and the line passing through the normal constraint and its paired boundary constraint should be parallel to the desired normal to the curve. The function that is returned is an implicit function that describes our curve and the interpolation curve

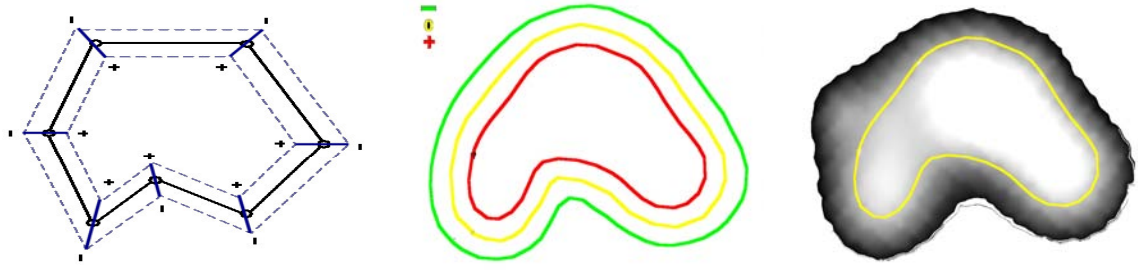

(a) (b) (c)

Figure 3-4. Extraction of normal constrains from the original contour (a). The off-surface points have the form of closed contours. They are generated along the contour normals and are indicated with plus and minus symbols. In (b) a manual generated (middle yellow line) and its normal constrains interior and exterior from the contour

will exactly pass through our boundary constraints.

Seven pairs of constrains are illustrated in Figure 3-4(a), with the boundary constraints shown as circles and the normal constraints as plug/minus signs. When we invoke implicit function interpolation with such constraints, the result is a function that takes on the value of zero exactly at our zero-value constraints and that is positive in the direction of our normal constraints (towards the interior of the shape). The closed curve passing through the zero-value constraints in Figure 3-4(c) is the iso-contour of the implicit function created using as input constrains those from Figure 3-4(b). Given enough suitably placed boundary constraints we can define any closed shape.

We now turn our attention to defining boundary and normal constraints for a given 2D shape. Assume that a given shape is represented as a gray-scale image. White pixels represent the interior of a shape, black pixels will be outside the shape, and pixels with intermediate gray values lie on the boundary of the shape. Let m be the middle gray value of our image's gray scale range. Our goal is to create constraints between any two adjacent pixels where one pixel's value is less than m and the other's value is greater. Identifying these locations is the 2D analogue of finding the vertex locations in a 3D marching cubes algorithm [Loren87].

The grey-scale image can be generated on different level, where contours have to get extracted, using predefined regular spaced grid. Each grid corner is a point ***(x, y, z)*** lying on the plane of the current level. To evaluate each corner the coefficients calculated from Eq 3.4 used. Thus, each point of the grid is substituted with the corresponding function value. Due to the nature of the implicit function shape, it is expected that at those levels where contour shape is about to be extracted grid edges will be marked with positive and negative values. To extract the contours, we try first to detect any edge in the grid whose end points being of opposite signs as shown in Figure 3-5. The opposite signs in the grid cell implies that in-between the cell edges there will be a point where the function can be evaluated and will result to zero value. Binary sectioning over the edge is used to localize the position of this value. After having this original point (shown as red square in Figure 3-5), the algorithm jumps to the positive corner and continues scanning the corners clockwise until a corner with opposite signed is found. We traverse the entire grid of each level until the contour is closed, visiting each grid cell that contains edges with opposite signs. The algorithm is capable to detect and extract more than one contour on a level.

3.2.1.3 Surface Reconstruction from Parallel Contours

In this chapter, we do not aim to present and compare the implicit surface reconstruction scheme with existing methods. Instead, we present a workflow on how to use the implicit functions interpolation as a tool for defining anatomical volumes from 3D data. The first type of problem we attempt to solve using implicit function interpolation is the reconstruction of 3D objects from parallel contours. Linear interpolation between key slices is a very common approach used in RTP process to accelerate target volume definition. Almost all contour interpolation methods consider only pairs of contours at any one time [Boiss88], [Payne94], [Bajaj95], and thus suffer from such normal discontinuities at the planes of the original slices. In the plane of slice i, the surface created between slice pairs $i-1$ and i will usually not agree in surface normal with the surface created between slices i and $i+1$.

To avoid discontinuities in surface normal, we must use information that involves more than just two slices at a given time. We can accomplish this using a generalization of the implicit function interpolation approach. Assume that we begin with k sets of constraints, one set for each 2D data slice. Instead of considering the contours in pairs, we place the constraints for all of the k slices into 3D simultaneously. Specifically, the constraints of slices i are placed in the plane $z = si$, where s is the spacing between planes. Once the constraints from all slices have been placed in 3D, we invoke the implicit function interpolation once to create a single implicit function in 3D for the complete set of contours. The zero-valued iso-surface exactly passes through each contour of the data. Due to the smooth nature of implicit function interpolation, the gradient of the implicit function is everywhere continuous. This means that surface normal discontinuities are rate, appearing in pathological situations when the gradient vanishes such as when two features just barely touch.

The contour interpolation result between parallel contours is illustrated in Figure 3-6. The kidney surface reconstructed in Figure 3-6(b) is a product of well-known reconstruction method from [Geige93]. The method used ten contours as input and produced near to 600 triangles. In Figure 3-6(c) the implicit function, interpolation is used to produce a mesh out of 19000 triangles. To extract the mesh for the implicit function we used the polygonizer proposed from Bloomenthal et. al. [Bloom94][Bloom97]. During the parallel and non-parallel contour constrain generation the contour spacing used in all of our results corresponds to the real contour spacing according to the acquired voxels size from the CT images. The contour spacing is an important control parameter for the implicit surface result. If the distance is small, only pairs of features from the two shapes that are very close to each other will be preserved through all the intermediate shapes. If the separation distance is large, the intermediate shape is guided by more global properties of the two shapes. In some sense, the separating distance specifies whether the shape transformation is local or global in nature.

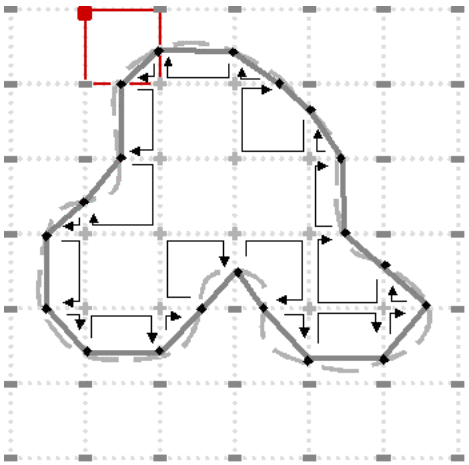

Figure 3-5. Contour tracing on a grid (single level) after evaluating the implicit function on each grid edge. The red arrow indicates the starting point of the algorithm

The results illustrate that implicit surface reconstruction produces much smoother results than conventional triangulation algorithms. To achieve similar mesh quality with conventional triangulation methods larger amount of input planar contours and point samples are required. A very interesting and useful side benefit of using the implicit function interpolation method is that it produces smoothly rounded caps on the ends of surfaces, which is a very acceptable and suitable effect for describing anatomical structures.

Notice that in Figure 3-6(c) the reconstructed surface extends beyond the last contour constraints in the positive and negative z direction (the direction of slice stacking). This "hemispherical" component at the end of the stack is a natural side effect of the implicit function, and need not to be explicitly specified. This effect can improve organ shape rep-

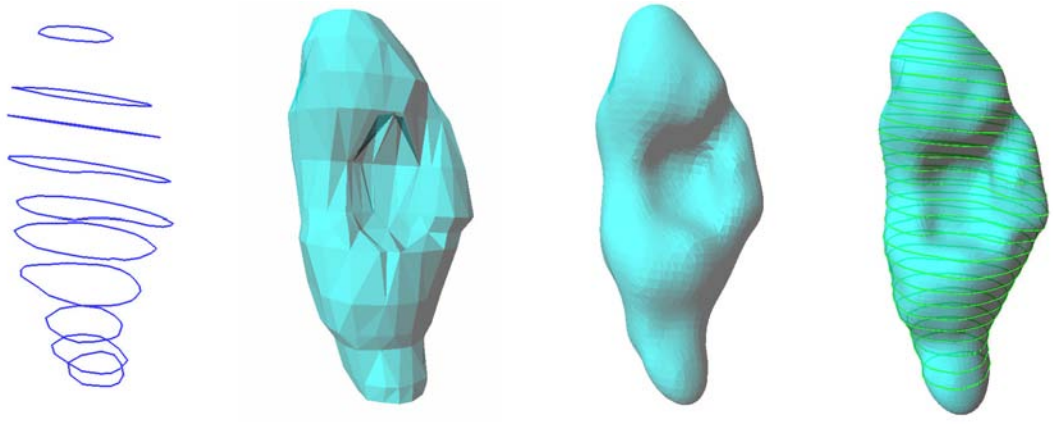

(a) (b) (c) (d)

Figure 3-6. Reconstruction of kidney surface from parallel contours. In (a) eleven manual segmented contours have been used as input to the NUAGES polygon reconstruction algorithm (b) and in the implicit surface interpolation algorithm (c). In addition implicit contours have been extracted and using the contour tracing algorithm and reconstructed with the implicit surface.

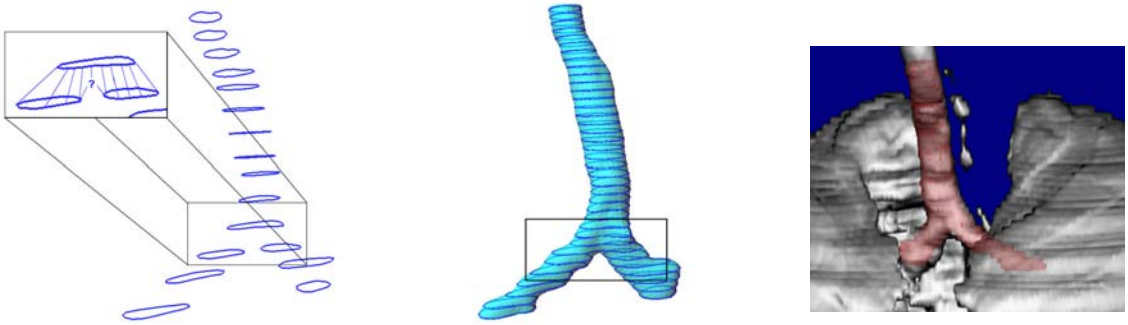

(a) (b) (c)

Figure 3-7. Contour samples defined according to trachea shape (a). In (b) the 3D surface reconstruction of the trachea shape using implicit surface interpolation. The extracted axial implicit contours have been used to allocate voxel grid reconstructed with red in (c), for comparison with the direct surface volume rendering.

resentation and in addition can reduce the number of contours needed for organ representation.

Reconstruction of organs with branches is a common issue in RTP. The common cases are the bronchial tree, prostate seminal vesicles, neck regions and immune system branches. In those cases, the user has to define a bigger amount of planar contours. Omitting key contours between single contour shapes and spited contours is usually not a options since advanced interpolation methods are required to feel the missing gaps. In a similar category belong key contours with concave that have to be interpolated with convex contour shapes. As shown in Figure 3-6 the kidney concave cavity can be represented very well using implicit surfaces in comparison to the standard contour-by-contour triangulation algorithm that lead to unreasonable triangle connections. For branching contour interpolation, it is usually difficult to decide a reasonable triangular connection rule,

when and where contours in a slice should be intersected or not. In Figure 3-7(a), an example is given where a number of contours describe the shape of the trachea. The main challenge for the contour interpolation of surface reconstruction algorithm is how to handle the bifurcation problem.

For the implicit surfaces, the definition of bifurcation is a property that can be handled with flexibility. The degree of bifurcation is highly related to the continuity degree of the implicit functions and to the distance between the single and contour pairs. As previously mentioned for contour distances we use the physical units as given from the CT volume data. The surface rounding-off presented in previous examples, is an effect not always useful. In this particular case round of the end of the branches is not needed. This feature can be controlled using a bounding box, applied during implicit function polygonization. In most of our examples the bifurcation approximation of the implicit surface fits very well with the natural bifurcation of the trachea (see Figure 3-7(c)).

3.2.1.4 Non-Parallel Contours

In the previous section, we only considered placing constraints within planes that are all parallel to one another. In this work the most powerful advantage provided from the implicit function interpolation is the capability to interpolate constrains located in 3D space. In RTP but also other medical images MPR images are often used for navigation and diagnosis. Investigating anatomical structures in those images provides very often more information than the standard cross-section (axial) images. Probably the greatest advantage is that organ length and shape can be better appreciated. For example if one is looking for the length of the kidney though the axial slices then more than 20 slices with 5mm voxel thickness in z direction have to be investigated until the positive and negative z direction limit is found. In case of course the slice thickness is smaller then number of slices increases and even more slices has to be investigated. In the frame of 3D simulation, powerful and efficient segmentation tools must be present. Hence, we adapted a fully 3D manual contour definition for the organ and tumour segmentation with the help of the implicit function interpolation.

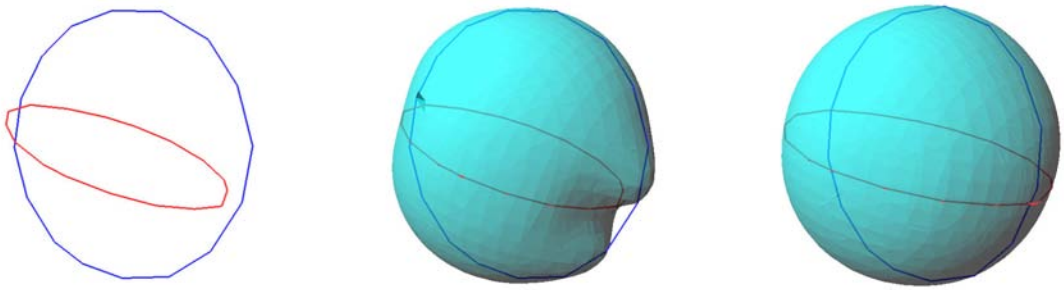

(a) (b) (c)

Figure 3-8. A simple surface reconstruction example from orthogonal contours.

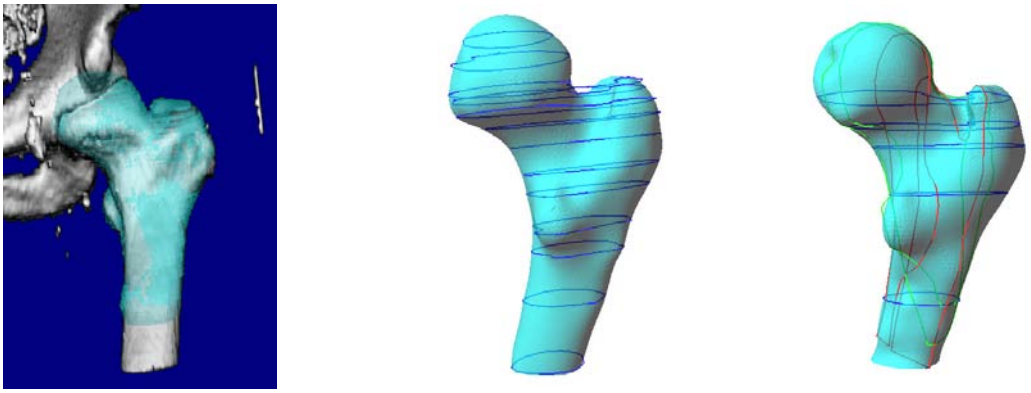

(a) (b) (c)

Figure 3-9. Surface reconstruction of a femur. In (a) the 3D volume reconstruction with the femur bone marked. In (b) an implicit surface reconstruction model of the femur using only parallel contours. In (c) a combination of different non-parallel contour and the final implicit surface of the femur.

To realize this concept the system allows the user to define closed planar contours on any of these planes. An even bigger degree of organ definition could be offered by allowing the segmentation of structures on any arbitrary cutting plane of the volume. The limitation of such approach will be the difficulty to orient the cutting plane in the volume. Definition of anatomical structures on the sagittal and coronal MPR images offers better description of the organ end shape providing more information than the axial contours. A common example is the round-off shape of organs, which is omitted when using axial planar contours as show in the previous example. However, this important detail must be included and taken into account for visualization and calculation purposes.

The most obvious problem one might face during non-parallel contour definition is the possibility to have different contour sizes. Usually anatomical structures in the MPR images have different appearance. This is due to image quality such as CT acquisition parameters, slice thickness and internal organ movements. During manual contour definition, it is often the case that the sagittal or the coronal contours have unequal slice length at the organ extremities. Considering this effect to the global surface shape we are about to reconstruct, it is rather less important. However, this problem becomes more noticeable when getting near those regions where the non-parallel contour constrains are close to each other (organ extremities) and the implicit function is forced to pass though all sample points.

In Figure 3-8(a) two orthogonal contours are generated with circular shapes. The coronal contour (red) has been designed smaller in diameter than the axial (blue). For those two contours we apply the implicit surface interpolation. Surface discontinuity is obvious in Figure 3-8(b) at the location where the coronal contour edge is far from the axial contour. This effect produces rapid changes on the final implicit surface shape since the implicit function will pass through every contour constrain. The way to solve this problem is by considering as reference the size of the bounding box of the first designed contour. The next contour designed from the user is forced to reach the size of the reference contour. To achieve this we apply a linear scaling on the second designed contour until the desired

contour size is reached and the contour edges are near to each other. The result of this approach is presented in Figure 3-8(c), where the size of the red contour is adjusted to the size of the blue contour. This is a rather simple example where only two contours are used. It is reasonable that in the clinical routine much more contours are used and the same problem will occur on several surface locations. The ***contour scale matching*** is omitted when the difference of the bounding box sizes is smaller than few millimetres (in our case 3mm). This can be an adjustable parameter from the user.

The implicit surface interpolation algorithm can be applied even if we consider a large number of contours in all three main planes. This will increase the number sample points and will make their topological relation among them more complex. As already mentioned defining structures on the sagittal and coronal reconstructions presumes that the image quality used is good enough to discriminate the necessary structures. The example Figure 3-9 illustrates the definition of the femur head, which is considered as a complex structure with a rather irregular concave shape. To reconstruct the femur shape using parallel contour (axial direction) we needed to place more than 13 contours Figure 3-9(b). The total area defined within the axial contours was 245.5 cm² and the number of sample points used was 315. For the same shape we needed to place 9 non-parallel contour as Figure 3-9(c) illustrates; five(5) axial, two(2) coronal and two(2) sagittal, which covered 282.3 cm² with number of sample point of 320. An example of non-parallel contour definition over the CT slices is given in Figure 3-10. Both implicit surface shapes have been reconstructed with small topological differences from the original shape. One can notice the difference of the femur head between the parallel and the non-parallel implicit surfaces.

An interesting issue to notice when reconstructing implicit surfaces from non-parallel contours is the inaccuracies of the surface at those points where contours from different direction are intersecting. From the algorithmic point of view this effect illustrates one important property of the implicit surface interpolation. On the other hand introduces topologic errors on the shape of the structure we attempt to reconstruct. To solve this problem we introduce the averaging of the two neighbour sample points. The result can replace the two ore more original sample points with a new one decreasing the surface inconsis-

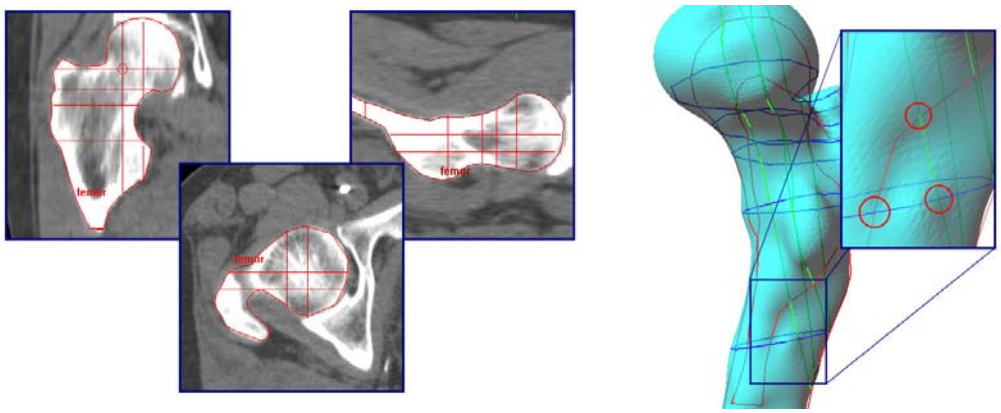

(a) (b)

Figure 3-10. Definition of non-parallel contours on CT slices. In (a) from left to right: coronal, axial and sagittal contours. In (b) surface inconsistence at the intersection locations of the non-parallel contours.

tence. Probably the best way to prevent this effect is provide the necessary tools to the user in order to be able to adjust mismatches of the sample points interactively and also to be able to see the result in real time in 2D and 3D views.

The surface reconstruction of non-parallel contours can be applied to several organ type. There is nothing special about any particular set of planes once we are specifying constraints in 3D. We can mix together constraints that are taken from planes at any angle whatsoever, as long as we know the relative positions of the planes (and thus the constraints). Most contour interpolation procedures cannot integrate data taken from slices in several directions, but the implicit surface approach allows complete freedom in this regard. In the previous figures, all contours have been placed perpendicular to one another.

3.3 Segmentation of Normal Tissues

Several organs within the human body have very distinguishable characteristics, depending on the modality used to visualize them. In the frame of this work, we will focus on a specific organ the spine canal, which is of great importance for the workflow of the RT planning. In this work the base of the implemented segmentation, are the edge-detection techniques modified accordingly. All the segmentation algorithms have been applied and tested with CT images. However, they are not limited only to CT images, but they can also be used for segmenting MRI and US images. These techniques have been selected as optimum solutions between speed, effectiveness and complexity. It is well known that active contour and region base algorithms need from the user to pre-define conditions.

3.4 Segmentation of the spinal cord

The spinal canal is the anatomical region, which hosts the spine, one of the most vital organs in the human body. Its length starts from the base of the skull ending at the top of

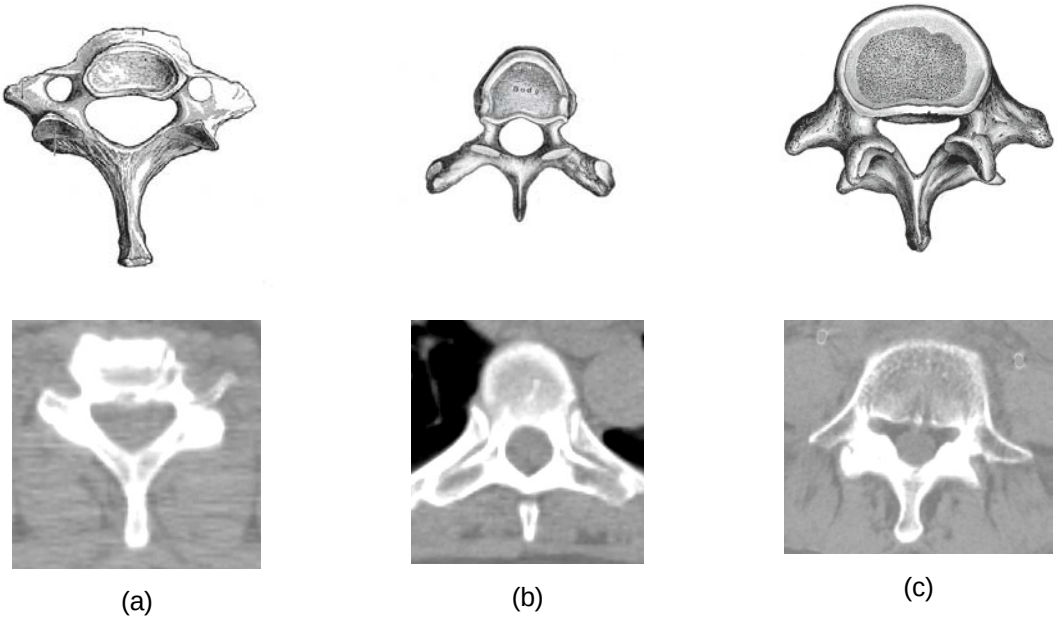

(a) (b) (c)

Figure 3-11. Illustration of different spinal cord vertebras as anatomical sketches (top row) and as CT axial section (bottom row). In (a) a cervical vertebras, in (b) thoracic and in (c) lumbar vertebras.

the pelvic region. Spine is the channel of communication between the brain and the rest of the human body. Every signal transmitted from the brain follows the spine before the delivery to anatomical region. In radiation therapy it is very critical the accurate segmentation of the spine in order to calculate the allowed amount of dose during the treatment of the patient. The spinal canal is indicated as hole in the vertebras with irregular ellipsoid and circular shapes, which in most cases are convex. Using CT imaging the contrast of the spine in very low compared with the surrounding tissues, which are mainly the bodies of the vertebras.

Figure 3-12 illustrates several shapes of the spinal canal from different spine regions. The top row includes 3D sketches of vertebras of the cervical, thoracic and lumbar level and the bottom row some axial CT images of the vertebras in the corresponding levels respectively. Interesting to notice is that the spinal canal of the illustrated CT images is closed and well defined. This geometry can be segmented easily using image thresholding techniques. Nevertheless, except from the circular closed shapes, the spinal canal might be open, this happens at the locations where the vertebras are joined, and the nerve tree distributes. Figure 3-12 illustrates such examples. At that region, the surrounding tissue contrast is very similar with the spine contrast and therefore any simple threshold segmentation technique like region-growing and edge tracking will fail.

In this section of the thesis, a new approach is described for the 3D segmentation of the spinal canal. The algorithm is a mixture of the edge detection combined with contour linear interpolation and a 2D radial ray-casting algorithm. The technique aims to detect the whole shape of the spinal canal with minimum user interaction. Main steps of the method are:

1. Definition of the starting point (User interaction)
2. Detection of the first sample contour using boundary tracking. Evaluate contours consistency (shape, location and texture)
3. Extract of the new starting point considering the centre of gravity of the current contour.
4. Propagation of the starting point to above and below cross sections from the original starting point

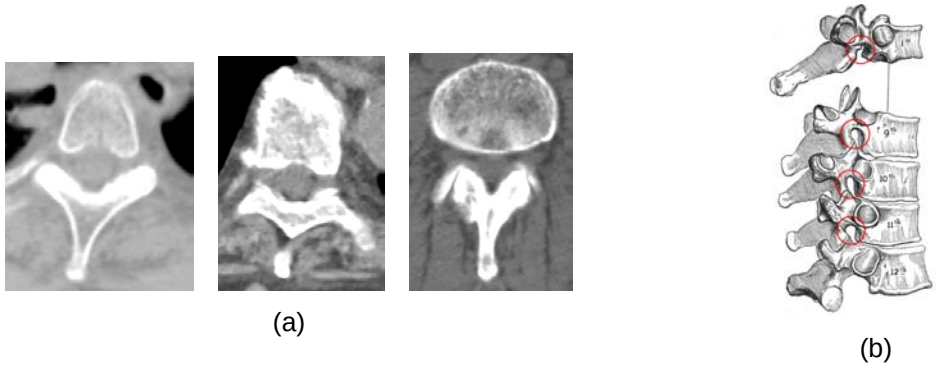

(a) (b)

Figure 3-12. Discontinue spinal canal. In (a) three examples of CT images with open spinal canal. In (b), the red circles on the sketch indicate potential locations in the spine that will produce open vertebras bodies when a CT acquisition will be made.

5. Repeat steps 2, 3 & 4 until all cross sections have been examined.

3.4.1 Definition of starting point

There are three choices one could have when attempting to define a starting point:

a) Selection of a point inside a closed vertebra canal (see Figure 3-12)

b) Selection of a point inside an open vertebra canal (see Figure 3-12)

c) Selection of a point outside the vertebra body.

Selecting of a starting point as outside the vertebra point should result to a warning for the user that the algorithm cannot proceed with the spine tracing. To qualify such a case we use the HU range as an indicator. The selection of the starting point based on case a) is the optimal situation and the algorithm can proceed to the next step without any problem. If a starting point is defined inside an open vertebra then most likely the boundary-tracking algorithm will fail to continue. Due to the restrictions of the BT mentioned above, in this case it is not possible to initialize the tracing process from an arbitrary slice. Instead, a slice with closed vertebra's canal must be selected from the user. Due to this limitation the user must be trained under the trial-and-error principle until the wanted contour is found. As solution to this problem we developed an angular ray-casting (ARC) algorithm that enables the tracing of the vertebra location in an angular behavior using predefined values of angles (see Figure 3-13). This step is activated only if the BT fails to trace the spinal cord with a specific area and HU content of low range. The result of the ARC will be the generation of a number of points on the boundaries of the open vertebra. In order to generate the final contour shape we interpolate the traced points using the Spline approximation.

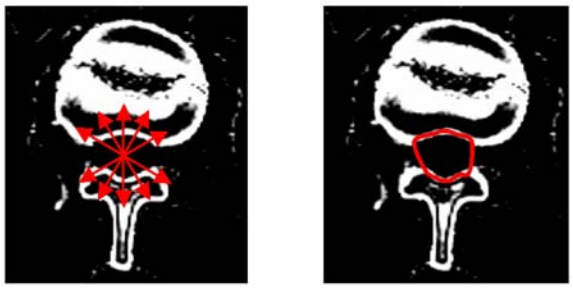

(a) (b)

Figure 3-13. Angular tracing of open vertebra boundaries. In (a) the tracing of boundary points using angular scanning. In (b) the result contours after interpolating the original contours.

3.4.2 The Boundary-Tracking Algorithm

The key component of the method is the boundary-tracking (BT) algorithm [Haral85]. The implemented technique works on a 2D level and scans one CT image at a time. The CT image level corresponds to the original cross section image. The BT algorithm requires an initial point to start the tracing of the edge of the object under investigation. The initial point travels to one direction, vertical or horizontal until and edge of the investigated object is reached. In case the tracing point fails to reach the edge moving in one direction (e.g. vertical), the other one is used. This is repeated until the required edge is found.

Then the algorithm will start to investigate the surrounding pixel of that edge and check whether they belong to the current edge or not. This is done by selecting a range of HU

levels. The algorithm uses a constant threshold selection with levels [300 to 600] HU range. If the pixel under investigation is within the range then is classified as 1, otherwise as 0. Concurrently the classified pixels as 1 are stored in the memory with the detected sequence, recording the shape of the investigated organ. The edge detection algorithm has low complexity and therefore is quiet fast on processing. During the tracing process a large number of points is collected, and depending from the segmented area it might reach more than 300 sampled points. This has the benefit that every voxel detail is recorded providing high accuracy to the description of the contour shape. Alternatively, all these voxels enhance sharp edges giving an uncomfortable optical effect. Therefore, the original voxels are decimated to approximately 40% of the original number. Simultaneously the contour shape is also smoothed.

The main drawback of the BT is that is a binary approach and hence is very sensitive to grey value variations. If the threshold value is not selected properly then the system will fail to detect the appropriate canal shape. In case the algorithm slides from its edge path though a gap, then the algorithm will generate an overflow of points. To avoid this situation a maximum number of points is used as the limit. This can be very often the case when the vertebra's shape is interrupted from tumour metastasis or bone osteoporosis. Most of the inaccuracies of the segmentation method require the user intervention to optimise the result. An example of contour tracing using edge detection on single slice can be found in Figure 3-14. In image (a) an accurate edge detection of the spine. A misleading result of the algorithms due to boundary bridging is illustrated in image (b). Image (c) shows a completely erroneous segmented region. Instead of the spinal canal, the lower bony part of the vertebra is detected. To improve the algorithm performance we calculate a secondary volume map using the gradient estimators as described in [Levoy88]. This approach allows a comprehensive representation of tissue boundaries compared to the conventional thresholding techniques. The example in Figure 3-15 demonstrates how the boundary description can be improved using the gradient estimators.

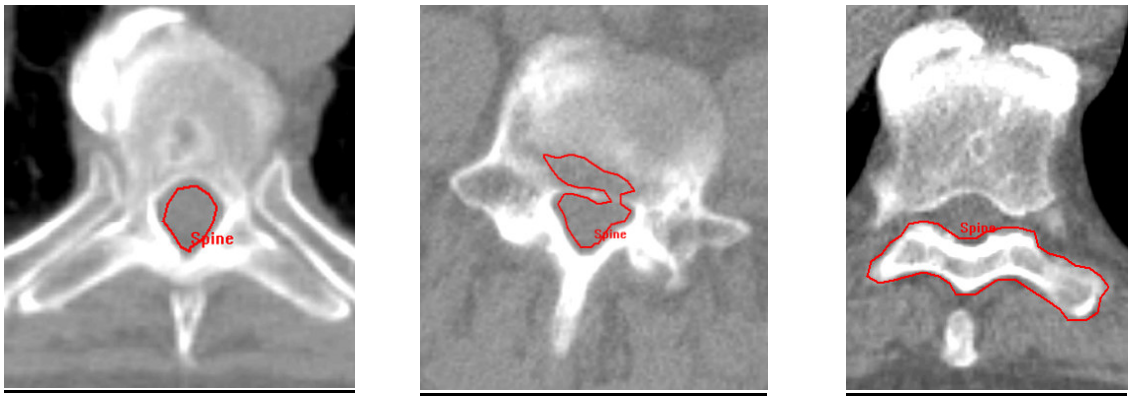

(a) (b) (c)

Figure 3-14. Spine boundary tracking of single slices. In (a) an accurate detection of the spine, in (b) a misleading detection of the spine due to osteoporosis and in (c) a failure of the BT algorithm due to open vertebra shape.

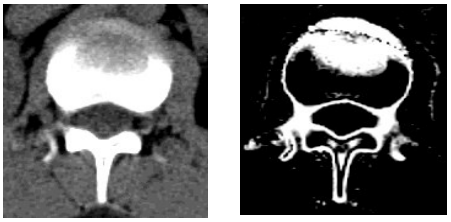

(a) (b)

Figure 3-15. Difference between simple image thresholding (a) and gradient detection (b).

3.4.3 Tracing Conditions

After the user has defined the starting point, the edge detection algorithm is activated trying to specify the boundaries of the spinal canal. The threshold value we used for the segmentation has a range between from 50HU (inside spine) to 450HUs. This range of HU values might be slightly different among CT acquisition protocols. The edge detection algorithm is effective only in those cases where the shape of the canal describes a closed contour. If that is the case, the centre of gravity of the new generated contour is calculated. If there are two starting points existing then they will be used to generate a straight line between them. The end of that line will propagate towards to the scanning direction within the CT volume. The intersection point with the next available cross section at the Z-direction will be used as starting point for the BT algorithms.

To segment the whole data volume we have to repeat the above step to both directions, left and right from the starting point. This process will generate automatically a virtual path that will reach even the last slice of the CT volume when this is necessary. During contour tracing some of the contours generated from the BT will be rejected due to incompatibility with the rest of the normal spine contours. The criteria used to qualify contours as belonging to the spine are:

a) Contour area

b) Distance of the centre of gravity of the current contour from the previous found.

c) Texture value content.

Contours that do not fulfill the above properties will be deleted from the system and the system will continue searching and tracing contours on further cross sections. The deleted contours will be replaced with linear interpolated contours between. The contours found during BT will be used as the key contours for the linear interpolation algorithm.

To perform this, a slope factor **A** is calculated between the key slices. The value is

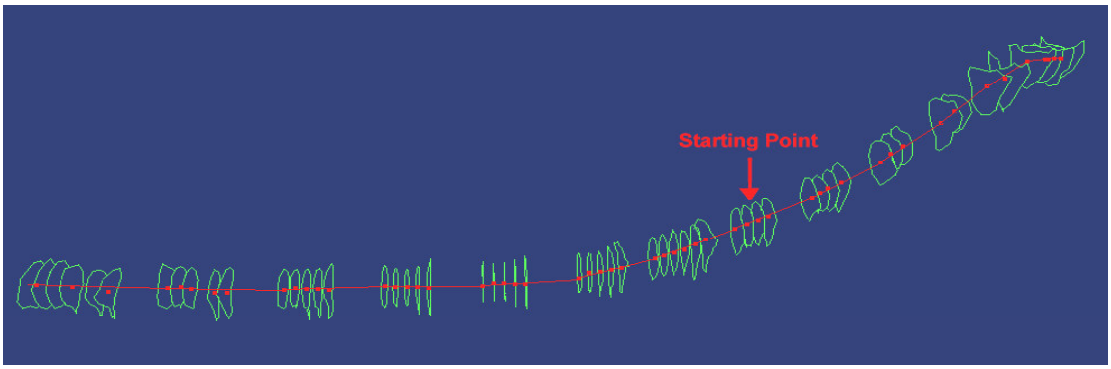

Figure 3-16. Wire loop display of the traced spine contours. The starting point is illustrated with an arrow. The sampling point path is drawn with the red line and the centre of gravity of each contour is shown using the red dot.

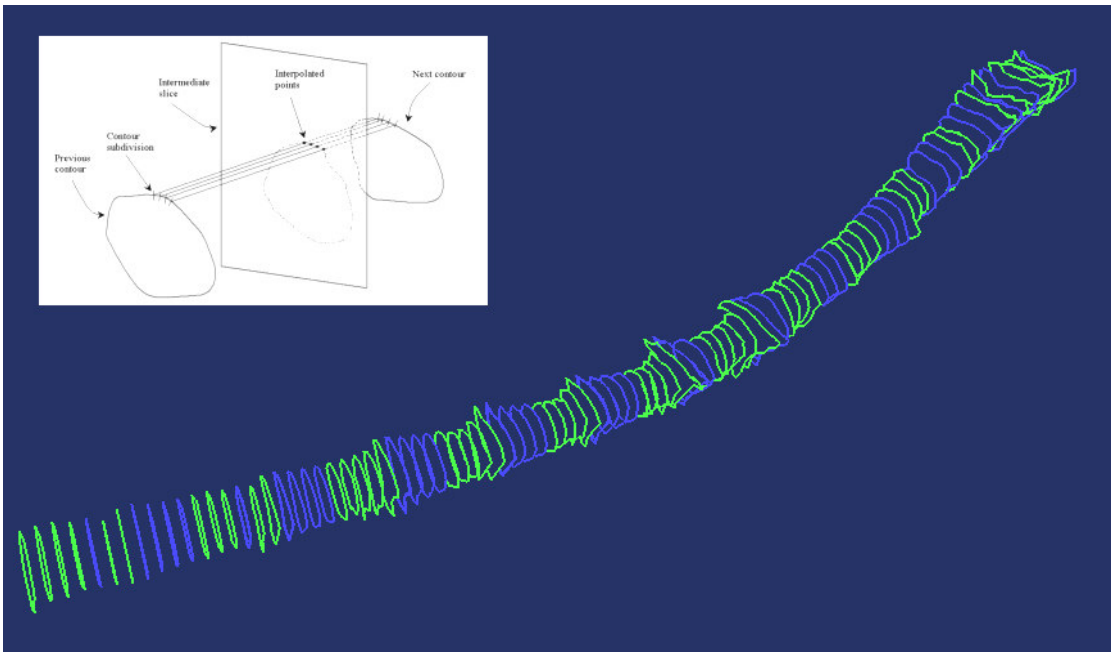

(a)

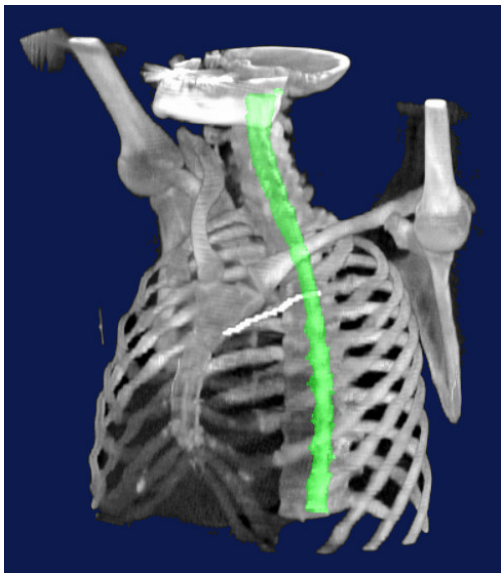

(b)

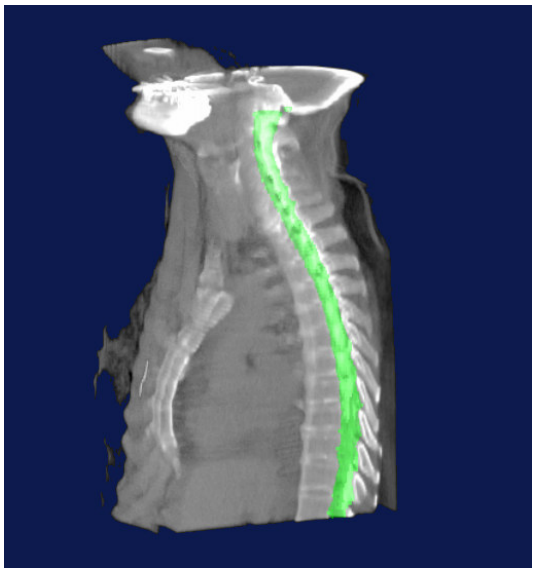

(c)

Figure 3-17. Linear interpolation between key contours. In (a) the principle of the linear contour interpolation is shown in the small image top left. In the spine shape the key contours are illustrated with green and the interpolated contours are illustrated with blue. Images (b) and (c) show spine segmentation results on CT data.

given by the equation:

$$A = \frac{(\text{Current\_slice\_pos} - \text{Previous\_contour\_pos})}{(\text{Previous\_contour\_pos} - \text{Next\_contour\_pos})} \qquad \text{Eq 3.6}$$

Since each key contour has individual number of samples of segment points, the algorithm subdivides each contour into the same number of points in order to simplify the contour interpolation step. Then a starting point is selected, which is usually the point of the 12o'clock position of the contour. To calculate the X and Y pixel (or voxel) position of the interpolated point we use the following formula:

$$X_{int} = X_{previous\_cnt} + A*(X_{next\_cnt} - X_{previous\_cnt}) \qquad \text{Eq 3.7}$$
$$Y_{int} = Y_{previous\_cnt} + A*(Y_{next\_cnt} - Y_{previous\_cnt})$$

The principle and the result of the linear contour interpolation are shown in Figure 3-18 (a). Figure 3-19 (b) and (c) show spine segmentation results on CT data set.

3.4.4 Results

The algorithm was evaluated using 14 CT datasets from 14 arbitrary selected subjects. All subjects were scanned using spiral CT with equal slice thickness and space. Overall 1229 slices with 3mm thickness were collected. The segmentation accuracy was assessed by comparing the automatic computer-based segmentation, with the results obtained by manual analysis. Differences on the contour border on each slice level were assessed by computing the mean and RMS distance between the computer defined borders and the manually defined borders [Chala97]. In addition, the overall difference of the spinal cord volumes was assessed between the computers defined and the manually defined structures. These results are shown in Figure 3-18. The range of variation in volume meas-

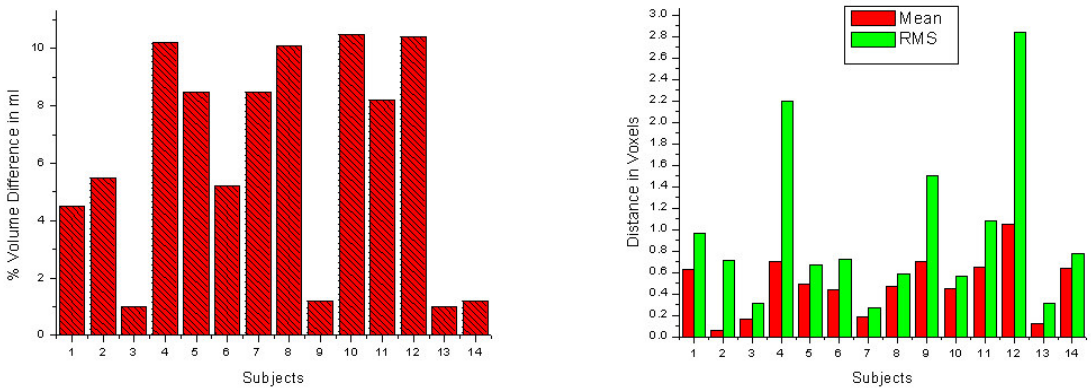

(a) (b)

Figure 3-18. Comparison of manual and computer traced spinal cord contours. In (a) The percentage of volume difference in ml. In (b) Mean and RMS values between contour boundary distances.

urement was 1.0%-10.2%, with a mean variation of 6.14% ± 3.82% (mean ± standard deviation). The range of variation in boundary distance measurement was 0.05-1.05 in voxels, with a mean variation of 0.48±0.27. In addition the algorithm provides good speed performance since 1-2 seconds are needed in average in order to segment a volume with 90 slices on a Pentium III 933MHz processor.

3.5 Summary

In this chapter, we discussed a daily clinical problem in the frame of 3D Simulation and RTP; the definition of anatomical structures in CT data. We present a number of computer-based tools that can assist the segmentation process during the 3D simulation process. The methods presented here are categorized to manual and semi-automatic methods. For the manual volume definition, we present a 3D interpolation method based on implicit functions. Due to the high order of continuity of the function, the interpolation scheme can reconstruct a surface from 3D sample points that describes very accurately the shape of different anatomical structures. The input samples can be the product of contours defined on parallel imaging cross sections. Even more advanced is the capability of the algorithm to handle the non-parallel contours either perpendicular or even arbitrary placed relative to each other. This has been a new concept for radiotherapy imaging applications.

The conventional 2D segmentation tools on the axial cross sections have been for many years now the standard methods used. Advantages of the new concept is the flexibility and freedom given to the clinicians to investigate new ways of defining anatomical structures taking advantage of the full 3D information available on the multiplanar reconstructed slices such as sagittal and coronal, As a result the segmentation process improves in terms of speed and selectivity. In addition, the time needed to segment structures can be dramatically reduced since fewer contours are required to describe the shape of structures.

In this chapter, we also demonstrate that segmentation of the spinal cord can be achieved very accurately, in a few seconds with minimum user interaction; the user needs only to define an initial starting point for the algorithm. The algorithm can automatically trace the spine path thought the complete volume of cross sections. False contours that are not correspond to the spine shape and position can be rejected automatically from the system and can be replaced with linear interpolated contours considering as key contours those already found by the system. The boundary-tracking methods used, belong to the deterministic approaches and therefore there is the tendency to produce misleading results under some circumstances. To reduce that effect data pre-processing and the gradient volume of the original CT data can be used as input to the segmentation routine.

Chapter 4

Fast Smoothing of Superficial Respiration Artifacts in CT-Volumes

4.1 Introduction

During CT data acquisition the normal breathing process, internal organ movements, and patient global movements might introduce motion artifacts in the acquired raw data. This motion may be in three dimensions and generally result in artifacts that appear as streaks or distorted semi-transparent structures in the general vicinity of the motion. Using conventional techniques for data acquisition the diagnostic information are significantly reduced due to the motion blurring. Therefore in diagnostic imaging examinations that include the chest or the upper abdomen, the patient must also hold the breath, and it may be necessary for multi-slice studies to be acquired in several single-breath-hold sections. In diagnostic imaging there are several perceptions proposed to overcome the motion blurring on the images [Ritch96], [RitmA90], [RitmB90].

In contrast to diagnostic imaging motion artifacts in CT images have a completely different impact and appreciation in RTP [Lange01]. During tumour irradiation the patient might be immobilized but the breathing process continues normally and freely. In radiation therapy we cannot demand from patient to regulate breathing as can be done in diagnostic imaging during data acquisition. Main reason for that is that the irradiation process lasts more than one minute and therefore is it not possible for the patient to stop breathing and in addition to that some of the patients are having severe respiration disruptions. Irradiation of patient with gating has been proposed as alternative, but these techniques still belong to the non-standardized methods [Wong99]. Considering the above it would be more accurate for a CT data acquisition that will be used for the RT planning to record most of organ movements that occur during normal patient conditions. The result of this acquisition will provide with useful information about the movements of specific organs that might be located near or attached on a tumour, and vice versa. This information could assist the more precise assignment of the field size and orientation that will be used to treat the tumour.

Our main interest in this work reflects on the body surface movements of the patient. Principally the surface of the patient can be visualized in 3D using voxel or polygon based techniques. Usually the polygon-based techniques are used since the body contours can be defined and modified if necessary from the user. Then triangulation techniques are used to generate a mesh out of the final planar contours [Boiss88]. Based on the mesh surfaces several calculations must and can be performed during dose distribution calculation. In addition to communicate the body contour coordinates between different software systems in the radiotherapy department, the planar contour representation is used as standard geometric format. An important aspect during RTP is the calculation of the Source-to-Skin-Distance (SSD). This parameter serves several functions including the following:

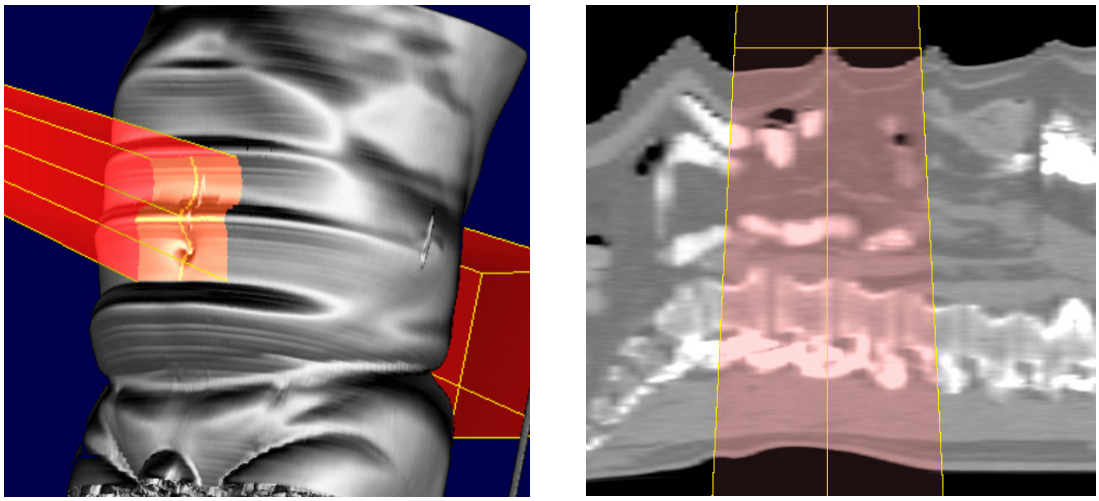

(a) (b)

Figure 4-1. Torso volume illustration with treatment field. In (a) volume rendering reconstruction of a male torso with an overlay of the 3D treatment beam. In (b) a 2D sagittal MPR of the CT data illustrating the iso-center placement of the beam on the crest of the breathing wave.

- Beam iso-center placement during geometric planning of the treatment and patient set-up verification prior to treatment.
- During dose calculation most commercial dose algorithms consider the body surface as the borders for starting the attenuation of the dose distribution on the target volume as well as on the organs at risk. Different anatomy of the body surface will result in variation of the dose distribution.

Hence it is common understanding in radiotherapy, that inaccuracies on patient's body planar contours will lead to inaccurate calculations and analysis related to the patient's body surface. In Figure 4-1 an example of surface reconstruction is presented where the treatment beam is projected over the patient's 3D surface. The corresponding sagittal view with the 2D beam overlay shows that considering the current volume information the iso-center of the treatment beam would be placed on the pick of the wave, which can be of course very misleading for the patient treatment.

4.2 Related Work

To our knowledge this is the only report trying to deal with the reduction of breathing artifacts on the patient's surface in RTP. Our method is motivated from previous reports appeared in computer graphics community related to polygonal meshes smoothing. Digitisation is a very common approach used to acquire the surface shape of complex geometric models. The 3D scanner technology enables us to capture detailed and dense clouds of points of objects surfaces. These samples are then organised into a triangular mesh for further development. However the original reconstructed models are usually contaminated with noise, and therefore mesh processing algorithms, such as mesh filtering, editing and mesh simplification are usually necessary for further refining of the reconstructed model. The Laplacian algorithm [Vollm99] is an approach that very often used for mesh fairing,

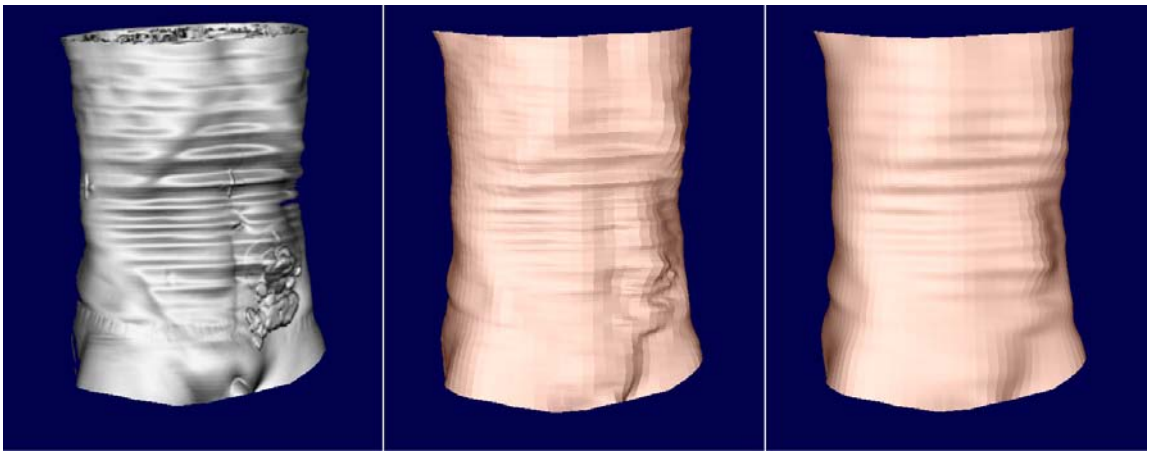

Figure 4-2. Most left-Original volume data reconstructed with volume rendering. Middle-The corresponding polygon model. Most right-Polygon surface after 60 iterations with the Taubin's explicit fairing algorithm

but results to serious shrinkage and distortion of the surface shape. This is the problem that most researchers addressed and tried to solve.

Taubin ***et al*** [Taubi95] first proposed the fairing algorithm for irregular meshes by adapting a signal processing approach. He adapted two derivatives of the discrete Laplacian, as well as an explicit iterative procedure to fair the meshes and minimise the shrinkage. Kobbelt ***et al*** [Kobbe98] used the ***umbrella operator***, which basically stands for the discrete Laplacian. Their approach was combined with Taubin's to stabilise the result of the ***umbrella operator*** and was used in the construction of fair interpolator subdivision schemes. Vollmer ***et al*** [Vollm99], improve the Laplacian smoothing method to attenuate the shrinkage. The basic idea was to move the vertices of the smoothed mesh towards their previous location by some distance. Probably the most effective and stable solution to the faring problem is given by Desbrun ***et al*** [Desbr99]. In his approach, the implicit fairing was based on Laplacian operators that were used for the design of the low pass filter. For reducing the degree of mesh shrinkage a scale operator was used in combination with the Laplacian operators as well as constrain parameter of volume preservation. This parameter was calculated as the relation between the volume of the mesh at a smoothing iteration and the volume of the original mesh. In the same work the inadequacy of the umbrella operator in terms of mesh distortion is discussed, if applied on irregular sampled meshes. The proposed solution to the problem was a curvature flow process that was used to preserve sliding of the vertices of flat areas and curvature for constant curvature areas.

The techniques described above have as basis the umbrella operator that is calculated directly from the neighbour vertices of the centre vertex ***p***. In every case the aim is to reduce the introduced noise at the reconstructed mesh or even for fine smoothing of the final surface. One requirement of the smoothing approach of course is the maintenance of the main characteristics of the surface, which represent the low frequencies of the mesh. Figure 4-2 illustrates a surface reconstruction of the abdominal region using volume rendering. The original volume data is composed of 165 slices that are equally spaced in 3mm distance. The breathing phases of the patient cause the abdominal region to expand and shrink. In the current example this process has been acquired as useful information

and can be observed on the skin surface as “waves”. The wave amplitude and phase varies from patient to patient but also in different time moments within the same study. The body contours from each slice have been automatically segmented and converted into planar contours. These planar contours have been used to reconstruct the polygon surface displayed in the middle image. As already mentioned in previous paragraph, these “waves” influence in several aspects calculations in radiation therapy treatment planning process. The goal now is to smooth the observed waves into an average position maintaining as much as possible the original mesh volume and basic surface curvatures. The most right image shows the results after applying 60 times iteratively the explicit fairing method as described in [Taubi95] without smoothing constrains. It is obvious from the results that this approach smoothens the small details, high frequencies, and maintains the main surface characteristics, low frequencies, quiet effectively without shrinking the original mesh. However the problem stated above is not reduced.

In this work a different approach compared to previous is introduced. Our method is able to minimize, and in some cases to eliminate, the motion artifacts introduced from to the respiration process in the CT data acquisition on the patient’s body surface. In the current method we consider as key step the extraction of the planar contours from the original CT data in a specific manner, following the motion of the breathing process as this is captured on the axial CT images. Important aspects at this point are the definition of the adequate number of sampling points that will compose the planar contour and will remain constant during the sampling process of every slice, as well as the location of the sampling points in terms of angular distance. The sampled points that compose the acquired contours will be filtered based on their angular value. This converts actually the mesh fairing problem into simply one dimensional signal processing. However the smoothing step will also cause deformation to the main features of the original mesh. Therefore we introduce constraints on the level of the planar contour as well as on the angular position. This allows the user to select specific level of axial contours from i to $i+n$, for smoothing. In a similar way angular ranges can be selected.

4.3 Generation of Body Surface

The breathing process is a complicate one and involves the combinatory work of several internal organs. Crawfort ***et al*** [Crawf96] generated a parametric model of the breathing process based on cross sectional images. Assuming that the acquired cross section image was with supine patient orientation, with the patient’s back resting on the scanner’s table, one can notice that breathing causes a time-varying magnification of factors ***Mg(x)*** and ***Mg(y)*** of the image in both image directions x, y respectively. Richies ***et al*** [Ritch96] in order to create simulated respiratory motion data, used a radial based warping function. The warping function consisted of angularity spatially and temporally varying magnification about a point at the posterior edge of the test object. Of course the above models are simplified ones since the physical breathing process involves also translation to the z direction, which is difficult to predict and correct based only on cross section images.

We also consider that the angular based magnification model represents better the respiratory process. In order to support this statement we consider an experiential comparison between different studies CT studies. Among 15-20 CT data sets of the abdominal and chest region most of them showed that the outer body contours translate similar to those illustrated in Figure 4-3. Both illustrated contours are extract from the original CT image on the same slice level and indicate the outer body contour in two different time

moments. Although the presented approach involves the correction of the motion artifacts between different slice levels the principle that will be used is similar. The magnification vector between the point $P(x,y)$ and $P'(x',y')$ could be easily calculated from the difference between the two points.

$$x' = x + dx \qquad \text{Eq 4. 1}$$
$$y' = y + dy$$

The parameter dx, dy is the translation vector that might have positive or negative values.

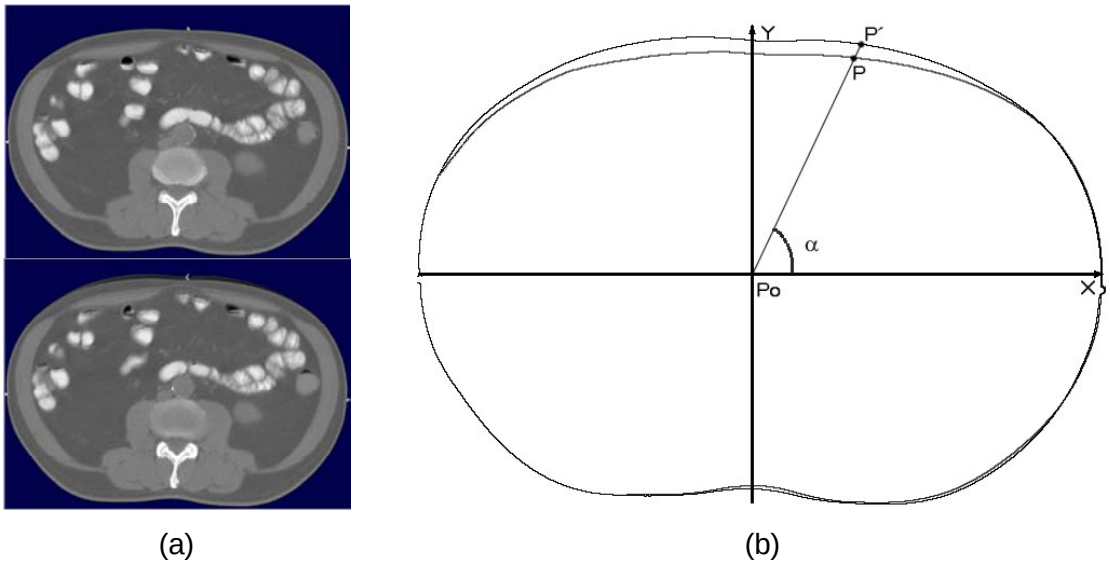

(a) (b)

Figure 4-3. Deformation of an axial body contour during breathing. In (a) two CT cross sections at two different time moments t and $t+1$. In (b) outline body contour comparison.

The point $Po(xo, yo, zi)$ represents the geometric centre of the volume bounding box. The breathing process is separated into inhale and exhale phase. The inhale phase lasts much less than the time of the exhale phase (see Figure 4-1). On can observe that the width of the picks is less than the width of the cavities. In that view the picks represent the frequency of the inhale process and the lower cavities the frequency rate of the exhale process. At this point we have to clarify that the collected digital images do not necessary describe the complete respiration process at every time moment. Some information might be neglected and some will appear as blurring artifacts due to low rate data acquisition. Aim of this work is to estimate and recover each contour deformation caused from the respiration process, in relation to the neighbour cross section images. By applying our method the magnification and shrinking vectors of the above model can be calculated automatically on each contour considering the neighbour contour deformation.

4.3.1 Generation of Body Planar Contours

At this point we need a few definitions. With $\boldsymbol{X}$ we will represent the polyhedral surface, $x_{i\alpha}$ a vertex of the surface at i slice level and α angle. In our polygonal surface we could have two types of neighbours of a vertex $x_{i\alpha}$. When the vertex is located at the same slice level and has different angular location then is indicated as $x_{i\alpha 1}$. When the vertex belongs to

the same angular location but in different slice level then is indicated as $x_{j\alpha}$. The edge connecting $x_{i\alpha}$ to $x_{j\alpha}$ is represented as $g_{ij\alpha}$. A discrete surface signal of the polygonal surface at a angular location α is a function of $\boldsymbol{S_\alpha = \{x_{i\alpha}, i=1,2,3,\ldots, L\}}$, where ***L*** the total number of cross sections.

The proposed methods can automatically extract from the original CT data volume the body planar contours. However the generation of the contours require two special conditions:

a) Every detected contour at each slice level must be composed from the same number of points. This parameter corresponds to the number of angular values ***Ai***.

b) Every contour point at slice level ***i*** must be collected with the same angular value from the point ***Po,*** in relation to its neighbour points in slices levels $x_{h\alpha}$, $x_{j\alpha}$, where ***{h=i-1}*** and***, {j=i+1}***.

The main reason for adapting this approach is the 2D inspiration model described in previous section. This model can by applied on the CT axial cross sections. The sampling points that will compose the final contour must be collected at specific angularity in relation to the central axis of the body bounding volume. This is necessary in order to be able for the filtering step to compose one-dimensional array from the sequence of points based on their angle value. These arrays will be the input data for the filtering function. The number of different angles that will be used for detecting the sampling points also defines the number of sampling points that will generate the planar contour. This sampling rate has no specific value but depends upon the user selection and the complexity of the surface that must be reconstructed.

The angular point-tracing algorithm (APTA) is based on a two-dimensional ray casting. The ray casting methods are well established in volume rendering techniques where the volume under investigation is sampled with multiple rays, which are emitted from the final image plane. To realize this concept a starting and an ending point of the ray must be defined. In volume rendering applications the ray points contain 3D information about their location. Depending on the camera model used during reconstruction the rays might follow parallel or perspective paths. In case of camera rotation the ray points are recalculated defining new directions for the ray paths. The most common approach used is a 3D digital differentiator analyser (DDA). The numbers of sampling steps that will be used for each sampling ray depend upon the resolution of the sampling rate and the accuracy of the final image.

To label the sampling voxel as the one belonging to the skin boundary region one could use a simple Hounsfield unit (HU) threshold value. However when sampling or processing images based on thresholds, the processing results become sensitive when dealing with noisy data as well as in case of not distinct organ boundaries. The most common problem appeared in our experiments were noise with high values appeared at the lower sides of the image, usually where the CT table is located. Therefore the precalculation of an opacity volume considered being necessary for optimising the collection of the sampling points. The opacity volume was calculated based on gradient operators, an approach established of [Levoy88] and used very often in volume rendering literature. The intersection point between the ray and the body boundary is selected based the opacity value of the voxel under sampling. Often the CT table-top where the patient is placed during scanning is included in the reconstructed slices. Currently it is extracted af-

ter manual definition of that level. In this work a specific approach is used for the generation of the body contours but the method is not restricted only to that principle.

4.3.2 Sampling Rate Selection.

For selecting the appropriate number of sampling points ***Ai*** that will adequately describe the body shape we select as criterion the comparison between the APTA contours and the original body contours as they are segmented using a boundary tracing method. At this point a quick but effective value is required in order to judge whether the calculated contour describes effectively the original body shape at the current cross section image. We consider the overlapping area as an adequate value for that comparison. The overlapping area is calculated for every contour belonging to a different slice levels. Then the mean value of the difference of the overlapping area is calculated. If this difference is above 10% then more angular points must be sampled in order to describe with higher detail the body shape. In our experiments we found that not more than 80 angle positions are required to describe the body shapes of the collected volume samples. For generating the triangulated mesh a very simple triangulation algorithm can be used by connecting the points that belong to different contour levels but on the same angular value. Examples of the conventional polygon reconstruction are given in Figure 4-2.

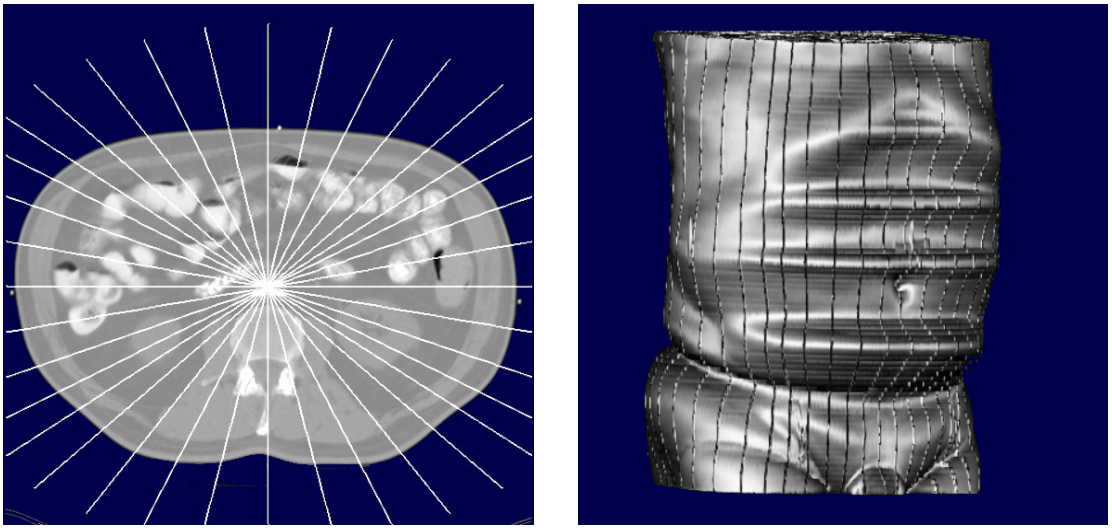

(a) (b)

Figure 4-4. Angular sampling rate selection. In (a) an example of radial sampling on a 2D cross section is shown. The 3D reconstruction of body volume (b) with longitudinal indication of the sampling rays (dark stripes).

4.4 Smoothing filter

As already mentioned the group of points that have been collected with the same angle, compose a group of one-dimensional signals that will be used as input in the surface smoothing algorithm. In the specific application we transact with very low frequencies and not with noise that represents high frequencies. The filtering process could take place in the frequency domain after decomposition of the signal to its frequency components. However this approach is computationally expensive and complex. Alternatively we con-

sider the low pass filters implemented by convolution. To distinguish between frequency and space domain we will refer with the term ***low-pass filter*** to the frequency domain and ***smoothing filter*** to the spatial domain. As primary smoothing filter for our application we consider the moving average since it can be implemented by convolution and aims to average the fluctuating values appeared in the signal.

The proposed surface smoothing approach aims to average the differences that exist on the longitudinal direction the breathing artifacts in order to minimize the skin (surface) distance calculations. The moving averaging (MA) filter is the first approach one could think to perform this task. The MA is the most common filter used in digital signal processing probably due to the simplicity in implementation and speed in performance. Although the MA filter is optimal on reducing random noise causes partial distortion on the original signal edges. The MA filter operates by averaging a number of points from the input signal to produce each point in the output signal. In equation form it can be written:

$$y[i] = \frac{1}{N} \sum_{j=-\frac{(N-1)}{2}}^{\frac{(N-1)}{2}} x[i+j] \qquad \text{Eq 4. 2}$$

Where $x[i]$ is the original signal, $y[i]$ the filtered signal and N the order of the neighbour samples or convolution kernel size.

In order to analyse the frequency response and performance let us consider a rectangular pulse of specific size as shown in Figure 4-5(a). The smoothing result of the MA can be amplified or reduced by controlling either the size N order of the neighbour samples or by maintaining a constant values N and performing multiple-passing of the MA. Figure (x)c illustrates the frequency response of the MA filter with different kernel size. On can observe that the MA filter has very poor frequency response. Small size of the kernel provides slow roll-off and poor stop-band attenuation. Even if the size of the kernel increases then it is still not possible to distinguish and isolate the high frequencies (see Figure 4-5(a) & (b)). By applying the filter with multiple passes we obtain an improved frequency response in comparison to the increased the kernel size. After 2 passes with the original MA kernel, the input rectangular pulse response has been converted into a triangular filter kernel. By continuing this process the shape of the kernel converts to a bell shape quiet similar to the Gaussian smoothing kernel, with attenuated amplitude. Actually this is the behaviour we request from a smoothing filter for our application since we have to suppress very low frequencies. The frequency response of the multiple pass MA filter is illustrated in Figure 4-5(c) & (d). The frequency response of the 4-pass MA filter can isolate the and completely cut off high frequencies. As one could expect the frequency response of the 4-pass MA is very similar to the frequency response of the Guassian smooth kernel. As Oliensis ***et al.*** [Olien93] pointed out et al the Gaussian kernel produces shrinkage because it is not a low-pass filter. Basically except the zero frequency all the frequencies are attenuated.

Filtering examples of the MA filter with multiple passes are illustrated in Figure 4-6. Two curves with different frequencies have been selected. A signal describing low breathing frequency is shown in Figure 4-6(e). High respiration frequency is shown in Figure 4-6(f). The last curve actually corresponds to the normal breathing conditions. The MA filter was applied to both curves iteratively for seven times. The dotted curves represent the

averaged result of the original curves. The higher picks of both curves have been flattened elevating at the same time their lower region.

$$\mu(i) = \frac{\sum_{i=1}^{N} x(i)}{N} \qquad \text{Eq 4. 3}$$

$$SD(i) = \sqrt{\frac{\sum_{i=1}^{N} \left(x(i) - \mu(i)\right)}{N}} \qquad \text{Eq 4. 4}$$

$$SDE(i) = \frac{SD(i)}{\sqrt{N}} \qquad \text{Eq 4. 5}$$

4.5 Surface Smoothing

4.5.1 Surface Signal Constrains

The proposed approach is applied to the complete data volume. The developing of an algorithm that automatically could detect the regions that include breathing artifacts is a difficult issue. The main limitation for such an approach is the body curves, which might have very similar frequency to the noisy curves. Therefore the algorithm should be applied on specific regions of the collected CT data. Basically there is two types of constrain that must be defined: the angular and the longitudinal constrains. The angular refer to the numbers contour points, which represent angles between the body surface and the body central axis of the body volume and the external surface position. These constrains could be applied as constant values since the breathing deformation effects specific regions of the patient's sides.

The second type of constrains, the longitudinal, are the most significant for producing accurate results and must be placed manually. The user can select the appropriate slice level in both directions cranial and caudal. In order to maintain continuity at the region of constrains among the original and filtered data the smoothing process is applied to the complete patient volume and the filtered results are merged with the original data at the constrain boundaries using linear interpolation. This concept is illustrated in Figure 4-6. The marks on both images illustrate constrains in the longitudinal direction. The smoothed curve Figure 4-6(a) has a rapid reduction value at the constrain points. This is eliminated after applying the linear interpolation between original and filtered values as shown in Figure 4-6(b).

4.5.2 Control of Filter Iterations

Most mesh fairing schemes require the manual adjustment of the filter iterations. In other words the user will decide for the level of smoothing that will be applied on the specific mesh. In some case this level can be predicted, e.g. when dealing only with noisy data. The semi-automatic control of the filter iteration process is a great mechanism

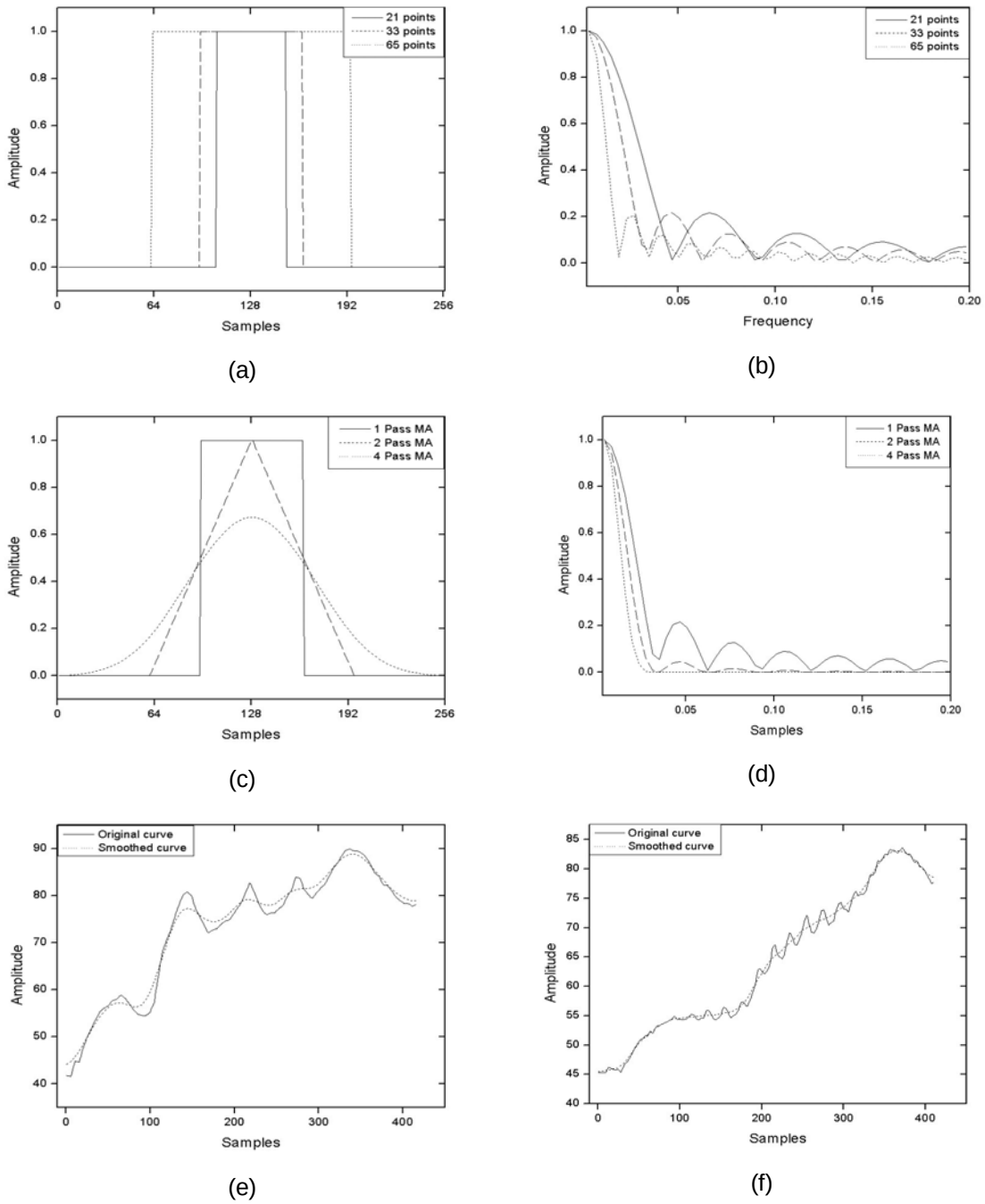

Figure 4-5. The moving average filter and filtering examples. In (a) and (b) MA kernel examples and their frequency response, using different kernel sizes. In (c) and (d) MA kernel examples and their frequency response using iterative filtering. In (e) and (d) filtering results on different respiration frequencies.

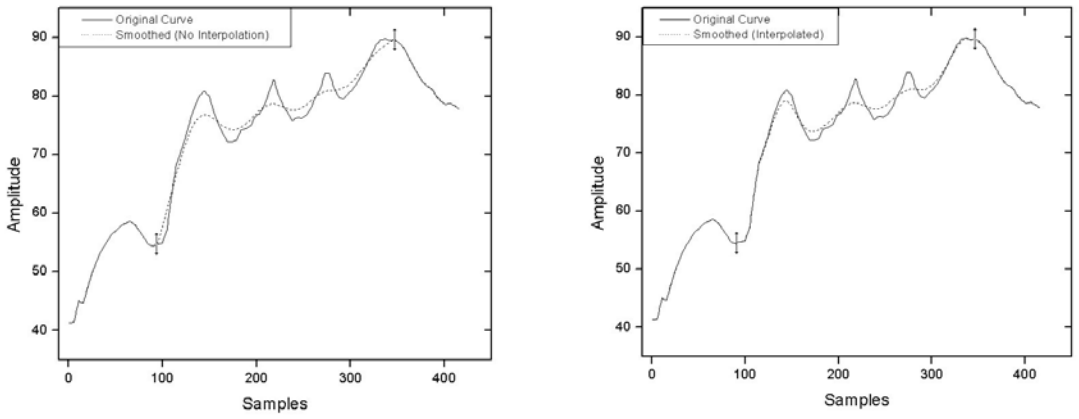

(a) (b)

Figure 4-6. Comparison between interpolated and non-interpolated smoothed curves. In (a) the filtered curve using the MA filter and after applying two constrains. In (b) the same filtering results but after applying linear interpolation at the constrain levels.

for a mesh-fairing scheme since minimum intervention is required from the user.

In order to automatically control the number of iterations of the smoothing filter the *SDE* is used as comparison criterion. After the first iteration the summation of the percentage of the error difference between the original and the smoothed surface is calculated. The calculation takes place on each angular curve that is involved in the smoothing process. The individual *SDE* are added to generate the final value. The equation form of the above description is as follows:

$$\Delta_{SDE}(i)\% = 100 \cdot \frac{SDE_o(i) - SDE_f(i)}{SDE_o(i)} \qquad \text{Eq 4. 6}$$

$$T_{SDE} = \sum_{i=\omega 1}^{\omega 2} \Delta_{SDE}(i) \qquad \text{Eq 4. 7}$$

Where SDE_o, SDE_f, are the standard errors of the mean for the original and smoothed curve respectively at the angular value ***i***. The value $SD_o(i)$ is the standard deviation of the original curve at angular value ***i***. ***N*** is the total number of samples in the longitudinal direction (also corresponds to the number of slices). The value Δ_{SED} stands for the percentage of the difference between original and smoothed *SDE* values and T_{SED} for the total summation of the Δ_{SED} values.

The first value of the Δ_{SED} can be considered as an indicator of the quantity of the filtering effect on the original surface. If Δ_{SED} has large value then the difference between the original and filtered surface is high and vice versa. The iteration loop will stop when the value of the T_{SED} reached four or five times the value of the first calculated Δ_{SED}. This approach work very efficiently as automatic prediction of the number of iterations for low and high frequency breathing artifacts.

4.6 Results

The purpose of the performed measurements was to assess the contribution of the proposed surface smoothing method on the correction of the shape of the original body contours. The proposed method was evaluated using 15 CT datasets from arbitrary selected subjects that were scanned in the abdominal and pelvic region. All subjects were scanned at free inspiration conditions using spiral CT (Siemens Somatom Plus 4). The average number of slices collected from each scan was 85 per patient, 3 or 5mm thin with equal slice distance respectively. For every volumetric data the original body contour was extracted using the ***APTA*** described in section. Surface signal constrains have been applied manually on different slice levels every subject surface. These constrain aim on protecting the main features and curvatures of the original body surface from deformation after surface smoothing.

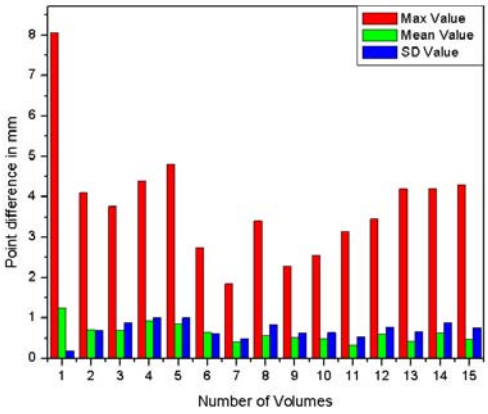

(a)

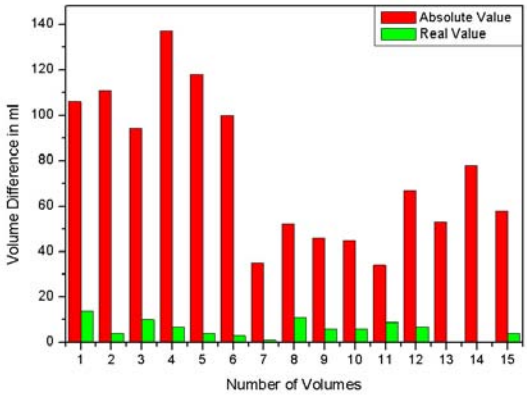

(b)

Figure 4-7. Results of quantitative comparison between original and reformatted torso-contours. Results in (a) show differences single contour points. Results in (b) show differences between original and smoothed volumes.

For each contour point we estimate the Euclidean distance between the original and the reformatted contours. The border positioning accuracy, was assessed by computing the ***Mean*** value, the ***SD*** value and the ***Maximum distance*** (***Max***). This method gave us the maximum difference between vertices of the original and the smoothed surface. The second criterion used was the total volume of the original and the filtered surface objects. A very common method for estimating the volume of closed mesh surface is described by Lien. However for open surfaces generated from contours one can calculate the surface of each contour, multiplying the final result with the corresponding slice thickness. The total interior surface volume will be given after adding the volume of each slice. The preserved interior surface volume of the smoothed surface can indicate that the filtering process did not cause severe shrinkage to the polygonal surface. This concept is very important is a very important property required in our application. However the interior surface volume does not provide any information level of smoothing on the original surface. For assessing the absolute variation of volume between original and reformatted mesh the partial volume variations was used. This parameter was calculated on each slice level as the absolute difference between original and smoothed contour volume. The total value of the absolute volume differences between original and smoothed mesh, was

estimated after addition of the partial volumes. These measurements provide a good factor for understanding the effect of the smoothing process.

The numerical results of the smoothing process are presented in Figure 4-7. The top chart presents the maximum the mean and the SD of the distances between original and reformatted contours of the complete contour set, for every volume sample. Among 15 volumetric CT data, which result to 1450 body contours, the maximum contour difference was 8mm and the minimum 2mm. The maximum mean value was 1.2mm with SD ± 0.2mm. The reason for the low mean values is the small amount of contour points that where repositioned at each contour. The absolute and the actual differences between

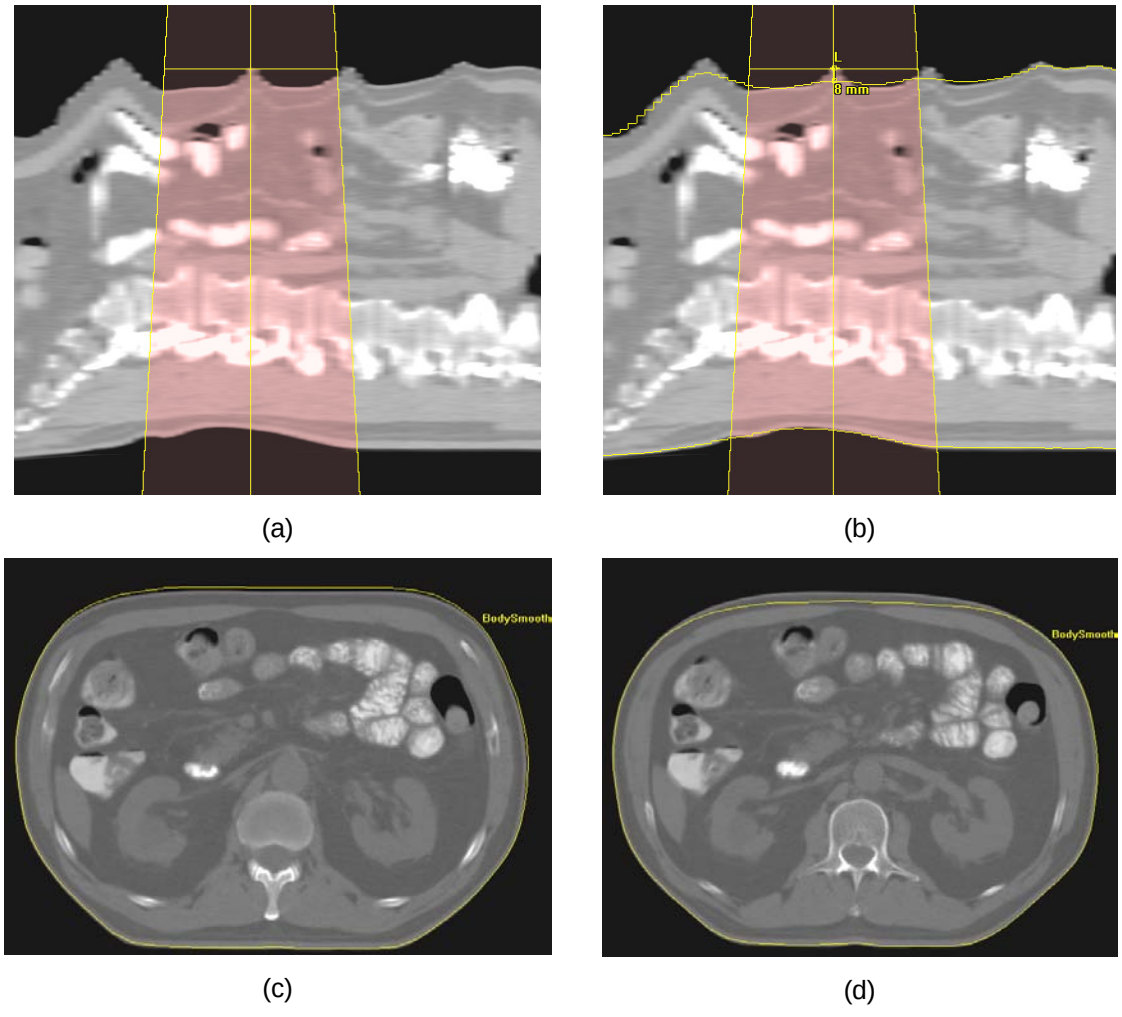

(a) (b)

(c) (d)

Figure 4-8. Comparison of contour smoothing results. Sagittal images (a) and (b) show the difference between original and proposed position of the beam iso-center. In (c) and (d) two different slices are used to indicate the difference between the original axial slice and the proposed contour.

original and smoothed surfaces are illustrated in the lower graph of Figure 4-7(b). The mean value of the original sample volumes was 22101ml. The mean value of the actual volume difference was 8ml, a very small value compared to the average volume of the all sample data. This certifies that the proposed method caused no shrinkage to the mesh volume. The maximum value of the absolute difference in mesh volume was 137ml and

the mean value 75.6ml with SD ±33.08ml. This volume variation represents only the 1% of the original mesh volume. However if one considers these variations locally then the influence in measurements can be valuable. Figure 4-8 illustrates the smoothing result of our method on a 2D image level. The sagittal images in Figure 4-8(a) and Figure 4-8(b) show the differences between original and proposed position of the beam iso-center. In the specific example up to 8mm contour distance has been corrected using our method. In Figure 4-8(c) and Figure 4-8(d) two different slices are used to indicate the correction effect between the original axial slice and the proposed smoothed contours.

The 3D surface smoothing results of the approach are shown in Figure 4-8. For visual

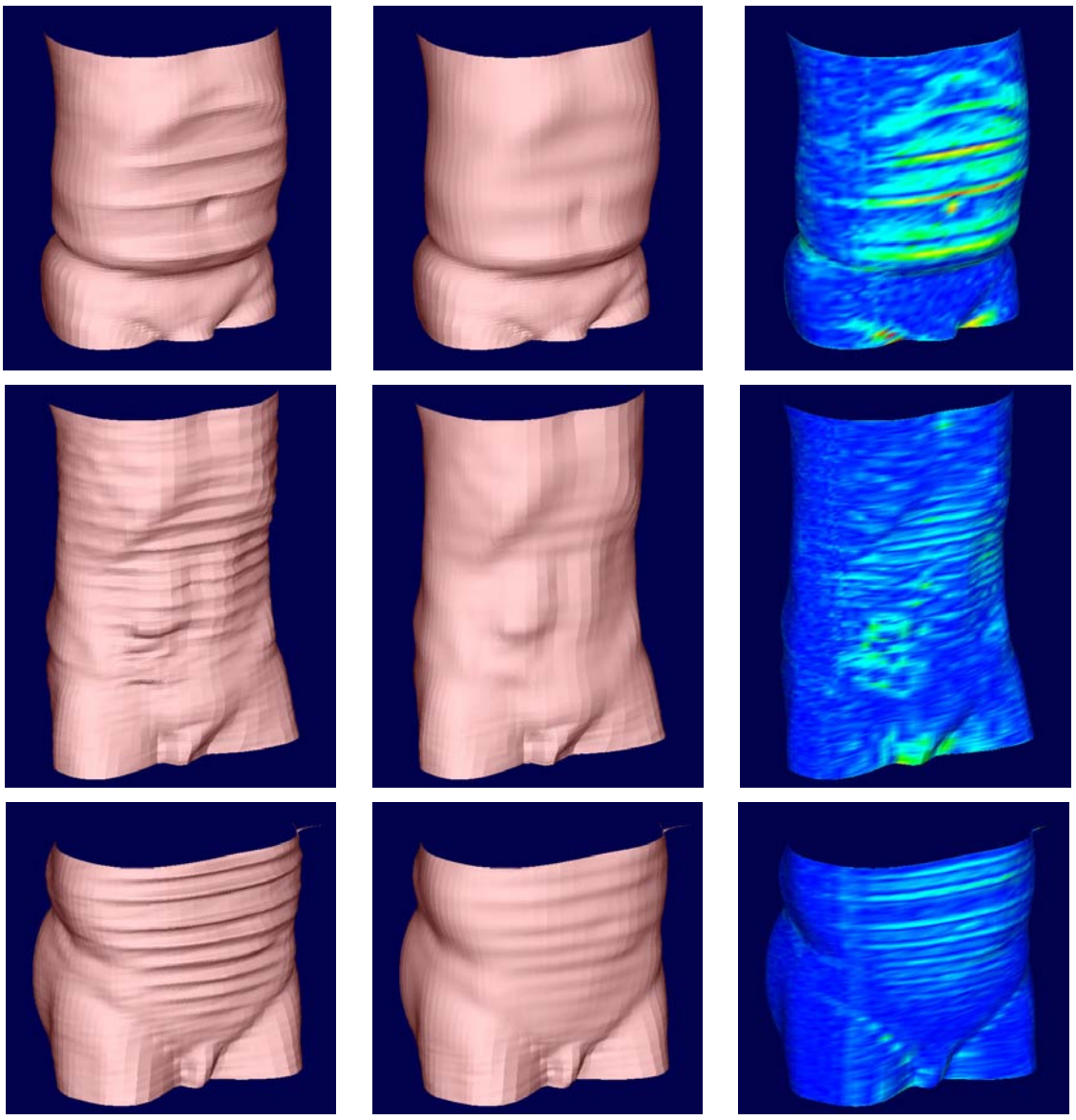

Figure 4-9. Different surfaces smoothing examples. Notice that the respiration artifacts are not developed uniformly but vary between high and low rates. The left column represents the original meshes. The middle the smoothed-reformatted. The right colour-mapped mesh indicates the areas with modified vertices.

comparison of the smoothing effect a colour-map index is given over the smoothed meshes. An optimal factor for the SDE was used to control the number of iterations of the smoothing process. This factor was the same for all sample data. However the number of iterations varied from 6 to 18, upon the frequency of the deformed surface. The estimated average number of iterations was 7. The processing time required for the smoothing of the surfaces depends on the number of vertices that compose the mesh. On the experiments performed in this work the mean value of vertices were 12200. In any sample case the processing time required for smoothing was below 1second on a Pentium III 933 MHz.

4.7 Summary

In this chapter we point out the affects of the respiration artifacts on torso surfaces reconstructed from CT data. The use of inaccurate information might lead to wrong calculations during RT planning and simulation. Considering previous models for correcting motion artifacts in CT imaging we can analyse the respiration process and correct it. Hence, a dedicated automatic approach is presented for the compensation of the respiratory artifacts on medical body surfaces reconstructed from planar contours. The method can handle fast and efficiently several types of body surfaces with respiratory artifacts that might include constant or arbitrary respiration frequencies. The system can detect and generate the body contours and surface automatically, and eliminate the respiration artifacts from the problematic regions. The user can define manually constrains on the angular or on the slice level. So far we cannot estimate how the proposed method will influence the results on the clinical environment. This is one part of our future work. In addition we investigate the development of a deformation model that will also compensate the movements of internal structures that deform during respiration.

Chapter 5

Improved Volume Rendering of Thoracic CT-Volumes

5.1 Introduction

Three-dimensional visualization in treatment planning is used to express information regarding radiation beam registration with the tumour, extend of disease and conformity of dose distribution to the target volume and organs at risk [Chen96]. Failure of radiation therapy to control the local or regional component of the malignancy can be due to misleading visual information in one of the above steps. The difficulty of delineating target volumes has been extensively discussed in the literature. However the increasing emphasis on 3D conformal therapy, with the more complex fields, increases the importance of accurate anatomic delineation and 3D representation. As mentioned in previous chapters, CT has been key to the development of the 3D treatment planning, providing the necessary anatomic information. Nowadays spiral CT provides high-resolution data, increasing the number of slices in a study, preventing the generation of motions artifacts and enhancing the boundaries of anatomical structures. As topographic information increases, various methods of display may be used to re-express this data into meaningful images, as demonstrated in Chapter 2.

In Chapter 3, volume segmentation methods have been briefly discussed, in order to extract volumes of interest from a series of tomographic images. In RTP these volume are necessary for display as well as quantitative purposes, such as dosimetry and volumetry. The communication of the geometric information of these structures among different planning software can be done only means of 3D coordinates of the object primitives. Traditional 3D visualization in radiotherapy planning, mostly in treatment planning systems, has been wire-loop and polygon based, typically requiring manual segmentation on consecutive CT or MR slices [Peliz98]. Despite the availability of several automatic segmentation tools, a significant portion of this task is manually performed, and can be time intensive for the user. In addition manual segmentation is binary process since the user must identify areas that sharply represent structure boundaries. The result of this process can be a polygon or voxel representation of the structure of interest. While these models provide useful information regarding the general anatomic and geometric relationships of the structures, permitting interactive BEV and OEV display, fine details of anatomy are typically lost. Polygonal models and binary voxel models, fail to represent the smooth transition of structure surfaces occurring at interfaces between tissues, and often do not preserve the sense of 3D connectivity. For this reason polygon render images they have not proven entirely satisfactory for displaying complex anatomy.

5.2 Related Work

In many radiation treatment planning instances, a geometric model of a given anatomical structure is not necessary. Common examples are patients that will receive palliative

treatment where no target volume is required. Patients with Hodgkin's disease are mostly treated with two mantel fields, typically from anterior to posterior direction (AP) and posterior to anterior (PA) isocentric beams. The field size and block beam apertures are designed directly on the DRR lack of and target volume and organ at risk. Similarly for patients with breast cancer, during whole breast treatment irradiation, the radiation field arrangement is performed based on the BEV. For the physician it is usually sufficient simply to appreciate the relationship of a target volume to surrounding normal organs. This might involve the visualization of the occlusion of several structures when viewed from a particular perspective. When the volume viewed from the BEV, perspective view, then the user can assess the potentially irradiated structures enclosed in the irradiation field superimposed. The alternative is to use the OEV, orthogonal reconstruction, where the radiation fields reconstructed as opaque or semitransparent polygons are projected with the original CT volume. An additional verification tool can be the use of the virtual light field that presents the intersection of the beam volume with treatment volume.

Pharynx, lungs and trachea belong to the category of the most important organs in the neck and thoracic region. Lung tissue is the one of the dose-limiting structures and it can be exposed in during irradiation of breast tumour, malignant lymphoma and intrathoracic tumours. On the other hand trachea is very often used as organ for orientating the physician during treatment planning of chest and neck tumours. Thus there is a vital importance on visualizing these structures in 3D in relation to neighbour anatomical volumes of the neck and chest region [Kuszy95], [Butke96]. There are several research works, which are capable to segment the lungs and the trachea volume semi-automatically. The most of them are voxel-based and use morphological approaches like region growing [Brown97], [Dehm99], [Hu01], [Shiyi01]. On the other hand an important issue is the visualization of those structures. Seemann et al. [Seema01] presented a hybrid approach for the 3D visualization of the chest for virtual endoscopy. In this work the airway volume have been segmented using the region growing approach. Then the corresponding volume was re-expressed as a triangulated surface. Usually the user must define an initial point and then the volume of the structures are filled, assigning a validity flag to those voxels that are identified as belonging to the structure under segmentation. Even if the segmentation algorithm provides fast and accurate results, a refinement of the final segmentation result is required due to several problems that might occur during segmentation. The use of the above methods can be optimal if the geometric information of the structures are required.

Pelizzari ***et. al***. [Peliz96] described a volume rendering principles applied on the treatment planning using CT data. Principally he presented visualization options for the 3D reconstruction of soft tissues of the male pelvis. The use of a translucent "tunnel" when screening the volume from specific viewing directions, allowed reconstructing the structures of interest with high intensity and the rest of the volume with reduced intensity. Thus the irradiation volume could be interactively emphasised. In a more recent work Lee ***et. al***., [Lee99] visualized with volume rendering the region lower head and neck. They used an opacity volume extracted from CT data, which have been acquired after injection of contrast medium, where the user could define the opacity of various tissues, prior to rendering. The result of this work demonstrated that organs like the lymph nodes the, salivary glands, vessels, and airway are visualized in detail without prior manual segmentation. Despite their positive general conclusion, their method could not eliminate partial volume effects (PVE) on the neck region that could obstruct the viewer from useful information.

In this chapter, we will partly explore the application of volume rendering in 3D virtual simulation of external beam and propose new volumetric visualization schemes for the anatomical regions of neck and thorax. Our focus will be the interactive visualization of

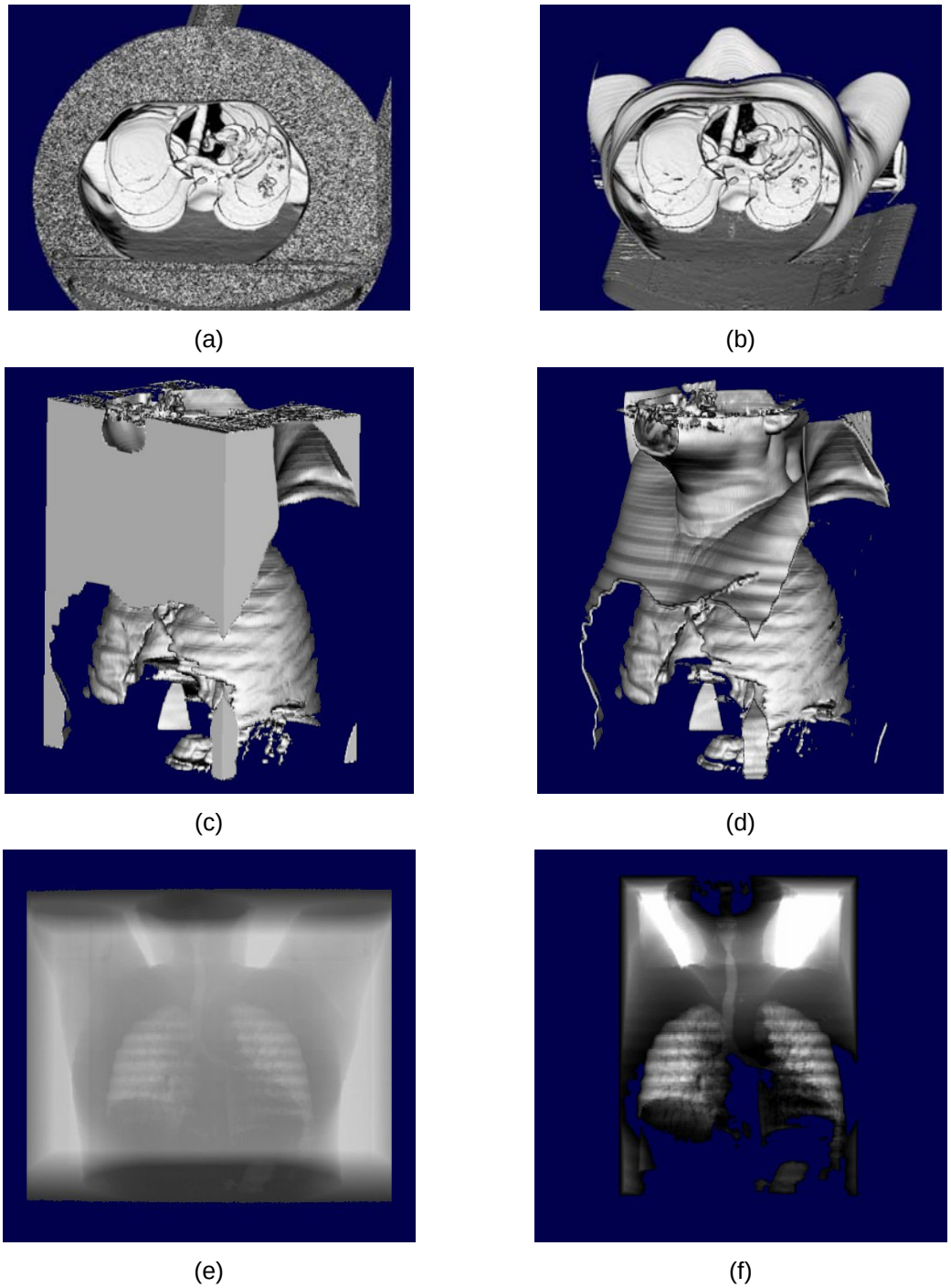

Figure 5-1. Reconstruction of the CT volume using direct volume rendering. Surface reconstruction is produced using iso-value (a), gradient opacity (b) volumes. In (c) and (d) the same information after applying a volume clipping box. DRR images are shown in (e) and (f).

the soft tissue of the chest region, in CT data that are acquired with conventional methods without prior manual segmentation. We believe that we give a very simple but effective solution to the PVE that occur on the skin surface, which is one of the problems the authors had to deal with in previous research work. The clear visualization of the trachea and lung volume from arbitrary viewing directions is not possible due to the skin surface of the neck and chest, which partially obstructs the view of these structures. The main idea is to use a region-growing algorithm at the data pre-processing step, in order to extract the background volume and skin surface and store it in a binary volume. Our aim is not to eliminate the semi-automatic or automatic segmentation procedures. In contrast we propose a visualization concept that will be of clinical use for several treatment cases, when volume segmentation is not required improving the rendering contrast of the soft tissue structures. For practical use these algorithms should perform the above operations in real time with minimum user interaction.

The volume shading methods used to display the results, involve those who are opacity based, metallic surface shading and transparent model reconstruction, mainly means of DRR on the BEV, with manipulated tissue absorption of the X-ray model. In addition the volume rendering algorithm used in this work is a hybrid ray casting capable of handling both polygon and volume data. In this instance the use of the Z-buffer principle allows us to reconstruct the radiation beam geometry in 3D as semi-transparent polygon object together with the volume data, as well as the projection of the virtual light field on the surface of the visualized structures at that level where both volumes, radiation beam and structures, intersect. The proposed approach gives a very clear illustration of structure surface and the their geometric interaction with the radiation field(s) in real time.

5.3 Conventional Volume Rendering

In Chapter 2 we first introduced the importance of volume rendering in RTP and virtual simulation. Volume rendering techniques is a family of methods for visualizing sampled scalar or vector fields of three spatial dimensions without fitting geometric primitives to the data. Volume rendering was introduced from several researchers in the context of medical imaging. The main volume visualization algorithm used in this application has been described in Chapter 2. Briefly our method involves ray casting through the data, and performing shading calculation along rays. The definition of the opacity map function attributes like colour and transparency are assign to the tissues types. This allows the user to selectively enhance or suppress structures of various intensities. As result such reconstruction methods can eliminate the explicit manual contouring step of structures in cases that is allowed.

If one attempts to reconstruct the lung and trachea volume using the standard gradient and iso-value opacity calculation functions as described from Levoy [Levoy88], then the result will be very similar to the one illustrated in Figure 5-1. Image Figure 5-1(a) illustrates the volume rendered from the iso-value opacity volume. The image is covered from noisy values, which represent the room air, and are the dominant voxels of the opacity volume containing very small HU. On Figure 5-1(b) the same CT volume is reconstructed from the opacity volume, which has been calculated using the gradient model. The result in this case is much better since background voxels can be omitted and the skin surface is clearly visible. However in both image illustration of the lungs and the trachea is possible only and from specific viewing directions. A partial solution to the above problem could provide an orthogonal volume clipping function that could remove part of the original vol-

ume in the three main directions Figure 5-1(c) and (d). In this case the clipping planes are adjusted manually and they move parallel to the main axis of the volume data. In radiotherapy this is a quiet useful functionality since the table support of the CT can be removed in order to observer the treatment field interaction with the posterior of the patient. Thus more interesting results can be produced when reconstructing the volume form a posterior point of view. Since the CT acquisition has been made using a flat tabletop the back of the patient has parallel alignment to the coronal volume-clipping plane. Limited information can be obtained also when using transparent illumination such as DRR. In this case the transfer function used has been modified such as the lungs and trachea are reconstructed as opaque organs having high absorption coefficients and the rest of the tissues as non-opaque objects. However in the reconstructed results the room air volume obstructs the clear view of the trachea and the lungs.

The use of the clipping planes is a significant improvement to the visualization results, but still not the optimum. Let us try to identify the reasons that lead to the above result. Figure 5-2 illustrates a single axial CT slice at the level of the thoracic region. The top left image is the original CT slice. The rest of the images illustrate the result after applying different contrast enhancement methods on the original image. The top right is the result of a triangular LUT for adjusting the image contrast. The lungs and the boundary of the trachea wall are clearly visible. Similarly the lower right image produces clear results of the wanted structures, improving the visualization of boundary structures. In both image result mentioned above, except the wanted structures, the skin boundaries are also visible. The

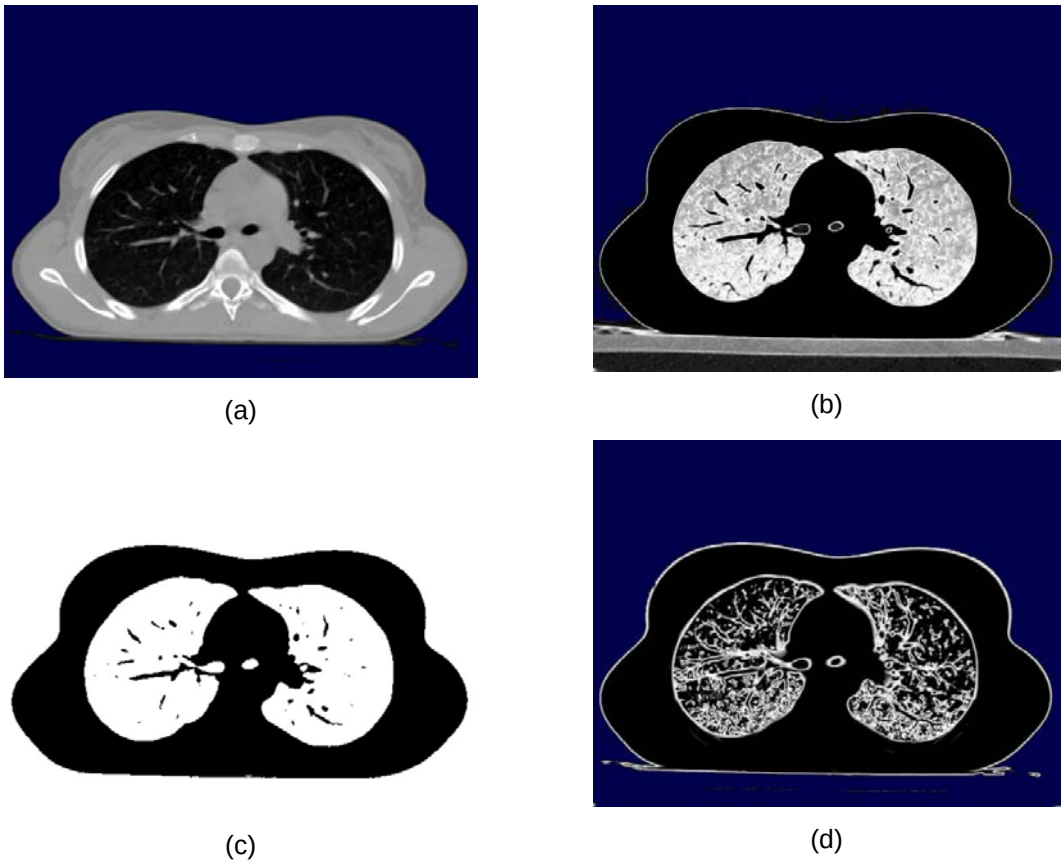

(a) (b)

(c) (d)

Figure 5-2. Examples of CT image windowing and edge enhancement.

lower left image illustrates the result using the iso-value (rectangular) LUT. In this case the wanted structures are illustrated as opaque objects but as well as the image background. These image examples illustrate very clearly that the HU values of lung and trachea borders are similar to the skin borders.

This problem is due to the partial volume effect (PVE), which is a well-known in medical imaging. When the object under scanning varies rapidly over distances comparable to the spatial resolution, one expects the voxel value to reflect the average value over the resolution element. In X-ray CT, a non-linear effect and artefacts can result when the object structure or edge detail occupies only part of the X-ray beam measured by a single detector element. Before reconstruction, the X-ray intensity measurements are converted into attenuation measurements by taking the logarithm. If a structure only intercepts part of an X-ray beam path, the measured intensity will be the average of the intensity over the X-ray path, and the resulting attenuation measurement is not the same as the average attenuation over the X-ray path. This effect is demonstrated in Figure 5-3, where a line sample represents the corresponding HU values of the CT image. One can clearly observe the HU variations at the boundary level of the skin, lungs and trachea. This 2D example demonstrates that it is very difficult to isolate on 2D or 3D level the lungs and the airway using thresholding techniques based on LUT.

So far there have been several methods proposed for the compression of the PVE artifacts that obstruct internal organs when 3D reconstruction methods are applied. A tissue classification method has been employed in combination with a multi-dimensional opacity function [Sato00]. The response of those filters and the original intensity values are used to define a multidimensional feature space in which multi-channel tissue classification strategies are designed. The applied method improved the overall quality of the 3D rendition. Beier ***et al.*** [Beier98] reported a method based on morphological filters in order to reduce the PVE for the reconstruction of diagnostic lung and brain volumes. The applied method, which was a combination of 3D dilation and erosion procedures, was capable to reduce the PVE on the surface of the above structures. Statistical models of PVE that assumed a Gaussian system for noise and fundamental material variances with Gaussian statistics have been proposed from Santago and Gage [SanGa95]. One of the most recent reports by Siadat [Siada01] combination of the intensity and structure information is used in identifying and overcome PVE. Their method utilizes a fundamental concept known as scale. The ***scale*** indicates the local structure size, which is determined at every voxel in a given image based only on intensity homogeneity criterion. The basic premise is that regions of small scale represent regions of potential PVE. Their method has been user to remove superficial (skin layer) artifacts in CT data.

In our concept we have to extract the background image volume and not only eliminate the PVE from the skin. Therefore we employ the following idea: Imagine that the background region of the CT volume (room air), is extracted together with the thin layer of the skin surface generated from the PVE that obstructs the viewing of the internal structures. This could be a binary volume with value one (1) when the region of interest is selected, room air and skin surface, and zero (0) for any other structure. For detecting this auxiliary volume we propose the use of a 3D region-growing algorithm. In order to reach the optimum result we propose the following processing steps:

a. Loading of CT data and store it into the main memory. Calculate the gradient volume using predefined parameters.

b. Select a default location for the seed voxel in order to initiate the region growing (RG) algorithm. In this step the background-auxiliary volume (BV) will be filled.

c. Apply opacity volume calculation using the BV exclusively.

The following paragraphs explain with detail the function of the above steps and the way to realize-integrate them in main visualization pipeline. Examples of single surface reconstruction using the opacity volume are given including DRR examples of the isolated volumes of the lungs and trachea. Further the optimised results of the full tissue range DRR combined with the surface reconstruction mode are presented demonstrating the advantages of the implemented method.

5.4 Region Growing

The region-growing (RG) algorithm is used very often in the region-based segmentation techniques and has been successfully incorporated into several medical imaging applications for the extraction of organ volumes [Masut96]. In this work we follow a simple design principle since the region boundaries that must be detected have low complexity and high contrast differences with the surrounding tissues. The RG algorithm is initiated with a seed voxel selected manually, which is known to be a part of the voxel of interest, room air or skin surface. If the difference in grey-level is between the voxel under investigation

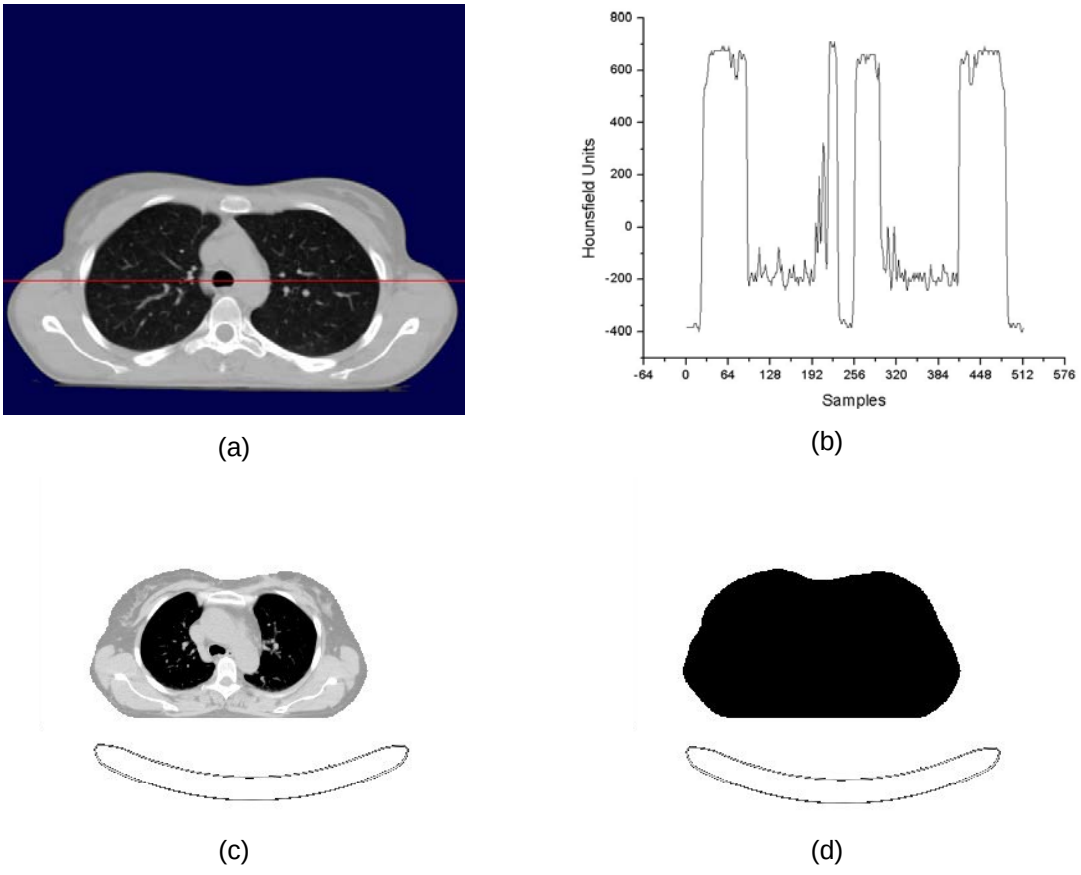

Figure 5-3. Line sampling over an axial CT slice. In (a) the CT slice with the red line indicator. In (b) the sampled valued reconstructed as signal. In (c) filling of the axial CT slice of the chest. In (d) the internal body volume is marked as empty (0).

and its six adjacent voxels is less than a given threshold, pre-classified using a binary LUT, then the current voxel is merged with the growing region. This process is repeated recursively to grow the object until not more voxels can be found.

An example with optimal RG result is presented in Figure 5-3(c) and (d). The seed point used for the RG process has been defined to be the upper left corner of the volume. The background volume and the skin layer have been completely extracted and are illustrated with white colour on the axial CT slices. Regardless of the successful application of the RD algorithm, the RG process might lead to erroneous results. Potential reason for that can be the sensitivity to changes of the acceptance criteria. This means that sub optimal parameter selection will force the region growing algorithm to "overflow" the skin surface boundaries and continue addressing voxels to the auxiliary volume that have similar HU e.g. fat soft tissue. Also discontinue or indistinct tissue boundaries in two or three dimensions are a problem that cannot be handled easily from the region growing method. Usually there is a small "bridge" of voxels that allow the transfer of the seed through them into a region with similar acceptance criteria. The CT data used in this work belong often to patients with disease on the neck region. In this case the error one can observe is the leak of the region growing approach from the room air through the cavity to the respiratory system (e.g. the mouth and the nose) and thus they reach the trachea, which has the same grey values as the room area. When this occurs it is not possible to visualize the shape of the trachea.

Generally speaking, to overcome the above limitations of the RG most researchers combine the method with data filtering and then an edge detection method [Pavlid90], [Masut96]. This edge detection step could provide additional information about the exact location of the region boundaries. Afterwards the region sorting and merging is always profitable. Our main concern is to eliminate bridges of voxels with low grey values, for simplicity we will call the air-voxels. Thus prior to the RG algorithm the edges of the complete grey-value volume are detected calculated and stored in the opacity volume. The edge detection is achieved using the gradient estimator from [Levoy88] since it provides good detection and localization and iso-contour value selectivity. An important feature of this method is that one can adjust the thickness of the boundaries. This allows merging of structure boundaries and closing gaps of air-voxels. This step optimises the object boundaries generating opaque borders. Important for our application is that by manipulation of the gradient estimator voxel "bridges" between structures are eliminated, stopping this way the RG algorithm from leaks. However there might be cases where edge detection is not enough to compensate the leaking error of the RG algorithm for this purpose, manual definition of the region borders must be then defined in means of a bounding box.

5.5 Rendering & RG Results

The reconstruction of 3D images using volume rendering directly from the original data is capable of re-expressing anatomic information with a high degree of realism. This is a great advantage against 3D reconstruction of segmented volumes or surfaces. This advantage is most apparent when visualizing small structures and complicated anatomical sites. The following sessions present the integration of the background volume defined above in the main rendering pipeline.

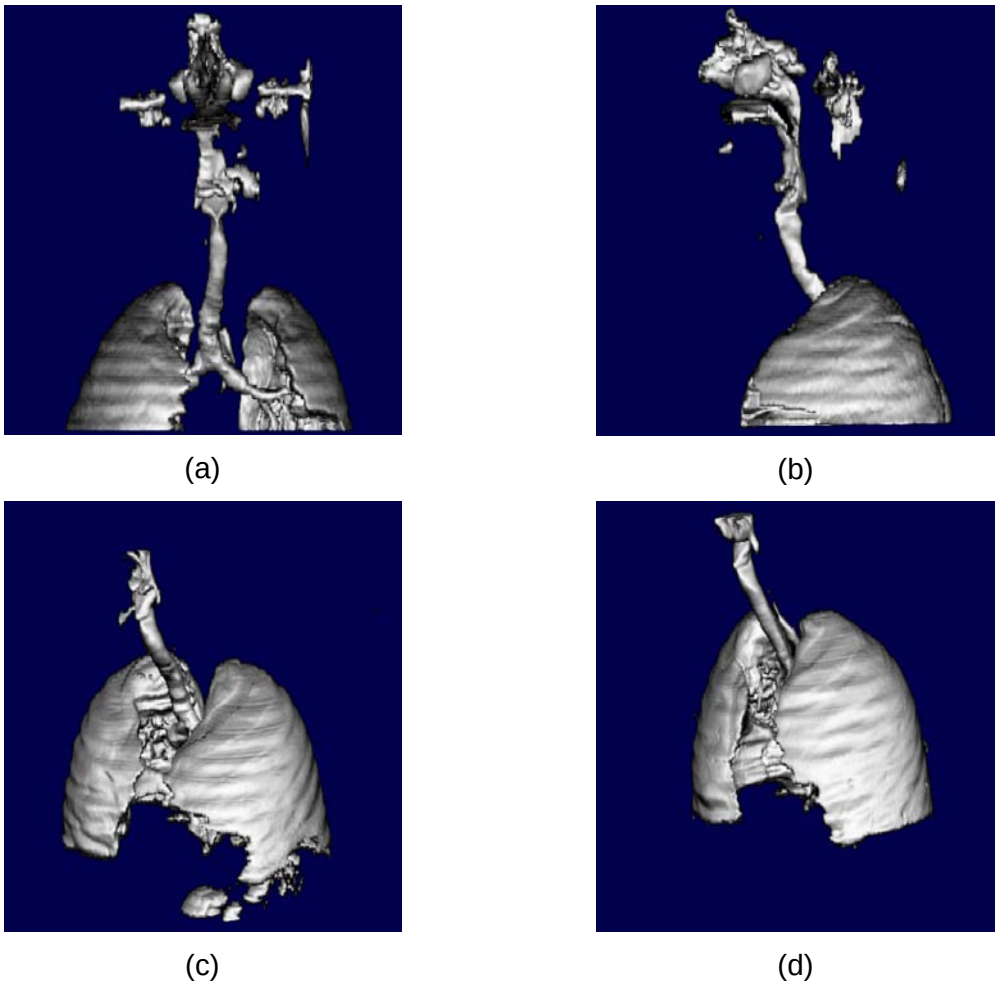

(a) (b)

(c) (d)

Figure 5-4. Surface reconstruction examples of the airway and lungs volumes on different patient cases. Reconstructions are done using opacity volumes.

5.5.1 Direct Surface Reconstruction

The background volume that has been extracted using the region growing approach will serve to the recalculation of the opacity volumes, gradient contour based and the iso-value region based, in order to obtain clear view of the lung and trachea volume. The opacity calculation employed in this work is based on the research paper from Levoy [Levoy88]. For the calculation of the iso-value contour opacity, the opacity classification procedure assigns an opacity value $\mathbf{a_v}$ to each voxel with value $\mathbf{f_v}$ and an opacity value close to $\mathbf{a_v}$ for those voxels that have a voxel value close to $\mathbf{f_v}$. The rest of the voxels will have zero opacity value. For the iso-value region based the opacity value have binary values: opacity value $\mathbf{a_v}$ to each voxel with value $\mathbf{f_v}$. During opacity volume calculation we incorporate now the background volume estimated above. In this case those voxels that belong to the β_v=1 will receive zero opacity values.

For the surface reconstruction of the lungs and airway a well-established surface visualization method has been used. In addition the opacity volume calculation generates thicker edges due to the principle of the algorithm. As shown previously the edge thick-

ness depends on the radius that will be selected for the opacity volume generation. Since the initial body boundaries are in a closer range than original HU volume boundaries during selective recalculation of opacity with the background volume only some parts of the skin surface will be neglected. The rest of them do not coincide for the background volume and therefore will appear on the final image. This problem can be solved after applying multiple dilations to the background volume, forcing the expansion of the volume size towards the skin surface and main body volume. This opacity volume will be further used for the surface reconstruction of the airway and lungs. The important outcome of these images is the clear visualization of the surface of the lungs and the airway path using the standard volume reconstruction pipeline and only after data pre-processing. At this point the lungs and airway volume have been completely isolated and reformed means of the opacity volume. The opacity volume has been used directly to generate the images illustrated in Figure 5-4. The next paragraph will demonstrate additional advantages of the opacity volume that could be due to its use in combination with the DRR reconstruction

5.5.2 Integration to DRR Reconstruction

The DRR images can be generated using direct volume rendering combined with a transfer function that will assign specific predefined values to the voxels under sampling (see section 2.4). One type of transfer functions allows the user to adjust the HU conversion simulating the physical properties of the tissues. More elaborate techniques can be employed to directly model the physical interactions and simulate the X-ray sources of different energies. In Chapter 2 we demonstrated that using user-defined transfer functions e.g. a triangular transfer function, one can amplify specific voxel values, converting the low attenuation tissues into tissue with high attenuation coefficients. The chest is a challenging region for visualization applications and especially the DRR. This anatomical site is more difficult for investigation than others because bone, soft tissues, as well as the lungs and airway must all be visible with sufficient contrast. The lungs and the airway are tissues that are not clearly visible during visualization of the DRR. In contrast, airway is clearly visible on both traditional radiographs and megavoltage portal images representing an important anatomic landmark.

Previous research works presented a number of methods in order to improve the DRR contrast for those lung and airway structures. These methods involve the use of user defined transfer functions, e.g. a triangular LUT, that one can amplify specific voxel values, converting the low attenuation tissues into tissue with high attenuation coefficients. The final DRR image could contain only the specific tissue type ignoring the rest of the structures. As an extension of this approach presented in [Killo01] the full tissue range DRR and the airway DRR could be “blended” as 2D images into a single image. The images can be combined by addition or one image can be subtracted from the other. However the disadvantages of this process are that two images must be generated, one with full tissue range and a second one including only the airway or lungs. Furthermore the final image is influenced from artifacts that are introduced from the amplified room air values. Therefore initially the user must introduce a volume bounding box region that will include only the volume of interest, excluding large parts of the volume data that contain room air.

An obvious standard for comparison of the DRR result is the traditional radiographs. DRRs and conventional radiographs appear different for several reasons. Among them the most important are image quality in terms of spatial resolution and image contrast. The main limiting factors for the spatial resolution of the final image is the image resolu-

tion as well the spatial resolution of the CT data. Most significant errors are introduced by the slice thickness and the only means to reduce this drawback is to increase the longitudinal resolution of the CT data. Conventional radiographs are generated with lower X-ray energy than that used in CT scanners. It is well known that the tissue attenuation coefficients are directly related to the X-ray energy. Thus attenuation coefficients derived from CT data represent a higher ratio of Compton to photoelectric interactions. In contrast the above drawbacks, CT imaging offers a great advantage on the result image contrast against the conventional radiographs. The image contrast on a slice image is given with direct comparison of the attenuation value of neighbouring volume elements and by the line integrals representing a path through the complete volume. Thus, small differences in the density or the composition of tissues can therefore be rendered with sufficient contrast as a matter of principle. This principle is true for all slice-imaging modalities. Nevertheless, recent studies [Dicks03], [Bolle03] have proven that DRRs quality and mainly accuracy of anatomical representation can be comparable to conventional X-ray films and can replace them through different clinical procedures. This is the case under the condition that DRRs are generated from CT volumes with slice thickness of equal or less than 6mm. Bollet et. al used DRRs, that have been generated using 3mm and 6mm slice thickness, and portal images, for the comparison of the patient position variation between CT planning and treatment phase. DRRs generated from 6mm slice thickness, gave less precision of set-up error evalution.

Based on that principle the generation of DDR images offer by far more features than the realistic radiographs. In this work the proposed two different approaches that extent beyond the standard transfer functions that are based to the physics by which a traditional radiograph is produced. Although this approach is contradictory to the physics of the X-ray radiographs the produced DRR images visualize more anatomical information for the lungs and airway and can be more clinically useful. In both methods a combinatory rendering using the original data values and the pre-calculated opacity volume of the mentioned anatomical structures has been realized. The first approach presents a modified version of the rendering pipeline for the X-ray absorption model. The second method involves a hybrid reconstruction of the X-ray absorption model and the surface illumination model based on the opacity volume.

5.5.2.1 Direct DRR Deconstruction

The physical principle of X-ray attenuation is the basis of DRR rendering. The attenuation process of an X-ray beam traversing a distance ***D*** within a medium is an exponential function, as shown in Eq 5.1

$$I(s) = I_0 \exp(-\int_D \mu(x, E_0)\,\mathrm{dx}) \qquad \text{Eq 5.1}$$

Here ***I(s)*** is the intensity after the X-ray has traversed a distance of ***D*** within the medium, I_0 is the intensity of the incident X-ray, μ is the linear attenuation coefficient and E_0 is the energy for a monochromatic X-ray beam at point x. Eq 5.1

simply states that the intensity of an X-ray beam exiting an object is reduced from the incident intensity of the X-ray according to the linear attenuation coefficient of the

traversed material. The linear attenuation coefficient is closely related to the density of the material as well as the energy of the X-ray beam. In addition, Eq 5.1

can be approximated by the discrete summation form of Eq 5.2:

$$I_s = I_0 \exp(-\sum_{i=1}^{N} \mu_i x) \qquad \text{Eq 5.2}$$

I_s is the X-ray intensity when it arrives at the film. The less intensity of an X-ray reaching the film, the brighter the film is. Considering the X-ray film exposure process, a DRR image represents the negative image of the film rather than the same picture. Therefore, the intensity of one pixel in a DRR image is normalised by the transparency ***T***, see Eq 5.3. The final pixel intensity is then corrected by a gamma correction to simulate the X-ray film exposure process.

$$I_p = I_0 * (1 - T) \qquad \text{Eq 5.3}$$

where $T = \exp(-\Gamma(P_0P_1))$ is called transparency and $\Gamma(s) = \sum \mu_i \; x$ is the optical length.

In addition, based on Eq 5.2 the main computation cost in DRR volume rendering is to calculate the optical length, $\Gamma(s)$, i.e. the average attenuation coefficient.

$$\Gamma(s) = \frac{L}{N}\sum_{i=1}^{N}\mu_i = L(\frac{1}{N}\sum_{i=1}^{N}\mu_i(E)) \qquad \text{Eq 5.4}$$

where $x = L/N, L = |P_0P_1|$, ***N*** is the number of sampling points when using the equal distance sampling method.

In this work the HU values are categorized in four different tissue types: air, fat, muscles and bones. To reconstruct DRR images with smooth contrast at the tissue boundaries, the tissue attenuation transfer function is generated after linear interpolation between the attenuation coefficients that belong to different tissue types. For each tissue type a weighting index is introduced in order to manipulate their contribution to the final image contrast. For example high index to the bones and low to the soft tissue will result to an image with improved contrast of the bone structures. This approach provides adequate contrast between bones, soft tissues and air. However the definition of “optimal” contrast or “realistic” DRR is somewhat subjective and might vary between different volume data and different observers. The weighted transfer function provides acceptable contrast for bones and soft tissues. The lungs and airway appear with black colour on the DRR image but since the demand for higher contrast for bone and soft tissues dominates the boundaries of the low attenuation structures are not clearly visible.

Most researchers for simplicity during calculations (and in order to produce better results during DRR generation) use the attenuation formula in Eq 5.1. This formula refers to a monochromatic radiation spectrum. However in reality the X-ray radiation spectrum produced from most medical imaging devices that use an X-ray tube is polychromatic. This principle is very often the reason why the X-ray imaging systems, including the CT scanners, may produce artificial structures that deviate from reality. One type of image artifacts that appear in CT images are those caused by the beam hardening effect. Beam hardening is visible in CT images mostly as dark zones or streaks between bone structures and it is caused by preferential attenuation of lower energy photons in polychromatic

radiation. In addition the beam hardening effect depends on the object type and the projection direction. Principally μ_i is a function of the varying mean energies. Thus a specific mass attenuation coefficient e.g. μ_1 will vary with the projection direction since different structures will influence differently the beam attenuation causing fluctuation to beam hardening effect as well. Currently a number of solutions are proposed to eliminate the beam hardening [Yan00], [Elbak02]. The artifacts caused by the beam hardening effect are intensified when metallic implants are present within the volume of the object under scanning. In such cases the image contents might be completely extinguished in the vicinity of the metallic object, leaving only disturbing noise structures. In standard X-ray radiographic imaging modalities the beam hardening effect is especially noticeable in those procedures where "clear" beam energy spectrums are required (e.g. digital mammography). However this problem is more noticeable in the CT imaging as a matter of principle because the back-projection algorithms used for the image reconstruction consider the projection data as being generated using a monochromatic beam spectrum.

By omitting the virtual model of the beam hardening effect when reconstructing the standard DRR images will result to better image contrast since constant values for the attenuation coefficients are used. In this work we will try to simulate the results of the beam hardening effect in terms of linear influence of the beam spectrum during the ray-sampling step. The aim is to produce a better image contrast between the low attenuation structures (lungs-airway) and the surrounding tissues. In order to generalize Eq. 5.2 we assume that the X-ray beam has polychromatic spectrum:

$$I(d) = I_0 \int_E S(E) \exp(-\int_D \mu(x,E)\,\mathrm{dx})\mathrm{dE} \qquad \text{Eq 5.5}$$

Where ***S(E)*** is the beam spectrum profile and satisfies the following properties:

$$S(E) > 0, \ \text{for} \ \forall E \qquad \int_E S(E)dE = 1 \qquad \text{Eq 5.6}$$

A projection ***p(D)*** along a line integral will result to the following equation:

$$p(D) = -\log\frac{I(d)}{I_0} \approx \int_D \int_E S(E)\mu(x,E)\,\mathrm{dE}\,\mathrm{dx} \qquad \text{Eq 5.7}$$

The approximation errors in Eq. 5.4 result in a nonlinear artifacts known as beam hardening in CT imaging. In our projection model we assume that the beam spectrum is composed of two energies E_0 and E_1 that will effect the linear attenuation coefficient function respectively.

$$p(D) = -\log\frac{I(d)}{I_0} \approx \int_D \left(S(E_0)\mu(x,E_0) + S(E_1)\mu(x,E_1)\right)\mathrm{dx} \qquad \text{Eq 5.8}$$

The discrete approximation of Eq 5.4 is given by:

$$I_d = I_0 \exp\left(-\sum_{i=1}^{N}(S(E_0)\mu^0{}_i x + S(E_1)\mu^1{}_i x)\right) \qquad \text{Eq 5.9}$$

The energy E_0 corresponds to the attenuation function $\mu(x,E_0) = \mu_i^0$ the energy E_1 to the $\mu(x,E_1) = \mu_i^1$. Considering Eq 5.6 the relation between $S(E_0)$ and $S(E_1)$ can be expressed as:

$$S(E_0) + S(E_1) = 1 \Rightarrow S(E_1) = 1 - S(E_0) \qquad \text{Eq 5.10}$$

And Eq 5. 7 can be approximated accordingly:

$$I_d = I_0 \exp\left(-\sum_{i=1}^{N} (S(E_0)\mu^0{}_i x + (1 - S(E_0))\mu^1{}_i x) \right) \qquad \text{Eq 5.11}$$

For simplicity the relation between the two attenuation functions could be defined as linear:

$$\mu^1{}_i = \mathrm{w}\mu^0{}_i, \quad w \in [0, 2] \qquad \text{Eq 5.12}$$

The parameter w is user defined. We will name this parameter here attenuation weight. When the $0<w<1$, then the attenuation function μ_i^1 contains reduced values in relation to μ_i^0. If w ranges are $1<w<2$ then the attenuation function μ_i^1 has larger values than the μ_i^0. In case $w = 1$, then both attenuation function have equal values.

The proposed "beam hardening" model depends on the projection direction and the sampling object. The above approach can be easily integrated in the main rendering pipeline. In section 5.5.1 we demonstrate how we can isolate the lung-airway volume using the opacity volume. The same volume will be used during DRR reconstruction so as to activate the "beam hardening" process. Principally as long as the ray traverses voxels that do not belong to the opacity volume, the attenuation weight will be equal to one ($w = 1$), other the weight will obtain the user defined value. The energy spectrum parameter $S(E_0)$ is used with default value 0.5. The following pseudocode presents this principle:

```
SE0 = 0.5;  SumVal = 0.0;
for  i=0 to N (Number of Steps for current ray)
{
      voxel_pos.x = Step_list[i].x;
      voxel_pos.y = Step_list[i].y;
      voxel_pos.z = Step_list[i].y;
      voxel_μi1 = voxel_μi0  = μI(TEXTURE_VOLUME(voxel_pos))0

      if ( OPACITY_VOLUME(voxel_pos) )
      {
            voxel_μi1 = μI(TEXTURE_VOLUME(voxel_pos))1
            voxel_μi0 = μI(TEXTURE_VOLUME(voxel_pos))0
      }
      voxel_value = SE0* voxel_μi0 + (1.0 - SE0) * voxel_μi1

      SumVal += voxel_value;
}
```

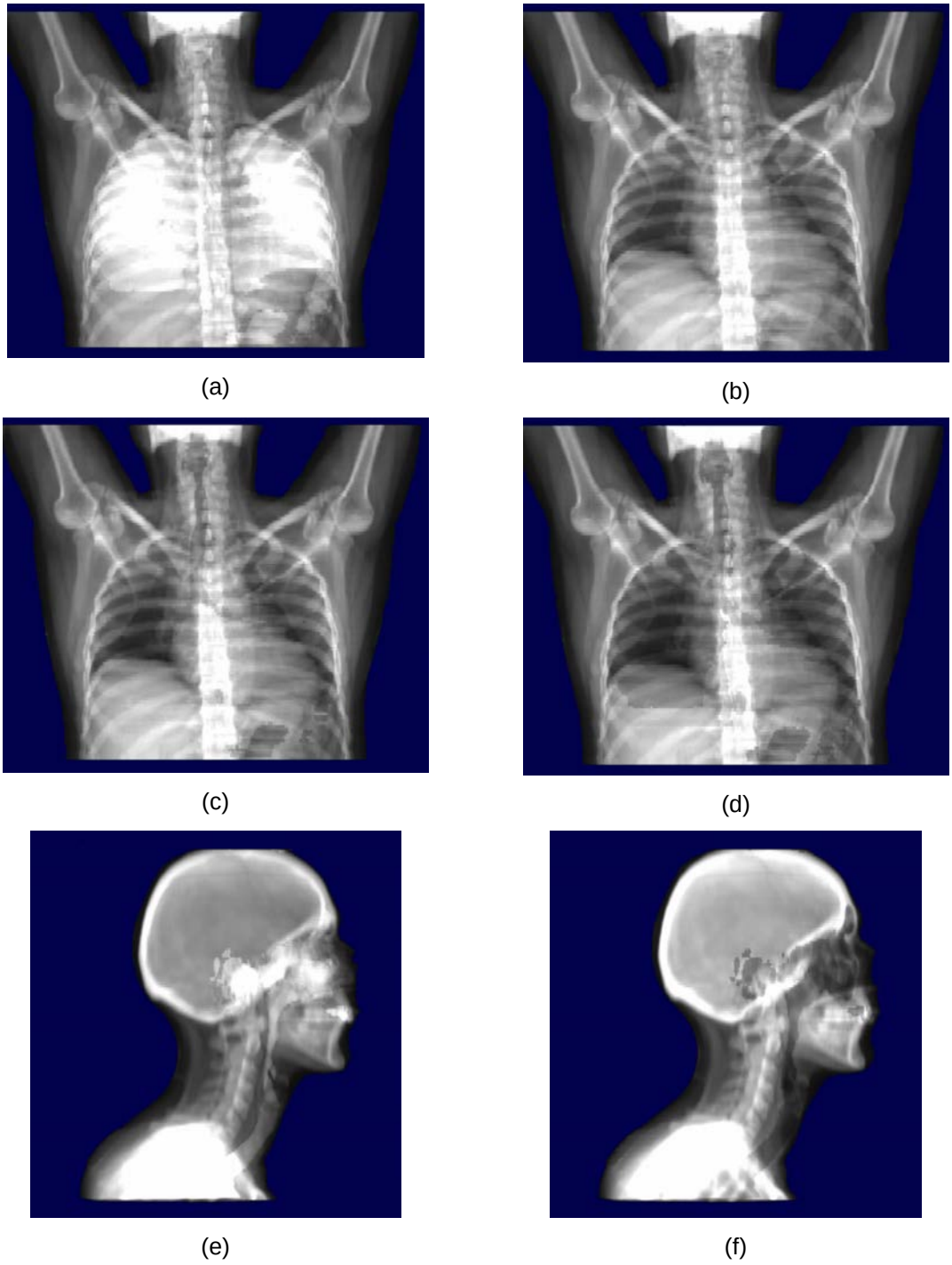

Figure 5-5. Volume reconstruction of CT volumes simulating the beam hardening effect.

The application results of this method are shown in Figure 5-5. Two different CT volumes have been selected: the first from the neck and chest region and the second from the head and neck region. Images (a) and (e) indicate the reconstruction of internal structures with high contrast. This means that the weighting factor in the beam hardening at-

tenuation model takes values greater than one. In the rest of the images Figure 5-5 the internal structures are reconstructed will lower contrast than the surrounding tissues. This indicates weighting values smaller than one.

5.5.2.2 DRR and Direct Surface Rendering Mixing

So far we exploit the possibility of reconstructing the opacity volume of using a single illumination model and by sampling the same volumetric information; the CT values data and their relation to the attenuation coefficients. The results of this approach illustrated the generation of non-physical based DRR images that improve the contrast of tissues with low attenuation. By using an optical model that simulates the X-ray process we generate superimposed images. In such a case that final pixel information is collected under the partial contribution of the specific property of each anatomical structure. Although each structure has a different impact to the sampling process the final result will be always affected from the structure that dominates the ray path quantitatively and qualitatively. In other word structures with small volume and lower contrast will be overlaid from "competitor" structures. In addition depth information will be neglected.

An alternative visualization method could be the reconstruction of both information volumes, CT and opacity volume. In this occasion we have to deal with two different illumination models: the X-ray model and the volume-surface reconstruction model, which is based on standard light shading methods. Data intermixing could be achieved in different levels [CaiSa99]: illumination model level intermixing, accumulation level intermixing and image level intermixing. Considering the two candidates-visualization models one important information is omitted from the DRR model: the depth information. The lack of depth information in the DRR model does not allow the selective distinction between different organ surfaces. As result one cannot apply the volume intermixing steps as this could be done using the surface boundaries of the objects. The following paragraphs describe the approach that has been employed in this work to merge the volumetric information generated using the two different illumination models.

This approach is the simplest and most common used in order to fuse two or more images. The image merging process, similar to the known process of image blending, can be applied on the final images after mixing the pixel intensities of both images. Defining a blending factor $\boldsymbol{w}$, $\boldsymbol{I_T}$ and $\boldsymbol{I_L}$ the corresponding pixel intensities of the DRR image and the surface reconstructed image of the lungs-airway respectively, then the pixel intensity of the result image will be defined as:

$$I_F = Min\left((I_T + \mathrm{w} * I_L), 255.0\right) \qquad \text{Eq 5.13}$$

We consider as focal image the DRR view. Thus we aim to visualize the surface volume within the transparent view of the DRR. The visual effect of Eq. 5.13 is the fade-in and out of the surface volume when the blending factor $\boldsymbol{w}$ is modified interactively. Large w value will intensify the surface image and vice versa. In addition with interactive manipulation of the intensity value in one image e.g. intensity reduction in $\boldsymbol{I_T}$, will result in domination of the intensity values of the final image $\boldsymbol{I_F}$ from the image $\boldsymbol{I_L}$. This effect allows the investigation of structure relationship between the two volumes, DRR and surface, on the projection plane (see Figure 5-6(a) & (b)).

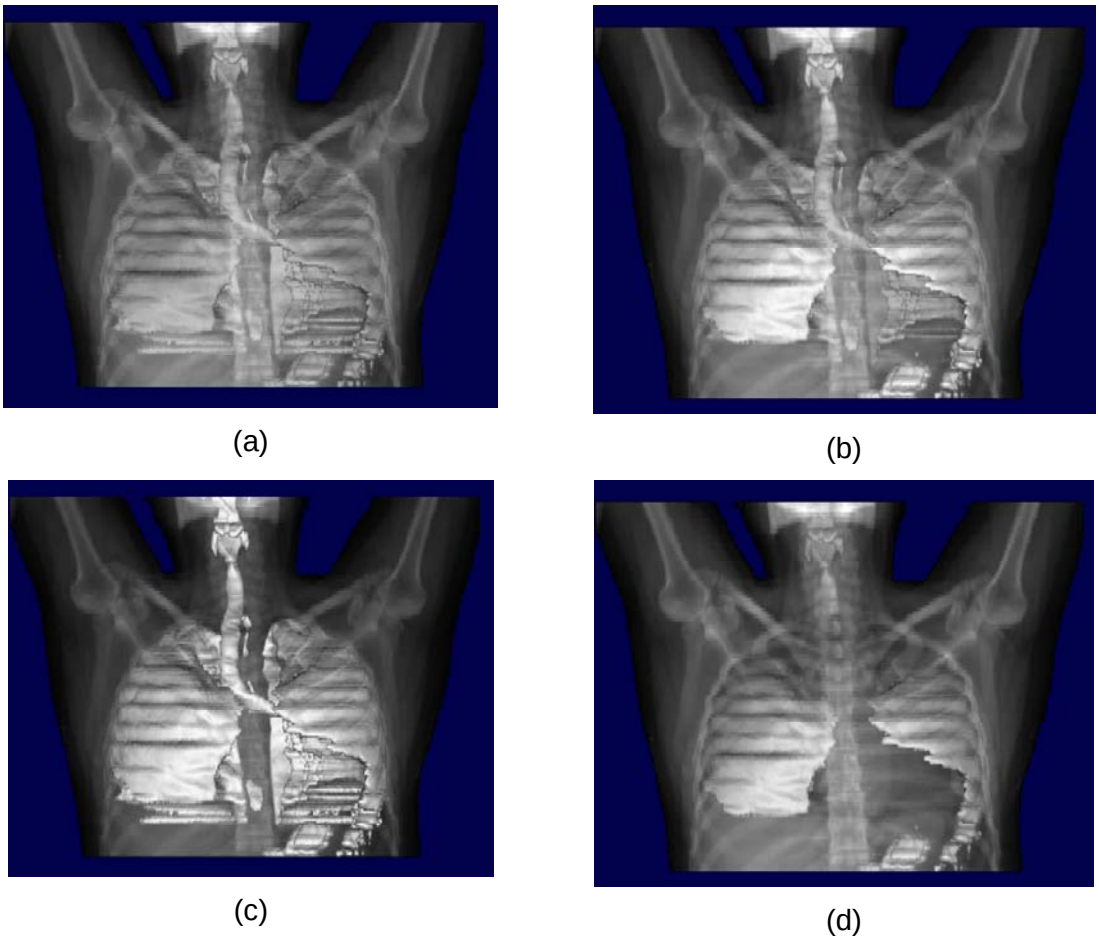

(a) (b)

(c) (d)

Figure 5-6. Reconstruction of chest DRR and internal structure surface. In images (a) and (b) the DRR and surface information are merged on image level using then image intensity values. In (c) and (d) image intensity values of the surface reconstruction are weighted using the depth information.

An extension of this approach could involve the contribution of the depth information of the surface position. The new image intensity could be defined accordingly:

$$I_F = Max\left((I_T + \mathrm{w} * \mathrm{d}_\mathrm{o} * I_L), 255.0\right) \qquad \text{Eq 5.14}$$

Where d_o is the optical depth calculated in relation to the viewing direction:

$$d_o = \sqrt{Max\left(0.0, \left(1.0 - \left(\frac{Z_{Min} - Z_S}{Z_{Min} - Z_{Max}}\right) * w_d\right)\right)} \qquad \text{Eq 5.15}$$

Where Z_{Min}, Z_{Max} the minimum and maximum depth value of the viewing box respectively, Z_S the corresponding depth value of the surface for the current pixel and w_d a weighting factor defined and manipulated from the user. The visual effect of Eq. 5.14 is presented in Figure 5-6 (c) & (d). By increasing the weighting factor w_d the deeper re-

gions of the surface volumes in relation to the viewer direction are getting diffused allowing the viewer to screen regions of the transparent image. The advantage of this method is that one can better appreciate the location of the surface volume in depth in relation to the transparent volume when needed. In this application the lung-airway volume has higher priority than the transparent volume.

5.6 Integration into 3D Simulation

In the frame of this work it is important to incorporate conventional generated volume rendered images with into the treatment planning routine. A crucial step of the plan evaluation during radiotherapy planning is the geometric comparison of the field configuration with the defined GTVs and in relation with the rest of the patient anatomy. Standard visualization techniques in radiotherapy use the BEV projection onto the DRR combined with the treatment beam shape and the GTV projection. Such reconstructions assure the tumor coverage during irradiation. As already mentioned standard DRR techniques can effectively display bony and surface/skin anatomy, but they are ineffective for displaying soft tissue anatomy as demonstrated in previous paragraphs (see section 5.3). In this section we demonstrate the integration of the proposed reconstruction method into the CT simulation visuals as part of the treatment planning process. The proposed method is integrated in both available reconstructed mode of the CT Simulation: in the BEV and in the OEV. In both cases the reconstruction pipeline used is the same as in the previous reconstructed results. However for the BEV reconstruction a perspective projection is used in order to simulate conventional X-ray reconstruction.

Figure 5-7 demonstrates a patient with neck carcinoma. In this case the GTV is defined and the spinal canal volume is segmented and marked as organ at risk. Under normal circumstances the standard DRR reconstruction would provide the visual result as shown in Figure 5-7(a). The pharynx and trachea borders can be hardly seen on the rendered image even after contrast manipulation. The volume the isolated soft tissue and air (STA) volumes are illustrated with blue color in order to enhance rendering contrast. The mixing model between all volumes has been done on the image level. The color intensity between the segmented volumes and the STA volume is done considering the depth location of the surface. This depth weight can be adjusted depending on user demand and the pixel intensity of the images is given using the formula:

$$I_F = \begin{cases} w * I_{VOI} + (1.0 - w) * I_{STA}; \text{if } d_{VOI} \le d_{STA} \\ w * I_{STA} + (1.0 - w) * I_{VOI}; \text{if } d_{VOI} > d_{STA} \end{cases} \quad \text{Eq 5.16}$$

Where w, defines the blending factor I_{VOI} and I_{STA} the corresponding pixel intensities of the reconstructed segmented volumes (VOI) image and the STA volume reconstructed image respectively.

The second example illustrates a female patient with breast carcinoma. In this case the target volume is very near the lung volume and the treatment field is crossing part of the right lungs. Using the proposed reconstructed method the lung volume is clearly visible and their project area on the DRR can be easily isolated in contrast to the conventional reconstruction methods. Further more the exposed lung region to the treatment field can be better observed on the OEV image on the surface reconstruction mode rather than on the 2D slices. This is shown in Figure 5-8 where the virtual light field projection is originally overlaid on the patient's skin. The same technique is applied on the isolated lung

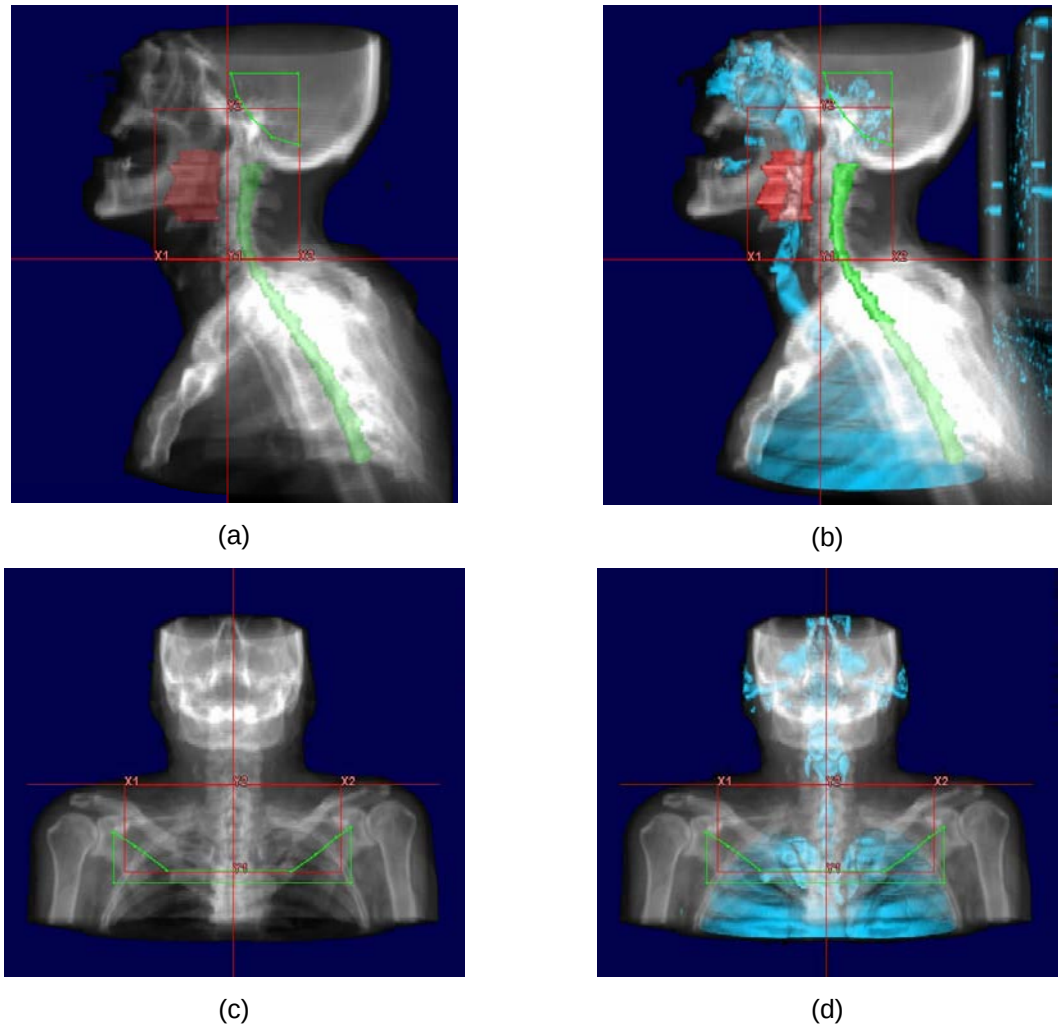

(a) (b)

(c) (d)

Figure 5-7. BEV reconstruction of a patient with neck carcinoma. On the left image the standard volume rendering techniques are used to render the CT volume and the segmented organs. On the right side the low contrast volume of the trachea and lungs is automatically extracted using the RG methods and rendered using the image blending method. On the lower row the BEV is reconstructed from the anterior view lack of volumes of interest.

volume and the result is shown on the second image. In this case the user can see the lung region exposed on the irradiation field.

So far it has been illustrated that air volumes can be interactively isolated lack of any user adjustments. The only requirement has been to setup the preconditions related to the HU range of lungs and trachea volumes. Nevertheless there are treatment cases where the trachea brunches are covered from the lung volumes and they are not visible when using surface reconstruction modes. To isolate the trachea volume we incorporate the depth buffer in combination with the RG algorithm. The depth buffer refers to the surface depth position relative to the viewer and is found at that point where the ray traversing process ends after hitting the surface of a structure. The information stored at the depth will be immediately the corresponding 2D slice level as a reference of the coordinate point. The user can interactively select from the screen the location of the trachea and the corresponding 3D point will be used as the starting point for the RG algorithm.

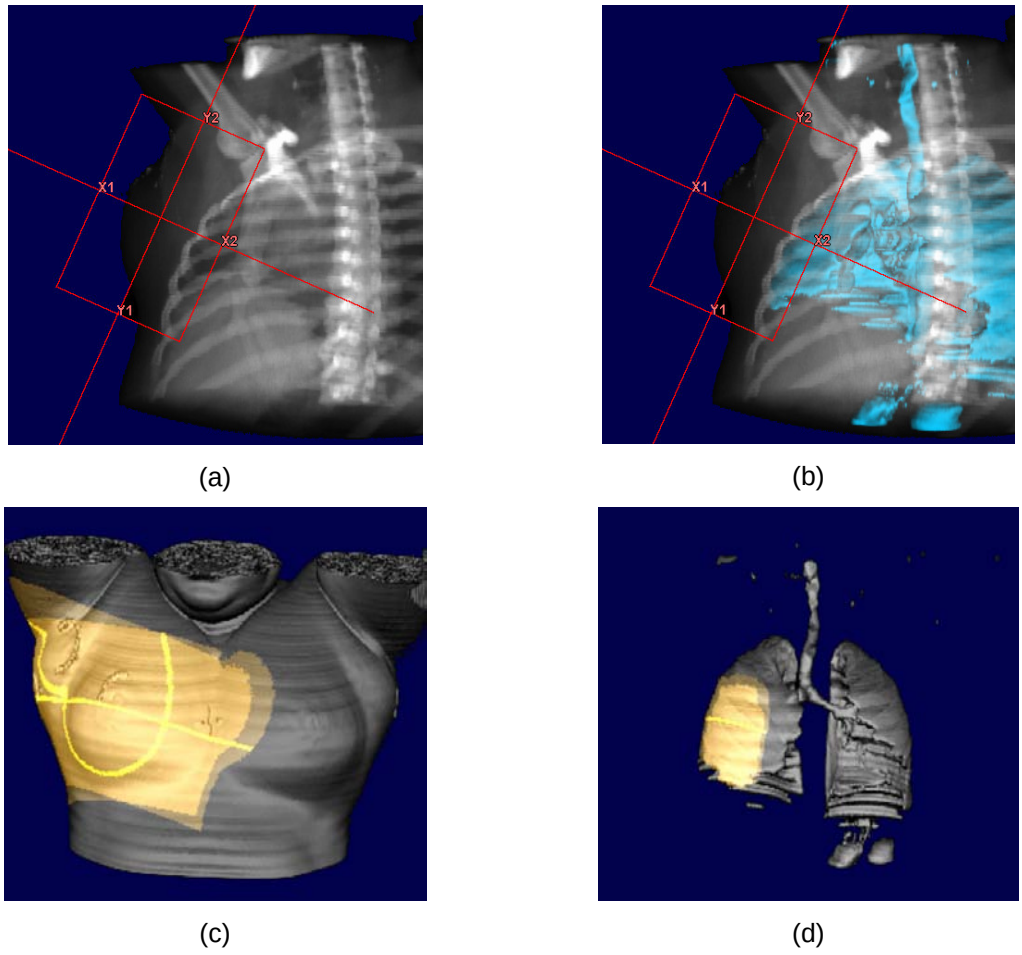

Figure 5-8. OEV reconstruction of a female patient mamma carcinoma. On the top row DRR reconstructions with standard (left) and combined (right) rendering techniques. The lower images indicate the impact of the new method over the virtual light field projection of the treatment beams.

The range of the values used for the volume filling are in the range of –700 to –500 HU and the product of this process will reset every opacity value outside the trachea volume. The results of this process are shown in Figure 5-9 where the organ tissue absorption is manipulated in order to increase contrast of low-density structures during DRR generation. One can notice the weak contrast of the air-way path in Figure 5-9(a). Extraction of the complete air volumes can lead to a mixed image between DRR and surface reconstruction as presented so far, which hints information related to the air way brunching path (see Figure 5-9(b)). A minor modification of our algorithm can trace the air paths until their entrance in the lungs and the contrast achieved is superior to the standard DRR reconstruction techniques Figure 5-9(c).

5.7 Summary

In this chapter we present the utility of volume rendering reconstruction in the frame of the CT based 3D simulator of radiotherapy planning, focusing on the thoracic and neck region. Volumetric surface representation of the critical organs in the above region, such as trachea and lungs, are essential to use as anatomical reference markers and as organs

at risk respectively. In addition we presented how our approach can delineate the airways, especially the trachea bifurcation point, an important landmark for localization and treatment planning. The mentioned anatomical structures must appear with optimum visibility on the reconstructed DRR along the complete 3D simulation process.

The proposed method can be integrated into any rendering pipeline and requires minimized or no user interaction for adjusting the necessary parameters. Taking advantage of the volume rendering techniques that offer high quality visualization, we dramatically reduce user effort required for the segmentation of the previous mentioned anatomical structures. The method can be used to present detailed anatomical structures using the direct volume rending principle that would have been very difficult to reconstruct using standard segmentation techniques.

One of the important components of our approach is the use of a binary volume map in order to address all voxels that belong to the air volume that surrounds the patient's body. This processing step is initialised and completed automatically at the data pre-processing level. Then air volume map is used during ray traversing to reject or accept the sampling voxels. Also, the method can improve the reconstruction of the DRR enhancing the contrast of the subject structures making them applicable for clinical use. By merging both visual information mentioned above we can produce unique images for clinical purpose extending the capabilities of the 3D-Sim process and improving treatment planning outcome. Further more the method could be extended and used for standard diagnostic and volume measurement procedures. Isolating the soft tissue volumes is a process that can be fully automatic without any user intervention. Isolating the trachea volume needs a user starting point selection. The processing time required for soft tissue volume extraction is at the range of half a minute even for volumes with 120 to 150 slices and the 3D reconstruction can be considered as real time on a Pentium III processor of 933 MHz.

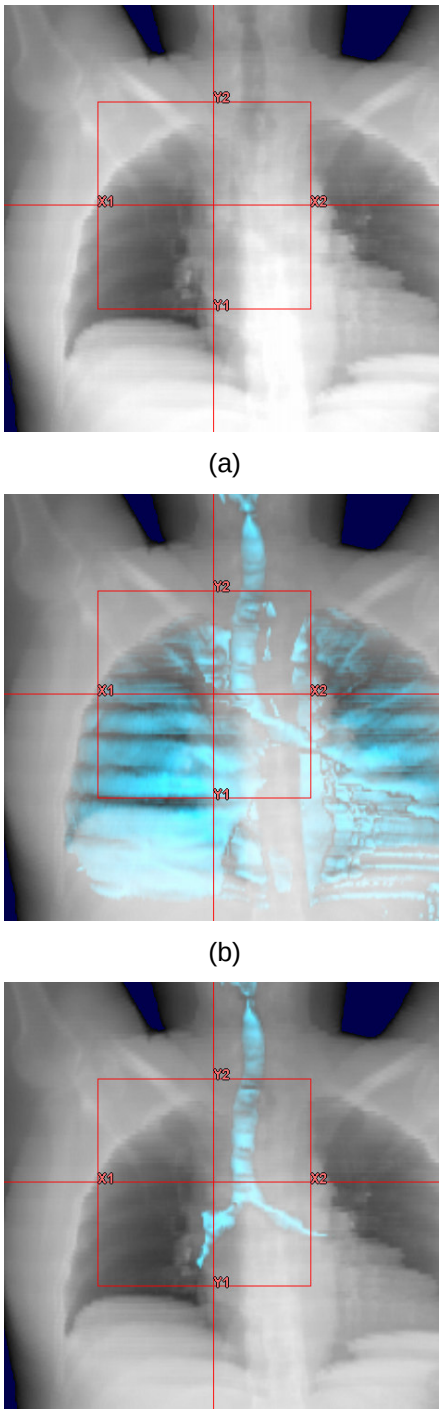

Figure 5-9. DRR reconstruction simulating megavoltage X-ray energy (a). Surface reconstruction of soft tissues (b) and isolation of trachea volume (c)

Finally an extension of this approach could be used for the development of an automatic segmentation of the lung and trachea anatomy.

Chapter 6

Efficient Visualization of Dose Distribution

6.1 Introduction

Completing the steps of the RTP process described in the previous chapters of this thesis, we enter now into a different area that involves the evaluation of the treatment planning results. As already mentioned, the CT-Simulation of standard treatment cases follows, the calculation of dose distribution for the proposed radiation field arrangement. Recently we pierce a new era in RTP where exchange of planning data among different processing and visualization modalities happens more freely and standardized using DICOM-RT, than never before. In previous chapters we demonstrated graphical tools that can be available during the CT-simulation of the planning process, involving the definition, selection and display of volumes of interest in relation to the neighbor anatomy and radiation beam geometry. These tools are meant to augment the traditional display methods giving physicians and physicists the ability and flexibility to visualize complex information in various formats. The product of the simulation process is forward to the dose calculation engine. For calculating dose distributions the density information is taken from the CT volume. Additional important information for this process is the geometric primitives of the volumes of interest and the radiation beam orientation and shape.

The dosimetric analysis is important in order to choose between a number of apparently radiation beams arrangements and to optimise the weighting of doses from a number of beams in a given arrangement [Peliz96]. By appropriately weighted integrations of calculated doses over the volume of tumour and normal structures segmented from the CT data, dose volume histograms (DVH), estimates of tumour control probability (TCP) and normal tissue complication probabilities can be produced. The group of dose verification tools is completed with additional visual verification in two and three dimensions. The ability to make such calculations relies on the accurate definition of the 3D region of integration and dose volume grid resolution.

It is very common in dose distribution computations, to make a trade-off between performance and accuracy. Due to visualization performance and interactivity issues most RTP systems reduce the dose volume grid, which usually has four to eight times smaller resolution compared with the original CT volume. In any case the aim of dose display is the same: clear illustration of the spatial relationship between the structures of interest and the dose distribution. Commonly this is achieved using a surface representation (polygon or voxel based) of the corresponding objects, selecting among opaque and semi-transparent appearance. To answer the question why surfaces are most suitable for this task, one should consider as remarks that our world is dominated by surfaces. Thus we can better evaluate the shapes and spatial relationships of objects from reflections of their bounding surfaces than from transmission or scattering of light through their interior [LeFuP90].

Most RTP applications distinguish the rendering methods into surface (polygon) rendering and volume rendering methods. Originally 3D RTP systems displayed the surfaces of 3D objects as stacks of contours. The wire-loop visualization conveys the defined important features of the 3D image scene using a minimal amount of on-screen information. These visualization techniques can still be found useful and are widely used [Purdy93], [Perez95], [Peliz98]. The most important advantage of this representation approach is the minimization of the amount of information used to define a 3D structure shape, meaning that the displayed objects may be manipulated at interactive rate without any preprocessing and interpolation step of missing data. The more developed surface rendering displays using polygon models of surfaces have also been heavily used in treatment planning systems. Hardware acceleration to directly render polygon scenes has a long history and currently is available at modest cost e.g. personal computers. To complete the visualization scene all regions of interest, target and critical normal structures, are manually or semi-automatically segmented and geometric models of them are generated. Dose iso-surfaces are automatically extracted from the dose volume into polygon meshes using marching cubes. Wire-loop and surface-based visualizations are effective for displaying geometrically defined objects and have the advantage that all objects involved in the RTP process such as dose iso-surfaces, objects of interest and radiation beam boundaries, can be included in the rendered view, as opaque or semitransparent surfaces and intermixed ease using the same graphics techniques.

Despite the above advantages of the wire-loop and surface-based visualizations, they have not proven entirely satisfactory for displaying anatomy and dose. This is part because surface rendering requires that each anatomic featured must be contoured, a time consuming and labour intensive process. The resulting polygonal mesh not only omits potentially useful information, but also creates the false illusion that features have well defined surfaces. For display radiation dose with a smooth mesh a large number of polygons must be used. In order to display different dose levels separated meshes must be generated in the same manner.

Volume rendering is a well-established method in medical imaging for generating high realistic three-dimensional images lack of intermediate contours or polygon meshes. As described in Chapter-5, volume rendering generates images after direct sampling of the volume data values. Voxel classification if often used to assign to each voxel a set of visual attributes, such as colour and intensity. In addition the opacity is commonly used property that measures how much intensity of the sampling ray will pass through a given material. Similarly to the visualization principles of multi-volume rendering methods used in data fusion of different imaging modalities, in RTP the data volumes involved in the process, volumes of interest, CT data and dose volume, are combined under the same graphic environment independent from their resolution [Vanuy99]. Common volume rendering examples are applications in stereotactic treatments [Gehri91], [Peliz98], [VDBer00]. The principal advantage of volume rendering over wire-loop and polygon-based visualization are their superior image quality and the ability to generate images without explicitly defining the geometry of the structures. Even when object geometry must be defined, as it often happens in RTP, using volume rendering one has always the possibility to reconstruct selectively parts of the original volume without significant effort but with significant visual benefits. One approach is to use an auxiliary volume, which will have the same size as the original data volume [Schim93]. The segmented objects will allocate a corresponding amount of voxels in the auxiliary volume addressing their geometrically shape. Then the 3D reconstruction could be achieved using the same rendering

pipeline. A different approach is the use of hybrid rendering where the object's shape is defined as polygons objects. The ability to effectively combine volume and surface graphics has important implications for intra-operative visualization and haptic rendering systems [LeFuP90], [Bhale00], [Seem01].

CT simulation offers high quality 3D images that are mostly used for the planning of the patient treatment. Important influence on producing these results has the high resolution CT volume used. The 3D visualization of all the necessary information combined, can be done interactively, which is of great benefit for the clinical routine. In combination to the above advantages the display of the treatment plan registered with the dose volume information produced from the TPS will further enhance the treatment evaluation process and the role of CT-simulation in the RTP process. In this chapter we will present a visualization strategy that described the dose display process within the CT-simulation environment. The work of this chapter could be separated into two parts: the dose resampling and dose visualization part. The first part involves the interpolation of the original dose volume data; a critical step when aiming to produce accurate calculation results as well as high quality 3D illustrations. The second part involves the mixed visualization between the dose and the CT-volume in two and three dimensions. Volume rendering is the vital component used for the implementation of the visualizations tools that will be presented, and aim to augment the qualitative verification of the dose distribution, the volumes of interest and the CT data.

6.2 Related Work

One could assign the simultaneous display of dose and CT volume to the multi volume visualization problem. The information acquired from the multimodality volumes can be combined and presented on 2D or 3D schemes. Volume rendering is probably the most common visualization principle technique employed among the existing visualization methods. Cehring ***et al.*** [Cehri91] presented a system in the frame of stereotactic RTP. There dose volumes could be merged with CT data and segmented volumes. The basis of this application was volume rendering but nevertheless 2D visualization capabilities such as virtual cutting planes and multiplanar reconstructions where also presented as important tools. Levoy ***et al.*** [LeFuP90] reported a working frame where multimodal anatomical volumes could be rendered registered with the corresponding dose distribution in the frame of RTP. Zuiderveld in his work [Zuide95] presented complete solution on how to combine different imaging modalities such as CT, MR and SPECT. Pelzzari ***et al.*** in his report [Peliz98], has been more application oriented reviewed several systems involved in visualization issues on RTP. Most of the reviewed systems used as basis volume rendering for visualizing patient's anatomy and volumes of interest. Cai ***et al.*** [CaiSa99] used volume-rendering techniques to visualize CT-volume of interests and dose volumes under the same visualization scene, investigating all possible optical models that could be adapted on the frame of this task. The results included visualization models based voxel-surface representation as well as on transparent illumination models. This work provided detailed information on a number of potential methods that could be used in RTP visualization.

The aim of this work is to define and present an imaging strategy employed in the frame of 3D-Simulation that would be able to evaluate the dose volume distribution of the applied treatment plan merged with the CT data and the volumes of interest. Basically our aim is to merge three different volumes:

1. The anatomical volume. This represents the original digital patient data as acquired from the imaging modality (this could be CT or MR volumes).
2. The volumes of interest (VOIs). These involve the representation of anatomical regions such as the tumour and organs at risk, defined manually or automatically from the user during the segmentation step.
3. The dose volume. The dose volume is generated from a dose calculation engine considering the corresponding treatment plan, target volume and organs at risk.

For the sake of understanding we have to make clear that the CT volume is the only digital information produced with direct relation from the patient's anatomy. We could call it as ***first level*** of information. The volumes of interest have been generated based on the anatomical-geometric information provided from the CT data, and thus they belong to the ***second level*** of information. Finally the dose volumes are also a product of the second level of information and thus we could address it as ***third level*** of information. Despite the fact that in each level of information an error might be introduced either systematic or randomised, there could be several combinations of the above information so as to produce the best visual outcome. The following diagram illustrates an overview of all possible volume grouping. One could separate the volume illustration methods into three groups of

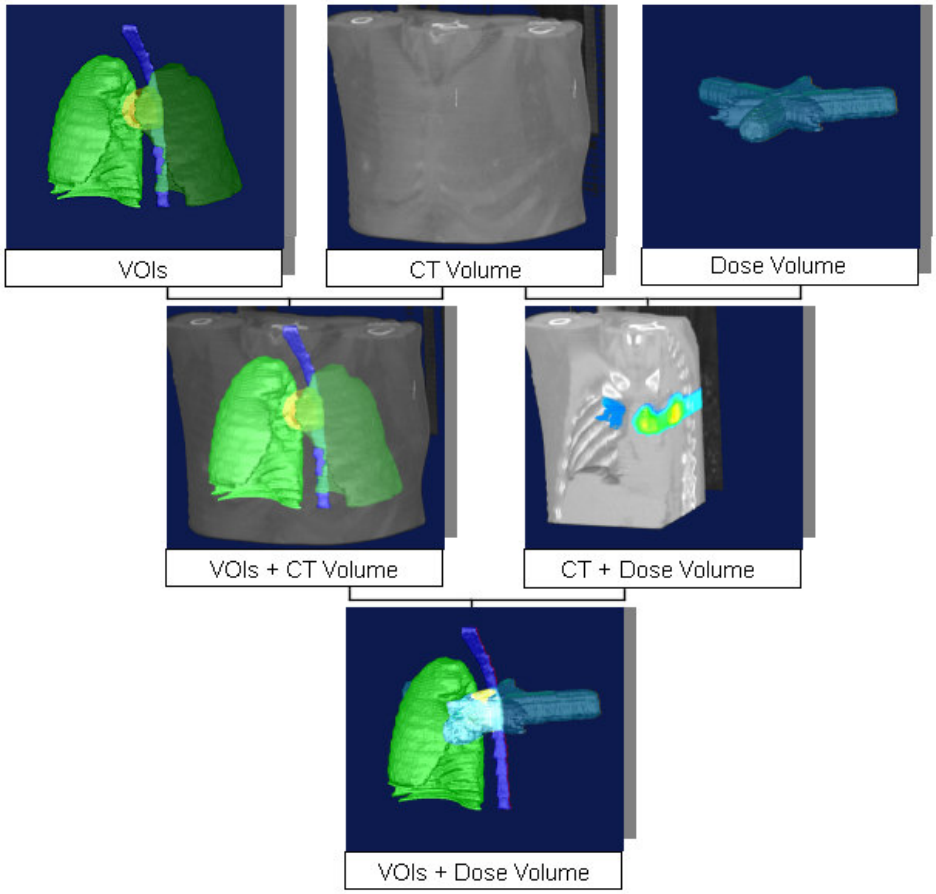

Figure 6-1. Selective combination of RTP volumes. The different levels of information are illustrated on the top row; segmented VOIs, CT volume and dose distribution volume. The lower rows indicate different combination possibilities.

information; in the first group of information all volumes are visualized separated from each other. In the second group of information the CT volume is the one who could be combined with the two generate. At this point we have to mention the illustration of the irradiation beams will not provide any additional information when combine with the dose treatment volume.

The way to the final visual outcome must go through several steps such as pre-processing and visualization. A complete approach for the efficient visualization of RTP information should include a range of 2D and 3D tools. In this work we focus in the 3D display of the treatment planning information. The strategy used here involves:

1. **Dose Volume Interpolation:** One problem that often occurs in dose and anatomical volume visualization is the fact that data with different resolutions must be merged. Dose volumes are calculated in a much smaller resolution than the corresponding anatomical volumes (CT or VOIs). Therefore a step is required order to upgrade the dose volume. In this work the interpolation scheme will be applied as a data pre-processing step. Main advantages for that decision is the optimal integration of the interpolated volume to the existing working pipeline, the quantitative and qualitative improvement of the optical result including, the reduction of the processing costs.
2. **Volume Registration:** This step is necessary in order to bring all volumes under the same coordinate system. This can be achieved by applying transformations on the volume geometry.
3. **Visualization:** Visualization aims to merge the CT, VOIs and dose information. The result can be represented in 2D and 3D.

6.3 Dose Volume Interpolation

In daily clinical routine the CT devices produce digital data volumes that are composed of 2D slices, with constant resolution $\boldsymbol{I_m}$ = ***(U, V)*** = ***(512x512)***. An average resolution for radiotherapy volumes in 3D-Simulation is $\boldsymbol{V}$ = ***(X, Y, Z)*** = ***(512x512x85)***. However the radiotherapy treatment planning systems, due to their design limitations use much less slices. In addition the patient's CT data are then further converted to a density volume, which has a much lower resolution than the original CT data. The main reason for that is the calculation performance. Finally the generated density volume is feed into the dose calculation engine with the defined anatomical structures and the radiation field configuration. The result of this process is a dose volume that contains missing information when one attempts to combine it with the original CT data volume. Additional reasons to reduce the dose volume during the calculation step but also during the communication (I/O) step is the data visualization. As already discussed, in radiation therapy applications the polygon reconstruction methods are used to illustrate the dose iso-surfaces [Zelez97]. However one can realize the higher the resolution of the dose grid the more demanding are the requirements on memory capacity and processing power during user interaction.

Basically one could use two different approaches to handle missing data. One uncommon approach used in scientific visualization is "by indicating the missing data by mapping colour outside the valid data domain or by making those areas completely transparent" [Twidd94]. However this method would give an abstracting feeling to the clinicians since the presented result is much different from what they have been trained to use as "real". However the most common method used in scientific and medical visualization to

eliminate discarding gaps caused from missing data is interpolation. Interpolation is the process that serves to determine the values of a function at the positions of the missing data, which of course are lying between the original data samples. This is achieved by fitting a continuous function through the discrete input samples [Wolbe90]. The advantage and disadvantage of the interpolation process, usually causes smoothing to the sampled data and do not allow distinguishing the original and interpolated data.

Data interpolation could be separated in two main categories: the scattered data interpolation and the Cartesian grid data interpolation. In the first category belong the interpolation methods that deal with unstructured data that have no special configuration. In contrast the data samples might lie on the vertices of a regular Cartesian grid. The data type used in this work belongs into the second category. For scatter data interpolation literature the reader can refer to [Vasil83], [Books89], [Niels93], [Savch95], [Lee97], [Carr97], [Rohli99], [Carr01], [Morse01], [Turk02].

Regular grid interpolation methods are very often applied in scientific visualization, mostly when at the image reconstruction step aiming to remove aliasing artifacts. An extended literature can be found on the comparison of interpolation schemes over visualization applications. Depending on the application one might use the perceptual approach or the mathematic approach to investigate the interpolation filter performance [Wolbe90], [Mölle97], [Carr98]. In the next paragraphs we will show the impact on the qualitative visualization of the three most common techniques used for the interpolation of regular grid data in scientific visualization, in the frame of RTP. The techniques under investigation will be the nearest neighbour (NN), the tri-linear data interpolation and the BC-Spline interpolation algorithms.

6.3.1 Nearest Neighbour (NN)

Nearest neighbour refer to the simplest replacement of missing data and is indeed the simplest interpolation algorithm from the computational point of view. Each interpolated output pixel or voxel is assigned the value of the nearest sample point in the input data. In the spatial domain the NN interpolation can be achieved by convolving the sampling data with a one-sample width rectangle. The interpolation kernel for the NN algorithm is defined as:

$$h(x) = \begin{cases} 1 \text{ when } 0 \le |x| < 0.5 \\ 0 \text{ when } 0.5 \le |x| \end{cases} \qquad \text{Eq 6. 1}$$

The NN achieves magnification by pixel replication and minimisation by sparse point sampling. The sampling result of the NN algorithm is images with blocky appearance and with potential shift errors of up to 1 ½ pixel-voxels. This approach is inappropriate when sub-sample accuracy is required from the application. Nowadays this interpolation scheme is rarely used in medical application but it is still suitable for real time interactions and data preview. In Figure 6-4 the row (b) illustrates 3D images of two phantom objects reconstruction using the NN interpolation.

6.3.2 Linear data interpolation

Assuming a simple 1D example of sampling points linear interpolation offers a first degree connectivity among the sampling points, passing a straight line through every two

consecutive points of the input signal. In the spatial domain, linear interpolation (LN) is equivalent to convolving the sampled data with the following interpolation kernel:

$$h(x) = \begin{cases} 1 - |x| & \text{when } 0 \le |x| < 1 \\ 0 & \text{when } 1 \le |x| \end{cases} \qquad \text{Eq 6. 2}$$

The above interpolation kernel corresponds to a reasonably good low-pass filter in the frequency domain [Wolbe90]. The linear interpolation filter has reasonably superior frequency response compared to the NN filter. Nevertheless, a significant amount of spurious high-frequency components continue to leak into the pass-band, contributing to aliasing. The linear interpolation offers improved interpolation results over NN.

In practice we can define the linear interpolation between two points p_0, p_1 in one dimension as follows:

$$p_x = (1-x)\,p_0 + xp_1 \Rightarrow \qquad \text{Eq 6. 3}$$
$$p_x = p_0 + x(p_1 - p_0)$$

The parameter x represents the fractional position between the data points and has value ranges as defined in Eq 6. 2. In two dimensions the interpolation scheme will involve four data points p_{00}, p_{01}, p_{10} and p_{11}. The interpolation can be formulated using the following formula:

$$p_{xy} = (1-x)(1-y)\,p_{00} + (1-x)yp_{01} + \qquad \text{Eq 6. 4}$$
$$x(1-y)\,p_{10} + xyp_{11}$$

This interpolation method is known as ***bi-linear*** interpolation and is commonly applied on image interpolation e.g. when magnifying raster images. In volumetric data linear interpolation is known as ***tri-linear*** interpolation and estimates the value of the result voxel considering the neighbourhood of eight (8) voxels. If the data points are defined as p_{000}, p_{001}, p_{011}, p_{010}, p_{100}, p_{110}, p_{101}, and p_{111} then the new voxel value p_{xyz} will be estimated by using the following formula:

$$\begin{aligned} p_{xyz} = {} & (1-x)(1-y)(1-z)\cdot p_{000} + \\ & x\cdot(1-y)(1-z)\cdot p_{100} + \\ & x\cdot y\cdot(1-z)\cdot p_{110} + \\ & (1-x)\cdot y\cdot(1-z)\cdot p_{010} + \\ & (1-x)(1-y)\cdot z\cdot p_{001} + \\ & x\cdot(1-y)\cdot z\cdot p_{101} + \\ & (1-x)\cdot y\cdot z\cdot p_{011} + \\ & x\cdot y\cdot z\cdot p_{111} + \end{aligned} \qquad \text{Eq 6. 5}$$

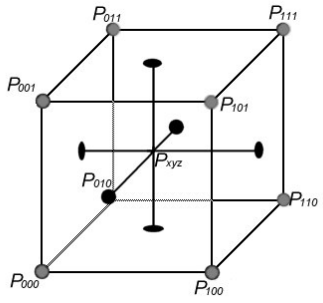

Figure 6-2. The geometry of a unit cube with the data points lying on the edges and the interpolated value in position (***x,y,z)***.

The parameters (***x, y, z)*** represent the fractional coordinates of the sampling point p_{xyz}. The ***tri-linear*** interpolation is the most common interpolation method used in volume rendering reconstruction and has been realized from several researchers. It is the most widely used interpolation algorithm since it produced reasonably good results at moderate cost. Interpolation result of LN are illustrated in Figure 6-4, row (c).

6.3.3 B-Spline Interpolation

Möller ***et al.*** [Molle97] has investigated the use of cubic spline filters in volume rendering and applied them to MRI data. Their work builds on earlier research by Mitchell ***et al.*** [Mitch88], which discusses cubic interpolation in computer graphics from a signal processing point of view. They use a Fourier analysis of the approximation error and subjective tests based on 2D image interpolation to argue for a practical cubic spline filter. In [Molle97] a Taylor series expansion is used to argue that the ***Catmull-Rom*** spline is the optimal interpolator. Interestingly, they choose a different filter, rather than the derivative of the interpolant, to determine gradients. In this paper we have found that, despite these previous analyses, a quasi-interpolant, which does not exactly interpolate the data is useful when rendering structures known to be smooth and continuous. We believe this is because the theoretical analyses do not consider the presence of noise in the sampled data.

By using the cubic B-Spline interpolation we aim to approximate the continuous function, which underlies the volumetric data. The spline control points are therefore derived from the points (voxel centres) where the function is known. In order to apply the B-Spline we will use an approach similar to the parametric representation of curves. If we consider the 1D case the spline interpolation *S(x)* specified over the interval $x_i<x<x_{i+1}$, can be extracted using the following parametric equation:

Since we refer to ***1D*** by multiplying out the above equation ***S(x)*** can be written as the weighted summation of four points *Pi-1, Pi, Pi+1, Pi+2,* which are equally spaced along the interval ***x***. M is a *4x4* matrix of weights which are chosen to provide various degrees of continuity between adjacent segments at the endpoints *x=0* and *x=1*. Specifically, we consider the family of BC-Splines where M is given by:

$$M = \frac{1}{6}\begin{bmatrix} -B-6C & 12-9B-6C & -12+9B+6C & B+6C \\ 3B+12C & -18B+12B+6C & 18-15B-12C & -6C \\ -3B-6C & 0 & 3B+6C & 0 \\ B & 6-2B & B & 0 \end{bmatrix} \qquad \text{Eq 6. 7}$$

This family is derived from the most general form for a symmetric cubic basis function. By requiring the value and first derivative to be continuous everywhere, the number of free parameters which determine the spline are the ***(B,C)***. Note that the BC-Spline family

$$S(x) = X \cdot M \cdot P =$$

$$S(x) = \begin{bmatrix} x^3 & x^2 & x & 1 \end{bmatrix} \cdot \begin{bmatrix} m_{11} & m_{12} & m_{13} & m_{14} \\ m_{21} & m_{22} & m_{23} & m_{24} \\ m_{31} & m_{32} & m_{33} & m_{34} \\ m_{41} & m_{42} & m_{43} & m_{44} \end{bmatrix} \cdot \begin{bmatrix} P_{i.-1} \\ P_{i.} \\ P_{i.+1} \\ P_{i.+2} \end{bmatrix} \qquad \text{Eq 6. 6}$$

includes the cubic B-Spline (1,0), the Cardinal cubic Splines (0,C) and the ***Catmull-Rom*** spline (0,0.5). In this application we select ***(B, C) = (1, 0)***. Thus matrix M becomes:

$$M = \frac{1}{6}\begin{bmatrix} -1 & 3 & -3 & 1 \\ 3 & -6 & 3 & 0 \\ -3 & 0 & 3 & 0 \\ 1 & 4 & 1 & 0 \end{bmatrix} \qquad \text{Eq 6. 8}$$

The properties of the B-spline curves or surfaces can be extended in the image or volume reconstruction very well. The most important properties are continuity, convex hull, local control, variation diminishing and representation of multiple values. The spatial distribution result from B-spline interpolation is smooth and exhibits second order continuity C^2. The convex hull property of the B-spline ensures that each point in the curve lies in the convex hull of the four control points. Thus, sample points bound the space of the reconstructed curve, surface or volume, so the reconstructed values will range within the voxel values forming the support. The local control property makes far points less influential on the segment of consideration. Thus rapid changes of the control point values in one segment will affect only those point values of the segments lying very near. One method to apply the B-spline interpolation is by estimating the control polygon of the B-spline approximation, such that the resultant case passes through the requested points.

As illustrated in [Foley90] the 1D approach can be extended to 2D as shown below:

$$S(y,x) = [Y \cdot M] \cdot \begin{bmatrix} P_{11} & P_{12} & P_{13} & P_{14} \\ P_{21} & P_{22} & P_{23} & P_{24} \\ P_{31} & p_{32} & P_{33} & P_{34} \\ P_{41} & P_{42} & P_{43} & P_{44} \end{bmatrix} \cdot [M^T \cdot X^T] \qquad \text{Eq 6. 9}$$

where:

$$X = [x^3 \;\; x^2 \;\; x \;\; 1]$$
$$Y = [y^3 \;\; y^2 \;\; y \;\; 1]$$

When the product of Eq 6. 9 is evaluated, it can be seen that the B-spline is constrained to lie within the ***convex hull*** of the four control points, since the coefficients of the four control points range in value between 0 and 1 and sum to 1 for $0<x<1$.

We now consider the analogous BC-spline in 3D where $t = (x, y, z)$. In 3D the control points lie on a regular grid in $\mathbf{R}^3$ and are denoted by Pi,j,k where (i,j,k) are integer indices referring to grid locations where the data are known. The nodes of the grid are the voxel centres. The 3D spline is a weighted average of 64 control points in a ***4x4x4*** neighborhood which describes the spatial distribution ***f(x)*** within the volume bound by the eight central voxels (see Figure 6-3). If the locations of these voxels are scaled and shifted such that they lie within the unit cube, then the spline can be formulated as:

$$S(z,y,x) = Z \cdot M \cdot \begin{bmatrix} Y_m & P'_{k-1} & X^t_m \\ Y_m & P'_k & X^t_m \\ Y_m & P'_{k+1} & X^t_m \\ Y_m & P'_{k+2} & X^t_m \end{bmatrix}$$ Eq 6. 10

Where:

$$Z = \begin{bmatrix} z^3 & z^2 & z & 1 \end{bmatrix}$$

$$P'_k = \begin{bmatrix} P_{i-1,j-1,k} & P_{i,j-1,k} & P_{i+1,j-1,k} & P_{i+2,j-1,k} \\ P_{i-1,j,k} & P_{i,j,k} & P_{i+1,j,k} & P_{i+2,j,k} \\ P_{i-1,j+1,k} & P_{i,j+1,k} & P_{i+1,j+1,k} & P_{i+2,j+1,k} \\ P_{i-1,j+2,k} & P_{i,j+2,k} & P_{i+1,j+2,k} & P_{i+2,j+2,k} \end{bmatrix}$$

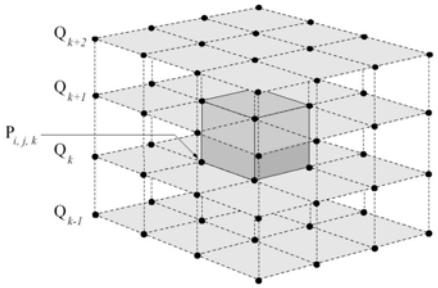

Figure 6-3. The geometry of the 64 control points defining the B-Spline in three dimensions.

The aggregate of BC-spline segments determines the scalar distribution over the entire data volume. The resulting spatial distribution is smooth and, in the case of the B-spline, exhibits second order continuity. The convex hull property of the B-Spline means that the fitted function is constrained to have values within the range of the voxel forming the support. Other choices of B and C, such as the ***Catmull-Rom*** spline, do not exhibit this property. The B-Spline is a ***quasi-interpolant*** of the voxel values at the interpolation nodes. It is not unreasonable to approximate the sampled data at voxel centers if the sampled data are noisy or do not represent the actual value of the parameter at the grid coordinates but are averages of the true parameter over the volume of the voxel. In such cases, the data can be viewed as having a noise component arising from the partial voluming effect.

In practice, the B-spline interpolant closely approximates the data except where sudden changes occur at a scale, which is small relative to the size of the B-spline support. The piecewise nature of the spline interpolant avoids the propagation of spurious ripples due to sudden changes or discontinuities in the data. Reconstruction examples using different interpolation functions are presented in Figure 6-4. The two phantom data used have original size of 128^3 with 1mm square voxel size. For our experiments we have been removing 75% of the original data in regular spaces. Although we expected that the interpolation algorithms would not be able to reconstruct the original object shapes due to the large amount of removed data, we wanted to exam the difference of the reconstructed result with the original shape. We choose that percentage of information reduction due to the fact that several commercial TPS systems that export the dose distribution matrices use a similar ratio for reducing the original data. We use the interpolation algorithms presented above to reconstruct the original shape of the objects. The results indicated that the NN interpolation method reconstructs the original shape with rather deformed edges far from the reality. Linear interpolation improved the situation giving more realistic edges to the original bars. However it has been incapable to reproduce the curvature of the sphere object. Finally the B-Spline has been more efficient on reconstructing the sphere object due the high degree of continuity. However we noticed that shrinkage has been caused to the bar phantom edges, an effect we also observe when interpolating clinical dose distribution data.

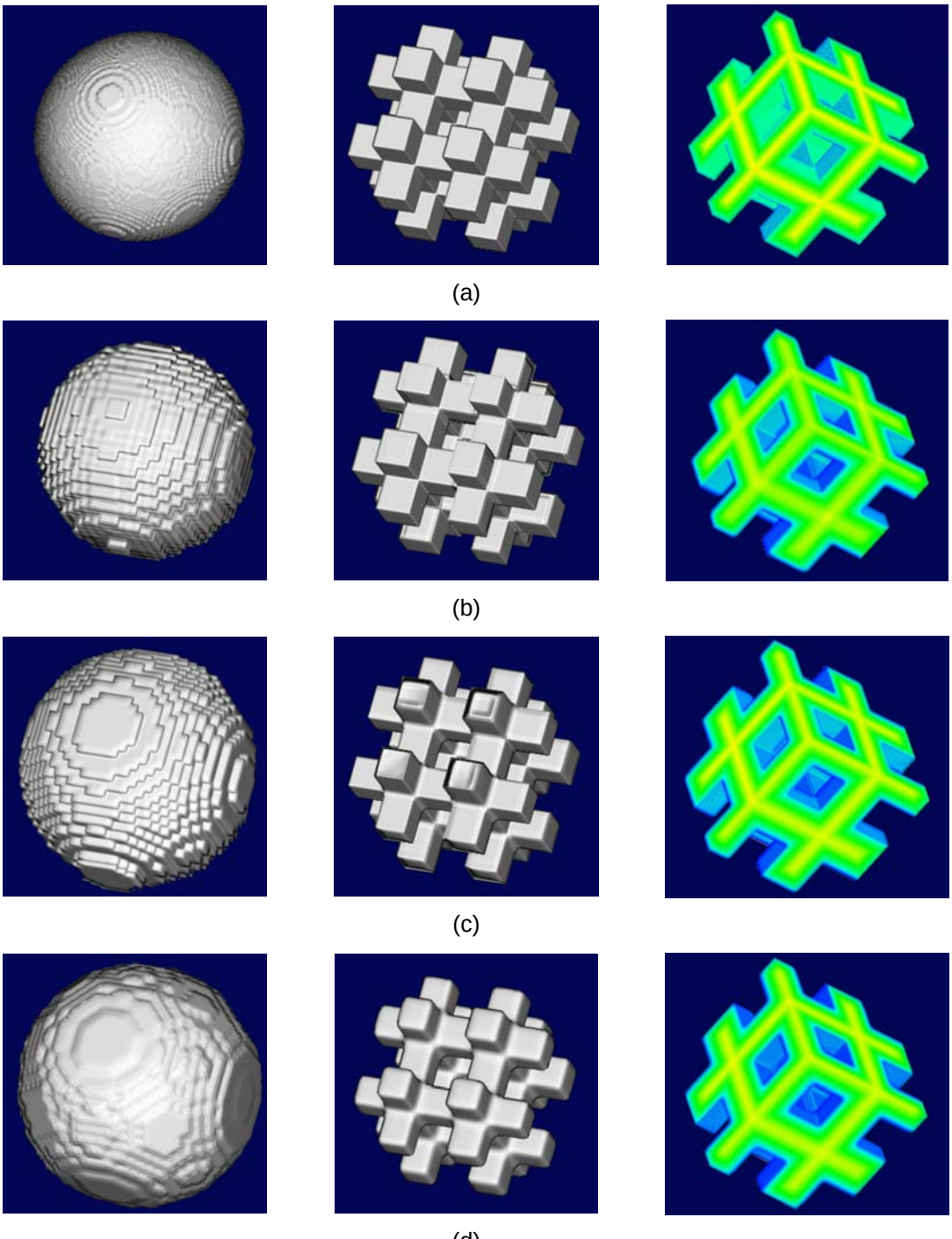

Figure 6-4. 3D Reconstruction results of phantom data using different interpolation algorithms. The phantom data have been reduced 75% of the original data volume. From top to bottom (a) represents the original data, (b) the reconstruction after interpolation using the NN, (c) the reconstruction after interpolation using the LN method and (d) the reconstruction after interpolations using B-Spline method.

6.4 Dose Volume Visualization

The key component for the volume visualization process is the rendering pipeline. Although the rendering pipeline is already presented in previous chapters, for the sake of integrity we will briefly mention that design again. Rendering algorithm is the ray casting algorithm based on [Sakas93] and [Sakas95]. The main rendering pipeline is similar to the mono-volume rendering pipeline described in [Saka93]. The data flow through three different stages, Geometric Transformation, Integration-in-Depth, and Mapping. In our context, since different volumes share the same size and position, geometric transformation and the mapping are the same as in mono-volume rendering. The difference is in the second stage (see Figure 6-5).

In case that the multi-volumes resolutions are different, the same start and end points in world co-ordinates would relate to different traversing co-ordinates in volume data spaces. In addition, the number of sampling points along the same ray should be different in different volumes due to the different resolutions. In that case simplicity, the largest numbers of sampling points in multi-volumes is used as the number of steps in the ray traversing, which results in an identical loop for all volumes causing over-sampling in the smaller resolution volume. In the context of our work the multi-volumes obtained the same resolution having as reference the volume with the highest resolution. This is one of the advantages having the volume interpolation step at the preprocessing level since the sampling process occurs at the same frequency for the multi-volumes. At each sampling point along the ray, the values from different volumes are obtained by sampling and interpolation in the corresponding volume data spaces. Thus, the first two steps in Integration-in-Depth stage become the parallel copies of the corresponding steps in mono-volume rendering.

Cai ***et al*** [CaiSa99] demonstrated that the multi-volume information can combined after the above processing step; the data intermixing maybe involved in different steps in the Integration-in-Depth stage: in illumination step, in accumulation step or after accumulation. They are corresponding accordingly to illumination model level intermixing, accumulation level intermixing, and image level intermixing. Different intermixing level results in different rendering pipelines. In the context of this work we are interested on qualifying the performance of the volume data mixing methods so as to achieve the best visual outcome.

As presented in section 6.2, in the volume visualization pipeline we should be able to handle three different data combinations obtaining all possible combinations mentioned above. Once again we must refer on the importance of the surface representation (opaque or semi-transparent) of the dose volume in the rendering scheme. The main reason for adapting this policy is the capability offered from the surface representation to better approximate and justify the dose boundaries within the rendering scheme. An X-ray like volumetric reconstruction could be

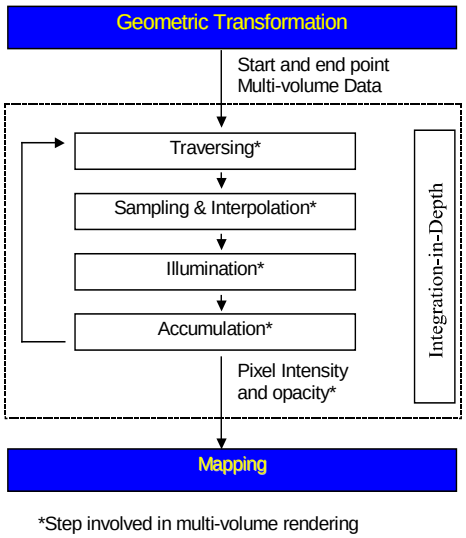

Figure 6-5. Simplified diagram of the volume rendering pipeline.

of much less use during dose verification since the accumulated information along the ray and the cloudy appearance of the final result will cause mostly confusion to the observer. Thus in the frame of this work we will use the volumetric surface representation for every volume used.

6.4.1 Merging VOIs and CT Volume

The surface representation of volumetric data has been an old subject in scientific visualization community. Levoy [Levoy88], [LevoA90], [LevoB90] was one of the most successful pioneers in the field presenting the iso-value and gradient representation of volumetric surfaces. The key components of this approach are the calculation of the opacity volume, that has been used to assign transparency properties on the reconstructed surfaces, and the gradient vector estimation that will be used for the shading model as normal vector. The approach employed for this work aims to assign a semitransparent view of the surface of different structures [Höhne90]. In this approach the opacity volume is extracted based on a transfer function (TF) that is generated upon user request similar to the iso-value reconstruction. The TF shape might have a linear or triangular and or higher order of interpolation. During ray traversing and volume sampling a texture value is recorded and filtered with the opacity TF so as to produce an opacity value, lack of gradient vector. Thus the final pixel colour is not affected from any shading model as in the previous case. The interesting affect of this approach is the cloudy appearance of those structures that have been sampled with low opacity values and of course the opaque illustration of the higher opacity values. This approach can be quite useful on illustrating low-density tissues in CT volumes.

The VOIs volume is a product volume of the segmentation process that has been applied on the original CT data. It is very common that the segmented structures are composed of 2D planar contours. There are two common representations used to illustrate a 3D surface from a set of contours. One is to generate a triangulated surface using standard triangulation algorithms. The approach employed in this work is to render-fill the internal region of the contours using a scan conversion algorithm, so as after stacking them to compose a volume that will have the same resolution and size with the original CT data. The filled voxels are addressed with bit values in order to indicate their colour properties and priority properties such as target volume for example. In addition an opacity value is used so as to assign transparency to the segmented objects during the 3D object representation.

An essential part on the shading phase of the binary surfaces is the normal vector on the surface point. There are a number of methods available to estimate normal vectors of discrete surfaces. Usually the normal vector at a surface point is obtained by examining a certain neighbourhood of this point. The methods are denoted as image space or object space techniques, depending on the fact that the neighbourhood is considered in the projected image on in the 3D scene, respectively. Object space techniques are preferred, since they do not suffer from loss of information due to projection. Furthermore, enable rendering techniques like ray tracing, where normal vectors are required in 3D space. The method employed in this work is an object space technique that produces a first estimate of the normal at a surface voxel $\boldsymbol{p}$ considering a set of voxels in the neighbourhood. For more information on these approaches please refer to [Thürm97], [Thürm01].

The best visual outcome of these two volumes will bring the information about the spatial relation between the segmented structures and the original CT volume. It is important

for the clinical routine to be able to see within the original volume the location of the VOIs. Figure 6-6 shows a single volume reconstruction of the two volumes sampling volumes. The most common method used to merge this different volume information is by blending the two rendering images. For each volume, one result image (intensity and opacity after Integration-in-Depth) is rendered respectively. Then, the final image is calculated by intermixing pixel intensity and opacity coming from the different volumes.

Among the several methods used for image level mixing, the more suitable for the integration of the CT volume and the VOIs, in the content of 3D-Simulation is the use of the following methods:

- Intensity mixing
- Intensity mixing with Z-buffer depth differences.

6.4.1.1 Intensity Intermixing Only

Defining an intermixing factor (or weight) ***w***, where I_1 and I_2 are intensities coming from two different images, then the result image intensity is the linear composition of two images, i.e.

$$I = w * I_1 + (1.0 - w) I_2 \qquad \text{Eq 6. 11}$$

The visual effect of Eq 6. 11 is the fade-in and fade-out of two images when weight is changed interactively. With this effect, user can investigate the relationship of objects in two volumes on a projection plane (see Figure 6-6(c)).

6.4.1.2 Intensity Intermixing with Z-buffer Depth Difference

The main problem of image level intermixing is the lack of correct depth cueing in the overlapping area, where different objects coming from different data set overlap. For example, in Figure 6-6(c), it is difficult to determine the depth location between the two reconstructed structures when they are directly merged with the 3D surface anatomy. For accurate visualization it must be determined, which of these two structures is more near to the viewer. We partially solved the problem using the Z-buffer value[1] of each pixel that represent surface on the image. There are two ways to make use of the Z-buffer depth value. One could be the Z-buffer depth weighting value that could be used during VOIs image generation. The second way is after generating reconstructing the VOI image and the depth values are stored in the Z-buffer. If d_{CT} and d_{VOIs} are the depth values in Z-buffer of the two images, then we estimate their depth value difference. The depth difference is normalized and the product is used as the mixing factor between the two images:

$$norm\_d = 1/\sqrt{(d_{CT})^2 + (d_{VOIs})^2}$$
$$d'_{CT} = d_{CT} * norm\_d, \quad d'_{VOIs} = d_{VOIs} * norm\_d$$
$$w = w_d * | d'_{CT} - d'_{VOIs} |$$
$$I = w * I_{VOIs} + (1.0 - w) * I_{CT} \qquad \text{Eq 6. 12}$$

[1] In volume rendering, the Z-buffer value is defined as the depth along the ray from viewpoint to the first visible voxel of a certain segmented object.

Image level intermixing is very simple and we do not need to change the basic rendering algorithm. Drawback is that the results do not provide the exact correct depth cueing between the two volumes. In Figure 6-6, different mixing factors are used to mix two rendering images, one is CT gradient opacity rendering image, another is segmented object LUT volume rendering image. From left to right, the mixing factor of CT gradient surface image is changed from large to small. Since the mixing of two images is finished interactively, the user can change the mixing factor interactively and viewing the fade-in and the fade-out of two images to smooth over the disadvantage.

6.4.2 Merging VOIs and Dose Volume

The accurate dose volume reconstruction is essential for the efficient radiation plan verification. As already mentioned the dose volume has been re-sampled from lower resolution to higher using one of the interpolation methods mentioned above. The highest priority on this visualization step is the common representation of the dose volume in relation with the VOIs. The volumetric surface of the dose has been generated the same reconstruction pipeline used for the VOIs (see Figure 6-8). The colour and opacity properties of the dose volume are assigned means of LUTs (see Figure 6-8). This will allow us to reconstruct different iso-dose levels interactively with different transparencies. For merging the two volumes in this step the image level mixing approach produce poor results since the depth relation of the structures can be misleading. For a better approximation the inclusive opacity intermixing approach is employed. This volume-mixing step is applied during the sampling phase. More precisely within the loop of ray casting, one ray samples voxel values in different volumes at each point and mixes their visual contributions step by step along the ray in accumulation in Integration-in-Depth stage.

The accumulation involves opacity and intensity. Opacity and intensity are derived from the voxel density by a transfer function in the volume illumination model. Since different volumes have different physical background and value ranges, their transfer functions are also different. But opacity and intensity have the same range (between 0.0 and 1.0) and the same optical property after transfer function mapping. Thus, another way is to intermix different opacities and intensities coming from different volumes during the accumulation step. The model used for mixing opacities is based on the inclusive opacity model.

6.4.2.1 Inclusive Opacity (INCOP)

Volume mixing using inclusive opacity is a very effective method when using volumes. Furthermore it can be used in surface and volume (surface-voxel) mixing as it has been presented in [Frue91]. Generally speaking, it can be applied in most of the intermixing cases if we can map the voxel value (or any object, like surface and line) into opacity and intensity. Inclusive opacity is to sum up the accumulative effect caused by both opacities from two different volumes and regarding it as the current point opacity. So, the result opacity at the sampling point is,

$$\begin{aligned} opacity &= 1.0 - (1.0 - opacity_1) * (1.0 - opacity_2) \\ &= opacity_1 + opacity_2 - opacity_1 * opacity_2 \end{aligned} \qquad \text{Eq 6. 13}$$

Then, the intensity is,

$$I = norm\_opacity_1 * I_1 + norm\_opacity_2 * I_2 \qquad \text{Eq 6. 14}$$
$$norm\_opacity_i = opacity_i \,/\, \sum opacity_n$$

where ***I*** is the object colour $I = (R, G, B)$.

In Eq 6. 14, we use the normalized opacity instead of the original opacity. It means that high opacity voxel has more contribution on the intensity than low one. Although opacity and intensity are mapped from different methods, for example, gradient opacity, iso-value opacity, attenuation opacity, they can be always intermixed by Eq 6. 13 and Eq 6. 14, after mapping them to corresponding opacity and intensity. In Figure 6-8(a) and (b) different dose surface iso-values are reconstructed from the dose volume. The interactive iso-value selection is very useful to view the iso-dose distribution in VOIs. Traditionally, we have to model the iso-surface of dose using polygon surfaces and then mix it into the

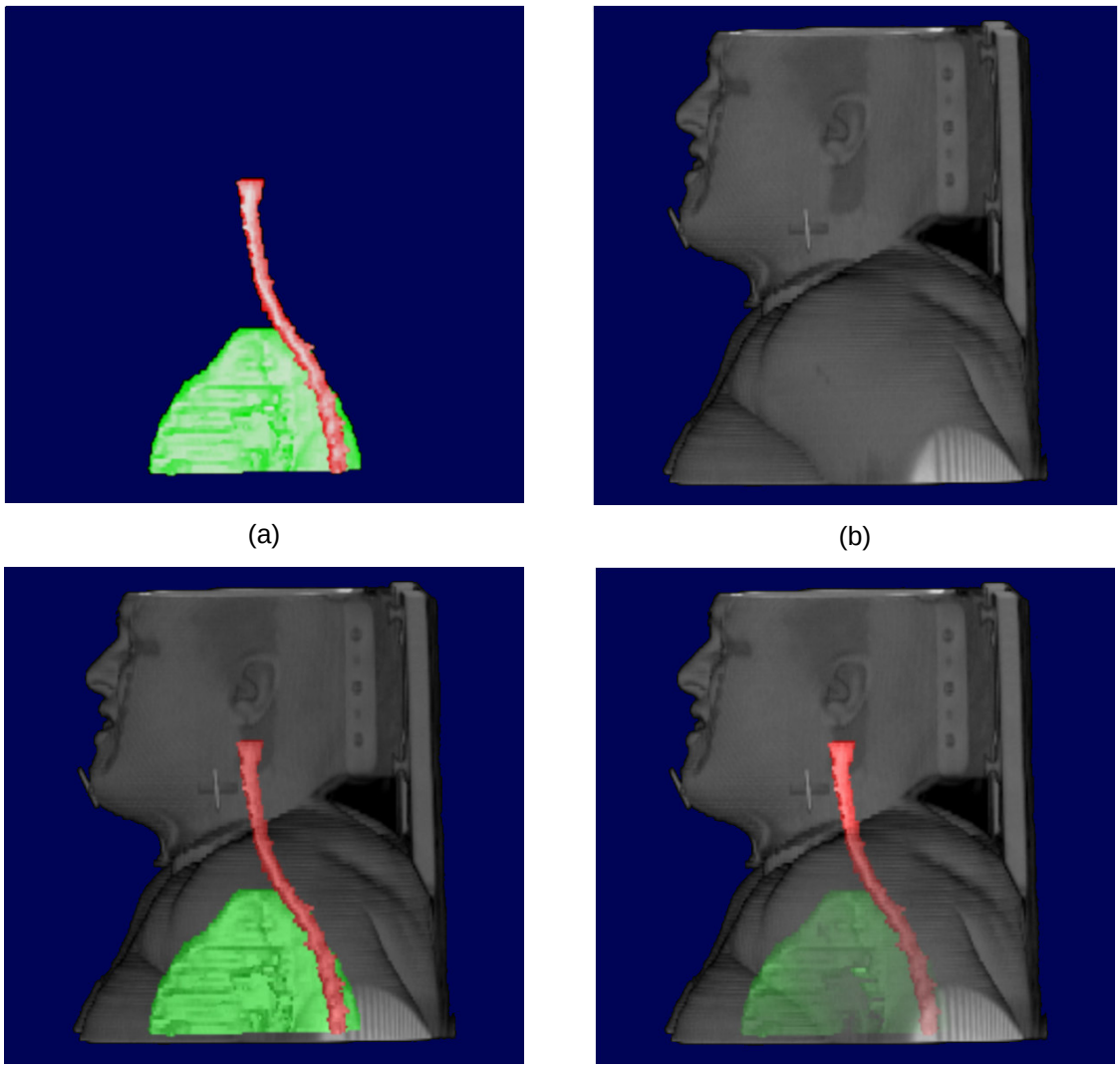

(a) (b)

(c) (d)

Figure 6-6. Volume image mixing using single image intensity blending. In (a) mixing using simple fading effect. In (b) mixing with depth difference weighting.

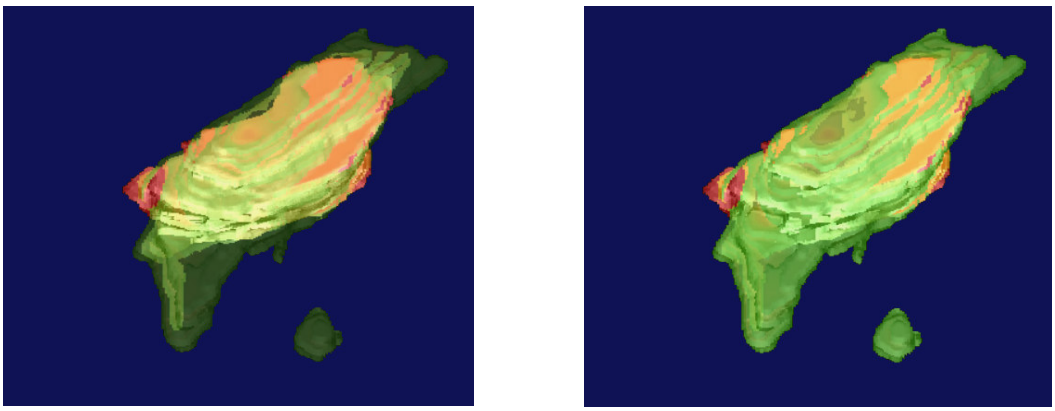

(a) (b)

Figure 6-7. Target volume and iso-dose volume mixing using the inclusive opacity. From top left to bottom right semi-transparent to opaque reconstruction of the dose volume.

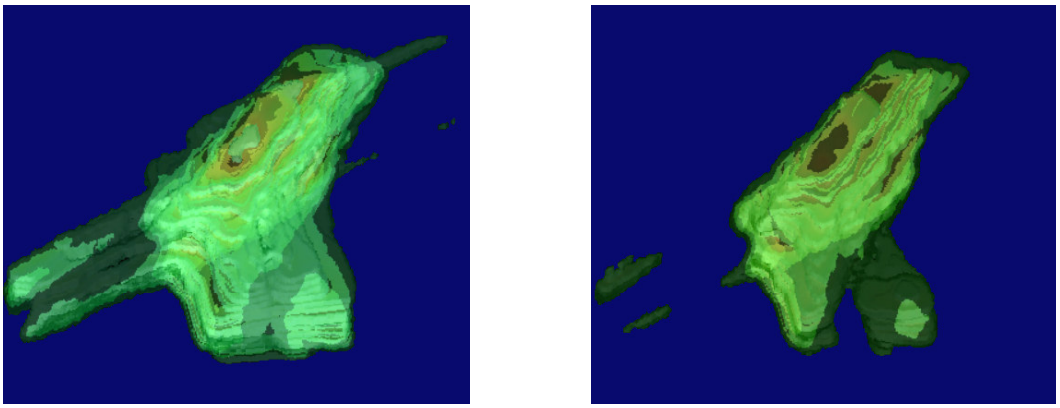

(a) (b)

Figure 6-8. Iso-value representation of the dose volume. In (a) the selected dose value is lower than the one in (b). In both cases different level of transparencies are used for the corresponding iso-dose values.

anatomy surface structure. Because modeling is a time consuming process and the number of triangles of iso-surface is very large, interactive iso-dose display is almost impossible in iso-surface rendering context.

In Figure 6-7 the segmented volume (in red) is intermixed with the iso-dose volume. The colour and opacity of segmented object is calculated from a lookup table defined by users, while opacity of iso-dose volume is calculated by a function as in [Levo88]. One can observer that iso-dose opacity level can interactively manipulated to provide better geometric relation between the volumes.

6.4.2.2 Dose Mapping on VOIs

The colour mapping process aims to paint the surface of a object with a range of a colour that will refer to the value range of the corresponding metric. These techniques are very commonly employed to other sciences like satellite picture analyses and geographic map

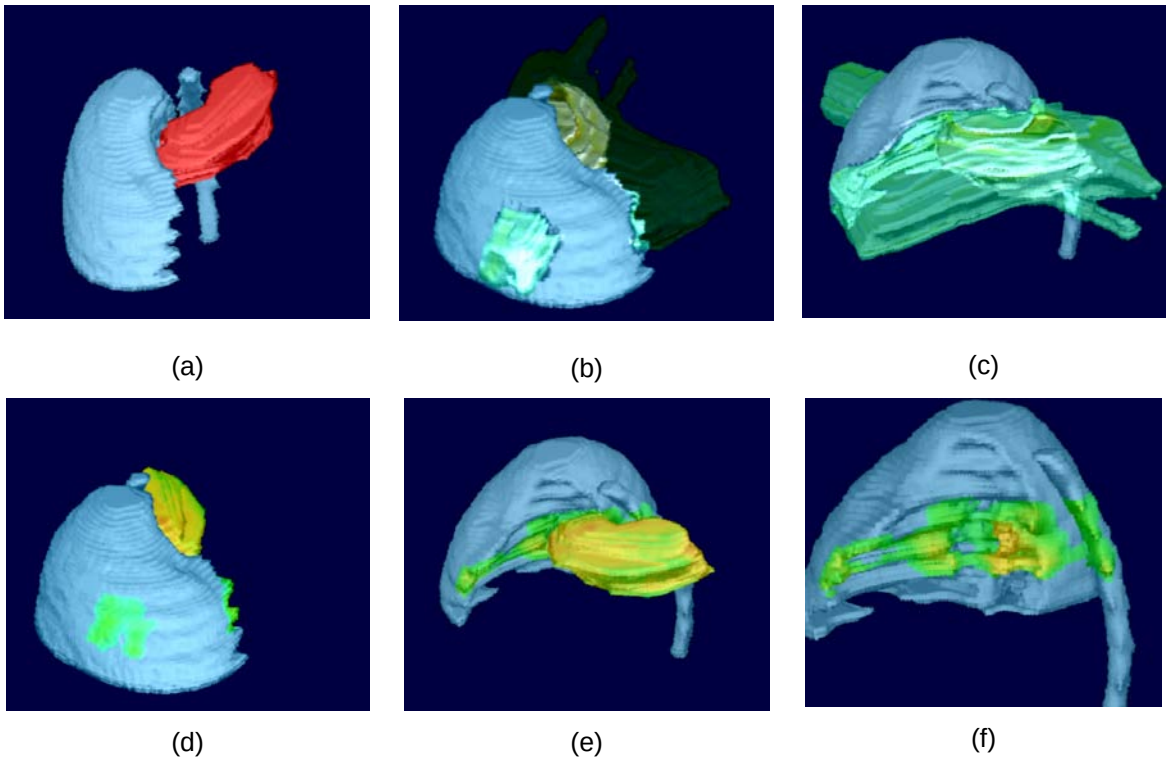

Figure 6-9. The effect of dose mapping on VOIs surfaces. In (b) and (c) merging of VOIs and dose volumes. In (d), (e) and (f) illustration of cold and hot spots on the surface of the VOI and target volume.

representation. This technique is often use as an evaluation visualization tool that can enhance the value spread of a metric over the geometry of a second metric which is usually considered the one with the priority privileges in the scheme under visualization. In our application we aim to map the dose volume over the VOIs surface, which are our priority volume. This approach could provide an overview of the exposed surface of the VOIs on different dose levels.

The volume mapping can be achieved based on the surfaces depth information collected from the Z-buffer. This means that if surface positions exist for the VOI and at the same time the dose volume intersects that surface then the colour of the VOI surface can be replaced with the colour of the dose volume. In that case the colour value will be combined with the surface normal and the opacity value as calculated from the VOI surface. Basically the rendering pipeline must be modified on the colour accumulation level.

The dose mapping approach is a low cost processing action with very interesting optical results. Figure 6-9 illustrates a semi-transparent representation of the dose volume mixed with the VOIs. The right lung and spine (blue-grey structures) are exposed to the maximum allowed dose levels. The question is what is that level of exposure and where. The level of exposure can be verified using the dose volume histogram approach. However there is still the question of where this exposure takes place. The semi-transparent or the opaque view of the dose volume provides the user with limited information about the exact borders of the exposed region (b). This problem can be solved using the dose mapping approach. In Figure 6-9 (b) one can clearly see the region of the organ exposed

and also the level of the dose. The minimum dose level is defined from the selected iso-dose value. Although the dose mapping effect provides an overview of the dose distribution spread on the segmented volume surface no information are present about the dose distribution depth within the organ volume.

6.4.2.3 3D Visualization of the DVH

The term histogram is commonly used in image processing. The image histogram is used as information tool to provide a general description of the image contrast appearance. In a similar manner the dose volume histogram (DVH) provide a description of the radiation dose distribution over the VOIs and can graphically summarize large amounts of 3-D dose distribution information throughout the volume of the tumour or a normal anatomical structure [Drzym91]. The dose volume histogram curve is calculated for each volume of interest by performing a 3D analysis of the dose distribution within a segmented volume. This analysis involves the reappearance of each dose percentage within the volume under investigation. The DVH for a particular dose level ***Di*** can be defined as:

$$DVH(Di) = \left(Vol * \sum_{j=1}^{N_D} \delta_j \right) / N_D \qquad \text{Eq 6.15}$$

Where δ_j **= 0** if $D_j < D_i$ and δ_j **= 1** if $D_j > D_i$, and N_D the number of dose points within the volume of the VOI and ***Vol*** the total volume of the organ of interest.

For example if a dose level covers the complete organ volume then this dose level is marked with 100 % (see Figure 6-10). The DVH is probably the most regular tool for treatment plan evaluation and is proven that summarizes large volumes of dose-distribution data to allow rapid screening of rival plans. However the information provided by DVH graph are limited in two ways:

a. DVHs do not provide spatial information, such as the location of the high- and low-dose regions inside the VOI. In addition no information are provided for the actual organ volume and length under study.

b. There are algorithms that do not study the dose distribution relation of the organ volume within the treatment field. Instead the complete organ volume is used. This means that large organ volume will give low-risk DVH curve and vice versa.

Considering the above situations the information provided to the user by the DVH might be limited or wrong since it is never clear which part of the structures and the sizes receiving the dose distributions. Several authors worked in the direction of improving the quality and the amount of the DVH information. Niemerko et al. [Niemi94] developed the concept of dose-volume distribution (DVD) and the corresponding differential dose-volume distribution (dDVD) for treatment-plan evaluation. The dose-volume information inherent in the calculation points is used in the calculation of DVDs and dDVDs. An additional variant of the DVH the dose-surface histogram (DSH) [LuY95] and dose-wall histograms (DWH) [Meije99], have been proposed as a treatment-planning tool for hollow structures in prostate conformal therapy. For this walled hollow structures, such as the rectum and the bladder, estimation of the dose-surface is more biologically relevant than the dose to the volume. DVH estimation related with the spatial information of the dose distribution and the VOI information is presented by [Chee99]. Their concept is called the

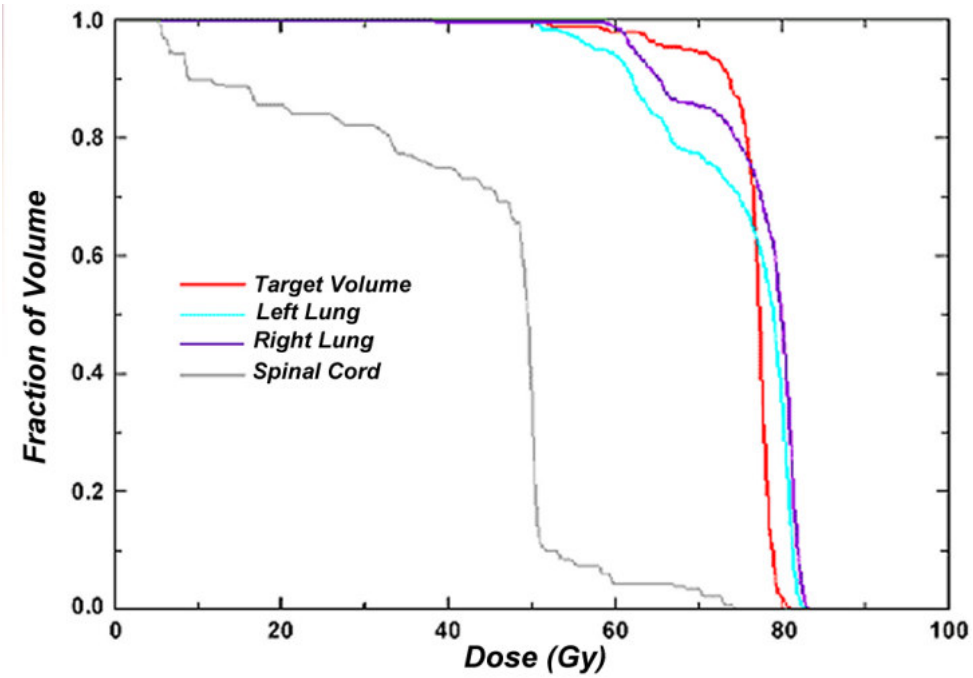

Figure 6-10. Illustration of a DVH over four different structures. One can have an overall appreciation of the dose distribution on the different organs. However any conclusion about the treatment is difficult to by taken because due to the luck of spatial information.

z-dependent dose-volume histogram (zDVH) and provides the spatial variation, as well as the size and magnitude of the different dose regions within the region of interest. Thus although DVH provides an average dose-volume information, zDVH provides differential dose-volume information with respect to the CT slice position.

An additional approach related with the DVH and the visualization of the dose distribution is presented in [Kessl94]. Their technique is presented for overcoming a major deficiency of histogram analysis in radiotherapy treatment planning which is the lack of spatial information. In their technique, histogram data and anatomic images are displayed in a side-by-side fashion. The histogram curve is used as a guide to interactively probe the nature of the corresponding 3-D dose distribution. Regions of dose that contribute to a specific dose bin or range of bins are interactively highlighted on the anatomic display, applied to 2D and 3D views as a window-style cursor is positioned along the dose-axis of the histogram display.

In this work we provide a unique graphical solution to that problem, aiming to create a 3D representation of the DVH. To achieve this we have to consider the definition of the DVH. What we are interested is to illustrate the dose distribution over the normal structures exclusively. This means that the rest of the dose volume must be excluded from the reconstruction scene in order to reduce the complexity of the view. When one uses voxel representation for the dose and the segmented organs can apply very easy this explicit operation during the ray traversing process at the sampling step i :

$$\mathrm{Voxel}_{\mathrm{Dose}}(\mathrm{C_i}, \mathrm{O_i}) = \begin{cases} voxel_{Dose}(C_i, O_i); & \text{if } voxel_{VOIs}(C_i, O_i) \neq 0 \\ 0; & \text{else} \end{cases} \qquad \text{Eq 6. 16}$$

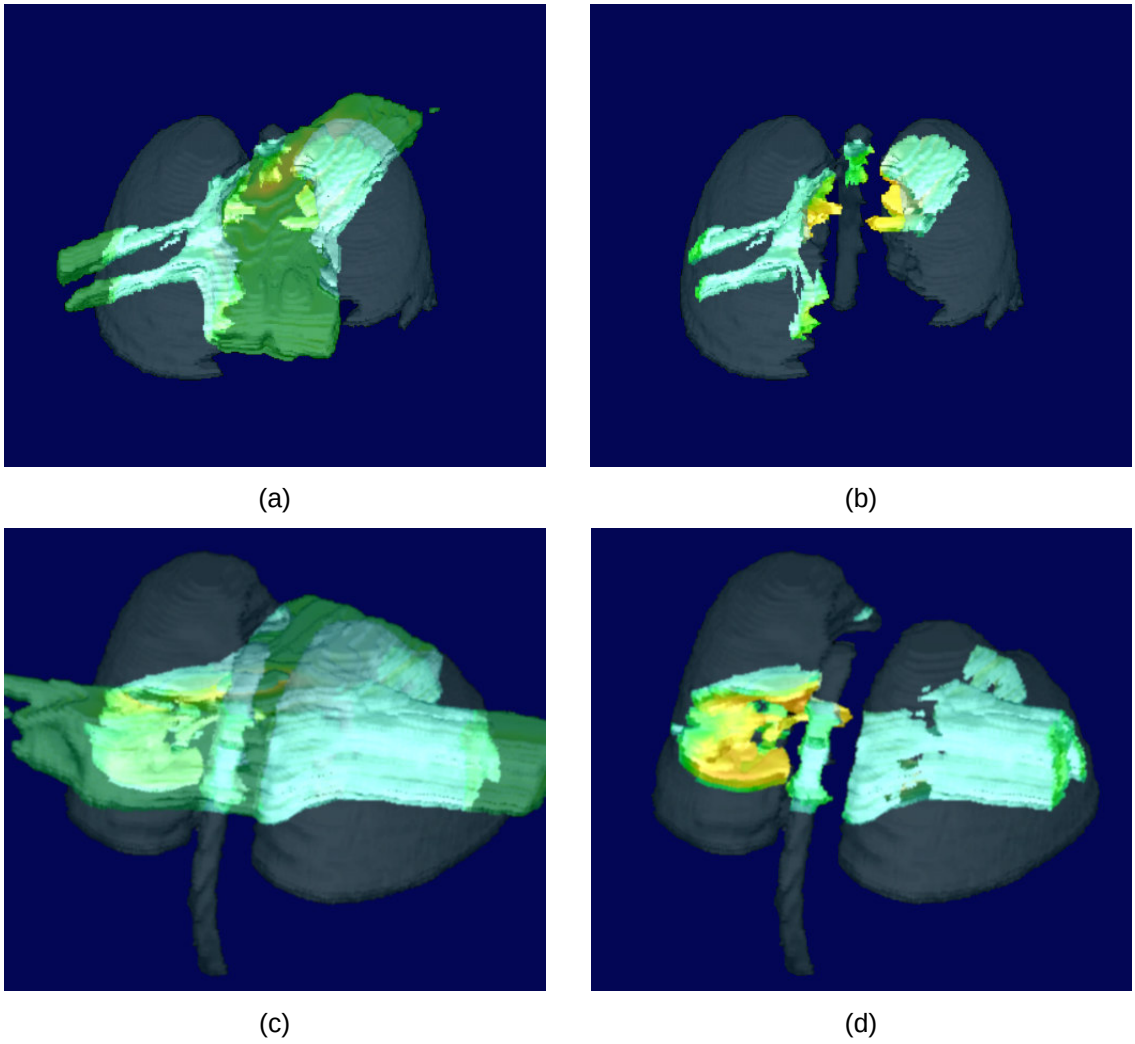

(a) (b)

(c) (d)

Figure 6-11. 3D representation of the DVH. On the left side mixture of the dose volume and segmented organs volume. On the right side the dose volume is reconstructed isolated in the organ volume.

The result of using the Eq 6. 16 will be the isolation of the dose volume within the segmented structure while performing the ray traversing. The next step we have to take is to illustrate the dose distribution within the internal of the structure. This assumes of course that the VOIs are transparent and we illustrate their internal. The volume mixing principle used here is the inclusive opacity. Critical locations for the reconstruction quality of the dose distribution remain the border of the VOI objects where the exclusivity rule is applied on the dose volume. At those locations the calculation of normal is crucial in order to provide smooth results. Basically we have to deal with two different occasions when estimating the normal or gradient estimation of the dose volume in this specific case:

a. Dose volume grid that is included inside the VOI. Here the normal estimation will be done considering only the dose volume.

b. Dose volume at the borders of the VOIs. Here the normal estimation will be done according to the voxels distribution of VOIs.

As in the previous reconstruction schemes also here the user can set interactively the level of the dose distribution under investigation.

The results of this approach are presented in Figure 6-11. In all reconstructed images the organs have been reconstructed with transparent surfaces and having the same colour among them. The images reconstructed with the standard INCOP approach (a and c) provide a more confusing visual result than the 3D DVH images (b and d). The reason is that several transparent object are involved in the same visual scene causing loss of the accurate depth information of the surfaces. As a result the observer's eye is obstructed from the main focus, which is the dose distribution inside the organ volume. When the dose volume isolation step is applied from Eq 6.15 the result is much more clear and one can notice the differences between the two approaches. This visual effect can be a superior qualitative tool for the dose distribution verification compared to the standard DVH method. The approach can be extremely useful for the verification of the spinal cord exposure on radiation dose. The reason is that the spinal cord is high-risk organ and the maximum allowed levels of exposure are also related with the spine length. The 3D reconstruction of the DVH demonstrates very clear the exposed volume and length of the spine.

6.4.3 Merging CT Volume and Dose Volume

In previous sections of this work we demonstrate the visual results when mixing the dose volume and the geometrically defined structures. This mixing approach is the most important graphical verification tool since the view of the segmented objects (VOIs) is enhanced and better appreciated in relation to the dose volume. The geometric definition of the anatomical structures is necessary for visualization and calculation purposes e.g. DVH and is done selectively by the user manually. However in several instances it may be sufficiently to appreciate the relation of the dose volume boundaries to the surrounding organs. In order to avoid the tedious manual organ segmentation process to generate anatomy model of the organ we could use the texture-based volume reconstruction of the anatomical data mixed directly with the dose volume. The reconstruction methods proposed for this task could involve the following alternatives:

a. direct dose mapping

b. selective and inclusive opacity

6.4.3.1 Direct dose mapping

In this approach we use the similar principle as in the dose volume mapping on the segmented organs. The ray sampling process accumulates the colour (texture) and the opacity values. If the opacity value has reached the maximum level, which is 1.0 then the accumulation process will be terminated and the corresponding colour $\boldsymbol{C_{CT}}$ and opacity $\boldsymbol{op_{CT}}$ value will be exported for the final pixel value $\boldsymbol{C_{out}}$ calculation Eq 6. 17. At this step, where the ray reached an opaque surface, the dose colour $\boldsymbol{C_{Dose}}$ value will be sampled if there is any. This colour value will be mixed with the texture colour value to create the final pixel colour using the linear intensity composition of the two colour:

$$C_{\text{out}} = \begin{cases} C_{Dose} * w + (1.0 - w) * C_{CT}; & \text{if } voxel_{Dose} \neq 0 \\ C_{CT} * opacity_{CT}; & \text{else} \end{cases} \qquad \text{Eq 6. 17}$$

The result of this approach can be seen in the Figure 6-12 and illustrate the dose mapping on the surface of the CT data surface. One can observe the locations where CT opacity is 0 no dose colour is assigned. In addition at locations where the surface is cloudy it is rather uncertain where to assign the dose mapping resulting into unclear visual results. However this method could be ideal when organ surfaces are clearly reconstructed and one wants to verify the level of dose exposure on the structure.

6.4.3.2 Selective and Inclusive Opacity

The second method employed in this work involves volume-mixing approach based on the inclusive opacity approach with a small variation; the opacity sampled from the CT data have higher priority than the dose opacity. Thus in case that no CT opacity is found no accumulation step will occur for the dose volume sampling. However if the CT opacity exists the voxel intensity value will be sampled considering the inclusive opacity. The method improves the visual result of the volume mixing in comparison to the direct dose mapping. The dose volume surface relation with the CT volume can be better appreciated and the intensity variations of the dose volume have smoother transitions since the volume continuity during reconstruction is preserved when CT opacity exists. In anatomical regions with low or zero opacity are dose volume will not be illustrated at all. This effect could be considered as positive if the observer is concentrated on the dose distribution on the opaque structures ignoring the less opaque giving a more clearly image. On the selective opacity approach could lead to wrong decision results since big regions of the dose volumes are not visualized. To over come this problem we sample both volumes using the standard inclusive opacity model where the complete dose volume will be reconstructed. The results of both approaches are presented in Figure 6-12.

6.5 Summary

Evaluating dose volume distribution information in the frame of a 3D-Simulation system is a new concept in the field of RTP. To achieve that a multi-volume methodology is required that will be able to handle several grid data volumes such as CT, segmented organs and dose distribution. First task is to register the different volumes and resample them to the highest resolution available. This step can take place as a pre-processing step using different interpolation algorithms. In this chapter common interpolation methods have been compared using different phantom data. The NN approach is rather inaccurate but fast. Although not reported it can be found even today in commercial radiotherapy applications. The interpolation results shown that LN interpolation can be suitable for the dose data interpolation. In practice most commercial system use this approach for illustrating dose distribution in 2D and 3D. More attractive and smoother results can be achieved using the B-Spline interpolation.

The second part of this chapter involves the visualization of dose information. Among several ways for visualizing dose volumes with medical data, volume rendering has been selected. Since volume rendering is the heart of a 3D-Simulation system we consider this solution closer to our architecture and demands. Thus a voxel-based approach could lead to the smooth integration of this visualization capability within a 3D-Simulation system or more general into a volume visualization package. In addition original CT information can

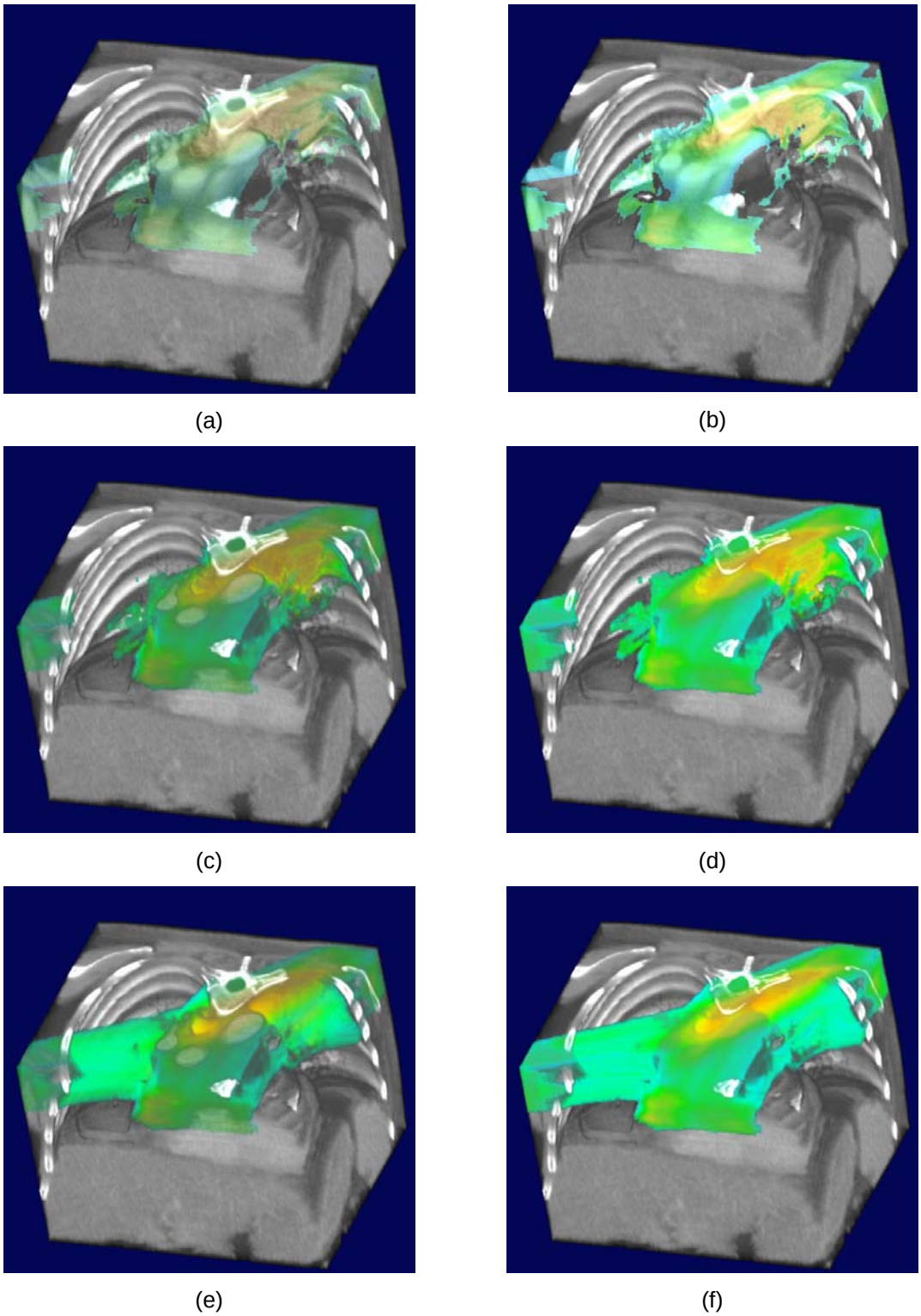

(a) (b)

(c) (d)

(e) (f)

Figure 6-12. Merging of CT and Dose volume. The first row (a, b) presents results based on the direct mapping of the dose values on the CT surface. On the second row (c, d) illustration of the CT and dose volumes using selective opacity with priority on the CT volume. On the last row (e, f) the two volumes are mixed including both their opacities.

be visualized at any step and combined with the dose volume creating images that represented effectively the clinical reality.

Here we presented various ways for visualizing of the dose volume information. Scope was to present efficient qualitative dose evaluation tools. Among others unique images are resented that can assist clinicians interpret the DVH information spatially with direct visual comparison of the VOIs. By integrating displays of 3-D doses and the corresponding histogram data, it is possible to recover the positional information inherently lost in the calculation of a histogram. Important questions such as the size and location of hot spots in normal tissues and cold spots within target volumes can be more easily uncovered, making the iterative improvement of treatment plans more efficient.

Chapter 7

Summary

3D-Simulation comprises two important key words, which recently have often been used to describe a technique for planning the application of radiotherapy without using conventional or in the absence of the actual patient. As an alternative to patient and X-ray simulator, 3D-Simulation uses 3D data set and a series of software tools for accurate planning and re-positioning of the patient. In this work we presented a number of tools of the accurate definition and localization of the tumor volume and further more the evaluation of treatment data and parameters. This chapter provides a summary of the contribution of this thesis in the field of 3D-Simulation. Several algorithms presented here, have been also integrated into 3D-Sim ***Exomio***. The clinical relevance and impact of ***Exomio*** in the treatment of different patient cancer cases can be found in [Zambo02], [Houst02], [Karan02], [Dicks03], [Stras04], [StraV04].

7.1 Segmentation of Anatomical Structures

Segmentation is the process that separates an image into its important features (primitives) so that each of them can be addressed separately. This converts the planar pixel of the image into a distinguishable number of individual organs or tumour that can be clearly identified and manipulated. The segmentation process might involve complicate structures and in this case usually only an expert can perform the task of the identification manually on a slice-by-slice base. Humans can perform this task using complex analysis of shape, intensity, position, texture, and proximity to surrounding structures.

In ***Chapter 3***, we discussed a daily clinical problem in the frame of 3D simulation and RTP; the accurate definition of anatomical structures in CT data. We present a number of computer-based tools that can assist the segmentation process during the 3D simulation process. The methods presented here are categorized to manual and semi-automatic methods. For the manual volume definition, we present a 3D interpolation method based on implicit functions. Due to the high order of continuity of the function, the interpolation scheme can reconstruct a surface from 3D sample points that describes very accurately several anatomical structures. The input samples can be at the form of parallel contours usually a product of contours defined on parallel imaging cross sections. Even more advanced is the capability of the algorithm to handle the non-parallel contours either perpendicular or even arbitrary placed relative to each other. This has been a new concept for radiotherapy imaging applications.

The conventional 2D segmentation tools on the axial cross sections have been for many years now the standard methods used. Advantages of the new concept is the flexibility and freedom given to the clinicians to investigate new ways of defining anatomical structures taking advantage of the full 3D information available on the multiplanar reconstructed slices such as sagittal and coronal, As a result the segmentation process improves in terms of accuracy. In addition, the time needed to segment structures can be

dramatically reduced since fewer contours are required to describe the shape of the structures.

We demonstrate that segmentation of the spine can be achieved very accurately, in a few seconds with minimum user interaction; the user needs only to define an initial starting point for the algorithm. The algorithm can automatically trace the spine path thought the complete volume of cross sections. False contours that are not correspond to the spine shape and position can be rejected automatically from the system and can be replaced with linear interpolated contours considering as key contours those already found by the system. The boundary-tracking methods used belong to the deterministic approaches and therefore there is tendency to produce misleading results under some circumstances. To reduce that effect data pre-processing and the gradient volume of the original CT data can be used as input to the segmentation routine.

7.2 Fast Smoothing of Superficial Respiration Artifacts in CT-Volumes

During CT data acquisition the normal breathing process, internal organ movements, and patient global movements might introduce motion artifacts in the acquired raw data. This motion may be in three dimensions and generally result in artifacts that appear as streaks or distorted semi-transparent structures in the general vicinity of the motion. During tumour irradiation the patient might be immobilized but the breathing process continues normally and freely. In diagnostic imaging it is required from the patient to stop breathing during acquisition to optimise image quality. However the irradiation process lasts more than one minute and therefore is it not possible for the patient to stop breathing. Considering the above it would be more accurate for a CT data acquisition that will be used for the RT planning to record most of organ movements that occur during normal patient conditions. The result of this acquisition will provide with useful information about the movements of specific organs that might be located near or attached on a tumour, and vice versa. This information could assist the more precise assignment of the field size and orientation that will be used to treat the tumour.

Our main interest in the work of ***Chapter 4*** reflects on the surface movements of the patient. Principally the surface of the patient can be visualized in 3D using voxel or polygon based techniques. Usually the polygon-based techniques are used since the body contours can be defined and modified if necessary from the user. Then triangulation techniques are used to generate a mesh out of the final planar contours. Based on the mesh surfaces several calculations can be performed accurately. In addition to communicate the body contour coordinates between different software systems in the radiotherapy department, the planar contour representation is used as standard geometric format. In radiotherapy it is a common understanding that inaccuracies on patient's body planar contours will lead to inaccurate calculations and analysis related to the patient's body surface since the planar contours are used for reconstructing the patient's surface model.

In ***Chapter 4*** a dedicated approach is presented for the compensation of the respiratory artifacts on medical body surfaces reconstructed from planar contours. The method can handle fast and efficiently several types of surfaces with respiratory artifacts that might include constant or arbitrary respiration frequencies. The user can define manually constrains on the angular or on the slice level. So far we cannot estimate how the proposed method will influence the results on the clinical environment. This is one part of our future work. In addition we investigate the development of a deformation model that will also compensate the movements of internal structures that deform during respiration.

7.3 Improved Volume Rendering of Thoracic CT-Volumes

In many radiation treatment-planning instances, a geometric model of a given anatomical structure is not necessary. Common examples are patients that will receive palliative treatment where no target volume is required. Patients with Hodgkin's disease are mostly treated with two mantel fields, typically from anterior to posterior direction (AP) and posterior to anterior (PA) isocentric beams. The field size and block beam apertures are designed directly on the DRR lack of and target volume and organ at risk. Similarly for patients with breast cancer, during whole breast treatment irradiation, the radiation field arrangement is performed based on the BEV. For the physician it is usually sufficient simply to appreciate the relationship of a target volume to surrounding normal organs. This might involve the visualization of the occlusion of several structures when viewed from a particular perspective. When the volume viewed from the BEV, perspective view, then the user can assess the potentially irradiated structures enclosed in the irradiation field superimposed. The alternative is to use the OEV, orthogonal reconstruction, where the radiation fields reconstructed as opaque or semitransparent polygons are projected with the original CT volume. An additional verification tool can be the use of the virtual light field that presents the intersection of the beam volume with treatment volume

Lungs and trachea belong to the category of the most important organs in the neck and thoracic region. Lung tissue is the one of the dose-limiting structures and it can be exposed in during irradiation of breast tumour, malignant lymphoma and intrathoracic tumours. On the other hand trachea is very often used as organ for orientating the physician during treatment planning of chest and neck tumours. Thus there is a vital importance on visualizing these structures in 3D in relation to neighbour anatomical volumes of the neck and chest region.

In ***Chapter 5*** we presented the utility of volume rendering reconstruction in the frame of the CT based 3D simulator of radiotherapy planning, focusing on the chest region. Volumetric surface representation of the critical organs in the above region, such as trachea and lungs, are essential to use as anatomical reference markers and to protect respectively. The mentioned anatomical structures must appear with optimum visibility on the reconstructed DRR along the complete 3D simulation process. The proposed method can be integrated in to the main rendering pipeline and requires minimum user interaction for adjusting the necessary parameters. Taking advantage of the volume rendering techniques that offer high quality visualization, we dramatically reduce user effort required for the segmentation of those anatomical structures.

One of the important components of our approach is the use of a binary volume map in order to address all voxels that belong to the air volume that surrounds the patient's body. This processing step is initialised and completed automatically at the data pre-processing level. Then air volume map is used during ray traversing to reject or accept the sampling voxels. The method can improve the visualization of the lungs and trachea surfaces compared to those reconstructed from planar contours. Also, the method can improve the reconstruction of the DRR enhancing the contrast of the subject structures making them applicable for clinical use. Finally by merging both visual information mentioned above we can produce unique images for clinical purpose extending the capabilities of the 3D simulation process and improving treatment planning outcome.

7.4 Efficient Treatment Dose Visualization in CT-Simulation

The dosimetric analysis is important in order to choose between a number of apparently radiation beams arrangements and to optimise the weighting of doses from a number of beams in a given arrangement. By appropriately weighted integrations of calculated doses over the volume of tumor and normal structures segmented from the CT data, dose volume histograms (DVH), estimates of tumor control probability (TCP) and normal tissue complication probabilities can be produced. The group of dose verification tools is completed with additional visual verification in two and three dimensions. The ability to make such calculations relies on the accurate definition of the 3D region of integration and dose volume grid resolution. Since the concept of CT simulation focus to reach physicians the qualitative evaluation of dose distribution is essential.

CT simulation offers high quality 3D images that are mostly used for the planning of the patient treatment. Important influence on producing these results has the high resolution CT volume used. The 3D visualization of all the necessary information combined, can be done interactively, which is of great benefit for the clinical routine. In combination to the above advantages the display of the treatment plan registered with the dose volume information produced from the TPS will further enhance the treatment verification process and the role of CT-simulation in the RTP process. In this chapter we will present a visualization workflow that described the complete dose display process within the CT-simulation environment.

Chapter 6 could be separated into two main parts: the dose resampling and dose visualization part. The first part involves the interpolation of the original dose volume data; a critical step when aiming to produce accurate calculation results as well as high quality 3D illustrations. The second part involves the mixed visualization between the dose and the CT-volume in two and three dimensions. Volume rendering is the vital component used for the implementation of the visualizations tools that will be presented, and aim to augment the qualitative verification of the dose distribution, the volumes of interest and the CT data.

Among several ways for visualizing dose volumes with medical data, volume rendering has been selected, which for our application is the heart of the 3D-Simulation system. Thus a voxel-based approach could lead to the smooth integration of this visualization capability within a CT-simulation system or more general into a volume visualization package. In addition original CT information can be visualized at any step and combined with the dose volume creating images that represented effectively the clinical reality. By integrating displays of 3-D doses and the corresponding histogram data, it is possible to recover the positional information inherently lost in the calculation of a histogram. As shown by the results qualitative display of information can answer important questions such as the size and location of hot spots in normal tissues and cold spots within target volumes. This concept makes the iterative improvement of treatment plans more efficient

7.5 Future Directions

Future directions of this work involve the continuation of part of the work done here as well as the investigation of new research directions in the frame of RTP. Future activities will involve:

Volume Segmentation: Volume segmentation is an issue where researchers invested many years of efforts. Until today, impressive results have been achieved on segmenting volumes in different application, but no global solution has been adapted, like for example in volume rendering. Radiation therapy is indeed a very demanding era in volume segmentation and definition. The reason for that can be the inconsistency of the CT acquisitions, as well as the variations of patient anatomy due to the disease or patient and organ movements. We believe that the need of further improved manual segmentation tools that can be applied at any image plane will be useful for several occasions in RTP. In addition easy-to-use editing tools can be of great importance. Further more efficient automatic tools can improve the segmentation performance of normal structures. However we believe that this can be achieved up to a number of organs and great influence to that will be the image quality of the imaging modalities.

Visualization Tools: Volume visualization is and will continue to be for long time the standards for 3D-Simulation and RTP. Verification procedures, like comparison of electronic portal images with the DRR, require the extraction of anatomical marks or regions from the 2D or 3D data. On this step volume rendering and 2D image processing could be involved. Further more the comparison of multiple dose trials is an essential component for completing the treatment plan evaluation step. We believe that volume rendering can provide interesting results towards this direction.

Treatment Position Verification: Verification of patient positioning is a vital process for efficient outcomes in radiation therapy. Currently electronic portal images are used for patient position evaluation. This is achieved after direct comparison with the DRRs. This approach based on 2D methods and thus it can be hard to control the position variations. New techniques are currently under development, which employ the use of 3D imaging directly in the treatment room. For this technique to get established volume visualization and registration techniques have to be investigated and proposed.

References

[AcqSim] http://www.medical.philips.com/main/products/ros/products/Acqsim/

[Agost01] S. Agostinelli, and F. Foppiano; ***A Prototype 3D CT extension for radiotherapy simulators***, Computerized Medical Imaging and Graphic, Vol: 25, pp:11-21, 2001

[Alast01] H. Alast, M.P. Petric, C.N. Catton, and P.R. Warde; ***Portal Imaging For Evaluation Of Daily On-Line Setup Errors And Off-Line Organ Motion During Conformal Irradiation Of Carcinoma Of The Prostate,*** Radiation Oncology Biol.Phys., Vol: 49, pp:869-884, 2001

[Ament98] N. Amenta, M. Bern, and M. Kamvysselis; ***A New Voronoi-Based Surface Reconstruction Algorithm,*** Computer Graphics, SIGGRAPH' 1998, pp: 415-421, 1998

[AMERSH] http://www,amershamhealth.com

[Aruga00] T. Aruga, J. Itami, M. Aruga, K. Nakajima et al.; ***Target Volume Definition For Upper Abdominal Irradiation Using CT Scans Obtained During Inhale And Exhale Phases***, Int. J. Radiation Oncology Biol. Phys., Vol: 48, pp:465-469, 2000

[Atari95] N. Atari, R. Zwicker, and R. Schmidt-Ullrich; . ***Performance evaluation of a prototype high resolution digital radiographic near real-time fluoroscopic computerized tomographic system for radiotherapy simulation***, Int. J. Radiation Oncology Biol. Phys., Vol: 32, pp:421-436, 1995

[Bajaj95] C. Bajaj, F. Bernardini, and G. Xu; ***Automatic Reconstruction of Surfaces and Scalar Field from 3D Scans***, Computer Graphics, SIGGRAPH' 1995, pp: 109-118, 1995

[Balta93] D. Baltas, K.M. Sievers, and B. Kober; ***Preliminary results of a intercomparison of quality control referring to therapy simulators***, ESTRO, Second Biennial Meeting on Physics in Clinical Radiotherapy. Prague 1993

[Bedfo98] J.L. Bedford, and G.S. Shentall; ***A Digital Method for Computing Target Margins in Radiotherapy,*** Med.Physics, Vol: 25, pp:224-231, 1998

[Behr00] J. Behr, S.M. Choi, S. Großkopf, H. Hong, S.A. Nam, Y. Peng, A. Hildebrand, M.H. Kim, and G. Sakas; ***Modeling, Visualization, and Interaction Techniques for Diagnosis and Treatment Planning in Cardiology,*** Computer & Graphics, Vol: 24, pp: 741-753, 2000

[Beier98] J. Beier, R.C. Bittner, N. Hosten, J. Troger, and R. Felix; ***Morphological Image Processing Operators: reduction of partial volume effects to improve 3D visualization based on CT data, Radiologie***, Vol: 38, pp:860-866, 1998

[Bel93] A. Bel, M.van Herk, H. Bartelink, and J.V. Lebesque; ***A Verification Procedure to Improve Patient Set-up Accuracy Using Portal Images,*** Radiother. Oncol., Vol: 29, pp:253-260, 1993

[Belsh97] R. Belshi, D. Pontvert, J.C. Rosenwald, and G. Gaboriaud; ***Automatic Three-dimensional Expansion of Structures Applied to Determination of the Clinical Target Volume in Conformal Radiotherapy***, Int. J. Radiation Oncology Biol. Phys., Vol: 37, pp:689-696, 1997

[Bergm95] L.D. Bergman, B.E. Rogowitz, and L.A. Treinish; ***A Rule-based Tool for Assisting Colormap Selection***, In Proceedings of 5th IEEE Visualization Conference, pp:118-124, 1995

[Beyer00] T. Beyer, D.W. Townsend, T. Brun, et al; ***A Combined PET/CT scanner for Clinical oncology***, Journal of Nuclear Medicine, Vol: 41, pp: 1369-1379, 2000

[Bhale00] A. Bhalerao, H. Pfister, M. Halle, and R. Kikinis; ***Fast Re-Rendering Of Volume And Surface Graphics By Depth, Colour and Opacity Buffering***, Medical Image Analysis, Vol:4, pp:235-251, 2000

[Blake98] A. Blake, and M. Isard; ***Active Contours: The Application of Techniques from Graphics, Vision, Control Theory and Statistics to Visual Tracking of Shapes in Motion.*** Springer-Verlag, London, 1998

[Boer01] J.C.J. de Boer, and B.J.M. Heijmen ; ***A Protocol for the Reduction of Systematic Patient Setup Errors with Minimal Portal Imaging Workload,*** Int.J. Radiation Oncology Biol. Phys, Vol: 50, pp: 1350-1365, 2001

[Boer02] J.C.J. de Boer, and B.J.M. Heijmen ; ***A New Approach to Off-Line Setup Corrections: Combining Safety with Minimum Workload,*** Medical Physics, Vol: 29, pp: 1998-2012, 2002

[Boiss88] J. Boissonat; ***Shape Reconstruction from Planar Cross Sections***, Computer Vision, Graphics and Image Processing, Vol: 44, pp:1-29, 1988

[Bolle03] M.A. Bollet, H.A. McNair, V.N. Hansen et al; ***Can Digitally Reconstructed Radiographs (DRRs) Replace Simulation Films in Prostate Cancer Conformal Radiotherapy?,*** Int. J. Radiation Oncology Biol. Phys., Vol: 57, pp:1122-1130, 2003

[Books89] F. L. Bookstein, ***Principal Warps: Thin Plate Splines and the Decomposition of Deformations,*** IEEE Transactions on Pattern Analysis and Machine Intelligence, Vol: 11, pp:567-585, 1989

[Brown97] M.S. Brown, M.F. McNitt-Gray, N.J. Mankovich, J.G. Goldin, J. Hiller, and L.S. Wilson D.R. Aberle; ***Method for Segmeting Chest CT Image Data Using an Anatomical Model: Preliminary Results***, IEEE Trans. On Medical Imaging, Vol: 16, pp: 828-839, 1997

[Butke96] E.K. Butker, D.J. Helton, J.W. Keller, L.L. Hughes, T. Crenshaw, and L.W. Davis; ***A Totally Integrated Simulation Technique for Three Field Breast Treatment Using a CT Simulator, Med. Phys.***, Vol: 23, pp: 1809-1814,1996

[CaiJ99] J. Cai, J.C. Chu, D. Recine et al; ***CT and PET lung Image Registration and Fusion in Radiotherapy Treatment Planning Using the Chamfer-Matching Method***, Int. J. Radiation Oncology Biol. Phys., Vol: 43, pp:883-891, 1999

[Cai98] W. Cai, and G. Sakas; **Maximum intensity projection using splatting in sheared object space.** In Proceedings EUROGRAPHICS '98, pp: 113-124, 1998

[Cai99] W. Cai; ***Transfer functions in DRR volume rendering***, In Proceedings of Computer Assisted Radiology and Surgery, CARS'99, Paris, France, 1999

[CaiSa99] W. Cai, and G. Sakas; ***Data Intermixing and Multi-Volume Rendering***, In Proceedings of Eurographics'99, Vol:18, 1999

[Caldw03] C.B. Caldwell, K. Mah, M. Skinner et al; ***Can PET Provide the Extend of Tumor Motion for Individualized Internal Target Volumes? A Phantom Study of The Limitations of CT and Promise of PET***, Int. J. Radiation Oncology Biol. Phys., Vol: 55, pp: 1381-1393, 2003

[Carr01] J.C. Carr, T.J. Mitchell, R.K. Beatson, J.B. Cherrie, W.R. Fright, B.C. McCallumm and T.R. Evans; ***Reconstruction and representation of 3D Objects with Radial Basis Functions***, Computer Graphics, SIGGRAPH' 2001, pp: 67-76, 2001

[Carr97] J.C. Carr, W.R. Fright, and R.K. Beatson; ***Surface Interpolation with Radial Basis Functions for Medical Imaging***, **'** IEEE Trans. Medical Imaging, Vol: 16, pp:96-107, 1997

[Carr98] J.C. Carr, A.H. Gee, R.W. Prager, and K.J. Dalton; ***Quantitative Visualization Of Surfaces From Volumetric Data***, Proceedings Of WSGC'98 - The Sixth International Conference In Central Europe On Computer Graphics And Visualization, Pilzen, Czech Republic, Vol:1, pp:57-64, 1998

[Castr98] S. Castro, A. König, H. Löffelmann, E. Gröller; ***Transfer Function Specification For The Visualization Of Medical Data***, Technical Report TR-186-2-98-12, Institute of Computer Graphics and Algorithms, Vienna University of Technology, 1998

[Cehri91] M.A. Cehring, T.R. Mackie, S.S. Kubsad, B.R. Paliwal, M.P. Mehta, and T.J. Kinsella; ***A Three-Dimensional Volume Visualization Package Applied To Stereotactic Radiosurgery Treatment Planning***, Int. J. Radiation Oncology Biol. Phys., Vol:21, pp:491 -500, 1991

[Chala97] V. Chalana, Y. Kim; ***A Methodology for Evaluation of Boundary Detection Algorithms on Medical Images,*** IEEE Trans.On Medical Imaging, Vol:16, pp:642-652, 1997

[Chee99] C. Chee-Wai, and D.J. Indra; ***Treatment Plan Evaluation Using Dose-Volume Histogram (DVH) and Spatial Dose-Volume Histogram (zDVH)***, Int. J. Radiation Oncology Biol. Phys., Vol: 43, pp:1143-1150, 1999

[Chen96] G.T.Y. Chen, C.A. Pelizzari, and S. Vijayakumar; ***Imaging: The Basis for Effective Therapy***, Front Radiat Ther Oncol, Vol: 29, pp:31-42, 1996

[Cho98] P. S. Cho, K. L. Lindsley, J. G. Douglas, K. J. Stelzer, and T. W. Griffin; ***Digital Radiotherapy Simulator***, Computerized Medical Imaging and Graphic, Vol: 22, pp:1-7, 1998

[Cohen01] E. Cohen, R.F. Riesenfeld, and G. Elber; ***Geometric Modeling with Splines: An Introduction,*** A.K. Peters Ltd, 2001

[Conw97] J. Conway, and M.H. Robinson; ***CT Virtual Simulation***, British Journal of Radiology, Vol: 70, pp:106-118, 1997

[Crawf96] C. Crawford, K. King, C. Ritchie, and D. Dodwin; ***Respiratory Compensation in Projection Imaging Using a Magnification and Displacement Model***, IEEE Trans. On Medical Imaging, Vol: 15, pp: 327-332, 1996

[Culli93] T.J. Cullip, J.R. Symon, J.G. Rosenman, and E.L. Chaney; ***Digitally Reconstructed Fluoroscopy And Other Interactive Volume Visualizations In 3-D Treatment Planning***, Int. J. Radiation Oncology Biol. Phys., Vol:27, pp:145-151, 1993

[DasCh98] I.J. Das, E.C. Cheng, G. Freedman, and B. Fowble; ***Lung And Heart Volume Analyses With CT Simulator In Radiation Treatment Of Breast Cancer***, Int. J. Radiation Oncology Biol. Phys., Vol:42, pp:11-19, 1998

[Dawso98] L.A. Dawson, K. Mah, E. Franssen, and G. Morton; ***Target Position Variability Throughout Prostate Radiotherapy***, Int. J. Radiation Oncology Biol. Phys., Vol: 42, pp:1155-1161, 1998

[Dehm99] J. Dehmeshki; ***An Adaptive Segmentation and 3-D Visualisation of the Lungs***, Pattern Recognition Letters, Vol: 20, pp:919-926, 1999

[Desbr99] M. Desbrun, M. Meyer, P. Schröder, and A.H. Barr; ***Implicit Fairing Of Irregular Meshes Using Diffusion And Curvature Flow***, Computer Graphics, SIGGRAPH' 99, pp: 317-324, 1999

[Dicks03] S. Dickson, G. Lawrence, D. Parr, and G. Lambert; ***CT Simulation in a Large Department Using SOMATOM Emotion Duo Scanner***, Electromedica, Vol: 71, pp:28-35, 2003

[Donov00] E. Donovan, U. Johnson, G. Shentali, P.M. Evans, A.J. Neal, and J.R. Yarnold; ***Evaluation Of Compensation In Breast Radiotherapy: A Planning Study Using Multiple Static Fields***, Radiation Oncology Biol.Phys, Vol: 46, pp:671-679, 2000.

[Drebi88] R.A. Drebin, L. Carpenter, and P. Hanrahan; ***Volume Rendering***, Computer Graphics, SIGGRAPH 1988, pp: 65-74, 1988

[Drzym91] R.E. Drzymala, R. Mohan, L. Brewster, J. Chu, M. Goitein, W. Harms, and M. Urie; ***Dose-Volume Histograms***, Int. J. Radiation Oncology Biol. Phys., Vol: 21, pp: 71-78, 1991

[EdWon02] G. K. Edmundson, J. Wong, D. Yan, D. Lockman, D. Brabbins ***et al.***; ***Adaptive Radiation Therapy [ART] for Prostate Cancer at William Beaumont Hospital***, In Progress in CT-3D Simulation, 1rst Exomio User Meeting, Lemessos-Cyprus, November, 2002

[Encar96] J. L. Encarnação, W. Straßer, R. Klein; ***Graphische Datenverarbeitung II. Modellierung komplexer Objekte und photorealistische Bilderzeugung*** In: Oldenbourg Verlag, ISBN 3-486-23469-2, 1996

[Encar01] J. L. Encarnação, In: Earnshaw, Rae A. et al.; ***Challenges and Frontiers of Computer Graphics: A Vision for an Applied Research Agenda***, Frontiers of Human-Centred Computing, Online Communities and Virtual Environments, London, Berlin, Heidelberg: Springer-Verlag, pp: 367–393, 2001

[Encar03] J. L. Encarnação and P. Blachetta; ***Entwicklung der Graphischen Datenverarbeitung seit 1975,*** Die Darmstädter, deutsche und europäische Sicht - insbesondere gesehen durch die Printmedien Darmstadt: INI- GraphicsNet-Stiftung, 2003

[Exomio] http://www.igd.fhg.de/www/igd-a7/pro/Exomio/EXOMIO.html

[Elbak02] A. Elbakri, and J.A. Fessler; ***Statistical Image Reconstruction for Polyenergetic X-Ray Computed Tomography***, IEEE Trans. Medical Imaging, Vol: 21, pp: 89-99, 2002

[FangB98] S. Fang, T. Biddlecome, and M. Tuceryan; ***Image-Based Transfer Function For Data Exploration In Volume Visualization***, In Proceedings of IEEE Visualization'98, pp: 319-316, 1998

[FocalS] http://www.cms-stl.com/

[Fraas98] B.A. Fraass, K.L. Lash, G.M. Matrone et al.; ***The Impact of Treatment Complexity and Computer-Control delivery Technology on Treatment Delivery Errors***, Int.J. Radiation Oncology Biol.Phys., Vol: 42, pp:651-659, 1998

[Galvi95] J.M. Galvin, C. Sims, G. Dominiak, and J. Cooper; ***The Use Of Digitally Reconstructed Radiographs For Three-Dimensional Treatment Planning And CT-Simulation,*** Radiation Oncology Biol.Phys, Vol: 31, pp: 935-942F, 1995

[GE] http://www.ge.com

[Gehri91] M.A. Gehring, T.R. Mackie, S.S. Kubsad, B.R. Paliwal, M.P. Mehta, and T.J. Kinsella; ***A Three-Dimensional Volume Visualization Package Applied To Stereotactic Radiosurgery Treatment Planning*****,** Radiation Oncology Biol.Phys, Vol: 21, pp: 491-500, 1991

[Geets04] X. Geets, J-F. Daisne, V. Gregoire, M. Hamoir, and M. Lonneux; ***Role of 11-C-Methionine Positron Emission Tomography for the Delineation of the Tumor Volume in Pharyngo-Laryngeal Squamous Cell Carcinoma: Comparison with FDG-PET and CT,*** Radiotherapy & Oncology, Vol: 71, pp:267-273, 2004

[Geige93] B. Geiger; ***Three-dimensional modeling of human organs and its application to diagnosis and surgical planning***, PhD Thesis, Ecole des Mines de Paris, 1993

[Gerst99] N. Gerstner, S. Wachter, T.H. Knocke, C. Fellner, A. Wambersie, and R. Pötter; ***The Benefit of beam's Eye View based 3D Treatment Planning for Cervical Cancer***, Radiotherapy and Oncology, Vol: 51, pp: 71-78, 1999

[GibsM98] S. Gibson; ***Constrained Elastic Surface nets: generating smooth surfaces from binary segmented data,*** In Proceedings of Medical Image Computing and Computer Assisted Interventions (MICCAI), W.M. Wells, A. Colchester, and S. Delp, eds., Lecture Notes in Computer Science 1496, Spinger-Verlag, pp. 888-898, 1998

[Gibso98] S. Gibson; ***Using Distance Maps For Accurate Surface Representation In Sampled Volumes,*** In Proceedings of the Symposium on Volume Visualization, ACM SIGGRAPH, pp. 23-30, 1998

[Gibso97] S. Gibson, and A. Mirtich; ***A Survey of Deformable Modeling in Computer Graphics***, Technical Report TR97-19, MERL Technical Report, 1997

[Gordo94] D. Gordon, M.A. Peterson, and R.A. Reynolds; ***Fast polygon Scan Conversion With Medical Applications***, IEEE Computer Graphics and Application, Vol: 14, pp: 20-27, 1994

[Grees00] H. Greess, A. Nömayr, B. Tomandl, M. Blank, M. Lell, M. Lenz, and W.A. Bautz; ***2D and 3D Visualisation of Head and Neck Tumours from Spiral-CT Data***, European Journal of Radiotherapy, Vol: 33, pp: 170-177,2000

[Gripp99] S. Gripp, R. Doeker, M. Glag, P. Vogelsang, et al.; ***The Role of CT Simulation in Whole-Brain Irradiation***, Int. J. Radiation Oncology Biol. Phys., Vol: 45, pp:1081-1088, 1999

[Gross98] S. Grosskopf, S.Y. Park, and M.H. Kim; ***Segmentation of Ultrasonic Images by Application of Active Contour Models***, In Proceedings CARS 1998, Computer Assisted Radiology and Surgery, Tokyo, Japan, pp: 871-877, 1998

[Gross02] S. Grosskopf, J.L. Encarnação (Referent); G. Sakas (Referent); **Realitätsnahe Modellierung und Visualisierung dynamischer medizinischer Bilddaten mittels aktiver Konturen, aktiver Regionen und deformierbarer Modelle**, Darmstadt, Techn. Univ., Diss., 2002

[Haral85] M. Haralick, and G. Shapiro; ***Image segmentation techniques***, Comput. Vis. Graph. Im. Proc., Vol: 29, pp: 100-132, 1985

[HeHoK96] T. He, L. Hong, A. Kaufman, and H. Pfister; ***Generation Of Transfer Function With Stochastic Search Techniques***, In Proceedings of IEEE Visualization, 1996

[Herma01] M.G. Herman, J.M. Balter, D.A. Jaffray et al.; ***Clinical use of Electronic Portal Imaging: Report of AAPM Radiation Therapy Committee Tak Group 58,*** Medical Physics, Vol: 28, pp:712-737, 2001

[Heusc99] D.J. Heuscer, M. Vembar; ***Redused Partial Volume Artifacts using Computed Tomography and an Interpolator*****,** Medical Physics, Vol: 26, pp:276-286, 1999

[Höhne90] K.H. Höhne, M. Bomans, A. Pommert, et al.; ***3D Visualization Of Tomographic Volume Data Using The Generalized Voxel Model***, The Visual Computer, Vol:6, pp:28-36, 1990

[Hoppe92] H. Hoppe, T. DeRose, T. Duchamp, J. McDonald, and W. Stuetzle; ***Surface Reconstruction from Unorganised Points***, Computer Graphics, SIGGRAPH' 1992, pp: 71-78, 1992

[Houst02] M. Houston, A. Gribbin, and M. Maher; ***Virtual Simulation: Breast, Pelvic and Head & Neck Cancers***, In Progress in CT-3D Simulation, 1rst Exomio User Meeting, Lemessos-Cyprus, November, 2002

[Hu01] S. Hu, E.A. Hoffman, and J.M. Reinhardt; ***Automatic Lung Segmentation for Accurate Quantitation of Volumetric X-Ray CT Images***, IEEE Trans. On Medical Imaging***,*** Vol: 20, pp:490-498, 2001

[Humm95] J.L. Humm, D. Pizzuto, E. Fleischman, and R. Mohan; ***Collision Detection and Avoidance During Treatment Planning***, ***Int. J. Radiation Oncology Biol. Phys.***, Vol: 33, pp:1101-1108, 1995

[Hurkm01] C.W. Hurkmans, J.H. Borger, B.R. Pieters, N.S. Russell, E.P.M. Jansen, and B.J. Mijnheer; ***Variability in Target Volume Delineation on CT Scans of the Breast***, Int. J. Radiation Oncology Biol. Phys., Vol: 50, pp:1366-1372, 2001

[Kalen01] W.A. Kalender; ***Computed Tomography: Fundamentals, System Technology, Image Quality, Applications,*** Wiley & Sons, New York, 2001

[Kalet97] I.J. Kalet; ***Designing Radiotherapy Software Components and Systems that will work together***, Seminars in Radiation Oncology, Vol: 7, pp:11-20, 1997

[Karan01] G. Karangelis, N. Zamboglou, G. Sakas, and D. Baltas; ***EXOMIO: A 3D Simulator for External Beam Radiotherapy***, International Workshop on Volume Graphics, Stony Brook, New York, 2001

[Karan02] G. Karangelis, N. Zamboglou; ***Evaluation of Patient Treatment Setup in Exomio Using Digital Portal Images***, In Progress in CT-3D Simulation, 1rst Exomio User Meeting, Lemessos-Cyprus, November, 2002

[Kass87] M. Kass, A. Witkin, and D. Terzopoulos; ***Snakes: Active Contour Models***, IEEE First Int. Conf. Comput. Vision, pp: 259-268, 1987

[Kessl94] M.L. Kessler, R.K. Ten Haken, B.A. Fraass, and D.L. McShan; ***Expanding the Use and Effectiveness of Dose-Volume Histograms for 3D Treatment Planning. I: Integration of 3D Dose-Display.*** Int. J. Radiation Oncology Biol. Phys., Vol: 29, pp:1125-1131, 1994

[Kessl95] M.L. Kessler, D.L. McShan, and B.A. Fraass; ***A Computer-Controlled Conformal Radiotherapy System. III: Graphical Simulation And Monitoring Of Treatment Delivery***, Radiation Oncology Biol.Phys, Vol: 33, pp:1173-1180, 1995

[Ketti97] C.H. Ketting, M.A. Seymour, I. Kalet et al.; ***Automated Planning Target Volume Generation: An Evaluation Pitting A Computer-Based Tool Against Human Experts***, Int. J. Radiation Oncology Biol. Phys., Vol: 37, pp:697-704, 1997

[Khoo97] V.S. Khoo, D.P. Dearnaley, and Finnigan D.J.; ***Magnetic Resonance Imaging (MRI): Considerations and Applications in Radiotherapy Treatment Planning***; Radiotherapy and Oncology, Vol:42, pp:1-15, 1997

[Khoo98] V.S. Khoo, J.L. Bedford, S. Webb, and D.P. Dearnaley; ***Comparison of 2D and 3D Algorithms for Adding a Margin to the Gross Tumor Volume in the Conformal Radiotherapy Planning of Prostate Cancer***; Int. J. Radiation Oncology Biol. Phys., Vol: 42, pp:673-679, 1998

[Killo01] H.J. Killoran, H.E. Baldini, J.C. Beard, and L. Chin; ***A Technique for Optimization of Digitally Reconstructed Radiographs of the Chest in Virtual Simulation***, Int. J. Radiation Oncology Biol. Phys., Vol:49, pp:231-239, 2001

[Kobbe98] L. Kobbelt, S. Campagna, J. Vorsaiz, and H.P. Seidel; ***Interactive Multi-Resolution Modeling on Arbitrary Meshes***, Computer Graphics, SIGGRAPH'98, pp: 105-114, 1998

[Kolot99] C. Kolotas, D. Baltas, and N. Zamboglou; ***CT-Based interstitial HDR brachytherapy,*** Strahlenther Onkol., Vol: 175, pp: 419-27, 1999

[Kuszy95] B.S. Kuszyk, D.R. Ney, and E.K. Fishman; ***The Current State of the Art in Three Dimensional Oncologic Imaging: An Overview***, Int. J. Radiation Oncology Biol. Phys., Vol:33, pp:1029-1039, 1995

[Kwa98] S.L. Kwa, J.C. Theuws, and M. Van Herk; ***Automatic three-dimensional Matching of CT-SPECT and CT-CT to Localize Lung Damage After Radiotherapy***, J. of Nuclear Medicine, Vol: 39, pp:1074-1080, 1998

[Lange01] K. Langen, and D. Jones; ***Organ Motion and its Management,*** Int. J. Radiation Oncology Biol. Phys., Vol: 50, pp: 265-278, 2001

[Laure94] P.J. Laurent, A.Le Mehaute, and L.L. Schumaker; ***Curves and Surfaces in Geometric Design,*** A.K. Peters Ltd, 1994

[Lee97] S. Lee, G. Wolberg, and S.Y. Shin; ***Scattered Data Interpolation With Multilevel B-Splines***, IEEE Transactions On Visualization And Computer Graphics, Vol:3, pp:228-244, 1997

[Lee99] J.S. Lee, A.B. Jani, C.A. Pelizzari et al.; ***Volumetric Visualization Of Head And Neck CT Data For Treatment Planning***, Int. J. Radiation Oncology Biol. Phys., Vol:44, pp:693-703, 1999

[LeFuP90] M. Levoy, H. Fuchs, S,M. Pizer, et al.; ***Volume Rendering In Radiation Treatment Planning***, First Conference On Visualization In Biomedical Computing, pp:4-10, 1990

[LevoA90] M. Levoy; ***Efficient Ray Tracing Of Volume Data***, ACM Transactions On Graphics***,*** Vol: 9, pp:245-261,1990

[LevoB90] M. Levoy; ***Volume Rendering By Adaptive Refinement***, The Visual Computer, Vol: 6, pp:2-7, 1990

[Levoy88] M. Levoy; ***Display of Surface from Volume Ddata***, IEEE ***Computer*** Graphics & Applications, Vol: 8, pp:29-37, 1988

[Levoy90] M. Levoy; ***A Hybrid Ray For Rendering Polygon and Volume Data***, IEEE Computer Graphics And Applications, Vol:10, pp:33-40, 1990

[Lien84] S. Lien, and T. Kajiya; ***A Symbolic Method For Calculating The Integral Properties Of Arbitrary Nonconvex Polyhedra***, IEEE Computer Graphics And Applications, Vol:4, 1984.

[Liu01] X. Liu, H. Bao, P. Heng, T.T. Wong, and Q. Peng; ***Constrained Fairing for Meshes***, Computer Graphics, Vol: 20, pp:115-123, 2001

[Loren87] W. Lorenson, and E.C. Harvey; ***Marching Cubes: A High Resolution 3-D Surface Construction Algorithm,*** Computer Graphics, SIGGRAPH'87, pp: 163-169, 1987

[LuH99] H.M. Lu, and L. Chin; ***Virtual Light Field Projection for CT-Simulation***, Med. Phys., Vol: 26, pp:1222-1229, 1999

[LuY95] Y. Lu, S. Li, D. Spelbring, P. Song, S. Vijayakumar, C. Pelizzari, and G. Chen; ***Dose-surface histograms as a treatment planning tool for prostate conformal therapy***, Med. Phys., Vol: 22, pp:279-284, 1995

[Maise02] M.N. Maisey; ***Overview of Clinical PET***, British Journal of Radiology, Vol: 75, pp: 1-5, 2002

[McIne96] T. McInerney, and D. Terzopoulos; ***Deformable Models in Medical Image Analysis: A Survey***, Medical Image Analysis, Vol: 1, pp: 91-108, 1996

[Masut96] Y. Masutani, K. Masamune, and T. Dohi; ***Region-Growing based Feature Extraction Algorithm for Tree-like Objects***, In Lecture Notes in Computer Science, K.H. Höhne and R.Kikinis Berlin, Germany :Springer Verlag, Vol: 1131, pp:161-171, 1996

[Max95] N. Max; ***Optical Models For Direct Volume Rendering***, IEEE Transactions On Visualization And Computer Graphics, Vol: 1, pp:99-108, 1995

[McJur01] M. McJury, P.M. Fisher, S. Pledge et al.; ***The Impact of Virtual Simulation in Palliative Radiotherapy for non-small-cell Lung Cancer***, Radiotherapy and Oncology, Vol: 59, pp:311-318, 2001

[Mcken00] A.L. McKenzie, M.V. Herk, and B. Mijnheer; ***The Width of Margins in Radiotherapy Treatment Plans***, Phys.Med.Biol., Vol: 45, pp:3331-3342, 2000

[Meyer92] D. Meyers, S. Skinner, and K. Sloan; ***Surfaces from contours***, ACM Transactions On Graphics, Vol: 11, pp: 228-258, 1992

[Meyer96] J.L. Meyers, J.S. Purdy; ***3D Conformal Radiotherapy,*** Frontiers in Radiotherapy and Oncology, Basel, Vol: 29, 1996

[Micha96] J.M. Michalski, J.A. Purdy, W. Harms, and J.W. Matthews; ***The CT-Simulation 3D Treatment Planning Process***, Front Radiat Ther Oncol, Vol: 29, pp:43-56, 1996

[Mihaj99] Z. Mihajlovic, and A. Coluban; ***The B-Spine Interpolation in Visualization*****,** Journal of Computing and Information – CIT 7, Vol:3, pp:245-253, 1999

[Mock99] U. Mock, K. Dieckmann, U. Wolff, T.H. Knocke, and R. Pötter; ***Portal Imaging Based Definition Of The Planning Target Volume During Pelvic Irra-***

diation For Gynecological Malignancies, Radiation Oncology Biol.Phys, Vol: 45, pp:227-232, 1999

[Mölle97] T. Möller, R. Machiraju, K. Mueller, and R. Yagel; ***Evaluation And Design Of Filters Using A Taylor Series Expansion,*** IEEE Transactions On Visualization And Computer Graphics Vol: 3, pp:184-199, 1997

[Morse01] B.S. Morse, T.S. Yoo, P. Rheingans, D.T. Chen, and K.R. Subramanian; ***Interpolating Implicit Surfaces from Scattered Surface Data Using Compactly Supported Radial Basis Functions***, In Proceedings of International Conference on Shape Modelling and Applications. IEEE Computer Society Press, pp: 89-98, 2001

[MorzK00] L. Mroz, A. König, and E. Gröller; **Maximum intensity projection at warp speed, *Computers & Graphics***, Vol: 24, pp: 343-352, 2000

[MorzH00] L. Mroz, H. Hauser, and E. Gröller; **Interactive high-quality maximum intensity projection,** In Proceedings of EUROGRAPHICS' 00, pp: 341-350, 2000

[Nagat90] Y. Nagata, T. Nishidai, M. Abe, et al.; ***CT Simulator: A New 3-D Planning and Simulating System for Radiotherapy: Part 2. Clinical Application***, Int. J. Radiation Oncology Biol. Phys., Vol: 18, pp:505-513, 1990

[Niels93] G.M. Nielson; ***Scattered Data Modeling***, IEEE Computer Graphics & Applications, Vol: 13, pp: 60-70, 1993

[Niemi94] A. Niemierko, and M. Goitein; ***Dose volume distributions: a new approach to dose-volume histograms in three dimensional treatment planning***, Med. Phys., Vol: 21, pp:3-11, 1994

[Nishi90] T. Nishidai, Y. Nagata, M. Takahashi, et al.; ***CT Simulator: A New 3-D Planning and Simulating System for Radiotherapy: Part 1. Description of System***, Int. J. Radiation Oncology Biol. Phys., Vol: 18, pp:499-504, 1990

[O'Doh02] M.J. O'Doherty, E.A. Macdonald, S.F. Barrington, N.G. Mikhaeel, and S. Schey; ***PET in the Management of Lymphomas***, Clinical Oncology, Vol: 14, pp: 415-426, 2002

[Ohtak01] Y. Ohtake, A. Belyaev, and I. Bogaevski; ***Mesh Regularization and Adaptive Smoothing***, Computer-Aided Design, Vol: 33, pp: 789-800, 2001

[Olien93] J. Oliensis; ***Local Reproducible Smoothing Without Shrinkage***, IEEE Trans. on Pattern Analysis and Machine Intelligence, Vol: 15, pp: 307-312, 1993

[Pavlid90] T. Pavlidis, and Y.Tay Liow; ***Integrating Region Growing and Edge Detection***, IEEE Trans. on Pattern Analysis and Machine Intelligence, Vol: 12, pp: 225-233, 1990

[Payne94] B.A. Payne, and A.W. Toga; ***Surface Reconstruction By Multiaxial Triangulation***, IEEE Computer Graphics and Applications, Vol: 14, pp:28-35, 1994

[Pekar04] V. Pekar, T.R. McNutt, and M. R. Kaus; ***Automated Model-based Organ Delineation for Radiotherapy Planning in Prostatic Region***, Int. J. Radiation Oncology Biol. Phys., Vol: 60, pp:973-980, 2004

[Peliz96] C.A. Pelizzari, R. Grzeszczuk, G.T.Y. Chen, et al.; ***Volumetric Visualization Of anatomy For Treatment Planning***, Int. J. Radiation Oncology Biol. Phys., Vol:34, pp:205 -211, 1996

[Peliz98] C.A. Pelizzari; ***Image Processing In Stereotactic Planning: Volume Visualization and Image Registration***, Medical Dosimetry, Vol: 23, pp: 137-145, 1998

[Perez94] C. Perez, J.A. Purdy, W. Harms, et al.; ***Design of a Fully Integrated Three-dimensional Computed Tomography Simulator and Preliminary Clinical Evaluation***, Int. J. Radiation Oncology Biol. Phys., Vol: 30, pp:887-897, 1994

[Perez95] C.A. Perez, J.A. Purdy, W. Harms, et al.; ***Three-dimensional Treatment Planning and Conformal Radiation Therapy: Preliminary Evaluation***, Radiotherapy and Oncology, Vol: 36, pp:32-43, 1995

[Press93] W.H. Press, B.P. Flannery, S.A. Teukolsky, and W.T. Vetterling; ***Numerical Recipes in C : The Art of Scientific Computing,*** 1993.

[Purdy93] J.A. Purdy, W.B. Harms, J.W. Matthews, et al.; ***Advances In 3-Dimensional Radiation Treatment Planning Systems: Room-View Display With Real Time Interactivity***, Radiation Oncology Biol.Phys, Vol: 27, pp:933-944, 1993

[Purdy96] J.A. Purdy; ***3D Radiation Treatment Planning: A New Era***, Front Radiat Ther Oncol. Basel, Karger, Vol: 29, pp:1-16, 1996

[Ragan96] D.P. Ragan, J.D. Forman, T. He, and C.F. Mesina; ***Clinical Results of Computerized Tomography-based Simulation with Laser Patient Marking***, ***Int.J.Radiation Oncology Biol.Phys*** ., Vol: 34, pp:691-695, 1996

[Rams98] C.R. Ramsey, and A.L. Oliver; ***Magnetic Resonance Imaging based Digitally Reconstructed Radiographs, Virtual Simulation, and Three-dimensional Treatment Planning for Brain Neoplasms***, Medical Physics, Vol: 25, pp: 1928-1934, 1998

[Ritch96] C. Ritchie, C. Crawford, D. Godwin, K. King, and Y. Kim; ***Correction of Computer Tomography Motion Artifacts Using Pixel-Specific Back-Projection***, IEEE Trans.On Medical Imaging, Vol: 15, pp:333-342, 1996

[RitmA80] E. Ritman; ***Physical and Technical Considerations in the Design of the DSR, and High Temporal Resolution Volume Scanner***, American Journal of Roentgenology, Vol: 134, pp: 369-374, 1990

[RitmB90] E. Ritman; ***Fast Computed Tomography for Quantitative Cardiac Analysis-State of the Art and Future Perspectives***, Mayo Clin Proceedings, Vol: 65, pp:2724-2727, 1990

[Rohli99] R. Rohling, A. Gee, and L. Berman; ***A Comparison of Freehand Three-dimensional Ultrasound Reconstruction Techniques***, Medical Image Analysis, Vol: 3, pp:339-359, 1999

[Rose96] J. Rosenman; ***Where Will 3D Conformal Radiation Therapy Be at the End of the Decade?***, Front Radiation Therapy Oncology, Vol: 29, pp:264-271, 1996

[Rosen91] J. Rosenman, S. Sailer, G. Sherouse, E.L. Chaney, and J.E. Tepper; ***Virtual Simulation: Initial Clinical Results***, Int. J. Radiation Oncology Biol. Phys., Vol: 20, pp:843-851, 1991

[Sabel88] P. Sabela; ***A Rendering Algorithms for Visualizing 3D Scalar Fields***, Computer Graphics, SIGGRAPH' 88, pp: 51-58, 1988

[Sakas93] G. Sakas; ***Interactive Volume Rendering of Large Fields***, The Visual Computer, Vol: 9, pp:425-438, 1993

[Sakas95] G. Sakas, M. Grimm, and A. Savopoulos; ***Optimised maximum intensity*** projection (MIP), Rendering Techniques'95, Springer Verlag, pp:51-63, 1995

[Sakas01] G. Sakas, G. Karangelis, and A. Pommert; ***Advanced Applications of Volume Visualization Methods in Medicine***. In Advanced Signal Processing Handbook, Theory and Implementation for Radar, Sonar, and Medical Imaging Real-Time Systems, Edited by Stergios Stergiopoulos, CRC Press, ISBN 0-8493-3691-0, 2001

[SanGa95] P. Santiago, and H.D. Gage; ***Statistical-models of Partial Volume Effect***, IEEE Trans. On Image Processing, Vol: 4, pp.1531-1540, 1995

[Sato00] Y. Sato, C. Westin, A. Bhalerao, S. Nakajima, N. Shiraga, T. Tamura, and R. Kikinis; ***Tissue Classification Based On 3D Local Intensity Structures for Volume Rendering***, IEEE Trans. On Visualization and Computer Graphics, Vol: 6, pp.160-179, 2000

[Savch95] V. Savchenko, A. Pasko, O. Okunev, and T. Kunii; ***Function Representationof Solids Reconstructed from Scatter Surface Points and Contours,*** Computer Graphics Forum, Vol: 14, pp181-188, 1995

[Schie00] M. Schiebe, and W. Hoffmann***; CT-Based Virtual Simulation Using the Advantage Sim 4.1. System***, Strahlenther Onkol, Vol: 8, pp:377-380, 2000

[Schim93] T. Schiemann, B. Dippold, R. Schmidt, et al.; ***3D Visualization For Radiotherapy Treatment Planning***, In Proceedings of Computer Assisted Radiology and Surgery, CARS '93 (H.U. Lemke, M.L. Rhodes, C.C. Jaffe, and R. Felix, eds.), Springer-Verlag, Berlin, pp:669-675, 1993

[Seem01] M.D. Seemann, and C.D. Claussen; ***Hybrid 3D Visualization of the Chest and Virtual Endoscopy of the Tracheobronchial System: Possibilities and Limitations of Clinical Application***, Lung Cancer, Vol: 32, pp:237-246, 2001

[Seymo95] M.A. Seymour, I. Kalet, J. McDonald, et al.; ***Three Dimensional Planning Target Volumes: A Model And A Software Tool***, Radiation Oncology Biol.Phys, Vol: 33, pp:1073-1080, 1995

[Shale95] S. Shalev; ***Treatment Verification Using Digital Imaging,*** Radiation Therapy Physics ed.AR Smith.Springer, pp:155-173, Berlin1995

[Shero87] G. Sherouse, C. Mosher, K. Novins, J. Rosemann, and E.L. Chaney; ***Virtual Simulation: Concept and Implementation***, Proceedings of 9th International Conference of the Use of Computers in Radiation Therapy (ICCR), pp:433-436, 1987

[Shero90] G.W. Sherouse, J.D. Bourland, K. Reynolds, H.L. McMurry, T.P. Mitchell, and E.L. Chaney; ***Virtual Simulation in the Clinical Setting: Some Practical Considerations***, Int. J. Radiation Oncology Biol. Phys., Vol: 19, pp:1059-1065, 1990

[Shero91] G. Sherouse, and E.L. Chaney; ***The Portable Virtual Simulator***, Int. J. Radiation Oncology Biol. Phys., Vol: 21, pp:475-482, 1991

[Shiyi01] H. Shiying, E.A. Hoffman, and J.M. Reinhardt; ***Automatic Lung Segmentation For Accurate Quantitation Of Volumetric X-Ray CT Images***, IEEE Transactions On Medical Imaging, Vol: 20, pp:490-498, 2001

[Siada01] M.R. Siadat, and H. Soltanian-Zadeh; ***Partial Volume Estimation using Continuous Representations,*** SPIE Proc., Vol: 4322, pp:1025-1034, 2001

[SmartS] http://www.medical.philips.com/main/products/ros/products/smartsim/

[Smith90] B. Smith; ***Cone-beam tomography: recent advances and a tutorial review***, Opt. Eng., Vol: 29, pp: 521-534, 1990

[VanSo03] J.R. Van Sornsen, R.H. Schuchhard-Schipper, S. Senan, B.J. Heijmen; ***Procedures for high precision setup verification and correction of lung cancer patients using CT-simulation and digitally reconstructed radiographs (DRR)***, Int. J. Radiation Oncology Biol. Phys., Vol: 55, pp:804-810, 2003

[Spath95] H. Spath; ***Two Dimensional Spline Interpolation Algorithms,*** A.K. Peters Ltd, 1995

[Stras04] G. Strassmann, P. Vacha, I. Braun, D. Richter, and R. Engenhart-Cabillic; ***Methodology of Continuous Extracranial Radiosurgery for Lung Cancer Using EXOMIO 3-D CT Simulation***, Strahlentherapie und Oncologie, Vol: 180, pp:241-244, 2004

[StraV04] G. Strassmann, P. Vacha, T. Osterhaus, A. Battmann et. al.; **Evaluation of a Laser System for CT Software Simulation (EXOMIO) in Patients with Breast Cancer**, Strahlentherapie und Oncologie, Vol: 180, pp:597-600, 2004

[Taubi95] G. Taubin; ***A Signal Processing Approach To Fair Surface Design***, Computer Graphics, SIGGRAPH' 95, pp: 351-358, 1995

[Terzo88] D. Terzopoulos, and K. Fleischer; ***Deformable Models***, The Visual Computer, Vol: 4, pp: 306-331, 1988

[Thürm01] G. Thürmer; ***Smoothing Normal Vectors On Discrete Surfaces While Preserving Slope*** **Discontinuities**, Computer Graphics, Vol: 20, pp:103-114, 2001

[Thürm97] G. Thürmer, and C.A. Wüthrich; ***Normal Computation For Discrete Surfaces In 3D Space***, In Proceedings of Eurographics'97, Vol: 16, 1997

[Tsiak01] M.F. Tsiakalos, E. Schrebmann, K. Theodorou, and C. Kappas; ***Graphical Treatment Simulation and Automated Collision Detection for Conformal and Stereotactic Radiotherapy Treatment Planning***, Med.Physics, Vol: 28, pp:1359-1363, 2001

[Turk02] G. Turk, and J.F. O'Brien; ***Modelling with Implicit Surfaces that Interpolate***, ACM Transaction on Graphics, Vol: 21, pp: 1-19, 2002

[Turk99] G. Turk, and J.F. O'Brien; ***Shape Transformation Using Variational Implicit Functions***, Computer Graphics, SIGGRAPH'1999, pp. 335-342, 1999

[TurkB99] G. Turk, and J.F. O'Brien; ***Variational Implicit Surfaces***, Tech Report GIT-GVU-99-15, Georgia Institute of Technology, May 1999

[Twidd94] R. Twiddy, J. Cavallo, and S.M. Shiri; ***Restorer: A Visualization Technique for Handling Missing Data***, In Proceedings of IEEE Visualization'94, pp:212-216, 1994

[Valen03] V. Valentini, A. Piermattei, A.G. Morganti, M.A. Gambacorta, L. Azario, ***et al***; ***Virtual simulation: fifteen years later***, Rays. Vol. 28, pp:293-298, 2003

[ValiA97] R.K. Valicenti, F.M. Waterman, B.W. Corn, and W.J. Curran; ***A Prospective Randomized Study Addressing the Need for Physical Simulation following Virtual Simulation***, Int. J. Radiation Oncology Biol. Phys., Vol: 39, pp:1131-1135, 1997

[ValiB97] R.K. Valicenti, F.M. Waterman, R.J. Croce, B. Corn; and W.J. Curran; ***Efficient CT Simulation of the Four-Field Technique For Conformal Radiotherapy of Prostate Carcinoma***, Int. J. Radiation Oncology Biol. Phys., Vol:37, pp:953-957, 1997

[VanHe94] M. VanHerk, and H.M. Kooy; ***Automatic Three-Dimensional Correlation of CT-CT, CT-MRI, and CT-SPECT using Chamfer Matching***, Medical Physics, Vol: 21, pp: 1163-1178, 1994

[Vanuy99] L. Vanuytsel, and C. Weltens; ***Imaging Techniques for Radiotherapy Planning***, Oncology in Practice, Vol: 2, pp: 18-21, 1999

[Vasil83] V.A. Vasilenko; ***Spline-functions: theory, Algorithms, Programs,*** Novosibirsk, Nauka Publishers, 1983

[VDBer00] D.L. Van De Berge, M.De Ridder, and G.A. Storme; ***Imaging In Radiotherapy***, European Journal Of Radiology, Vol:34, pp:41-48, 2000

[Verel99] D. Verellen, V. Vinh-Hung, P. Bijdekerke, et al.; ***Characteristics and clinical application of a treatment simulator with CT-option***, Radiotherapy And Oncology, Vol: 50, pp:355-366, 1999

[Vijay95] S. Vijayakumar, and G.T.Y. Chen; ***Implementation of Three Dimensional Conformal Radiation Therapy: Prospects, Opportunities, and Challenges***, Int. J. Radiation Oncology Biol. Phys., Vol: 33, pp:976-983, 1995

[Vollm99] J. Vollmer, R. Mencl, and H. Müller; ***Improved Laplacian Smoothing Of Noisy Surface Meshes***, In Proceedings of Eurographics'99, Vol: 18, 1999

[Vuong00] T. Vuong, W. Parker, H.J. Patrocinio, et al.; ***An Alternative Mantle Irradiation Technique Using 3D CT-based Treatment Planning for Female Patients with Hodgkin's Disease***, Int.J. Radiation Oncology Biol.Phys., Vol: 47, pp: 739-748, 2000

[Wang94] S.W. Wang, and A.E. Kaufman; ***Volume-Sampled 3D Modeling***, IEEE Computer Graphics And Applications, Vol: 14, pp: 26-32, 1994

[Weist00] D. Weinstein; ***Scanline Surfacing: Building Separating Surfaces from Planar Contours***, In Proceeding of 11th IEEE Visualization'2000, 2000

[Wells98] D.M. Wells, and J. Niederer; ***A Medical Expert System Approach Using Artificial Neural Networks for Standardized Treatment Planning***, Int.J.Radiation Oncology Biol. Phys**.**, Vol: 41, pp:173-182, 1998

[Welte99] L. Weltens; ***Imaging Techniques for Radiotherapy Planning***, Oncology in Practice, Vol: 2, pp: 18-21, 1999

[Whita00] R. Whitaker; ***Reducing Aliasing Artifacts in Iso-Surfaces of Binary Volumes,*** In Volume Visualization and Graphics Symposium 2000. ACM SIGGGRAPH, pp:23-32, 2000

[Willn03] J. Willner, A. Jost, K. Baier, and M. Flentje; ***A Little to a Lot or a Lot to a Little?,*** Strahlentherapie und Oncologie, Vol: 179, pp:548-556, 2003

[Wolbe90] G. Wolberg; ***Digital Image Warping***, Wiley-IEEE Press, 1rst Edition, 1990

[Wong99] J.W. Wong, M.B. Sharpe, D.A. Jaffray, et al.; ***The Use of Active Breathing Control (ABC) to Reduce Margin for Breathing Motion***, Int. J. Radiation Oncology Biol. Phys**.**, Vol: 44, pp: 911-919, 1999

[Yan00] C.H. Yan, R.T. Whalen, G.S. Beaupre, S.Y. Yen, and S. Napel; ***Reconstruction Algorithm for Polychromatic CT Imaging: Application to Beam Hardening Correction***, IEEE Trans. On Medical Imaging, Vol: 19, pp:1-11, 2000

[Yan97] D. Yan, J. Wong, F. Vicini, J. Mchalski, C. Pan, A. Frazier, E. Horwitz, and A. Martinez; ***Adaptive Modification of Treatment Planning to Minimize the Deleterious Effects of Treatment Setup Errors,*** Int.J.Radiation Oncology Biol.Phys, Vol: 38, pp:197-206, 1997

[Yoo01] T. Yoo, B. Morse, K.R. Subramanian, P. Rheingans, and M. Ackerman; ***Anatomic Modeling From Unstructured Samples Using Variational Implicit Surfaces***, In Medicine Meets Virtual Reality, 2001

[Zambo94] N. Zamboglou, T. Schnabel, C. Kolotas, W. Achterrath, H. Strehl ***et al***; ***Carboplatin and radiotherapy in the treatment of head and neck cancer: six years' experience***. Semin Oncol. Vol: 21, pp:45-53, 1994

[Zambo02] N. Zamboglou, G. Karangelis, I. Nomikos, S. Zimeras, T.Helfmann ***et al***; **EXOMIO Virtual Simulation: Oropharynx, Prostate & Breast Cancer**, In Progress in CT-3D Simulation, 1rst Exomio User Meeting, Lemessos-Cyprus, November, 2002

[Zelez97] M.P. Zeleznik; ***3D Visualization: What Does it Mean?***, XII International Conference On The Use Of Computers In Radiation Therapy (ICCR), MO University of Utah, Salt Lake City, pp:27-30, 1997

[Zuide95] K.J. Zuiderveld; ***Visualization of Mulitmodal Medical Volume Data using Object-Orientated Methods***, PhD Thesis, Utrecht University, 1995